

UNIVERSITY OF CALIFORNIA,
IRVINE

Molecular Composition, Optical Properties, and Chemical Aging of Primary and Secondary
Organic Aerosol

DISSERTATION

submitted in partial satisfaction of the requirements
for the degree of

DOCTOR OF PHILOSOPHY

in Chemistry

by

Lauren Thomson Fleming

Dissertation Committee:
Professor Sergey A. Nizkorodov, Chair
Professor Donald R. Blake
Professor Barbara J. Finlayson-Pitts

2019

Chapters 2 and 3 © 2018 Lauren Thomson Fleming
Parts of Chapter 5 © 2019 American Chemical Society
All other materials © 2019 Lauren Thomson Fleming

TABLE OF CONTENTS

	Page
LIST OF FIGURES.....	v
LIST OF TABLES.....	x
ACKNOWLEDGMENTS.....	xiii
CURRICULUM VITAE.....	xvii
ABSTRACT OF THE DISSERTATION.....	xxii
CHAPTER 1: INTRODUCTION.....	1
1.1 Background and motivation: climate and health impacts.....	1
1.2 Formation, growth, and aging of aerosol particles.....	4
1.2.1 Summary of aerosol life cycle.....	4
1.2.2 Composition of biomass burning organic aerosol and its relationship with combustion processes.....	6
1.2.3 Photochemical aging of biomass burning organic aerosol.....	9
1.2.4 Secondary BrC formed during the processing of cloud droplets.....	13
1.2.5 Effect of relative humidity on the composition and mass of SOA particles.....	16
1.3 Research questions and dissertation structure.....	18
CHAPTER 2: Emissions from village cookstoves in Haryana, India, and their potential impacts on air quality.....	21
2.1 Introduction.....	22
2.2 Experimental methods.....	24
2.2.1 Field site and sample collection.....	24
2.2.2 Gas chromatography analysis.....	26
2.2.3 Gas and PM _{2.5} emission factor calculations.....	27
2.2.4 Modified combustion efficiency.....	29
2.2.5 SOA-forming potential.....	29
2.2.6 OH reactivity.....	35
2.2.7 Ozone-forming potential.....	35
2.2.8 Statistical analysis.....	36
2.3 Results and discussion.....	36
2.3.1 Chemical composition.....	36
2.3.2 Modified combustion efficiency.....	50

2.3.3 Secondary pollutant formation and reactivity	53
2.3.3.1 OH reactivity and ozone forming potential	53
2.3.3.2 SOA formation potential	54
2.4 Atmospheric implications and conclusions.....	55

CHAPTER 3: Molecular Composition of Particulate Matter Emissions from Dung and Brushwood Burning Household Cookstoves in Haryana, India..... 57

3.1 Introduction.....	58
3.2 Experimental Methods.....	63
3.2.1 Field site	63
3.2.2 Sample Collection	63
3.2.3 PM _{2.5} emission factor calculation	66
3.2.4 Nano-DESI-HRMS analysis	68
3.2.5 HPLC-PDA-HRMS	70
3.2.6 MAC _{bulk} and AAE	71
3.3 Results and Discussion.....	72
3.3.1 Nano-DESI-HRMS analysis of cookstove particles	72
3.3.2 Particle-phase biomass burning markers	76
3.3.3 Compounds common to dung/ <i>chulha</i> , dung/ <i>angithi</i> , brushwood/ <i>chulha</i> cook fires	80
3.3.4 Compounds found exclusively in the emissions from brushwood/ <i>chulha</i> cook fires	85
3.3.5 Species unique to dung smoke PM _{2.5}	87
3.3.6 Light-absorbing properties and chromophores from cookstove emissions	99
3.4 Summary.....	108

CHAPTER 4: Molecular composition and photochemical lifetimes of brown carbon chromophores in biomass burning organic aerosol particles generated during FIREX.. 110

4.1 Introduction.....	112
4.2 Experimental methods.....	118
4.2.1 Sample collection and information	118
4.2.2 HPLC/PDA/HRMS	119
4.2.3 Condensed-phase photolysis	120
4.2.4 Spectral flux/irradiance measurements for LED and Xe Arc lamps	123
4.2.5 Calculation of the estimated BrC absorption lifetime	124
4.3 Results and Discussion.....	126
4.3.1 BrC Chromophores	126
4.3.2 Condensed-phase photolysis	145
4.4 Conclusions and Implications.....	152

CHAPTER 5: Formation of light-absorbing organosulfates during evaporation of secondary organic material extracts in the presence of sulfuric acid..... 155

5.1 Introduction.....	156
5.2 Materials and Methods.....	158
5.2.1 SOM Generation.....	158
5.2.2 SOM Extraction.....	161
5.2.3 Evaporation Experiments and MAC measurements.....	161
5.2.4 Brown Carbon Chromophore Analysis.....	162
5.3 Results and Discussion.....	164
5.3.1 Optical Properties.....	164
5.3.2 BrC Chromophores.....	170
5.4 Summary and Implications.....	177

CHAPTER 6: The effect of water vapor and aerosol liquid water on the molecular composition of secondary organic aerosol..... 179

6.1 Introduction.....	180
6.2 Experimental Methods.....	182
6.2.1 SOA generation.....	182
6.2.2 Aging in humid air.....	183
6.2.3 Nano-DESI HRMS.....	183
6.3 Results and Discussion.....	184
6.4 Summary.....	190

REFERENCES..... 193

LIST OF FIGURES

- | | Page |
|--|-------------|
| Figure 2.1: Sampling train for collecting cookstove emissions. PCXR8 (blue) are sampling pumps, WAS or whole air samples (green) are the air samplers, and orange boxes are Teflon or quartz filters used to collect PM _{2.5} . | 26 |
| Figure 2.2: Emission factors (g VOC/ kg fuel C) versus moisture content of the fuel. Red markers indicate dung fuel was used, while blue markers indicate brushwood fuel. Filled square markers indicate <i>chulha</i> stoves, while open circles indicate <i>angithi</i> stoves were used. If a significant correlation was observed ($r^2 > 0.70$) for a particular fuel-stove combination, the linear regression trendline is shown. | 43 |
| Figure 2.3: Pie charts showing the contribution of each species class to gas-phase composition (a), OH reactivity (b), SOAP-weighted emissions (c), and ozone-forming potential (d). For (b) and (d), total aromatics are shown rather than the breakdown of aromatics shown in (a) and (c). Sums of all components are shown below the pie chart. | 44 |
| Figure 2.4: Comparison of EFs (g/ kg dry fuel) in the present study to those of Stockwell et al., 2016 (adjusted). The blue line indicates 1:1 agreement of the emission factors, with points above the blue line indicating higher EFs reported in Stockwell et al., 2016. Likewise, points below represent compounds that have a higher EF in the present study. | 49 |
| Figure 2.5: Emission factors (g/ kg fuel C) plotted as a function of modified combustion efficiency for select species. Open circles indicate cooking events conducted with <i>angithi</i> stoves, whereas filled squares indicate <i>chulha</i> stoves. Color indicates fuel, either brushwood (blue), dung (red), or mixed (purple). Crosses indicate measurements from Stockwell et al. 2016. | 50 |
| Figure 2.6: Emission factors as a function of modified combustion efficiency (MCE) for select species. Open circles indicate cooking events conducted with <i>angithi</i> stoves, whereas filled squares indicate <i>chulha</i> stoves. Color indicates fuel, either brushwood (blue), dung (red), or mixed (purple). | 52 |
| Figure 3.1: The field site and set-up for cooking events. A) The kitchen set-up at the field site. B) The stoves and fuels used in this study: <i>angithi</i> , dung-burning <i>chulha</i> , and brushwood-burning <i>chulha</i> . | 64 |
| Figure 3.2: Stoves used in the study, the <i>angithi</i> and <i>chulha</i> , are pictured. Stove measurements and distances from the stoves to the inlet probes are found in the tables below. | 65 |

Figure 3.3: Representative nano-DESI mass spectra collected for a) dung/*angithi* b) dung/*chulha* and c) brushwood/*chulha* cookfires. Relative abundance is plotted against m/z . Peaks are colored by their elemental makeup, $C_xH_yN_w$ (red), $C_xH_yO_zN_w$ (purple), $C_xH_yO_z$ (blue), potassium salts (green), and unassigned (black). The pie charts illustrate the fraction of count-based, normalized peak abundance that is attributed to each elemental category. **73**

Figure 3.4: An overview of the particle-phase compounds inventory based on the results of molecular characterization using nano-DESI-HRMS. Each area of the Venn diagram contains the bolded number of reproducibly-detected formulas in blue as well as the Table that lists peaks for each category. Merging all the tables listed here provides a complete inventory of compounds detected in this study. **77**

Figure 3.5: A summary of the inventory in terms of the count-based, normalized peak abundances. A) Contribution of $PM_{2.5}$ compounds to each elemental formula category for those found in all cookfires and those found in all dung-burning cookfires. B) The compounds by cookstove type classified as compounds common to all cookfires in grey, compounds common to all dung cookfires in brown, and unique compounds in orange. **79**

Figure 3.6: Double bond equivalent (DBE) as a function of the carbon number for a) a combined set of compounds detected from all dung cookfires (brown circle) and b) compounds all cookfires have in common (grey diamond) as well as compounds exclusively found in brushwood (blue circle). Markers representing one or multiple species are sized by their LOW, MEDIUM, and HIGH designations. The curves illustrate theoretically where terpenes (red) and polyenes (green) would fall. Similarly, the yellow-shaded region shows where PAHs would appear, including: cata-condensed PAHs with 0, 1, and 2 heterocyclic nitrogen atoms and circular PAHs. **96**

Figure 3.7: Possible structures of N-heterocyclic PAHs found in dung cookfire emissions. $C_{13}H_9N$ was detected reproducibly in dung/*chulha* emissions only, while $C_{12}H_9ON$ and $C_{11}H_8N_2$ were reproducibly detected in all dung cookfires. **97**

Figure 3.8: The CH_2 Kendrick mass defect plot for compounds emitted only from dung stoves. The marker color determines the compound category for $C_xH_yN_w$ compounds (red), $C_xH_yO_z$ (blue), or $C_xH_yO_zN_w$ (purple). Marker shape indicates the stove(s) that reproducibly produced the compound: *chulha* and *angithi* (\bullet), *angithi* (\square), or *chulha* ($+$). Homologous series are identified with dotted horizontal lines suggesting they have similar structures. **98**

Figure 3.9: Comparing MAC_{bulk} ($m^2 g^{-1}$) for organic solvent extractable material from brushwood/*chulha* (blue) and dung/*chulha* (red) samples. Shaded regions represent errors due to extraction efficiency and sampling flow rates. **100**

Figure 3.10: HPLC-PDA chromatogram showing BrC chromophores detected in the emission samples from a) brushwood and b) dung cookfires. Highly-absorbing molecules and their corresponding PDA retention times are given above the peak. **103**

Figure 3.11: UV-Vis absorption spectra from the PDA analysis of cookstove BBOA samples. The blue and red curves represent the background-subtracted absorbance at retention time of 15.57 min for brushwood-derived PM_{2.5} and dung-derived PM_{2.5}, respectively. The reference absorption spectrum of ethyl-3-methoxybenzoate (green) was reproduced from the NIST Chemistry WebBook database (Talrose et al., 2017). The structure of ethyl-3-methoxybenzoate is pictured. **107**

Figure 4.1: Spectral flux density (photons cm⁻² s⁻¹ nm⁻¹) approximated for a solar zenith angle of 0° (orange) as well as the 24-hour average for the latitude and longitude of Los Angeles (34° latitude, 118° longitude) on June 20, 2017 (red). The spectral flux density for the 300 nm LED (blue) and the filtered Xe arc lamp (green) are also shown. **122**

Figure 4.2: The natural logarithm of the integrated absorbance (300-700 nm), Abs/Abs₀, plotted as a function of irradiation time. The magnitude of the slope of the trend line corresponds to the first-order decay constant (s⁻¹) according to the integrated first order rate law. The inverse of the first-order decay constant is the lifetime of the overall absorption (300-700 nm) of the BBOA material. **125**

Figure 4.3: Absorption spectra of the same subalpine fir duff BBOA sample, recorded in a) the condensed phase (by measuring transmission through particle-loaded filter material) and b) the solution phase (by measuring transmission through a cuvette with a filter extract). The average of four absorption spectra is shown for each irradiation time point in a), and the standard deviation of these measurements are indicated with error bars. **125**

Figure 4.4: Lignin pyrolysis products sinapaldehyde (C₁₁H₁₂O₄) and coniferaldehyde (C₁₀H₁₀O₃) elute at slightly different retention times, at roughly 18.1 and 18.4 min, respectively. **135**

Figure 4.5: Chromophores present before (top panel) and after (bottom panel) photolysis for a conifer fuel, lodgepole pine. **146**

Figure 4.6: Chromophores present before (top panel) and after (bottom panel) photolysis for angiosperm fuel, ceanothus. **146**

Figure 4.7. Approximate atmospheric lifetime for select BrC chromophores due to direct photolysis that exist in BBOA particles from chamise, manzanita, and lodgepole pine fires (the photolysis times are listed in table 4.4). **148**

Figure 5.1: MAC values of SOM from (a) LIM/OH, (b) LIM/OH/NO_x, (c) APIN/O₃, (d) APIN/OH, (e) APIN/OH/NO_x, (f) BPIN/O₃, (g) ISO/OH, (h) ISO/OH/NO_x, (i) TOL/OH, and (j) TOL/OH/NO_x, in initial aqueous solution (black), after addition of H₂SO₄ to the solution until it reached pH 2 (red), after evaporation of acidified solution (green), after second evaporation of same solution (dark green), and after evaporation with SOM and water only (blue). **165**

Figure 5.2: MAC values of LIM/O₃ SOM dissolved in 2 mL of water (black trace in panel a) (black). Also shown are MAC values after the addition of H₂SO₄ to pH 2 in 2 mL of water and further dilution to 4 mL and 20 mL (red); after evaporation of the solutions (green), and after evaporation with LIM/O₃ SOM and water only (blue). In (b), the evaporated solution was re-dissolved in 4 mL of H₂O, and MAC values were calculated (green). In (c), the evaporated solution was re-dissolved first in 2 mL of H₂O (green) and then to a total volume of 20 mL of H₂O (dark dashed green). **167**

Figure 5.3: MAC values of LIM/O₃ SOM, with the solvent as (a) water, (b) acetonitrile, or (c) methanol, in initial solution (black), after addition of H₂SO₄ to pH 2 in water or addition of an equal amount of H₂SO₄ in acetonitrile and methanol (red), after evaporation of solution (green), and after evaporation with LIM/O₃ SOM and solvent only (blue). **169**

Figure 5.4: Combined positive and negative mass spectra when limonene ozonolysis SOM is extracted in a) acetonitrile and b) water, then evaporated and re-dissolved in the extraction solvent. Peaks in green and red appear when sulfuric acid (H₂SO₄) is added prior to evaporation. Peaks in red contain sulfur and four or more oxygens, and identified as potential organosulfates in this paper. Peaks in black occur when sulfuric acid is not added. The largest red peak corresponds to C₁₀H₁₆SO₇. **171**

Figure 5.5: Single ion chromatogram for the *m/z* 279 ion in the negative mode, corresponding to C₁₀H₁₆SO₇. The acetonitrile extract is in blue and water extract in red. **172**

Figure 5.6: Structures of organosulfates a) C₁₀H₁₈SO₇ reported in Iinuma et al. (2007) based on MSⁿ analysis b) C₁₀H₁₈SO₅ reported in Wang et al. 2017 based on synthetic standards. **173**

Figure 5.7: Dimer region of the mass spectrum corresponding to the LIM/O₃ SOM water extract evaporated in the presence of sulfuric acid. Horizontal blue lines indicate the loss of water. **174**

Figure 5.8: 3D (a) and 2D (b) HPLC-PDA chromatograms for the water LSOM extract. (b) shows the integrated PDA counts for 380 to 450 nm. Between 8 and 12 minutes, compounds absorbing visible light elute from the column, and are largely unresolved. **175**

Figure 6.1: Combined positive and negative ion mode mass spectra of α -pinene/photooxidation SOA formed in the presence of ammonium sulfate seeds (a and b) or exclusively from gas to particle conversion (c and d). a) and c) were formed under dry conditions, while b) and d) were formed at approximately 90% RH. In each mass spectrum, chemical formulas corresponding to monomer and dimer peaks with the highest abundances are shown. The average O:C and H:C ratios weighted by peak abundances are given for each mass spectrum. **185**

Figure 6.2: The dimer-to-monomer ratio for the reaction in equation (6.1) for fresh SOA and after it was aged in humid conditions. **187**

Figure 6.3: Modelled SOA particle viscosity as a function of RH for SOA formed in the presence of ammonium sulfate seeds (a and b) or exclusively from gas to particle conversion (c and d). a) and c) were formed under dry conditions, while b) and d) were formed at approximately 90% RH. The solid line indicates particles that were not aged, while the dashed line represents the particles that were aged in a humid atmosphere. The glass transition temperature (T_g) was calculated for the not aged particles, and is also indicated on the graph. **189**

Figure 6.4: Peak abundances in the mass spectra are binned by their volatility. Blue bars are for the particles that were not aged, and the orange bars represent particles that were aged in a humid atmosphere. **190**

LIST OF TABLES

Page

Table 2.1: Average emission factors and standard deviation of PM_{2.5} and gas-phase species (g kg⁻¹ dry fuel carbon) for dung-*chulha*, brushwood-*chulha*, mixed-*chulha*, and dung-*angithi* cook fires. Sample size (n) was n=12 for dung-*chulha*, n=14 for brushwood-*chulha*, n=13 for mixed-*chulha*, n=10 for dung-*angithi*. SOAP values, k_{OH}, and MIR values used to calculate predicted SOAP-weighted potentials, OH reactivity, and ozone-forming potential are included for the quantified species. SOAP values were taken from Derwent et al. (2010), k_{OH} were found in the NIST Chemical Kinetics Database, and MIR values are found in Carter et al. 1994.

31

Table 2.2: Averaged emission factors and standard deviation of PM_{2.5} and gas-phase species (g kg⁻¹ dry fuel) for dung-*chulha*, brushwood-*chulha*, mixed-*chulha*, and dung-*angithi* cook fires. Previously published emission factors (g kg⁻¹ dry fuel) from dung and hardwood cook fires are shown for comparison (Stockwell et al. 2016). Sample sizes for the current study (n) were n=18 for dung-*chulha*, n=14 for brushwood-*chulha*, n=13 for mixed-*chulha*, and n=10 for dung-*angithi*.

38

Table 2.3: Emission factors (g VOC/ kg fuel C) for select compounds. The mean differences between dung/*angithi* and dung/*chulha* are shown and similarly for dung/*chulha* and brushwood/*chulha*. The significance between fuel or stove and EF is indicated with asterisks. Accompanying the mean differences is the average emission factor (g VOC/ kg fuel C) for dung cook fires and *chulha* cook fires, as well as the overall average for all performed cook fires.

46

Table 3.1: Samples utilized in sections 3.3.1-3.3.5. Representative mass spectra shown in Figure 3.3, section 3.3.1 correspond to samples M10, L7, and M1. The % abundance for C_xH_yO_z, C_xH_yN_w, and C_xH_yO_zN_w peaks from the nano-DESI mass spectra are given as well as arithmetic means and standard deviations for each cookfire category: brushwood/*chulha*, dung/*chulha*, and dung/*angithi*.

74

Table 3.2: List of common compounds found in all PM_{2.5} samples regardless of fuel or stove type. Tentative molecular structure assignments are listed when the compound has previously been identified in the chemical biomass-burning literature, supported by the references in the last column. Count-based, normalized peak abundances are designated LOW (<1%), MEDIUM (1-9.99%), HIGH (10-100%). All species were detected as protonated ions.

82

Table 3.3. List of reproducible compounds found exclusively in the brushwood samples. Tentative molecular structure assignments are listed when the compound has previously been identified in the chemical biomass-burning literature. Normalized, relative peak abundances are designated LOW (<1%), MEDIUM (1-9%), High (10-100%). All species were detected as protonated ions.

86

Table 3.4: List of compounds found exclusively in the emissions from dung cookfires, regardless of stove type. The labels for the peak abundances are the same as in Table 3.2. All species were detected as protonated ions unless otherwise noted.	88
Table 3.5: List of reproducible compounds detected exclusively in the emissions from dung/ <i>chulha</i> cookfires. The labels for peak abundances are the same for Table 3.3. All species were detected as protonated ions.	93
Table 3.6: List of reproducible compounds detected exclusively in the emissions from dung/ <i>angithi</i> cookfires. The labels for peak abundances are the same for Table 3.3. All species were detected as protonated ions, except for C ₁₂ H ₁₃ ON, which was detected as a [M+Na] ⁺ ion.	94
Table 3.7: Samples utilized in section 3.3.6 for MAC and AAE analyses.	101
Table 3.8: Samples analyzed in section 3.3.6 via HPLC-PDA-HRMS.	102
Table 3.9: The list of retention times, absorption peak maxima, and chemical formulas of the BrC chromophores detected in the brushwood smoke sample. Tentative assignments are given based on compounds previously identified in the lignin pyrolysis literature.	104
Table 3.10: The list of retention times, absorption peak maxima, and chemical formulas of the BrC chromophores detected in the the dung smoke sample. Tentative assignments are given based on compounds previously identified in the lignin pyrolysis literature.	105
Table 4.1: Summary of the fires from which BBOA samples were collected.	119
Table 4.2: Chromophores common among multiple fuel types are listed by their range in HPLC retention times, absorption spectra, assigned elemental formulas, and examples of possible structures. The absorbance by each chromophore is binned by photodiode array absorbance normalized to the highest absorbance in each chromatogram: M-Major (75%-100%), I-Intermediate (25%-75%), or W-Weak (5%-25%). The absorption spectra of the standard may not fully match the absorption spectra of the eluents because the separation is not complete, and more than one compound is eluted at any given time. The shown absorption spectra are baseline corrected by subtracting the spectrum at a nearby retention time where the PDA absorbance is low.	128
Table 4.3: Chromophores found appreciably in only one fuel type listed by their HPLC retention times, absorption spectra, assigned elemental formulas, and examples of possible structures. The absorbance by each chromophore is binned by photodiode array absorbance normalized to the highest absorbance in each chromatogram: M-Major (75%-100%), I-Intermediate (25%-75%), or W-Weak (5%-25%).	139

Table 4.4: Filter irradiation times for different samples used to estimate lifetimes of individual chromophores. **147**

Table 4.5. Lifetimes for the loss of the measured integrated absorbance from 300 to 700 nm (expressed in equivalent days of solar exposure). The lifetimes were calculated from the transmission spectra measured for particles on PTFE filters. The irradiation was done in the condensed phase, on the filter, for all samples. **150**

Table 5.1: Names and abbreviations of VOCs used to generate SOM samples from OH photooxidation in the smog chamber. The samples are hereafter referred to as VOC/OH if prepared under low-NO_x conditions, and VOC/OH/NO_x if prepared under high-NO_x conditions. The reaction time in the chamber is equivalent to the irradiation time. **160**

Table 5.2: Names and abbreviations of VOCs used to generate SOM samples from flow tube ozonolysis. The initial VOC concentration in flow tube experiments is the steady-state mixing ratio the VOC would have in the absence of ozone. Ozone was added in small excess with respect to the VOC. The flow tube residence time is on the order of minutes. The samples are hereafter referred to as VOC/O₃. **160**

Table 5.3: Brown carbon chromophores in ACN and H₂O extracts with H₂SO₄ present that were separated with HPLC. For each separated absorbance, we give the observed PDA retention time, the PDA spectrum, assigned, neutral chemical formula, as well as the ranking of abundance in the mass spectrum with the most abundant compound being first, or 1. **176**

Table 6.1: Dimer-to-monomer ratio of integrated peak abundances in α -pinene photooxidation SOA mass spectra. “Chamber” refers to SOA generated in the chamber according to the “system” conditions, collected onto PTFE filters, and frozen until HRMS analysis. “Aged in humidity” refers to SOA that was suspended in a saturated K₂SO₄ solution for 48 hours (ensuring 97.6% RH) after collection from the chamber, and then frozen until HRMS analysis. **186**

ACKNOWLEDGMENTS

There are many people that made my success, and this dissertation, possible. First, I would like to thank Sergey Nizkorodov, my primary advisor. He gave me many opportunities over the past five years that have made me a better scientist. Right out of the gate in December 2015 I attended Pacificchem and presented a poster on the very first analysis of the India data (what has evolved into chapters 2 and 3). He encouraged me to give talks at conferences, which I did at AAAR 2017 and IAC 2018. He even sent me to a science meeting for FIREX when he could not present himself. I also went to the 3rd Sino-European School on Atmospheric Chemistry, in Shanghai where I got to learn about Atmospheric Chemistry from professors from all over the world. I really appreciate all of these opportunities. I would like to thank him for always believing in me.

I would like to thank Don Blake for always being supportive of where I wanted to take my Ph.D. I learned a lot about field work by being a part of the KORUS-AQ campaign. This was also a really great networking experience, and helped to shape my current career goals. I am very grateful for everyone in the Rowland-Blake group that helped me run my India cans and subsequently make sense of the data. In particular, Simone Meinardi advised me on VOC emissions from biomass burning. I really appreciate his support the past few years.

I thank Alex Laskin, Julia Laskin, and Peng Lin for allowing me to come to their laboratories and use the HPLC-PDA-HRMS platform as well as the nano-DESI-HRMS. Without this collaboration, this dissertation would not be possible. I thank Peng for taking the time to mentor me during my visits to the Pacific Northwest National Laboratory and Purdue University. My visits were much more productive with your help.

I thank Professor Finlayson-Pitts for teaching me atmospheric chemistry through CHEM 245, CHEM 245B, and CHEM245C. It is an honor to have her serve on my advancement and dissertation committees. She is someone I admire very much.

I thank Rufus Edwards and Robert Weltman for their help in setting up the Indian cookstove experiments, and their involvement in the data analysis process when we returned home. I learned a lot from both of you about emissions sampling and emission factors. I really appreciate Robert's friendship while we were in India and since our return. I wish Robert the best in finishing his Ph.D.

I am very grateful for our Indian collaborators, Narendra K. Arora, Sneha Gautam, and Ankit Yadav. They handled all of the logistics for the Indian cookstove study (chapters 2 and 3) in terms of hiring a cook and securing a village kitchen, as well as our accommodations. I owe a special thanks to Ankit, who handled the day-to-day concerns while we were there, and since—he has always been prompt about answering my emails! Also, thank you for taking me and Robert all around India.

There were a lot of people who supported the Indian Cookstove project that I haven't named yet. Kirk Smith and Ajay Pillarisetti chatted with Robert and I every week to ensure the project was successful. Also, thank you for your edits to paper drafts. I also thank the village of Khatela for allowing us to make a scene and conduct our experiments. I am very grateful for our cook, who always showed up for us, even though she had malaria and was enduring tough times.

I am very thankful for Nujhat Ali, who carried out the experiments in section 5.3.1 entitled "Optical Properties" of Chapter 5. It is because of your hard work as an undergraduate at UCI that this paper could be possible.

I am very grateful for each and every member of the Aerosol Photochemistry Group that overlapped with me at UCI. Thank you for giving me feedback at group meetings, teaching me how to use things in the lab, sharing a room with me at conferences, and looking over drafts of my orals papers. I couldn't have done this without you. In particular, I would like to thank Kurtis Malecha for his friendship and support while he was here, as well as after he graduated. Thank you for helping me with actinometry calculations, pack for FIREX, and teaching me to ski. I cannot list all of the ways you have helped me in graduate school—there are too many. Just know I am so glad you were on this journey with me. To Alexandra Klodt, Natalie Smith, and Vahe Baboosian—I was initially really worried about all of you joining the group at the same time, to be honest. But, I have really enjoyed showing you all the ropes and becoming the “social group” with you all. I am especially grateful to Alex, for unwinding with me on the weekends and cooking dinner with me, as well as encouraging me to go to the gym.

I also need to thank Sandra Tsing Loh and the Loh Down on Science hive. Being a part of this program really helped me hone my science communication skills. I am really grateful for the community that we've created across the various science departments. My relationship with Sandra encouraged me to keep presenting and always do better at it.

I am very grateful to my undergraduate research advisor at the College of Wooster, Karl J. Feierabend. Thank you for encouraging me to pursue graduate school, and introducing me to atmospheric chemistry.

I am very thankful for Josh Barber, and all the ways he has encouraged me, big or small. Thank you for listening to me talk about my failed experiments, setbacks, and frustrations. And thank you for always being there to celebrate my successes. Also, you were supportive of me

from afar, when I would leave for 2 or 6 weeks at a time for India, Montana, or PNNL. Even when I missed your birthday! It is the best to live out our individual dreams, together.

I am so thankful for the support of family. My parents, Mike and Linda Fleming, have always supported me in following my dreams, even if it means moving half way across the country (or across the pond). Thank you, Mom and Dad, for visiting me regularly, and being proud of what I have accomplished at UCI.

Lastly, I acknowledge my research funding sources. The Indian cookstoves project (Chapters 2 and 3) was supported by EPA STAR grant R835425 Impacts of household sources on outdoor pollution at village and regional scales in India. The contents are solely the responsibility of the authors and do not necessarily represent the official views of the US EPA. The US EPA does not endorse the purchase of any commercial products or services mentioned in the publication. Chapter 4 was supported by NOAA grants NA16OAR4310101 (PNNL) and NA16OAR4310102 (UCI) for supporting nano-DESI and HPLC-PDA-HRMS analysis of samples. The HRMS measurements in Chapters 3 and 4 were performed at the W.R. Wiley Environmental Molecular Sciences Laboratory (EMSL) – a national scientific user facility located at PNNL, and sponsored by the Office of Biological and Environmental Research of the U.S. DOE. PNNL is operated for U.S. DOE by Battelle Memorial Institute under Contract No. DE-AC06-76RL0 1830. Parts of Chapter 5 are preprinted here with permission from the American Chemical Society. Chapter 6 was funded by DOE grant DE-SC0018349, Impacts of phase state and water content on secondary organic aerosol formation and partitioning.

CURRICULUM VITAE

Lauren Thomson Fleming

EDUCATION

University of California, Irvine, Ph.D. (June 2019) **GPA: 3.95** Irvine, CA
Department of Chemistry, atmospheric chemistry track, advanced to Ph.D. candidacy on
10/03/2016
Thesis advisors: Sergey Nizkorodov and Donald Blake

University of California, Irvine, M.S., June 2018 **GPA: 3.95** Irvine, CA

The College of Wooster, B.A., *magna cum laude*, May 2014 **GPA: 3.84** Wooster, OH
Major: Chemistry
Thesis and research advisor: Karl J. Feierabend

Awards/fellowships/memberships: Michael E. Gebel award (2018), Second place finalist--
Peter B. Wagner memorial award for women in atmospheric sciences (2018), NASA group
achievement award for KORUS-AQ (2017), National Science Foundation Graduate Research
Fellowship Program honorable mention (2015), Rowland Fellowship (2014-2015), Iota Sigma Pi
society for women in chemistry, Clare Boothe Luce Research Scholar (2012-2014), Local
Wooster ACS Section Senior Chemistry Award (2014), CRC Press Chemistry Achievement
Award (2011), Phi Beta Kappa honor society (2013, junior inductee), American Chemical
Society member (2012-present)

PUBLICATIONS

1. Montoya-Aguilera, J., Fleming, L. T., Zhu, S., Wingen, L. M., Perraud, V., Lin, P., Laskin, A., Laskin, J., Dabdub, D., and Nizkorodov, S. A.: Nighttime production of secondary organic aerosol from nitrate radical and ozone oxidation of indole. (first draft completed, and reviewed by co-authors)
2. Fleming, L. T., Lin, L., Roberts, J. M., Laskin, J., Laskin, A., Nizkorodov, S. A.: Molecular composition and photochemistry of brown carbon chromophores in biomass burning organic aerosol particles generated during FIREX. (expected submission June 2019)
3. Simpson, I. J., Blake, D. R., Blake, N. J., Meinardi, S., Barletta, B., Hughes, S., Vizenor, N., Fleming, L. T., Schroeder, J., Crawford, J. H., Diskin, G., Woo, J. H., Kim, J., Emmons, L., Barré, J., Knote, C., Lee, M., Peterson, D.: Characterization and Sources of VOCs in the Seoul Region during KORUS-AQ. (expected submission Spring 2019)
4. Fleming, L.T., Ali, N. N., Blair, S.L., Roveretto, M., George, C., and Nizkorodov, S.A.: Formation of light-absorbing organosulfates during evaporation of secondary organic material extracts in the presence of sulfuric acid, ACS Earth Space Chem., 2019. (accepted)

5. Rooney, B., Zhao, R., Bates, K., Pillarisetti, A., Sharma, S., Kundu, S., Bond, T., Lam, N., Ozaltun, B., Xu, L., Fleming, L., Weltman, R., Meinardi, S., Blake, D., Nizkorodov, S., Edwards, R., Yadav, A., Arora, N., Smith, K., and Seinfeld, J.: Impacts of household sources on air pollution at village and regional scales in India, *Atmos. Chem. Phys. Discuss.*, <https://doi.org/10.5194/acp-2018-1198>, 2018.
6. Fleming, L. T., Weltman, R., Yadav, A., Edwards, R. D., Arora, N. K., Pillarisetti, A., Meinardi, S., Smith, K. R., Blake, D. R., and Nizkorodov, S. A.: Emissions from village cookstoves in Haryana, India, and their potential impacts on air quality, *Atmos. Chem. Phys.*, 18, 15169-15182, [https://doi: 10.5194/acp-18-15169-2018](https://doi:10.5194/acp-18-15169-2018), 2018.
7. Laskin, A., Lin, P., Laskin, J., Fleming, L.T.; and Nizkorodov, S. A.: "Molecular Characterization of Atmospheric Brown Carbon." ACS Symposium Series volume 1299, Chapter 13, pp 261-274 in "Multiphase Environmental Chemistry in the Atmosphere", Hunt S., Laskin A., Nizkorodov S.A. Eds., 2018; ISBN13: 9780841233638, doi:10.1021/bk-2018-1299.ch013, 2018.
8. Lin, P., Fleming, L.T., Nizkorodov, S.A., Laskin, J., and Laskin, A.: Comprehensive Molecular Characterization of Atmospheric Brown Carbon by High Resolution Mass Spectrometry with Electrospray and Atmospheric Pressure Photoionization, *Anal. Chem.*, 90(21), 12493–12502, doi:10.1021/acs.analchem.8b02177, 2018.
9. Fleming, L. T., Lin, P., Laskin, A., Laskin, J., Weltman, R., Edwards, R. D., Arora, N. K., Yadav, A., Meinardi, S., Blake, D. R., Pillarisetti, A., Smith, K. R. and Nizkorodov, S. A.: Molecular composition of particulate matter emissions from dung and brushwood burning household cookstoves in Haryana, India, *Atmos. Chem. Phys.*, 18(4), 2461–2480, <https://doi.org/10.5194/acp-18-2461-2018>, 2018.
10. Montoya-Aguilera, J., Horne, J. R., Hinks, M. L., Fleming, L. T., Perraud, V., Lin, P., Laskin, A., Laskin, J., Dabdub, D., and Nizkorodov, S. A.: Secondary organic aerosol from atmospheric photooxidation of indole, *Atmos. Chem. Phys.*, 17, 11605-11621, <https://doi.org/10.5194/acp-17-11605-2017>, 2017.

Conference Presentations:

* indicates the presenting author

Talks:

L.T. Fleming,* P. Lin, J. Laskin, A. Laskin, S.A. Nizkorodov: Photolysis of brown carbon chromophores produced from simulated forest fires during the FIREX campaign, AirUCI Internal Symposium, January 17, 2019, Irvine, CA, USA.

L. T. Fleming,* J. Montoya-Aguilera, W. W. DeRieux, Y. Li, P. Lin, A. Laskin, J. Laskin, M. Shiraiwa, S. A. Nizkorodov: Competing effects of water vapor and aerosol liquid water on the yield and molecular composition of secondary organic aerosols, 10th International Aerosol Conference, September 2-7, 2018, St. Louis, MO.

P. Lin, L. T. Fleming, Y. Li, W. W. DeRieux, J. Laskin, M. Shiraiwa, S. A. Nizkorodov, A. Laskin*: Comprehensive chemical characterization of brown carbon aerosols, 10th International Aerosol Conference, September 2-7, 2018, St. Louis, MO.

L. T. Fleming,* P. Lin, A. Laskin, J. Laskin, R. Weltman, R. D. Edwards, N. K. Arora, A. Yadav, S. Meinardi, D. R. Blake, A. Pillarisetti, K. R. Smith, and S. A. Nizkorodov: Molecular composition of particulate matter emissions from dung and brushwood burning household cookstoves in Haryana, India, Peter B. Wagner Women in Atmospheric Sciences Seminar, July 19, 2018, Reno, NV.

L. T. Fleming,* S. A. Nizkorodov, P. Lin, A. Laskin, and J. Laskin: Climate-relevant compounds produced from burning forest fire fuels in conjunction with the FIREX campaign, 36th American Association for Aerosol Research meeting, October 16-20, 2017, Raleigh, NC.
Also presented at the FIREX science meeting in Boulder, CO on November 7, 2017.

P. Lin,* L. T. Fleming, N. Bluvshstein, Y. Rudich, S. A. Nizkorodov, J. Laskin, A. Laskin: Molecular Characterization of Individual Chromophores in Atmospheric Brown Carbon, American Association for Aerosol Research meeting, October 16-20, 2017, Raleigh, NC.

I. J. Simpson,* D. R. Blake, N. J. Blake, S. Meinardi, S. Hughes, B. Barletta, L. T. Fleming, N. Vizenor, L. Emmons, J. Barre, J. Woo, J. Kim, J. Schroeder, and C. Knote: Characterization of VOCs in the Seoul Metropolitan Area (SMA) based on Whole Air Sampling (WAS), including comparison with Hong Kong, KORUS-AQ Science Team Meeting, February 27- March 3, 2017, Seogwipo, Jeju, South Korea.

Posters:

L. T. Fleming,* R. Weltman, A. Yadav, N. K. Arora, A. Pillarisetti, S. Meinardi, K. R. Smith, R. D. Edwards, D. R. Blake, and S. A. Nizkorodov: Particulate and gas emissions from village cook stoves in Haryana, India and their potential impacts on air quality, 35th Informal Symposium on Kinetics and Photochemical Processes in the Atmosphere (ISKPPA), March 30, 2018, Pasadena, CA, USA.

L. T. Fleming,* S. A. Nizkorodov, P. Lin, A. Laskin, and J. Laskin: Climate-Relevant Compounds Produced from Burning Forest Fire Fuels in Conjunction with the FIREX campaign, 34th Informal Symposium on Kinetics and Photochemical Processes in the Atmosphere (ISKPPA), May 12, 2017, San Diego, CA, USA.
Also presented at The Third Sino-European School on Atmospheric Chemistry, Shanghai, China, November 30, 2017.

J. Montoya,* J.R. Horne, M.L. Hinks, L.T. Fleming, V. Perraud, P. Lin, A. Laskin, J. Laskin, D. Dabdub, and S.A. Nizkorodov: Secondary organic aerosol (SOA) from photooxidation of indole, 34th Informal Symposium on Kinetics and Photochemical Processes in the Atmosphere (ISKPPA), May 12, 2017, San Diego, CA, USA.

D. R. Blake,* N. J. Blake, I. J. Simpson, S. Meinardi, S. Hughes, B. Barletta, L. T. Fleming, N. Vizenor, L. Emmons, J. Barre, J. Woo, J. Kim, J. Schroeder, and C. Knote: Overview of VOCs

measured by Whole Air Sampling (WAS) during KORUS-AQ: Urban, industrial, biogenic, marine, and long-range signals, KORUS-AQ Science Team Meeting, February 27- March 3, 2017, Seogwipo, Jeju, South Korea

N. J. Blake,* D. R. Blake, S. Meinardi, I. J. Simpson, S. Hughes, B. Barletta, L. T. Fleming, N. Vizenor, J. Schroeder, L. Emmons, and C. Knote: Markers for Chinese and Korean air masses: Halocarbons and other trace gas species measured during KORUS-AQ, KORUS-AQ Science Team Meeting, February 27- March 3, 2017, Seogwipo, Jeju, South Korea

L. T. Fleming,* S. A. Nizkorodov, D. R. Blake, R. Weltman, R. D. Edwards, P. Lin, A Laskin, J. Laskin, K. R. Smith, N. K. Arora, S. Gautam, and A. Yadav: Gaseous and particle-phase aerosol emissions from household cooking in rural Haryana, India, International Global Atmospheric Chemistry (IGAC), September 26-30, 2016, Breckenridge, CO, USA.

L. T. Fleming,* S. A. Nizkorodov, D. R. Blake, R. D. Edwards, P. Lin, A. Laskin, J. Laskin, K. R. Smith, N.K. Arora, and M. Vaswani: Biomass Burning Aerosol from Household Cooking in Rural Haryana, India, Pacificchem meeting, Honolulu, HI, December 17, 2015.

L. T. Fleming* and K. J. Feierabend: Photo-oxidation Kinetics of Aqueous Oxalic Acid, American Chemical Society National Meeting, Dallas, TX, March 17, 2014.

E. R. Villa,* L. T. Fleming, and K. J. Feierabend: The Ultraviolet Photochemistry of Aqueous Oxalate Species. American Chemical Society National Meeting, New Orleans, LA, April 8, 2013.

R. L. Craig,* L. T. Fleming, and K. J. Feierabend: Kinetics and Mechanism of the Reaction Between Aqueous Oxalate Species and the Hydroxyl Radical, American Chemical Society National Meeting, New Orleans, LA, April 8, 2013.

PROFESSIONAL EXPERIENCE AND SERCE AT UCI

Activate to Captivate Irvine, CA Winter 2019

- An 8-week certificate program designed to improve your public speaking skills
- Learn strategies to overcome anxiety, command a room, and communicate effectively with an audience of any size

Atmospheric Chemistry and Physics/Reviewer November 2018-present

Sino-European School on Atmospheric Chemistry/attendee November 2017
Shangahi, China

- A 9-day series of lectures for graduate students by experts in atmospheric chemistry from all over the world
- In the evenings we worked closely with our assigned professor on a presentation of their research

Science of the Total Environment/Reviewer August 2017-present

Loh Down on Science/Managing editor

March 2018-present

Script writer

April 2017- March 2018

- View recent Loh Downs I wrote at: <http://www.lohdownnonscience.com/author/fleming/>
- The NPR daily science segment that “is a fun way to get your daily dose of science plus a dash of humor in less than two minutes”
- Write and edit two scripts (185-195 words each) per month that feature recent publications and are accessible and fun for the average listener
- The two managing editors are responsible for editing scripts, consulting with the host Sandra Tsing Loh during recording, training new writers, and logistics.

Iota Sigma Pi/Calcium chapter treasurer

Summer 2015- present

- National honors society for women in chemistry
- Participated in science outreach activities in Orange County, professional development seminars and social events
 - Panelist at graduate student Q&A for undergraduates at UCI (April 2017, roughly 40 students attended)
 - Helped with Saturday chemistry class for children (8-12 years old) with disabilities at United Cerebral Palsy (October 2017)
- As activities coordinator (2015-2016), I planned social events for the club and was in charge of logistics
- As treasurer (2016-2017, 2017-2018) I prepared annual financial reports, was head of fundraising committee, and worked with other officers to make upcoming events possible
- Fundraising committee events:
 - Merchandise sale 2017: UCI chemistry key chains and insulated grocery bags
 - Hosted trivia night in association with Geeks Who Drink, raised \$273
 - Merchandise sale 2018: UCI chemistry T-shirts

Co-Chair of AAAR platform session (AC1)

Raleigh, NC

2017

- Confirm presenters in advance of the conference
- Moderate talks during the session

Chemistry Graduate Recruitment/Recruiter

March 2018

- Gave campus tours, helped with logistics, and acted as a graduate representative for the department

ACS Science Coach

Fall 2015- Spring 2016

- I worked with Ms. Lynn Chuang in her high school chemistry classroom at Godinez Fundamental High School
- Visited every other month throughout the academic year, helping with their labs and giving short presentations on my research

ABSTRACT OF THE DISSERTATION

Molecular Composition, Optical Properties, and Chemical Aging of Primary and Secondary Organic Aerosol

By

Lauren Thomson Fleming

Doctor of Philosophy in Chemistry

University of California, Irvine, 2019

Professor Sergey A. Nizkorodov, Chair

Aerosols are composed of solid or liquid particles and the gases they are suspended in. Primary aerosols are directly emitted and secondary organic aerosols (SOA) are formed in the atmosphere from the oxidation of volatile organic compounds (VOCs). The molecular composition of aerosol particles determines their optical properties, and affects the radiation balance of the Earth. Organic aerosol particles largely scatter solar radiation, however, there is a subset of organic particles called brown carbon (BrC) that absorb near-ultraviolet and visible radiation from the sun. Also, adverse effects on human health from exposure to aerosols are related to their molecular composition. The molecular composition of aerosol particles can also change during atmospheric transport, for example, due to the effects of sunlight and water vapor; and this makes the optical properties and human health effects of aerosols even harder to predict.

Chapters 2 and 3 examine the composition of smoke from biomass-burning cookstoves in rural India. This was done for two fuel types (wood and dung), as well as two stoves that are common to the area, the *chulha* and *angithi*. Chapter 2 quantifies the emission factors (EFs) of VOCs and PM_{2.5} from these emission sources, and estimates ozone and SOA production from

these emissions. The major finding was that dung fuels and *angithi* cookstoves significantly increase the EFs for most VOCs. In Chapter 3, the molecular composition of smoke particles are characterized using high resolution mass spectrometry techniques. We observed that particles produced from dung-burning cookstoves were more complex (in terms of numbers of components), and contained a higher fraction of nitrogen-containing molecules (by mass abundance).

Chapter 4 characterizes BrC chromophores found in aerosol particles produced by simulated wildfires during the FIREX campaign. Then, we estimate lifetimes of individual BrC chromophores as well as bulk BrC absorbance. We find that BrC absorption has lifetimes of 10 to 41 days due to photochemical aging.

Chapter 5 investigates the evaporative browning of various SOA extracts, acidified with sulfuric acid to pH=2. The optical properties were quantified for SOAs of various precursors, both anthropogenic and biogenic, and oxidants (OH, O₃, NO_x). The molecular composition of BrC chromophores were determined, all of which were organosulfates.

Chapter 6 explores the effect of water vapor and aerosol liquid water on the molecular composition of SOA, as it is formed and chemically aged. We have evidence that for α -pinene/OH SOA formed in the presence of ammonium sulfate seed, water likely participates in hydrolysis reactions that result in less viscous particles.

These results provide key inputs to air quality models to more accurately predict regional climate; including EFs for Indian cookstoves and lifetimes of BrC in biomass burning organic aerosol. Other observations regarding secondary BrC formation in CCN mimics and hydrolysis reactions occurring in model SOA further our understanding of the evolution and chemical processing of atmospheric aerosols.

CHAPTER 1

INTRODUCTION

1.1 Background and Motivation: Climate and Health Impacts

The Earth's atmosphere is mainly composed of nitrogen (78.1% in dry air), oxygen (20.9%), and argon (0.9%). The other 0.1% is made up of carbon dioxide, methane, neon, helium, and other trace species that includes a large number of different volatile organic compounds (VOCs). There are also particles suspended in atmospheric gases, ranging from clusters (nanometers) to cloud droplets (micrometers) in size (Finlayson-Pitts and Pitts, 2000). Aerosols are composed of solid or liquid particles and the air they are suspended in. Aerosols are generated from natural processes such as the suspension of dust, the jet action of seawater, and volcanic activity. They are also emitted from anthropogenic activities such as the burning of fossil fuels. Aerosols can also be formed from the oxidation of VOCs in the atmosphere, in which case they are called secondary organic aerosol (Pöschl, 2005). Particles and the VOCs they are suspended in, collectively termed "aerosols," make up a relatively small mass fraction of the atmosphere. However, aerosols adversely affect human health, and have a strong effect on global and regional climate.

While many VOCs are relatively harmless at the concentrations found in the atmosphere, certain VOCs such as 1,3-butadiene and benzene are known human carcinogens even at trace concentrations, while others such as acrolein, are toxic, and lead to short-term health effects such as respiratory infections (Environmental Protection Agency, 2009b, 2009a, 2012). Exposure to

aerosol particles increase mortality in populations due to cardiovascular and respiratory illnesses (Laden et al., 2006). In particular, aerosol particles less than 2.5 μm in aerodynamic diameter ($\text{PM}_{2.5}$) are sufficiently small to penetrate the human body's defenses and end up in lung fluid or the bloodstream (Elder and Oberdörster, 2006; Oberdörster et al., 2004). $\text{PM}_{2.5}$ alone been statistically linked to adverse health outcomes in epidemiology studies, but chemical composition likely modulates these effects (Atkinson et al., 2015). For example, polycyclic aromatic hydrocarbons (PAHs) are known mutagens. The main mutagenic pathway is thought to be via epoxy diols, metabolites of PAHs, which bind to nucleotides, the building blocks of deoxyribonucleic acid (DNA) (Xu et al., 2005; Zhou et al., 2017a). Fang et al. (2017) collected $\text{PM}_{2.5}$ from a road site and linked chemical constituents to the oxidative potential, a measure of reactive oxidation species (ROS) generation, and ultimately the human body's inflammatory response. They found that soluble transition metals, which are capable of ROS generation via redox reactions, were correlated with sulfate which they attributed to greater dissolution of metals due to the action of sulfuric acid. More studies need to correlate chemical composition and adverse health effects or toxicological mechanisms. At this point, we do not have a complete view of what chemical components lead to premature mortality by exposure to $\text{PM}_{2.5}$.

Both VOCs and aerosol particles also affect global and regional climate (IPCC, 2013). Greenhouse gases, such as carbon dioxide (CO_2), methane (CH_4), and chlorofluorocarbons absorb infrared radiation from the sun, resulting in a positive (warming) radiative forcing. The direct effect of particles on climate is more uncertain, and depends on their overall optical properties, which are dictated by their chemical composition. There are also two indirect effects that aerosols have on climate, and they both have to do with the ability of aerosol particles be cloud condensation nuclei (CCN) (Forster et al., 2007). First, the number of CCN is directly

proportional to the reflectivity of the cloud, with more CCN particles resulting in more reflective clouds with larger number of smaller water droplets in them. Second, they may have a complex effect on cloud lifetimes, with longer-living clouds scattering more solar energy back to space.

The optical properties of aerosol particles are often quantified to determine the aerosol direct effect. Two metrics are Absorption Angstrom Exponent (AAE), which describes how strongly the absorption coefficient depends on the wavelength (Ångström, 1929), and the Single Scattering Albedo (SSA), or the ratio of the scattering efficiency to overall extinction efficiency by particles (Bohren and Huffman, 1998). Mass absorption coefficient (MAC) is measured in situ using photoacoustic spectrometers (Moosmüller et al., 2009), and is related to the AAE in equation (1.1).

$$\text{MAC}(\lambda)_{aerosol} = K\lambda^{-AAE} \quad (1.1)$$

Where $\text{MAC}(\lambda)$ is the wavelength-dependent mass-normalized absorption coefficient (m^2/g), K is the pre-exponential factor that includes aerosol mass concentration. For soluble materials, MAC of the bulk material can also be measured from particles extracted from filters, referred to as MAC_{bulk} in this dissertation.

$$\text{MAC}(\lambda)_{\text{bulk}} = \frac{A_{10}^{\text{extract}}(\lambda) \times \ln(10)}{b \times C_{\text{mass}}} \quad (1.2)$$

Here, A_{10} is the base-10 absorbance for the extract obtained by a UV-Vis spectrometer, b is the pathlength of the cuvette (cm), and C_{mass} is the mass concentration of the extract (g/cm^3). The relationship between $\text{MAC}_{aerosol}$ and MAC_{bulk} depends on the particles size and shape distribution in a complex way going beyond the topic of this dissertation. Unless specified otherwise, the abbreviation MAC used in this thesis will correspond to MAC_{bulk} .

Inorganic particles, such as ammonium nitrate, and organic particles are effective at scattering radiation with SSA approaching unity, having a negative (cooling) radiative forcing

effect on climate. On the other hand, black carbon (BC), produced exclusively from various incomplete combustion sources, absorbs all visible wavelengths and has a net positive (warming) effect on radiative forcing. BC-containing particles have an SSA below 0.9 and an AAE of around 1, because the MAC of BC is not strongly wavelength-dependent (Bergstrom et al., 2002; Bond and Bergstrom, 2006; Laskin et al., 2015). Particle components referred to as brown carbon (BrC), are organic molecules that absorb near ultraviolet and shorter visible wavelengths (Andreae and Gelencsér, 2006; Laskin et al., 2018). Sources of BrC include combustion, as well as condensed-phase chemistry reactions between carbonyl functionalities and reduced nitrogen species such as ammonium (Hawkins et al., 2016). Presence of BrC in particles has a complex effect on climate, and is the least understood in terms of optical properties of aerosol particles. BrC is operationally defined as organic material having an AAE of greater than 2, giving a stronger wavelength dependence to light absorption than that for BC, but the AAE values are highly variable and depend on the source of BrC (Kirchstetter et al., 2004; Laskin et al., 2015). The radiative forcing due to absorption by BrC is estimated to be 0.1-0.25 W/m², or about a fourth of that of BC (1.07 W/m²) (Feng et al., 2013). However, in regions with abundant sources of primary BrC, the effect could contribute above 0.25 W/m² (Feng et al., 2013).

1.2 Formation, growth, and aging of aerosol particles

1.2.1 Summary of aerosol life cycle

There are primary and secondary sources of aerosol particles. Primary aerosol particles are directly emitted from various sources, such as, sea spray, combustion, and suspended dust (Pöschl, 2005). Alongside primary aerosol particles, VOCs are directly emitted into the

atmosphere by vegetation (61%), biomass burning (30%), and exclusively anthropogenic sources (9%) (Guenther et al., 2006; Yokelson et al., 2008). Emitted VOCs undergo successive oxidation steps with atmospheric oxidants, such as OH radical, NO₃ and ozone (Pöschl, 2005). Lower volatility products condense onto existing aerosol particles or in remote atmospheres may nucleate with other vapors to form new particles. In both cases, these particles are called secondary organic aerosol (SOA) (Pöschl, 2005). SOA is thought to make up to half of all CCN on a global scale (Wang and Penner, 2009).

Ultimately, the effects of aerosol particles on human health and climate depend on chemical composition, which is dictated by environmental conditions during aerosol particle formation, growth, and aging life stages of aerosol particles. Mechanisms for changes in chemical composition and aerosol particle mass concentration include, but are not limited to: heterogeneous reactive uptake of gases such as N₂O₅ (Dentener and Crutzen, 1993; Thornton et al., 2003), aqueous phase chemistry in cloud droplets or aerosol liquid water (Gilardoni et al., 2016; Herrmann et al., 2015; Lim et al., 2010; McNeill, 2015), direct photolysis (Epstein et al., 2014; Hodzic et al., 2015; Malecha et al., 2018; Wong et al., 2015a), photooxidation (Isaacman-VanWertz et al., 2018; Ortega et al., 2016), autooxidation of VOCs which can lead to particle formation (Ehn et al., 2017; Jokinen et al., 2014; Praske et al., 2018), hydrolysis of oligomers (Clafflin et al., 2018; Nguyen et al., 2012a), and oligomerization of organic compounds during the evaporation of cloud droplets (Nguyen et al., 2012b). SOA is removed from the atmosphere primarily by wet deposition, whereby CCN and aerosol particles are washed out by precipitation. Dry deposition, which is the process by which aerosol particles settle on surfaces, also contributes to removal of aerosols from air and creation of urban grime (Baergen et al., 2015; Styler et al., 2018). Depending on meteorological conditions, aerosol particles can be suspended

in the atmosphere for hours to weeks before they are deposited (Pöschl, 2005; Raes et al., 2000; Williams et al., 2002), so aging processes that occur on faster time scales are atmospherically relevant.

1.2.2 Composition of biomass burning organic aerosol and its relationship with combustion processes

The bulk of this dissertation focused on a type of primary organic aerosol, biomass burning organic aerosol (BBOA). There are both natural and anthropogenic sources of BBOA. There are natural forest fire cycles that yield benefits for ecosystems. On the other hand, both historically and even today, people have utilized fire to improve their standard of living for deforestation, cooking, agricultural activities, and heating purposes (Crutzen and Andreae, 1990).

Biomass is composed of three major biopolymer components: lignin, cellulose, and hemicellulose (Crutzen and Andreae, 1990). Lignin is made up of substituted, aromatic monomers that contain syringyl, coniferyl, and vanillyl moieties which are largely retained during pyrolysis (Simoneit et al., 1993). The frequency of particular monomer units depends on the genus of the plant. The monomer unit of cellulose is glucose, and the pyrolysis decomposition product of it is levoglucosan, a well-known biomass burning tracer (Collard and Blin, 2014). Hemicellulose is made up of various sugar monomers.

There are four main types of biomass combustion that yield different BBOA emissions (Andreae and Merlet, 2001; Yokelson et al., 1996). The first stage, starting when the fuel is lit, encompasses distillation and pyrolysis processes which tend to occur together. Distillation occurs when more plant volatiles are released at a higher temperature. Examples of distillation products

are terpenes and water. Co-emitted with distillation products are pyrolysis products, produced when there is thermal degradation of the fuel, or cracking. These molecules may be partially oxidized in the flame. Examples of pyrolysis products are acetic acid, formic acid, and methanol. This stage of combustion persists throughout the fire. Next, charring of the fuel occurs, beginning the next stage of combustion, termed glowing. Glowing combustion starts at 800 K, when oxygen is chemisorbed to char surfaces, producing small flames. This process emits CO₂, CO, and various hydrocarbons. This gives rise to flames a meter high or more, referred to as the flaming stage. CO₂, while emitted over the entire fire, is a major product of flaming combustion. Other products of flaming combustion are SO₂, NO, NO₂, PAHs, and BC. Once the flames subside, a large black cloud of smoke appears, signaling the last stage, smoldering combustion. Major products at this stage are CO, CH₄, NH₃, and ethane. Fire variables, such as wind speed and direction, fuel moisture content, fuel composition, and fuel components interact to determine the combustion conditions, and they are not easily predictable. For real fires, different stages of combustion will occur simultaneously and is difficult to objectively quantify contributions of different stages, for example, glowing combustion often occurs with smoldering and distillation/pyrolysis stages. For other fires, such as the burning of duff, only smoldering combustion occurs for days or weeks.

The variety of the types of fires, stages within a given fire, prompted the creation of parameters that can be used for correlating different properties of the fire and concentrations of trace species in the smoke. Modified Combustion Efficiency (MCE) is the most frequently used simplified metric of combustion, and is defined in equation (1.3).

$$\text{MCE} = \frac{\Delta\text{CO}_2}{\Delta\text{CO}_2 + \Delta\text{CO}} \quad (1.3)$$

Where ΔCO_2 and ΔCO is the change in the measured mixing ratio of the emission versus the background. For complete combustion, where all carbon is converted to CO_2 , the MCE is 1. Flaming combustion has an MCE of 0.99, whereas smoldering combustion is in the range of 0.8-0.88. In this dissertation, certain VOC emissions will be discussed in terms of their dependence on MCE.

There is a breadth of molecular components of BBOA that have been identified in BBOA, in addition to those already mentioned. Substituted aromatics have been detected as semi-volatile organic compounds (SVOCs) using offline two-dimensional (2D) gas chromatography and proton transfer reaction time-of-flight mass spectrometry (Hatch et al., 2015, 2018; Koss et al., 2018; Stockwell et al., 2015). Examples are phenol, guaiacol, and syringol. Furans, especially the SVOC furfural, has been detected in BBOA plumes, and are formed from the thermal decomposition of the glucose biopolymer, cellulose (Collard and Blin, 2014; Hatch et al., 2015, 2018; Koss et al., 2018; Stockwell et al., 2015). Levoglucosan is formed by a similar mechanism, but has a lower volatility, and is a widely used particle phase tracer (Aiken et al., 2009; Cong et al., 2015; Simoneit et al., 1999). Other particle-phase compounds include lower volatility substituted aromatics such as p-coumaryl, sinapyl, and coniferyl alcohols, which are the primary lignin pyrolysis products (Simoneit et al., 1993). Nitroaromatics are formed by the addition of NO_2 to the aromatic ring, and can be strong BrC chromophores (Harrison et al., 2005; Lin et al., 2017). Nitrocatechol and methylnitrocatechol are often used as markers of biomass burning (Inuma et al., 2010). Tar balls are light-absorbing spherical particles (Pósfai et al., 2004) that are emitted from primarily smoldering combustion (Einfeld et al., 1991). Traditionally, they have been detected using transmission electron microscopy, scanning electron microscopy, and scanning transmission X-ray microscopy

(Adachi and Buseck, 2011; Chakrabarty et al., 2006, 2010; China et al., 2013; Pósfai et al., 2004; Sedlacek III et al., 2018; Tivanski et al., 2007). Most recently, mass spectrometry was done on tar balls showing they are composed of both non-polar and polar components, containing many PAHs and substituted PAHs (Li et al., 2019). Organosulfates were a main class of BrC that were detected using ultra performance liquid chromatography interfaced with diode array and time-of-flight mass spectrometry detectors from smoldering peat or fern sample extracts (Budisulistiorini et al., 2017). Song et al. (2018) also detected organosulfates in BBOA particles using high resolution mass spectrometry, but observed significantly more from burning coal, compared to biomass. Organosulfates are likely much more abundant for fuels with high sulfur contents, such as peat and coal. Other components that have been identified are sterols, n-alkaloids, resin acids, as well as other sugars (Jen et al., 2019; Simoneit, 2002; Simoneit et al., 1993).

1.2.3 Photochemical aging of biomass burning organic aerosol

Many studies have focused on how BrC BBOA particle mass, optical properties, and chemical composition evolve during atmospheric transport. Observed changes in OA mass from secondary processes in the plume have yet to be incorporated into global air quality models, and could have significant effects. For example, in China, wintertime haze events result in hundreds of $\mu\text{g m}^{-3}$ of $\text{PM}_{2.5}$, and such rapid SOA formation events are currently unpredictable. Huang et al. (2014) used positive matrix factorization to correlate OA mass from an aerosol mass spectrometer (HR-ToF-AMS) to different emission sources, and ^{14}C analysis to quantify contributions of non-fossil and fossil carbon in OA. Their study determined that primary and secondary OA from both fossil fuels and biomass burning had significant contributions to the observed OA mass. Other studies have quantified the change in mass enhancement in the field.

For example, Akagi et al. (2012) sampled emissions of a prescribed wildfire burning in the central coast of California from an airplane, as well as the downwind plume that corresponded to approximately 4 hours of atmospheric aging. They measured a net decrease in OA of about 20% in the aged plume, suggesting evaporation from BBOA particles was dominant. They observed an increase in gas-phase photoproducts such as acetic and formic acids, by factors of 1.7 and 7.3, respectively. They also measured an increase in SSA by a factor of 2.5, suggesting photobleaching of BBOA. Gilardoni et al. (2016) sampled fog water in the Po Valley of northern Italy during the wintertime, when residential combustion of biomass is a common practice for heating. They used HR-ToF-AMS to look for signatures of fresh and aged BBOA, such as anhydrosugars, like levoglucosan, and oxidized aerosol. Their data analysis suggests that BBOA is a precursor for aqueous SOA that goes on to form fogs. They estimate that aqueous SOA makes up 4-20% of the total primary OA emissions there. On the modeling side, Alvarado et al. (2015) made updates to the Aerosol Simulation Program, and ran it based on data collected for sampled plumes from the Williams fire. They made assumptions about SVOCs, which were not determined in the field study. With these assumptions they were able to accurately simulate concentrations of SOA, as well as ozone, within measurement error.

Laboratory studies have attempted to discern the relationship between OA mass enhancement and fire conditions such as fuel type, oxidants, or combustion conditions. Grieshop et al. (2009) generated BBOA from burning soft and hardwoods in a wood-burning stove, and photooxidation of the diluted BBOA occurred in a chamber for a few hours. They found OA mass enhancements of 1.5-2.8 over the aging time. They also determined that much of the OA was composed of SVOCs, from passing OA into a thermodenuder before sampling. A similar experiment was performed in Hennigan et al. (2011) at the Fire Sciences Laboratory as a part of

FLAME-3. However, they observed an OA mass enhancement of less than 1 for some of the fires, with a range of 0.7 to 2.9. They also found that the aerosol composition was chemically changed; characterized by higher O:C ratios and lower volatility products. Also during FLAME-3, Ortega et al. (2013) aged BBOA emissions in an oxidation flow reactor (OFR), which exposes BBOA to an equivalent OH exposure of 5 days in the atmosphere. OA mass enhancement ratios peaked after 3 equivalent days of aging. Consistent with Hennigan et al. (2011), OA mass enhancement ratios ranged from 0.62 to 2.33, and they noted that SOA mass exceeded the concentration of detectable VOCs known to serve as SOA precursors suggesting that some undetected VOCs also contributed. During FLAME-4, Tkacik et al. (2017) exposed smoke to UV light, HONO, both HONO and UV, or ozone in the dark. As an improvement to FLAME-3, dual chambers were used as a more reliable control. The range of OA mass enhancement ratios they observed ranged from 0.7 to 4.4. While many studies have quantified secondary organic aerosol formation from BBOA, it is not clear which factors, i.e. environmental conditions, fuel type, combustion type, lead to the broad range of OA mass enhancement ratios observed.

Previous studies have also found that during atmospheric transport, the optical properties of BBOA change. For example, as a part of the 2013 NASA SEAC4RS campaign, Forrister et al. (2015) sampled BBOA plumes from forest fires in an airplane, both fresh and a plume that was aged ~2 days based on back trajectories. The filters were extracted, and their absorption spectra were recorded. Their results indicated that the amount of BrC, after accounting for the plume dilution, had a half-life of 9 to 15 hours based on the absorbance in the range of 360 to 370 nm. In Saleh et al. (2013), they found that aged BBOA was slightly more absorbing in the near UV and short visible wavelengths than the fresh emissions. This study was also during FLAME-3, and utilized the same chamber set-up as Hennigan et al. (2011). Zhong and Jang (2014)

introduced smoldering wood smoke to an outdoor chamber early in the morning. The smoke was aged under high NO_x (i.e., high combined concentration of NO and NO₂) photooxidation conditions for the whole day. Based on extracted filter samples, they found that the MAC_{bulk} at 550 nm peaked in the morning, and then decreased in the afternoon. This is likely due to the formation of highly-absorbing nitroaromatics which are not present in the fresh smoldering emissions, and their subsequent photodegradation as the BBOA becomes more aged. In another BBOA aging study by Sumlin et al. (2017), emissions from smoldering Alaskan peat were aged in an OFR and their online optical properties were monitored with an integrated photoacoustic nephelometer. They found that at 375 nm the MAC_{aerosol} decreased by 46%, while the SSA increased from 0.85 to 0.90 after 4.5 days of equivalent aging. Li et al. (2019) produced tar balls and aged them exclusively in the presence of OH, and then under high-NO_x conditions. They found that photooxidative aging decreased both the real (scattering) and imaginary (absorbing) parts of the refractive index. However, when they switched to high-NO_x conditions, the refractive index increased, especially the imaginary part. This was attributed to the formation of highly-absorbing nitroaromatics. These studies generally agree that BBOA over the long term photodegrades. However, specific perturbations, such as NO_x, combined with specific initial BBOA compositions, such as non-flaming emissions, can result in enhancement of BBOA absorption at near UV and short visible wavelengths.

The evolution of aerosol optical properties during atmospheric transport of BBOA is fundamentally determined by its chemical composition. Studies have attempted to characterize the chemical composition of BBOA. Zhou et al. (2017b) deployed an HR-ToF-AMS at the Mt. Bachelor Observatory to look at how BB emissions affect particle mass loading. Based on PMF analysis, they attributed about 50% of OA mass to a “secondary” category. This could be new

OA mass, or simply transformed, more oxidized mass. They emphasize the importance of understanding aged aerosol mass and composition, since it constituted a significant fraction. In Wong et al. (2017), smoldering emissions of hardwood were collected onto filters and extracted in water or methanol solvents, generating water-soluble and water-insoluble BrC extracts. They were irradiated in solution to mimic atmospheric aging, and run through a size exclusion column on a High Performance Liquid Chromatography instrument. They identified two major fractions, which they called high and low molecular weight fractions. They found that the high molecular weight compounds dominated BrC light absorption. They also observed photoenhancement followed by photobleaching of extracts for both high and low molecular weight categories. Other studies have found chemical signatures for atmospheric aging. For example, Kumar et al. (2018) measured the increase in OH reactivity downwind of crop residue and agricultural fires of the Indo-Gangetic Plain. This measurement probes the total, including unmeasured, VOCs in the aged BBOA plume. They attributed the increase in the OH reactivity to photochemical products such as acetaldehyde, isocyanic acid, and formamide, as well as photostable primary emission products, such as aromatics. Compared to the number of studies on aged BBOA optical properties, there are fewer studies that focus on the chemical composition of aged BBOA BrC and how this affects their optical properties. This topic is one focus of this dissertation.

1.2.4 Secondary BrC formed during the processing of cloud droplets

Light-absorbing organic compounds can be formed by secondary processes in the atmosphere resulting in so-called “secondary BrC.” Examples of these processes include nitration of aromatics mentioned above, as well as different kinds of aqueous processes occurring in cloud and fog droplets (Chang and Thompson, 2010; Gelencsér et al., 2003; Smith et al.,

2016). The secondary BrC literature is quite extensive, and was recently reviewed by Laskin et al., 2015.

Some of these aqueous processes that produce secondary BrC may be accelerated by the evaporation of the droplets. This is usually explained by two effects: (a) active removal of water promoting condensation reactions between organic compounds; (b) increased acidity during evaporation further promoting dehydration and acid-catalyzed oligomerization reactions. For example, glyoxal and methylglyoxal are common components of cloud droplets, and were found to officially form oligomers in evaporating droplets (De Haan et al., 2009). Glyoxal formed acetal oligomers while methylglyoxal formed aldol oligomers catalyzed by pyruvic acid. De Haan et al. (2011) made solutions of methylglyoxal and various amines at pH=5 and found that the solution turned brown when evaporated. With NMR and mass spectrometry methods, they determined products with methylimidazole moieties. Additional studies looked at the reaction between glyoxal or methylglyoxal and ammonium sulfate, and showed that organonitrogen species are responsible for the observed light absorption (Kampf et al., 2012; Lee et al., 2013; Lin et al., 2015; Nozière and Esteve, 2007; Sareen et al., 2010; Shapiro et al., 2009). The BrC formation in the glyoxal or methyl glyoxal + ammonium sulfate system was strongly accelerated by the evaporation of solution (Aiona et al., 2017b; Lee et al., 2013). Aiona et al. (2017) reacted another atmospherically relevant dicarbonyl, 4-oxopentanal with ammonium sulfate, and observed the absorbance of solutions increase with reaction time at 505 nm. They identified the reaction intermediate, 2-methyl pyrrole, and found that reacting just the intermediate with 4-oxopentanal or limonene SOA similarly produced an increase in absorbance in the visible. Further, they found that the reaction of 4-oxopentanal with ammonium sulfate was accelerated by evaporation.

Gaseous ammonia and ammonium ions were also found to react with limonene SOA and produce light-absorbing chromophores, while reacted α -pinene SOA remained colorless (Bones et al., 2010; Laskin et al., 2014). Evaporation similarly accelerated these reactions. Specifically, Nguyen et al., (2012b) found that molecules with carbonyl functional groups, which are abundant in limonene ozonolysis SOA, formed light-absorbing products when evaporated in the presence of ammonium sulfate at pH=4.5. High resolution mass spectra provided evidence for organosulfates produced by acid-catalyzed aldol condensation reactions. The researchers who observed ammonia-induced browning in SOA proposed that carbonyls in SOA particles react with ammonia to form primary imines, which react with other carbonyl species to form secondary imines in condensation reactions. They suggest that limonene SOA browning is due to intramolecular reactions between a primary imine and carbonyl, thus forming light-absorbing heterocyclic molecules. In contrast, molecules in α -pinene SOA are more rigid, and formation of BrC chromophores was hindered. A similar mechanism was proposed by Hawkins et al. (2018) to explain the observation of pyrazine-based chromophores from the reaction of methylglyoxal with ammonium sulfate over various pH ranges. They found that evaporation greatly enhances the product distribution and absorptivity under atmospherically-relevant, acidic conditions.

In summary, there is plenty of evidence that evaporation of cloud droplets could accelerate chemical aging and produce secondary BrC chromophores, such as N-heterocyclic and organosulfate oligomers, but only a few atmospherically relevant have been investigated. Part of this dissertation is devoted to the formation of secondary BrC in evaporative processes.

1.2.5 Effect of relative humidity on the composition and mass of SOA particles

Relative humidity fluctuations are common due to changes in temperature or weather. Besides temperature, relative humidity is another way that the viscosity of particles changes during atmospheric transport. The viscosity of SOA particles controls their aging in the atmosphere by limiting reactive uptake of gases, as well as bulk diffusion (Shiraiwa et al., 2011). Relative humidity also dictates SOA particle phase state. There has been much interest in quantitatively describing particle phase state under different conditions because it determines the radiative forcing direct effect of SOA particles (Martin et al., 2004; Wang et al., 2008), partitioning of organic species (Chang and Pankow, 2006; Zuend et al., 2010), heterogeneous uptake of gas-phase species (Anttila et al., 2006; Cosman et al., 2008; Cosman and Bertram, 2008; Escorcia et al., 2010; Folkers et al., 2003; McNeill et al., 2006; Park et al., 2007; Thornton and Abbatt, 2005), and their ability to act as ice condensation nuclei (Schill and Tolbert, 2013; You et al., 2014).

At low relative humidity, for typical atmospheric particles that have both organic and inorganic components, a solid core of inorganic salts is coated by an organic shell consisting of POA and SOA material. In addition, there can be insoluble inclusions such as soot or mineral dust. As the humidity is increased, the core may deliquesce and the shell takes up some water. At even higher relative humidity, the particle can undergo what is referred to as liquid-liquid phase separation, in which a core solution containing primarily inorganic solute is encapsulated (or phase separated in a more complex morphology) by a liquid mixture containing primarily organic solutes. Finally, at a high relative humidity (typically around 100%) the particle becomes well mixed and there is no longer any discernable phase separation (You et al., 2012, 2014). The phase state depends on the SOA and seed type, for example, α -pinene ozonolysis SOA with

ammonium sulfate seeds was found to be liquid-liquid phase separated at 98% RH, and effloresce in the range of 30-35%. This type of SOA particle is expected to be phase-separated under most atmospheric conditions (You et al., 2012, 2014).

Many studies have measured SOA particle yields at different relative humidities in smog chambers. In the presence of neutral seed particles, relative humidity can have a large effect on SOA particle yield. A deliquesced seed particle allows for aqueous phase chemistry, potentially increasing SOA mass by up to 50% depending on the SOA precursor (Faust et al., 2017). However, if SOA particles are formed by gas to particle conversion, relative humidity may have no effect on yields, like in the case of high-NO_x isoprene photooxidation (Nguyen et al., 2011), or in the case of low-NO_x toluene photooxidation, high relative humidity decreases the observed yield (Hinks et al., 2018). An abundance of water vapor could result in lower SOA yields by shifting the equilibrium of condensation reactions towards the more volatile monomers (Nguyen et al., 2011).

Very few studies have looked at the role relative humidity has on atmospheric aging. Wilson et al., (2015) formed α -pinene ozonolysis SOA at high RH (90%) and then evaporated the SOA particles in a high RH chamber in the absence of oxidants for 24 hours. The resulting particle volume was 20% less than the particle's original volume due to losses by evaporation. However, if the particles were evaporated after 24 hours of oxidative aging, ~60 % by volume evaporated due to the formation of low volatility oligomers. While the exact percentage varied when SOA particles were formed/aged under dry/wet, wet/dry, or wet/wet; in all cases, oxidative aging decreased evaporative losses of particle volume. In Tasoglou and Pandis, (2015) β -caryophyllene ozonolysis SOA was produced at 50% or 90% RH at 20°C in the presence of ammonium sulfate seed particles. Then, the temperature of the chamber was increased to 40°C

after reactions were complete. They found that the SOA particle yield increased by ~40% and O:C was moderately increased by 0.07. In Li et al. (2018), α -pinene ozonolysis SOA was generated in a flow tube, and then aged in the presence of OH radicals at low (28%) or high RH (90%) conditions. They found that SOA particles lost ~80% of their mass after 4 weeks when aged at low RH, but at high RH it only took a few days to lose the same mass percent. Mass loss was due to fragmentation of particle phase molecules (Isaacman-VanWertz et al., 2018).

1.3 Research questions and dissertation structure

Despite the growing literature on BBOA composition, primary and secondary BrC composition, and SOA aging, many unanswered questions remain. The studies in this dissertation were guided by the following overlapping questions.

- What are the emissions of various VOCs and fine particulate matter from biomass-burning cookstoves? Could these emissions significantly contribute to ambient PM_{2.5} and ozone levels in places where these cookstoves are used extensively, such as rural India?
- What is the composition of BBOA particles from the cookstoves? Is the composition of dung-burning cookstoves significantly different from wood-burning cookstoves which have been studied in more detail?
- Is the composition of BrC chromophores from wildfire emissions dependent on fuel type or combustion conditions? What is the photochemical lifetime of these BrC chromophores?
- Can secondary BrC form in evaporating cloud droplets containing different types of SOA? If so, how absorbing is the material and what types of chromophores are produced?

- Can aerosol liquid water and relative humidity affect the molecular composition of SOA, during both formation and aging stages? What mechanisms guide this chemical processing of SOA?

Chapters 2 and 3 aim to characterize emissions from biomass burning cookstoves in rural India. A hired cook prepared traditional meals at a village home in Haryana, India, while emissions of VOCs and fine particulate matter (PM_{2.5}) were sampled. The cook utilized two fuel types commonly used in this village, brushwood and dung. In addition, smoldering and flaming stoves, *angithi* and *chulha*, respectively, were used to cook different meals. Chapter 2 focuses on quantifying emissions of CO, CO₂, and 76 VOCs, and fine particulate matter (PM_{2.5}). Analysis of Variance statistical testing was used to determine if there was a significant relationship between emissions of specific gases and fuel type or stove type. We also estimated OH reactivity, ozone, and SOA formation in a theoretical village based on the measured VOCs. Chapter 3 investigates the molecular composition of PM_{2.5} from Indian cookstoves. We determine the fraction of compounds specific to dung cook fires, and the broad range of species in these BBOA particles. We also quantify the MAC_{bulk} for dung and brushwood cook fires and determine BrC chromophores that contribute to the observed absorptivity.

Chapter 4 characterizes BrC chromophores produced by simulated forest fires from the Fire Influence on Regional and Global Environments Experiment (FIREX) Fall 2016 laboratory intensive. We focus on twelve burns that include conifer and angiosperm fuel types, as well as a variety of ecosystem components such as canopy, litter, duff, and shrub. Fuel specific and common BrC chromophores are discussed. We also photochemically aged BBOA particles on filters, and discuss the photostability or lability of different BrC chromophore classes. We also quantify lifetimes of BrC in BBOA particles.

Chapter 5 explores the formation of secondary BrC from evaporated solutions of dissolved SOA in the presence of sulfuric acid. A variety of SOA types were tested, including biogenic and anthropogenic precursors, and different oxidants (OH, O₃, NO_x). The evaporated sample was reconstituted and MAC_{bulk} quantified the absorbance of the secondary BrC. In addition, individual BrC chromophores were characterized. We did rough calculations to determine whether filter extracts could produce artifacts via similar mechanisms during the sample preparation of laboratory or field collected SOA.

Chapter 6 investigates the effect of relative humidity on the molecular composition of α -pinene/OH SOA as it was formed and aged. SOA was formed in a laboratory smog chamber under dry (<5% RH) or humid (>90% RH) conditions and in the presence and absence of seeds, and then collected onto PTFE filters. SOA particles were aged on the filter, which was suspended in a supersaturated salt solution to control the humidity. We discussed the roles of water vapor or aerosol liquid water in determining SOA mass and composition.

CHAPTER 2:

Emissions from village cookstoves in Haryana, India and their potential impacts on air quality

Abstract. Air quality in rural India is impacted by residential cooking and heating with biomass fuels. In this study, emissions of CO, CO₂, and 76 volatile organic compounds (VOCs) and fine particulate matter (PM_{2.5}) were quantified to better understand the relationship between cook fire emissions and ambient ozone and secondary organic aerosol (SOA) formation. Cooking was carried out by a local cook and traditional dishes were prepared on locally built *chulha* or *angithi* cookstoves using brushwood or dung fuels. Cook fire emissions were collected throughout the cooking event in a Kynar bag (VOCs) and on PTFE filters (PM_{2.5}). Gas samples were transferred from a Kynar bag to previously evacuated stainless steel canisters and analyzed using gas chromatography coupled to flame ionization, electron capture, and mass spectrometry detectors. VOC emission factors were calculated from the measured mixing ratios using the carbon-balance method, which assumes that all carbon in the fuel is converted to CO₂, CO, VOCs, and PM_{2.5} when the fuel is burned. Filter samples were weighed to calculate PM_{2.5} emission factors. Dung fuels and *angithi* cookstoves resulted in significantly higher emissions of most VOCs ($p < 0.05$). Utilizing dung-*angithi* cook fires resulted in twice as much of the measured VOCs compared to dung-*chulha*, and four times as much as brushwood-*chulha* with 84.0, 43.2, and 17.2 g measured VOC/ kg fuel carbon, respectively. This matches expectations, as the use of dung fuels and *angithi* cookstoves results in lower modified combustion efficiencies compared to brushwood

fuels and *chulha* cookstoves. Alkynes and benzene were exceptions and had significantly higher emissions when cooking using a *chulha* as opposed to an *angithi* with dung fuel (for example, benzene emission factors were 3.18 g/ kg fuel carbon for dung-*chulha* and 2.38 g/ kg fuel carbon for dung-*angithi*). This study estimated that three times as much SOA and ozone in the Maximum Incremental Reactivity (MIR) regime may be produced from dung-*chulha* as opposed to brushwood-*chulha* cook fires. Aromatic compounds dominated as SOA precursors from all types of cook fires, but benzene was responsible for the majority of SOA formation potential from all *chulha* cook fire VOCs, while substituted aromatics were more important for dung-*angithi*. Future studies should investigate benzene exposures from different stove and fuel combinations and model SOA formation from cook fire VOCs to verify public health and air quality impacts from cook fires.

2.1 Introduction

Parts of rural India are comprised of densely populated villages with ambient ozone and PM_{2.5} levels that affect air quality for inhabitants (Bisht et al., 2015; Ojha et al., 2012; Reddy, 2012). For example, in the rural area of Anantapur in Southern India, monthly mean ozone levels varied between 29 ppbv (parts per billion by volume) in August during the monsoon season and 56 ppbv in April (Reddy, 2012). In Pantnagar, a semi-urban city, the maximum observed ozone concentration was 105 ppbv for one day in May, with the lowest maximum of 50 ppbv being in January (Ojha et al., 2012). In terms of PM_{2.5} levels, Bisht et al. (2015) observed an average of 50 $\mu\text{g m}^{-3}$ of PM_{2.5} over July-November 2011 in rural Mahabubnagar. While measurements of O₃ and PM_{2.5} in rural India are relatively scarce, it has become clear that household combustion is a major contributor to ambient levels of these pollutants. For example Balakrishnan et al. (2013)

measured PM_{2.5} concentrations in households and observed mean 24-hour concentrations of 163 µg m⁻³ in the living room and 609 µg m⁻³ in the kitchen. Over the last half-decade, several researchers have, through independent studies, come to the conclusion that a significant fraction (22-52%) of ambient PM_{2.5} is directly emitted from residential cooking and heating (Butt et al., 2016; Chafe et al., 2014; Conibear et al., 2018; GBD MAPS Working Group, 2018; Guttikunda et al., 2016; Klimont et al., 2017; Lelieveld et al., 2015; Silva et al., 2016).

Residences in India were estimated to consume 220, 86.5, and 93.0 Tg per year of dry matter of wood fuel, agricultural residues, and dung, respectively in the year 1985 (Yevich and Logan, 2003). While the fraction of Indians using biomass cook fuels is decreasing, the total population is increasing such that biomass fuels are still being utilized at approximately the same overall level (Pandey et al., 2014). Emissions of primary PM_{2.5} from residential cooking in India were estimated to be 2.6 Tg per year based on a compiled emissions inventory (Pandey et al., 2014). Additionally, Pandey et al. (2014) estimated that 4.9 Tg of non-methane volatile organic compounds (NMVOCs) are produced annually in India from residential cooking. This suggests that additional PM_{2.5} mass may be formed via secondary pathways from the oxidation of NMVOCs and either nucleation of new particles or condensation onto existing PM_{2.5}. Alternatively, these non-methane VOCs could contribute to photochemical ozone production in the presence of NO_x (Finlayson-Pitts and Pitts, 2000).

In this study, we quantified emissions of CO, CO₂, and 76 different VOCs from 55 cook fires carried out by a local cook in a village home cooking typical meals. This is a substantially updated version of the work done in simulated village houses in India and China in the 1990s, where 58 fuel-stove combinations were measured in semi-controlled conditions using water boiling tests including a number of non-biomass stoves although a similar set of pollutants were

measured (Smith et al., 2000b, 2000a; Tsai et al., 2003; Zhang et al., 2000). This time, we measured emissions in field conditions from two traditional, locally-made cookstoves, the *chulha* and the *angithi*. The former is a primarily flaming stove with generally higher modified combustion efficiencies or concentration ratios of carbon dioxide to the sum of carbon dioxide and carbon monoxide (average dung-*chulha* 0.865), used to cook village meals. The *angithi* is largely smoldering with lower modified combustion efficiencies (average dung-*angithi* 0.819) and is primarily used for cooking animal fodder and simmering milk. We measured emissions from cookstoves with two kinds of biomass; the most popular biomass type brushwood (Census of India, 2011) and dung cakes. The fuels and stoves used in this study are predominantly used in the Indo-Gangetic plains. Our first objective is to characterize emissions of select VOCs and PM_{2.5} from these fuel-stove combinations. Subsequently, with the aid of secondary organic aerosol (SOA) potential values from Derwent et al. (2010), incremental reactivities first described in Carter, (1994), and second-order rate coefficients with OH combined with our emission factors, we estimate SOA forming potentials, excess ozone mixing ratios in a VOC-limited regime, and OH reactivities, respectively. Given their widespread use in India, emissions from these biomass-burning stoves are estimated to impact regional air quality due to both primary and secondary organic aerosol and ozone formation.

2.2 Experimental Methods

2.2.1 Field site and sample collection

The field office was located at the SOMAARTH Demographic, Development, and Environmental Surveillance Site in Palwal District, Haryana, India run by the International

Clinical Epidemiological Network (INCLEN). The site consists of 51 villages in the area with roughly 200,000 inhabitants (Balakrishnan et al., 2015; Mukhopadhyay et al., 2012; Pillarisetti et al., 2014).

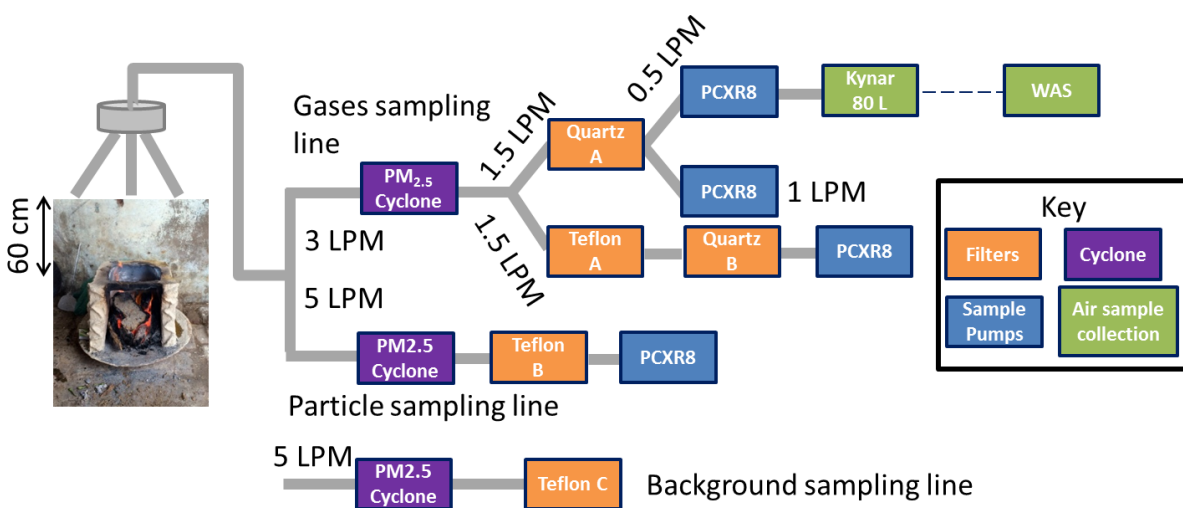
Samples were collected from cookstove emissions between August 5 and September 3, 2015. Cooking events occurred at a village kitchen in Khatela, Palwal District. A local cook was hired to prepare meals for human consumption consisting of either *chapatti* or rice with vegetables using a *chulha* stove, as well as animal food using an *angithi* stove.

Animal fodder simmers in a pot set upon smoldering dung in a clay bowl, referred to as an *angithi*. *Chulha* stoves are made from bricks and a covering of clay, and the availability of oxygen from the packing of biomass fuels results in primarily flaming combustion. The *chulha* is used to cook most meals for families in this village. Buffalo and cow dung patties and brushwood, in the form of branches and twigs, were used in *chulha* stoves, and for the 13 mixed fuel cooking events dung and brushwood were combined in a ratio determined by the cook's preference. Stoves and food ingredients were produced and fuels procured by the household or village. Additional information regarding the cooking events and set-up can be found in Fleming et al., 2018.

The sampling scheme is illustrated in Figure 2.1. Air sampling pumps (PCXR-8, SKC Inc.) created a flow of emissions through the sampling apparatus. Emissions were captured with three-pronged probes that were fixed 60 cm above the cookstove. PM_{2.5} emissions and gases were sampled through cyclones (2.5 µm, URG Corporation). The resulting flow of particles was captured on either quartz or PTFE filters, while gases were collected in an 80 L Kynar bag throughout the entire cooking event. Flows were measured both before and after sampling to ensure they did not change by more than 10% using a mass flowmeter (TSI 4140). After the

cooking event, pumps were turned off and a whole air sampler, consisting of a stainless steel canister (2 L) welded to a Bellows-sealed valve (Swagelok), was filled to ambient pressure from the Kynar bag. Whole air samplers were thoroughly flushed and evacuated in the Rowland-Blake laboratory before being shipped to India. At the end of the measurement campaign, whole air samplers were shipped back to the laboratory and analyzed within two months of the end of the field measurements. A “grab” whole air sample was collected before cooking commenced each day. This served as a background for all cooking events sampled on that day.

Figure 2.1: Sampling train for collecting cookstove emissions. PCXR8 (blue) are sampling pumps, WAS or whole air samples (green) are the air samplers, and orange boxes are Teflon or quartz filters used to collect PM_{2.5}.



2.2.2 Gas chromatography analysis

Colman et al., 2001 described the VOC analysis protocol in detail. Briefly, a known amount of the whole air sample (WAS) flowed over glass beads inside a U-shaped trap cooled by liquid nitrogen. The flow was regulated by a mass flow controller and resulted in a 600 Torr drop

in the pressure in the whole air sampler. High volatility gases such as O₂ and N₂ passed over the beads, while lower volatility gases adsorbed onto the beads. Compounds were re-volatilized by immersing the trap in hot water and were injected into a He carrier gas stream where the flow was split equally to 5 columns housed in 3 gas chromatographs (HP-6890). The compounds were separated by gas chromatography and subsequently detected by two electron capture, two flame ionization, and one quadrupole mass spectrometer detectors. Peaks corresponding to compounds of interest were integrated manually. CO/CO₂ and CH₄ were analyzed using separate GC systems equipped with thermal conductivity and flame ionization detectors as described in Simpson et al., 2014. The CO/CO₂ GC-FID system is equipped with a Ni catalyst that converts CO into detectable CH₄.

2.2.3 Gas and PM_{2.5} Emission factor calculations

Emission factors (EFs) were calculated using the carbon-balance method, which assumes that all carbon in the fuel is converted to CO₂, CO, VOCs, and PM when the fuel is burned. The total gas-phase carbon emissions were approximated with the concentrations of CO₂, CO, as well as 76 detected VOCs measured using WAS. This is a good approximation since most emitted carbon resides in CO₂ and CO (> 95 %), so the error associated with VOCs that are not detected is relatively small (Roden and Bond, 2006; Smith et al., 1993; Wathore et al., 2017; Zhang et al., 2000). The mass of carbon in species *i* (m_{*i,C*}) was calculated using equation (2.1).

$$m_{i,C} \text{ (g)} = \frac{C_{i,C} \text{ (g/m}^3\text{)}}{C_{CO_2,C} + C_{CO,C} + C_{CH_4,C} + \dots + C_{C_6H_6,C} \text{ (g/m}^3\text{)}} \cdot m_{T,C} \text{ (kg)} \cdot \frac{1000 \text{ g}}{1 \text{ kg}} \quad (2.1)$$

Where C_{*i,C*} represents the mass concentration of carbon for species *i*, and m_{T,C} refers to the carbon mass of the fuel, adjusted for ash and char carbon. Fuels were weighed before they were

burned, and the dry mass was calculated based on moisture content measurements. The ash was weighed after the cooking event and subtracted from the dry mass of the fuel giving the net dry fuel burned for the cooking event, m_T . When mixtures of dung and brushwood were used, both were individually weighed to more accurately determine the carbon mass burned. The fraction of carbon in the fuel used to yield $m_{T,C}$ was taken to be 0.33 for buffalo and cow dung and 0.45 for brushwood fuels based on Smith et al. 2000. Carbon in ash was estimated as 2.9% and 80.9% of the measured char mass for dry dung and dry brushwood, respectively (Smith et al., 2000b). For each species with $n_{c,i}$ carbon atoms in the formula and molecular weight MW_i , the emissions factor (EF_i) was calculated using equation (2.2).

$$EF_i \left(\frac{\text{g VOC}_i}{\text{kg fuel}} \right) = \frac{m_{i,c}(\text{g}) \cdot \frac{MW_i (\text{g/mol})}{n_{c,i} \times 12.00 (\text{g/mol})}}{m_T(\text{kg})} \quad (2.2)$$

In addition to the emission factor normalized by the total fuel mass, emission factors were normalized to the total carbon mass in the fuel, calculated via equation (2.3).

$$EF_i \left(\frac{\text{g VOC}_i}{\text{kg fuel C}} \right) = EF_i \left(\frac{\text{g VOC}_i}{\text{kg fuel}} \right) \cdot \frac{m_T(\text{kg})}{m_{T,C}(\text{kg})} \quad (2.3)$$

$PM_{2.5}$ mass was determined gravimetrically using Teflon filters (PTFE, SKC Inc., 47 mm) weighed on a Cahn-28 electrobalance with a repeatability of $\pm 1.0 \mu\text{g}$ after equilibrating for a minimum of 24 hours in a humidity and temperature-controlled environment both before and after sample collection (average temperature $19.5 \pm 0.5 \text{ }^\circ\text{C}$; average relative humidity $49 \pm 5\%$). Another gravimetric filter was collected in the background during the cooking event and was equilibrated and weighed in the same way (Figure 2.1, Teflon C). Five field blanks filters were prepared by opening filters and then immediately closing and sealing the filters the same way as

all samples; these filters had negligible mass loading (average: 0.40 μg) relative to samples (average: 1.57 mg). The method detection limit was determined to be 9.3 μg from the standard deviation of the field blank filters multiplied by 3. The background filter mass (Figure 2.1, Teflon C) was adjusted by matching the sampling volume to that of the sample gravimetric Teflon filter (Figure 2.1, Teflon A). This assumes that the mass of $\text{PM}_{2.5}$ collected on the filter is directly proportional to the flow rate through the filter. The background mass was then subtracted from the sample mass to obtain the mass of PM (m_{PM}) in equation (2.4) below.

$$\frac{EF_{\text{PM}}}{EF_{\text{CO}}} = \frac{m_{\text{PM}}/V_{\text{air}}}{m_{\text{CO}}/V_{\text{air}}} \quad (2.4)$$

2.2.4 Modified Combustion Efficiency (MCE)

Modified combustion efficiency (MCE) is defined as follows:

$$\text{MCE} = \frac{\Delta\text{CO}_2}{\Delta\text{CO} + \Delta\text{CO}_2} \quad (2.5)$$

where ΔCO and ΔCO_2 are background-subtracted mixing ratios of CO and CO_2 for the time-integrated whole air sample. The total carbon mixing ratio is approximated by the sum of carbon monoxide and carbon dioxide in this definition.

2.2.5 SOA Forming potential

Relative SOA forming potential from measured VOCs was estimated using secondary organic aerosol potential (SOAP) values from Derwent et al. (2010), who used a photochemical transport model to simulate the SOA mass increase from the instantaneous emission of a particular VOC in a single parcel of air travelling across Europe. The model was outfitted with

the Master Chemical Mechanism (MCM v.3.1) and the UK National Atmospheric Emission Inventory. The model was initialized with 2 ppbv NO and 6 ppbv NO₂ (Derwent et al., 1998). SOA mass was estimated assuming equilibrium partitioning of oxidation products. Partitioning coefficients were calculated using absorptive partitioning theory of Pankow, 1994. In the SOAP approach, all SOA mass increases from a particular VOC (*i*) are normalized to that of toluene as shown in equation (2.6).

$$\text{SOAP}_i = \frac{\text{Increment in SOA mass concentration with species } i}{\text{Increment in SOA mass concentration with toluene}} \times 100 \quad (2.6)$$

SOA forming potential was calculated from the published SOAP values using equation (2.7).

$$\text{SOA potential} = \sum_{i=0}^n \text{SOAP}_i \times \text{EF}_i \left(\frac{\text{g VOC}_i}{\text{kg fuel C}} \right) \quad (2.7)$$

Table 2.1 lists the SOAP values used to calculate SOA forming potential in this study. We emphasize that the SOA forming potential presented here is a relative value, and does not represent an absolute SOA yield.

Table 2.1: Average emission factors and standard deviation of PM_{2.5} and gas-phase species (g kg⁻¹ dry fuel carbon) for dung-*chulha*, brushwood-*chulha*, mixed-*chulha*, and dung-*angithi* cook fires. Sample size (n) was n=12 for dung-*chulha*, n=14 for brushwood-*chulha*, n=13 for mixed-*chulha*, n=10 for dung-*angithi*. SOAP values, k_{OH}, and MIR values used to calculate predicted SOAP-weighted potentials, OH reactivity, and ozone-forming potential are included for the quantified species. SOAP values were taken from Derwent et al. (2010), k_{OH} were found in the NIST Chemical Kinetics Database, and MIR values are found in Carter et al. 1994.

Compound	Dung- <i>chulha</i> Average (SD)	Brushwood- <i>chulha</i> Average (SD)	Mixed- <i>chulha</i> Average (SD)	Dung- <i>angithi</i> Average (SD)	SOAP	k _{OH} (x 10 ¹²) (cm ³ molec ⁻¹ s ⁻¹)	MIR (g O ₃ /g VOC)
Carbon dioxide (CO ₂)	3028 (80)	3365 (148)	3171 (83)	2745 (144)	0 ^a	0	0
Carbon monoxide (CO)	301 (33)	143 (78)	243 (47)	385 (61)	0 ^a	0.15	0.056
Methane (CH ₄)	21.3 (4.0)	12.9 (5.4)	15.8 (2.7)	46.7 (8.2)	0 ^a	0.006	0.0144
Sulfur-containing							
Carbonyl sulfide (OCS)	0.382 (0.135)	3.89 (1.36) x 10 ⁻²	0.279 (0.083)	1.09 (0.67)	0 ^a	0.002	0
DMS (C ₂ H ₆ S)	2.98 (1.55) x 10 ⁻²	3.68 (3.36) x 10 ⁻³	1.57 (0.74) x 10 ⁻²	0.134 (0.096)	0 ^a	5.4	0
Halogen-containing							
Dichloromethane (CH ₂ Cl ₂)	1.37 (1.48) x 10 ⁻³	5.79 (8.21) x 10 ⁻⁴	1.35 (2.20) x 10 ⁻³	1.41 (0.85) x 10 ⁻³	0 ^a	0.123	0.041
Chloromethane (CH ₃ Cl)	5.48 (2.41)	0.751 (0.393)	3.34 (1.37)	14.2 (5.8)	0 ^a	0.369	0.038
Bromomethane (CH ₃ Br)	2.02 (0.96) x 10 ⁻²	2.14 (0.57) x 10 ⁻³	1.42 (0.59) x 10 ⁻²	4.42 (1.75) x 10 ⁻²	0 ^a	0.0288	0.0187
Iodomethane (CH ₃ I)	1.88 (0.40) x 10 ⁻³	2.61 (0.61) x 10 ⁻⁴	7.87 (2.08) x 10 ⁻⁴	2.73 (0.51) x 10 ⁻³	0 ^a	0.0723	-0.56
Ethyl chloride (C ₂ H ₅ Cl)	7.83 (3.93) x 10 ⁻³	1.13 (0.95) x 10 ⁻³	5.23 (2.25) x 10 ⁻³	2.82 (1.08) x 10 ⁻²	0 ^a	0.423	0.29
Dichloroethane (C ₂ H ₄ Cl ₂)	2.71 (1.00) x 10 ⁻³	6.86 (5.78) x 10 ⁻⁴	4.04 (7.92) x 10 ⁻³	4.55 (2.82) x 10 ⁻³	0 ^a	0.023	0.21
Nitrates							
Methyl nitrate (CH ₃ ONO ₂)	5.62 (19.5) x 10 ⁻³	1.47 (4.00) x 10 ⁻²	2.19 (3.95) x 10 ⁻²	0.527 (1.048)	0 ^a	0.023	0
Ethyl nitrate (CH ₃ ONO ₂)	7.27 (14.5) x 10 ⁻⁴	1.50 (2.80) x 10 ⁻³	7.63 (21.77) x 10 ⁻³	0.140 (0.357)	0 ^a	0.178	0
i-Propylnitrate (C ₃ H ₇ ONO ₂)	5.85 (5.66) x 10 ⁻⁴	6.57 (13.64) x 10 ⁻⁴	1.37 (2.86) x 10 ⁻³	1.83 (3.75) x 10 ⁻²	0 ^a	0.287	0
n-Propylnitrate (C ₃ H ₇ ONO ₂)	1.94 (1.82) x 10 ⁻⁴	2.43 (3.83) x 10 ⁻⁴	4.81 (11.05) x 10 ⁻⁴	5.63 (13.44) x 10 ⁻³	0 ^a	0.731	0
2-Butylnitrate (C ₄ H ₉ ONO ₂)	8.27 (7.41) x 10 ⁻⁴	2.82 (3.07) x 10 ⁻⁴	2.39 (6.92) x 10 ⁻³	7.57 (15.15) x 10 ⁻³	0 ^a	0.93	0
3-Pentylnitrate (C ₅ H ₁₁ ONO ₂)	1.46 (0.49) x 10 ⁻⁴	6.15 (5.54) x 10 ⁻⁵	1.02 (0.62) x 10 ⁻⁴	6.01 (12.55) x 10 ⁻⁴	0 ^a	1	0

Compound	Dung- <i>chulha</i> Average (SD)	Brushwood- <i>chulha</i> Average (SD)	Mixed- <i>chulha</i> Average (SD)	Dung- <i>angithi</i> Average (SD)	SOAP	k_{OH} ($\times 10^{12}$) ($\text{cm}^3 \text{ molec}^{-1} \text{ s}^{-1}$)	MIR ($\text{g O}_3/\text{g VOC}$)
Nitrates (continued)							
2-Pentylnitrate ($\text{C}_5\text{H}_{11}\text{ONO}_2$)	$7.27 (4.52) \times 10^{-5}$	$4.41 (6.71) \times 10^{-5}$	$4.05 (4.04) \times 10^{-5}$	$5.61 (14.00) \times 10^{-4}$	0 ^a	1	0
Alkanes							
Ethane (C_2H_6)	2.21 (0.60)	1.02 (0.64)	1.38 (0.30)	6.38 (2.14)	0.1	0.244	0.28
Propane (C_3H_8)	0.650 (0.219)	0.253 (0.211)	0.378 (0.106)	2.53 (0.49)	0	1.1	0.49
i-Butane (C_4H_{10})	$5.31 (2.14) \times 10^{-2}$	$1.23 (1.22) \times 10^{-2}$	$3.12 (0.92) \times 10^{-2}$	0.225 (0.048)	0	2.12	1.23
n-Butane (C_4H_{10})	0.145 (0.058)	$4.20 (4.22) \times 10^{-2}$	$8.83 (3.06) \times 10^{-2}$	0.665 (0.148)	0.3	2.4	1.15
n-Pentane (C_5H_{12})	$6.18 (2.46) \times 10^{-2}$	$1.19 (1.03) \times 10^{-2}$	$2.99 (1.24) \times 10^{-2}$	0.210 (0.091)	0.3	3.8	1.31
n-Hexane (C_6H_{14})	$3.16 (1.30) \times 10^{-2}$	$5.25 (4.05) \times 10^{-3}$	$1.74 (0.63) \times 10^{-2}$	0.153 (0.034)	0.1	5.2	1.24
n-Heptane (C_7H_{16})	$2.22 (1.02) \times 10^{-2}$	$2.49 (1.86) \times 10^{-3}$	$1.29 (0.41) \times 10^{-2}$	$9.79 (2.63) \times 10^{-2}$	0.1	6.8	1.07
2-Methylpentane (C_6H_{14})	$1.91 (0.75) \times 10^{-2}$	$3.28 (2.51) \times 10^{-3}$	$8.44 (5.36) \times 10^{-3}$	$7.07 (5.18) \times 10^{-2}$	0	5.2	1.5
3-Methylpentane (C_6H_{14})	$1.14 (0.53) \times 10^{-2}$	$3.23 (2.64) \times 10^{-3}$	$5.12 (2.44) \times 10^{-3}$	$2.33 (1.33) \times 10^{-2}$	0.2	5.2	1.8
Alkenes							
Ethene (C_2H_4)	5.73 (1.36)	1.68 (0.73)	3.68 (1.15)	5.47 (1.09)	1.3	8.51	9
Propene (C_3H_6)	2.48 (0.60)	0.765 (0.506)	1.36 (0.28)	4.98 (1.04)	1.6	30.1	11.66
1-Butene (C_4H_8)	0.488 (0.140)	0.169 (0.115)	0.274 (0.058)	1.13 (0.30)	1.2	31	9.73
i-Butene (C_4H_8)	0.411 (0.125)	$9.25 (6.25) \times 10^{-2}$	0.209 (0.060)	1.09 (0.49)	0.6	51	1.23
trans-2-Butene (C_4H_8)	0.137 (0.047)	$5.36 (3.30) \times 10^{-2}$	$7.79 (2.22) \times 10^{-2}$	0.466 (0.170)	4.0	64	15.16
cis-2-Butene (C_4H_8)	0.104 (0.037)	$4.04 (2.45) \times 10^{-2}$	$5.88 (1.69) \times 10^{-2}$	0.331 (0.145)	3.6	56	14.24
3-Methyl-1-butene (C_5H_{10})	$4.50 (1.44) \times 10^{-2}$	$1.53 (1.13) \times 10^{-2}$	$2.39 (0.62) \times 10^{-2}$	0.118 (0.027)	0.6	32	6.99
2-Methyl-1-butene (C_5H_{10})	$8.33 (2.97) \times 10^{-2}$	$2.65 (2.72) \times 10^{-2}$	$3.92 (1.38) \times 10^{-2}$	0.238 (0.124)	0.9	61	6.4
2-Methyl-2-butene (C_5H_{10})	$7.72 (3.14) \times 10^{-2}$	$1.71 (1.24) \times 10^{-2}$	$3.61 (1.53) \times 10^{-2}$	0.284 (0.146)	1.9	87	14.08
1-Pentene (C_5H_{10})	0.128 (0.048)	$2.58 (1.64) \times 10^{-2}$	$6.99 (1.98) \times 10^{-2}$	0.378 (0.102)	0	27.4	7.21
trans-2-Pentene (C_5H_{10})	$5.34 (1.68) \times 10^{-2}$	$2.38 (1.49) \times 10^{-2}$	$7.79 (2.22) \times 10^{-2}$	0.159 (0.064)	3.1	67	10.56
cis-2-Pentene (C_5H_{10})	$3.08 (0.90) \times 10^{-2}$	$1.49 (0.94) \times 10^{-2}$	$5.88 (1.69) \times 10^{-2}$	$7.72 (3.98) \times 10^{-2}$	3.1	65	10.38

Compound	Dung- <i>chulha</i> Average (SD)	Brushwood- <i>chulha</i> Average (SD)	Mixed- <i>chulha</i> Average (SD)	Dung- <i>angithi</i> Average (SD)	SOAP	k_{OH} ($\times 10^{12}$) ($\text{cm}^3 \text{ molec}^{-1} \text{ s}^{-1}$)	MIR ($\text{g O}_3/\text{g VOC}$)
Alkenes (continued)							
1-Hexene (C ₆ H ₁₂)	0.188 (0.072)	$3.38 (1.83) \times 10^{-2}$	0.101 (0.030)	0.517 (0.157)	0	37	5.49
1,2-Propadiene (C ₃ H ₄)	0.116 (0.033)	$3.51 (1.57) \times 10^{-2}$	$7.55 (2.72) \times 10^{-2}$	$5.56 (2.84) \times 10^{-2}$	1.8 ^b	0.45	8.45
1,2-Butadiene (C ₄ H ₆)	$1.70 (0.48) \times 10^{-2}$	$7.54 (4.69) \times 10^{-3}$	$1.01 (0.33) \times 10^{-2}$	$1.34 (0.49) \times 10^{-2}$	1.8 ^b	27	9.35
1,3-Butadiene (C ₄ H ₆)	0.626 (0.221)	0.201 (0.105)	0.352 (0.195)	0.813 (0.254)	1.8	67	12.61
Isoprene (C ₅ H ₈)	0.275 (0.151)	$5.31 (3.88) \times 10^{-2}$	$9.89 (7.79) \times 10^{-2}$	0.582 (0.444)	1.9	100	10.61
1,3-Pentadiene (C ₅ H ₈)	$6.02 (3.37) \times 10^{-2}$	$2.47 (1.26) \times 10^{-2}$	$3.08 (2.11) \times 10^{-2}$	0.175 (0.091)	1.8 ^c	117	12.5
Alkynes							
Ethyne (C ₂ H ₂)	3.46 (1.21)	1.25 (0.39)	2.89 (1.00)	1.01 (0.74)	0.1	0.9	0.95
1-Propyne (C ₃ H ₄)	0.290 (0.084)	0.103 (0.045)	0.195 (0.070)	0.161 (0.087)	0 ^a	3.1	6.72
1-Buten-3-yne (C ₄ H ₄)	0.155 (0.048)	$5.01 (2.27) \times 10^{-2}$	0.113 (0.048)	$5.37 (3.87) \times 10^{-2}$	0 ^a	20	10.48
1-Butyne (C ₄ H ₆)	$2.37 (0.69) \times 10^{-2}$	$1.09 (0.57) \times 10^{-2}$	$1.46 (0.44) \times 10^{-2}$	$1.85 (0.60) \times 10^{-2}$	0 ^a	8	6.11
2-Butyne (C ₄ H ₆)	$1.33 (0.48) \times 10^{-2}$	$6.84 (3.70) \times 10^{-3}$	$8.06 (2.13) \times 10^{-3}$	$1.40 (0.44) \times 10^{-2}$	0 ^a	8	16.32
1,3-Butadiene (C ₄ H ₂)	$1.87 (0.75) \times 10^{-2}$	$7.27 (3.00) \times 10^{-3}$	$1.77 (0.62) \times 10^{-2}$	$4.74 (4.07) \times 10^{-3}$	0 ^a	16	5.76
Aromatics							
Benzene (C ₆ H ₆)	3.18 (1.09)	1.00 (0.37)	2.36 (0.68)	2.38 (0.55)	92.9	1.2	0.72
Toluene (C ₇ H ₈)	1.49 (1.03)	0.597 (0.218)	0.972 (0.250)	2.66 (0.52)	100.0	6.2	4
Ethylbenzene (C ₈ H ₁₀)	0.105 (0.027)	$3.34 (3.03) \times 10^{-2}$	$6.43 (1.20) \times 10^{-2}$	0.303 (0.052)	111.6	7.5	3.04
m/p-Xylene (C ₈ H ₁₀)	0.196 (0.044)	$7.45 (3.89) \times 10^{-2}$	0.131 (0.030)	0.458 (0.093)	75.8	19	2.51
o-Xylene (C ₈ H ₁₀)	$7.31 (2.44) \times 10^{-2}$	$2.24 (1.46) \times 10^{-2}$	$4.68 (1.21) \times 10^{-2}$	0.246 (0.060)	95.5	14	2.51
Styrene (C ₈ H ₈)	$5.88 (1.81) \times 10^{-2}$	$2.28 (1.50) \times 10^{-2}$	$3.40 (1.90) \times 10^{-2}$	$8.64 (5.96) \times 10^{-2}$	212.3	43	1.53
i-Propylbenzene (C ₉ H ₁₂)	$8.97 (2.73) \times 10^{-3}$	$3.21 (2.78) \times 10^{-3}$	$5.51 (1.31) \times 10^{-3}$	$2.88 (1.51) \times 10^{-2}$	95.5	6.6	6.23
n-Propylbenzene (C ₉ H ₁₂)	$2.00 (0.87) \times 10^{-2}$	$4.90 (4.14) \times 10^{-3}$	$1.30 (0.47) \times 10^{-2}$	0.122 (0.083)	109.7	5.7	6.23
3-Ethyltoluene (C ₉ H ₁₂)	$4.44 (1.67) \times 10^{-2}$	$1.46 (1.14) \times 10^{-2}$	$2.79 (0.98) \times 10^{-2}$	0.221 (0.128)	94.8	22.4	7.39
4-Ethyltoluene (C ₉ H ₁₂)	$1.96 (0.79) \times 10^{-2}$	$6.78 (4.65) \times 10^{-3}$	$1.35 (0.59) \times 10^{-2}$	0.115 (0.071)	69.7	13.6	4.44
2-Ethyltoluene (C ₉ H ₁₂)	$2.12 (0.87) \times 10^{-2}$	$7.22 (4.33) \times 10^{-3}$	$1.50 (0.62) \times 10^{-2}$	0.116 (0.083)	94.8	13.2	5.59
1,3,5-Trimethylbenzene (C ₉ H ₁₂)	$1.19 (0.55) \times 10^{-2}$	$4.37 (3.18) \times 10^{-3}$	$8.59 (4.28) \times 10^{-3}$	$6.89 (4.93) \times 10^{-2}$	13.5	60	11.76

Compound	Dung- <i>chulha</i> Average (SD)	Brushwood- <i>chulha</i> Average (SD)	Mixed- <i>chulha</i> Average (SD)	Dung- <i>angithi</i> Average (SD)	SOAP	k_{OH} ($\times 10^{12}$) ($\text{cm}^3 \text{ molec}^{-1} \text{ s}^{-1}$)	MIR ($\text{g O}_3/\text{g VOC}$)
Aromatics (continued)							
1,2,4-Trimethylbenzene (C_9H_{12})	$3.22 (1.59) \times 10^{-2}$	$1.14 (0.70) \times 10^{-2}$	$2.43 (1.28) \times 10^{-2}$	0.193 (0.160)	20.6	32	8.87
1,2,3-Trimethylbenzene (C_9H_{12})	$1.47 (0.78) \times 10^{-2}$	$3.11 (2.08) \times 10^{-3}$	$1.24 (0.82) \times 10^{-2}$	$9.30 (9.75) \times 10^{-2}$	43.9	29	11.97
Terpenes							
alpha-Pinene ($\text{C}_{10}\text{H}_{16}$)	$2.55 (1.92) \times 10^{-3}$	$1.44 (1.81) \times 10^{-3}$	$2.54 (2.08) \times 10^{-3}$	$6.97 (7.78) \times 10^{-3}$	17.4	52	4.51
beta-Pinene ($\text{C}_{10}\text{H}_{16}$)	$6.98 (5.20) \times 10^{-3}$	$3.69 (2.46) \times 10^{-3}$	$8.98 (10.14) \times 10^{-3}$	$8.93 (10.96) \times 10^{-3}$	18.1	74	3.52
Oxygenates							
Acetaldehyde ($\text{C}_2\text{H}_4\text{O}$)	2.48 (0.92)	0.897 (0.520)	1.46 (0.38)	5.26 (2.34)	0.6	16	6.54
Butanal ($\text{C}_4\text{H}_8\text{O}$)	0.132 (0.047)	$5.09 (3.32) \times 10^{-2}$	$8.77 (3.50) \times 10^{-2}$	0.334 (0.145)	0	24	5.97
Acetone ($\text{C}_3\text{H}_6\text{O}$)	2.17 (0.69)	0.977 (0.584)	1.36 (0.35)	6.34 (1.63)	0.3	0.19	0.36
2-Butanone ($\text{C}_4\text{H}_8\text{O}$)	0.530 (0.183)	0.214 (0.161)	0.338 (0.130)	1.54 (0.47)	0.6	1.2	1.48
2-Propenal ($\text{C}_3\text{H}_4\text{O}$)	0.573 (0.202)	0.342 (0.177)	0.414 (0.192)	0.914 (0.761)	1.0 ^a	20	7.45
MVK ($\text{C}_4\text{H}_6\text{O}$)	0.396 (0.121)	0.176 (0.117)	0.205 (0.087)	0.865 (0.458)	1.0 ^a	19	9.65
Furan ($\text{C}_4\text{H}_4\text{O}$)	0.336 (0.141)	0.160 (0.086)	0.223 (0.072)	1.17 (0.29)	1.0 ^a	40	9.15
2-Methylfuran ($\text{C}_5\text{H}_6\text{O}$)	0.360 (0.177)	0.158 (0.123)	0.226 (0.093)	1.51 (0.70)	1.0 ^a	62	8.3
Furfural ($\text{C}_5\text{H}_4\text{O}_2$)	0.263 (0.218)	0.113 (0.143)	0.265 (0.161)	0.981 (0.414)	1.0 ^a	35	10
Methanol (CH_3OH)	6.43 (3.77)	5.38 (5.20)	3.84 (1.26)	13.1 (10.6)	0.3	0.9	0.67
Ethanol (CH_3OH)	0.126 (0.220)	$5.80 (5.19) \times 10^{-2}$	0.184 (0.220)	0.236 (0.281)	0.6	3.4	1.53

^agiven values of either 0 or 1, SOAP values not reported

^bvalues based on 1,3-butadiene

^cvalue based on (*E*)-1,3-Pentadiene

2.2.6 OH reactivity

Total OH reactivity normalized by the mixing ratio of CO was calculated using equation (2.8).

$$\text{OH reactivity} \left(\frac{1}{\text{s}\cdot\text{ppbv CO}} \right) = \sum_{i=0}^n k_{OH,i} \left(\frac{\text{cm}^3}{\text{molec}\cdot\text{s}} \right) \times \text{ER}_i \left(\frac{\text{pptv VOC}_i}{\text{ppbv CO}} \right) \times 2.46 \times 10^7 \left(\frac{\text{molec}}{\text{cm}^3\cdot\text{pptv}} \right) \quad (2.8)$$

Second-order rate constants (k_{OH}) at 25°C were taken from the NIST chemical kinetics database (Manion et al., 2015). Table 2.1 reproduces the k_{OH} constants used in the study. ER_i is the emission ratio for compound i in pptv of VOC per ppbv of CO. The last term serves as a conversion factor from VOC mixing ratio to concentration at standard ambient temperature and pressure (25°C, 1 atm). By using the emission ratio to CO, we can track OH reactivity from VOCs depending on the extent of dilution from the plume. From here forward, the OH reactivity (s^{-1}) reported is the average at the location of the sampling probes, or roughly 60 cm above the cookstove.

2.2.7 Ozone-forming potential (OFP)

The ozone-forming potential was estimated from the incremental reactivity of VOCs tabulated in Carter, 2010. Incremental reactivities were calculated by comparing ozone formation before and after a VOC was introduced in a box model simulation. The Maximum Incremental Reactivity (MIR) scenario sets high NO_x concentrations, optimized to yield the largest incremental ozone production. In other words, ozone production was VOC limited. Because of this, the OFPs given here represent a scenario where VOC emissions from cooking have the largest impact on ozone production. This high- NO_x scenario was chosen for high sensitivity in ozone production from cooking emission VOCs. In addition, it is expected to be more realistic

for a smoke plume in which NO_x is co-emitted with VOCs. OFPs were calculated using equation (2.9).

$$\text{OFP} \left(\frac{\text{g O}_3}{\text{kg fuel C}} \right) = \sum_{i=0}^n \text{MIR} \left(\frac{\text{g O}_3}{\text{g VOC}_i} \right) \times \text{EF}_i \left(\frac{\text{g VOC}_i}{\text{kg fuel C}} \right) \quad (2.9)$$

OFPs used in this study are listed next to the corresponding compound in Table 2.1.

2.2.8 Statistical analysis

One-way analysis of variance (ANOVA) with Tukey Post-Hoc testing was utilized to determine if there were significant differences ($p < 0.05$) in emissions of specific VOCs among categorical variables, i.e., stove and fuel types. All analyses were performed in R version 3.4.0 and RStudio version 1.0.143 (RStudio Inc, 2016).

2.3 Results and discussion

2.3.1 Chemical composition

Average VOC and PM_{2.5} EFs (g/ kg dry fuel) as well as MCE are given in Table 2.2. The compounds are grouped by fuel-stove combination, with major species (CO₂, CO, CH₄, and PM_{2.5}) listed first, followed by sulfur-containing compounds, halogen-containing compounds, organonitrates, alkanes, alkenes, alkynes, aromatics, terpenes, and oxygenated compounds. The sample size (n) used for calculating the average values and standard deviations was n=18 for *dung-chulha*, n=14 for *brushwood-chulha*, n=13 for *mixed-chulha*, and n=10 for *dung-angithi*. For the majority of the compounds, the standard deviations are smaller than or comparable to the average values, indicating fair reproducibility. There are many factors that may lead to variability in biomass burning emissions including pyrolysis temperature (Chen and Bond,

2010), fuel moisture content (Tihay-Felicelli et al., 2017), and the wind speed/direction (Surawski et al., 2015), among others. Relationships between emissions and fuel moisture content (Figure 2.2) or meal cooked were not found to be significant for any compounds (all $p < 0.05$). This paper therefore focuses on the relationships between emissions and fuel-stove combination.

Table 2.2: Averaged emission factors and standard deviation of PM_{2.5} and gas-phase species (g kg⁻¹ dry fuel) for dung-*chulha*, brushwood-*chulha*, mixed-*chulha*, and dung-*angithi* cook fires. Previously published emission factors (g kg⁻¹ dry fuel) from dung and hardwood cook fires are shown for comparison (Stockwell et al. 2016). Sample sizes for the current study (n) were n=18 for dung-*chulha*, n=14 for brushwood-*chulha*, n=13 for mixed-*chulha*, and n=10 for dung-*angithi*.

Compound (formula)	Dung- <i>chulha</i> Average (SD)	Brushwood- <i>chulha</i> Average (SD)	Mixed- <i>chulha</i> Average (SD)	Dung- <i>angithi</i> Average (SD)	Stockwell et al. (2016) Dung Average (SD)	Stockwell et al. (2016) Hardwood Average (SD)
Modified Combustion Efficiency	0.865 (0.014)	0.937 (0.035)	0.892 (0.021)	0.819 (0.031)	0.898	0.923
PM _{2.5}	19.2 (7.1)	7.42 (5.67)	11.0 (2.0)	33.2 (7.6)	14.73 (0.33)*	7.97 (3.80)*
Carbon dioxide (CO ₂)	984 (23)	1242 (61)	969 (31)	888 (48)	1129 (80)	1462 (16)
Carbon monoxide (CO)	97.7 (9.5)	53.0 (30.1)	74.8 (16.0)	125 (20)	80.9 (13.8)	77.2 (13.5)
Methane (CH ₄)	6.92 (1.23)	4.80 (2.09)	4.84 (0.89)	15.1 (2.6)	6.65 (0.46)	5.16 (1.39)
Sulfur-containing						
Carbonyl sulfide (OCS)	0.124 (0.040)	1.44 (0.54) x 10 ⁻²	8.50 (2.42) x 10 ⁻²	0.352 (0.217)	0.148 (0.123)	1.87 (1.15) x 10 ⁻²
DMS (C ₂ H ₆ S)	9.69 (4.54) x 10 ⁻³	1.39 (1.34) x 10 ⁻³	4.81 (2.26) x 10 ⁻³	4.34 (3.11) x 10 ⁻²	2.37 (0.08) x 10 ⁻²	0.255 (0.359)
Halogen-containing						
Dichloromethane (CH ₂ Cl ₂)	4.46 (3.94) x 10 ⁻⁴	2.18 (3.13) x 10 ⁻⁴	4.04 (6.44) x 10 ⁻⁴	4.56 (2.73) x 10 ⁻⁴	nm	nm
Chloromethane (CH ₃ Cl)	1.78 (0.70)	0.280 (0.157)	1.02 (0.42)	4.58 (1.89)	1.60 (1.53)	2.36 (1.62) x 10 ⁻²
Bromomethane (CH ₃ Br)	6.57 (2.78) x 10 ⁻³	7.92 (2.13) x 10 ⁻⁴	4.35 (1.81) x 10 ⁻³	1.43 (0.57) x 10 ⁻²	5.34 (3.02) x 10 ⁻³	5.61 (3.01) x 10 ⁻⁴
Iodomethane (CH ₃ I)	6.10 (4.78) x 10 ⁻⁴	9.62 (2.31) x 10 ⁻⁵	2.41 (0.66) x 10 ⁻⁴	8.83 (1.62) x 10 ⁻⁴	4.39 (1.78) x 10 ⁻⁴	1.23 (1.11) x 10 ⁻⁴
Ethyl chloride (C ₂ H ₅ Cl)	2.54 (1.17) x 10 ⁻³	4.22 (3.72) x 10 ⁻⁴	1.59 (0.67) x 10 ⁻³	9.11 (3.50) x 10 ⁻³	nm	nm
Dichloroethane (C ₂ H ₄ Cl ₂)	8.80 (2.98) x 10 ⁻⁴	2.55 (2.17) x 10 ⁻⁴	1.21 (2.32) x 10 ⁻³	1.47 (0.91) x 10 ⁻³	4.97 x 10 ⁻³ (-)	1.24 (0.30) x 10 ⁻⁴
Nitrates						
Methyl nitrate (CH ₃ ONO ₂)	1.83 (5.18) x 10 ⁻³	5.34 (14.4) x 10 ⁻³	6.60 (11.7) x 10 ⁻³	0.170 (0.339)	1.46 (1.94) x 10 ⁻²	6.96 (5.73) x 10 ⁻³

Compound (formula)	Dung- <i>chulha</i> Average (SD)	Brushwood- <i>chulha</i> Average (SD)	Mixed- <i>chulha</i> Average (SD)	Dung- <i>angithi</i> Average (SD)	Stockwell et al. (2016) Dung Average (SD)	Stockwell et al. (2016) Hardwood Average (SD)
Nitrates (continued)						
Ethyl nitrate (CH ₃ ONO ₂)	2.37 (3.86) x 10 ⁻⁴	5.54 (10.2) x 10 ⁻⁴	2.27 (6.40) x 10 ⁻³	4.53 (11.6) x 10 ⁻²	nm	nm
i-Propylnitrate (C ₃ H ₇ ONO ₂)	1.90 (1.61) x 10 ⁻⁴	2.40 (4.92) x 10 ⁻⁴	4.10 (8.38) x 10 ⁻⁴	5.90 (12.1) x 10 ⁻³	nm	nm
n-Propylnitrate (C ₃ H ₇ ONO ₂)	6.32 (5.23) x 10 ⁻⁵	9.01 (14.1) x 10 ⁻⁵	1.44 (3.25) x 10 ⁻⁴	1.82 (4.35) x 10 ⁻³	nm	nm
2-Butylnitrate (C ₄ H ₉ ONO ₂)	2.69 (2.14) x 10 ⁻⁴	1.05 (1.13) x 10 ⁻⁴	7.10 (20.3) x 10 ⁻⁴	2.45 (4.09) x 10 ⁻³	nm	nm
3-Pentylnitrate (C ₅ H ₁₁ ONO ₂)	4.75 (1.61) x 10 ⁻⁵	2.29 (2.08) x 10 ⁻⁵	3.13 (1.97) x 10 ⁻⁵	1.94 (4.06) x 10 ⁻⁴	nm	nm
2-Pentylnitrate (C ₅ H ₁₁ ONO ₂)	2.37 (2.10) x 10 ⁻⁵	1.63 (2.46) x 10 ⁻⁵	1.25 (1.26) x 10 ⁻⁵	1.82 (4.54) x 10 ⁻⁴	nm	nm
Alkanes						
Ethane (C ₂ H ₆)	0.717 (0.193)	0.380 (0.247)	0.422 (0.096)	2.06 (0.69)	1.08 (0.30)	0.160 (0.122)
Propane (C ₃ H ₈)	0.211 (0.073)	9.48 (8.41) x 10 ⁻²	0.116 (0.032)	0.819 (0.157)	0.457 (0.137)	0.202 (0.140)
i-Butane (C ₄ H ₁₀)	1.73 (0.71) x 10 ⁻²	4.60 (4.86) x 10 ⁻³	9.51 (2.75) x 10 ⁻³	7.27 (1.54) x 10 ⁻²	0.215 (0.126)	0.406 (0.478)
n-Butane (C ₄ H ₁₀)	4.71 (1.88) x 10 ⁻²	1.57 (1.67) x 10 ⁻²	2.68 (0.88) x 10 ⁻²	0.215 (0.047)	0.29 (0.09)	1.11 (1.48)
n-Pentane (C ₅ H ₁₂)	2.01 (0.98) x 10 ⁻²	4.44 (4.08) x 10 ⁻³	9.12 (3.71) x 10 ⁻³	6.80 (2.95) x 10 ⁻²	0.190 (0.254)	2.18 (1.73) x 10 ⁻²
n-Hexane (C ₆ H ₁₄)	1.03 (0.47) x 10 ⁻²	1.96 (1.58) x 10 ⁻³	5.31 (1.87) x 10 ⁻³	4.93 (1.10) x 10 ⁻²	0.291 (0.248)	1.85 x 10 ⁻² (-)
n-Heptane (C ₇ H ₁₆)	7.21 (3.43) x 10 ⁻³	9.23 (6.94) x 10 ⁻⁴	3.92 (1.23) x 10 ⁻³	3.17 (0.85) x 10 ⁻²	0.114 (0.069)	1.01 (1.35) x 10 ⁻²
2-Methylpentane (C ₆ H ₁₄)	6.21 (2.81) x 10 ⁻³	1.23 (0.99) x 10 ⁻³	2.57 (1.61) x 10 ⁻³	2.29 (1.67) x 10 ⁻²	0.231 (0.192)	9.93 (12.9) x 10 ⁻³
3-Methylpentane (C ₆ H ₁₄)	3.71 (1.70) x 10 ⁻³	1.21 (1.01) x 10 ⁻³	1.57 (0.76) x 10 ⁻³	7.54 (4.30) x 10 ⁻³	0.155 (0.137)	6.79 (6.63) x 10 ⁻³
Alkenes						
Ethene (C ₂ H ₄)	1.86 (0.48)	0.626 (0.284)	1.13 (0.38)	1.77 (0.35)	4.23 (1.39)	2.70 (1.17)
Propene (C ₃ H ₆)	0.807 (0.235)	0.286 (0.202)	0.417 (0.091)	1.61 (0.33)	1.47 (0.58)	0.576 (0.195)
1-Butene (C ₄ H ₈)	0.158 (0.047)	6.32 (4.59) x 10 ⁻²	8.38 (1.83) x 10 ⁻²	0.366 (0.096)	0.399 (0.331)	0.726 (0.904)
i-Butene (C ₄ H ₈)	0.133 (0.057)	3.46 (2.50) x 10 ⁻²	6.40 (1.86) x 10 ⁻²	0.353 (0.158)	0.281 (0.091)	0.846 (1.113)

Compound (formula)	Dung- <i>chulha</i> Average (SD)	Brushwood- <i>chulha</i> Average (SD)	Mixed- <i>chulha</i> Average (SD)	Dung- <i>angithi</i> Average (SD)	Stockwell et al. (2016) Dung Average (SD)	Stockwell et al. (2016) Hardwood Average (SD)
Alkenes (continued)						
trans-2-Butene (C ₄ H ₈)	4.45 (1.60) x 10 ⁻²	2.00 (1.27) x 10 ⁻²	2.38 (0.70) x 10 ⁻²	0.151 (0.055)	0.151 (0.010)	6.78 (5.98) x 10 ⁻²
cis-2-Butene (C ₄ H ₈)	3.38 (1.19) x 10 ⁻²	1.51 (0.95) x 10 ⁻²	1.80 (0.52) x 10 ⁻²	0.107 (0.047)	0.102 (0.016)	5.51 (4.76) x 10 ⁻²
3-Methyl-1-butene (C ₅ H ₁₀)	1.46 (0.48) x 10 ⁻²	5.74 (4.49) x 10 ⁻³	7.30 (1.94) x 10 ⁻³	3.82 (0.88) x 10 ⁻²	5.58 (3.50) x 10 ⁻²	7.43 (5.79) x 10 ⁻³
2-Methyl-1-butene (C ₅ H ₁₀)	2.71 (1.28) x 10 ⁻²	9.96 (10.9) x 10 ⁻³	1.19 (0.42) x 10 ⁻²	7.70 (3.99) x 10 ⁻²	nm	nm
2-Methyl-2-butene (C ₅ H ₁₀)	2.51 (1.26) x 10 ⁻²	6.40 (4.78) x 10 ⁻³	1.10 (0.47) x 10 ⁻²	9.17 (4.70) x 10 ⁻²	nm	nm
1-Pentene (C ₅ H ₁₀)	4.17 (1.59) x 10 ⁻²	9.65 (6.55) x 10 ⁻³	2.13 (0.60) x 10 ⁻²	0.122 (0.033)	0.168 (0.086)	1.43 (0.94) x 10 ⁻²
trans-2-Pentene (C ₅ H ₁₀)	1.74 (0.65) x 10 ⁻²	8.89 (5.77) x 10 ⁻³	8.69 (2.22) x 10 ⁻³	5.14 (2.70) x 10 ⁻²	0.115 (0.035)	1.05 (0.83) x 10 ⁻²
cis-2-Pentene (C ₅ H ₁₀)	1.00 (0.36) x 10 ⁻²	5.55 (3.62) x 10 ⁻³	4.98 (1.26) x 10 ⁻³	2.50 (1.28) x 10 ⁻²	5.14 (0.76) x 10 ⁻²	8.69 x 10 ⁻³ (-)
1-Hexene (C ₆ H ₁₂)	6.10 (2.46) x 10 ⁻²	1.26 (0.73) x 10 ⁻²	3.09 (0.91) x 10 ⁻²	0.167 (0.050)	nm	nm
1,2-Propadiene (C ₃ H ₄)	3.76 (1.69) x 10 ⁻²	1.31 (0.62) x 10 ⁻²	2.32 (0.86) x 10 ⁻²	1.80 (0.923) x 10 ⁻²	7.15 (6.76) x 10 ⁻²	2.33 (1.07) x 10 ⁻²
1,2-Butadiene (C ₄ H ₆)	5.54 (1.68) x 10 ⁻³	2.82 (1.81) x 10 ⁻³	3.10 (1.06) x 10 ⁻³	4.33 (1.59) x 10 ⁻³	nm	nm
1,3-Butadiene (C ₄ H ₆)	0.203 (0.071)	7.44 (3.99) x 10 ⁻²	0.108 (0.061)	0.263 (0.082)	0.409 (0.306)	0.204 (0.144)
Isoprene (C ₅ H ₈)	8.94 (5.80) x 10 ⁻²	1.98 (1.48) x 10 ⁻²	3.03 (2.39) x 10 ⁻²	0.188 (0.143)	0.325 (0.443)	4.16 (2.23) x 10 ⁻²
1,3-Pentadiene (C ₅ H ₈)	1.96 (1.05) x 10 ⁻²	9.17 (4.79) x 10 ⁻³	9.39 (6.43) x 10 ⁻³	5.66 (2.94) x 10 ⁻²	nm	nm
Alkynes						
Ethyne	1.13 (0.42)	0.467 (0.160)	0.890 (0.323)	0.325 (0.238)	0.593 (0.443)	0.764 (0.363)
1-Propyne	9.42 (3.46) x 10 ⁻²	3.82 (1.76) x 10 ⁻²	5.99 (2.22) x 10 ⁻²	5.20 (2.83) x 10 ⁻²	nm	nm
1-Buten-3-yne (C ₄ H ₄)	5.04 (1.72) x 10 ⁻²	1.86 (0.90) x 10 ⁻²	3.46 (1.53) x 10 ⁻²	1.74 (1.26) x 10 ⁻²	nm	nm
1-Butyne (C ₄ H ₆)	7.72 (2.29) x 10 ⁻³	4.07 (2.24) x 10 ⁻³	4.48 (1.41) x 10 ⁻³	5.97 (1.93) x 10 ⁻³	2.29 (1.38) x 10 ⁻²	1.28 (0.47) x 10 ⁻²
2-Butyne (C ₄ H ₆)	4.31 (1.15) x 10 ⁻³	2.55 (1.44) x 10 ⁻³	2.47 (0.70) x 10 ⁻³	4.52 (1.40) x 10 ⁻³	1.86 (0.91) x 10 ⁻²	1.02 (0.66) x 10 ⁻²

Compound (formula)	Dung- <i>chulha</i> Average (SD)	Brushwood- <i>chulha</i> Average (SD)	Mixed- <i>chulha</i> Average (SD)	Dung- <i>angithi</i> Average (SD)	Stockwell et al. (2016) Dung Average (SD)	Stockwell et al. (2016) Hardwood Average (SD)
Alkynes (continued)						
1,3-Butadiyne (C ₄ H ₂)	6.07 (2.66) x 10 ⁻³	2.71 (1.21) x 10 ⁻³	5.43 (2.01) x 10 ⁻³	1.53 (1.31) x 10 ⁻³	nm	nm
Aromatics						
Benzene (C ₆ H ₆)	1.03 (0.33)	0.373 (0.149)	0.723 (0.218)	0.769 (0.175)	1.96 (0.45)	1.05 (0.19)
Toluene (C ₇ H ₈)	0.483 (0.273)	0.221 (0.085)	0.297 (0.077)	0.860 (0.167)	1.26 (0.05)	0.241 (0.160)
Ethylbenzene (C ₈ H ₁₀)	3.41 (0.791) x 10 ⁻²	1.25 (1.20) x 10 ⁻²	1.97 (0.40) x 10 ⁻²	9.78 (1.66) x 10 ⁻²	0.366 (0.085)	4.19 (4.25) x 10 ⁻²
m/p-Xylene (C ₈ H ₁₀)	6.36 (1.26) x 10 ⁻²	2.78 (1.56) x 10 ⁻²	4.03 (0.98) x 10 ⁻²	0.148 (0.030)	0.601 (0.294)	9.57 (7.99) x 10 ⁻²
o-Xylene (C ₈ H ₁₀)	2.38 (0.76) x 10 ⁻²	8.37 (5.78) x 10 ⁻³	1.44 (0.41) x 10 ⁻²	7.96 (1.91) x 10 ⁻²	0.228 (0.083)	3.93 (4.31) x 10 ⁻²
Styrene (C ₈ H ₈)	5.88 (1.58) x 10 ⁻²	2.28 (1.50) x 10 ⁻²	3.40 (1.90) x 10 ⁻²	8.63 (5.96) x 10 ⁻²	0.255 (0.091)	8.71 (6.69) x 10 ⁻²
i-Propylbenzene (C ₉ H ₁₂)	2.91 (0.77) x 10 ⁻³	1.20 (1.11) x 10 ⁻³	1.69 (0.45) x 10 ⁻³	9.30 (4.90) x 10 ⁻³	1.87 (1.40) x 10 ⁻²	1.70 (1.67) x 10 ⁻²
n-Propylbenzene (C ₉ H ₁₂)	6.48 (2.59) x 10 ⁻³	1.84 (1.65) x 10 ⁻³	4.02 (1.59) x 10 ⁻³	3.95 (2.69) x 10 ⁻²	3.10 (1.45) x 10 ⁻²	1.78 (1.58) x 10 ⁻²
3-Ethyltoluene (C ₉ H ₁₂)	1.44 (0.48) x 10 ⁻²	5.46 (4.40) x 10 ⁻³	8.59 (3.26) x 10 ⁻³	7.14 (4.13) x 10 ⁻²	5.61 (2.38) x 10 ⁻²	2.62 (0.54) x 10 ⁻²
4-Ethyltoluene (C ₉ H ₁₂)	6.35 (2.36) x 10 ⁻³	2.54 (1.81) x 10 ⁻³	4.18 (1.96) x 10 ⁻³	3.71 (2.30) x 10 ⁻²	3.57 (1.74) x 10 ⁻²	2.07 (1.19) x 10 ⁻²
2-Ethyltoluene (C ₉ H ₁₂)	6.89 (2.50) x 10 ⁻³	2.70 (1.68) x 10 ⁻³	4.63 (2.07) x 10 ⁻³	3.76 (2.69) x 10 ⁻²	3.39 (1.34) x 10 ⁻²	2.10 (1.16) x 10 ⁻²
1,3,5- Trimethylbenzene (C ₉ H ₁₂)	3.87 (1.71) x 10 ⁻³	1.63 (1.22) x 10 ⁻³	2.65 (1.43) x 10 ⁻³	2.23 (1.60) x 10 ⁻²	1.79 (0.83) x 10 ⁻²	2.14 x 10 ⁻² (-)
1,2,4- Trimethylbenzene (C ₉ H ₁₂)	1.04 (0.46) x 10 ⁻²	4.25 (2.69) x 10 ⁻³	7.52 (4.28) x 10 ⁻³	6.23 (5.18) x 10 ⁻²	3.91 (1.65) x 10 ⁻²	1.74 (2.35) x 10 ⁻²
1,2,3- Trimethylbenzene (C ₉ H ₁₂)	4.76 (2.59) x 10 ⁻³	1.16 (0.81) x 10 ⁻³	3.84 (2.69) x 10 ⁻³	3.01 (3.16) x 10 ⁻²	2.34 (0.43) x 10 ⁻²	2.16 x 10 ⁻² (-)
Terpenes						
alpha-Pinene (C ₁₀ H ₁₆)	8.30 (5.40) x 10 ⁻⁴	5.38 (6.94) x 10 ⁻⁴	7.82 (6.32) x 10 ⁻⁴	2.26 (2.53) x 10 ⁻³	0.35 (0.49)	2.02 (2.33) x 10 ⁻²

Compound (formula)	Dung- <i>chulha</i> Average (SD)	Brushwood- <i>chulha</i> Average (SD)	Mixed- <i>chulha</i> Average (SD)	Dung- <i>angithi</i> Average (SD)	Stockwell et al. (2016) Dung Average (SD)	Stockwell et al. (2016) Hardwood Average (SD)
Terpenes (continued)						
beta-Pinene (C ₁₀ H ₁₆)	2.27 (1.49) x 10 ⁻³	1.37 (0.91) x 10 ⁻³	2.76 (3.15) x 10 ⁻³	2.89 (3.56) x 10 ⁻³	0.471 (-)	4.67 x 10 ⁻² (-)
Oxygenates						
Acetaldehyde (C ₂ H ₄ O)	0.805 (0.279)	0.334 (0.199)	0.447 (0.119)	1.70 (0.75)	1.88 (1.63)	0.541 (0.362)
Butanal (C ₄ H ₈ O)	4.28 (1.50) x 10 ⁻²	1.90 (1.29) x 10 ⁻²	2.68 (1.05) x 10 ⁻²	0.108 (0.047)	5.40 (2.19) x 10 ⁻²	8.28 (6.27) x 10 ⁻³
Acetone (C ₃ H ₆ O)	0.705 (0.219)	0.365 (0.226)	0.416 (0.108)	2.05 (0.52)	1.63 (0.38)	0.524 (0.256)
2-Butanone (C ₄ H ₈ O)	0.172 (0.057)	8.00 (6.18) x 10 ⁻²	0.103 (0.038)	0.498 (0.151)	0.262 (0.109)	0.232 (0.286)
2-Propenal (C ₃ H ₄ O)	0.186 (0.060)	0.127 (0.069)	0.127 (0.059)	0.295 (0.245)	nm	nm
MVK (C ₄ H ₆ O)	0.129 (0.040)	6.59 (4.56) x 10 ⁻²	6.31 (2.76) x 10 ⁻²	0.280 (0.147)	nm	nm
Furan (C ₄ H ₄ O)	0.109 (0.041)	5.98 (3.37) x 10 ⁻²	6.81 (2.19) x 10 ⁻²	0.379 (0.093)	0.534 (0.209)	0.241 (0.024)
2-Methylfuran (C ₅ H ₆ O)	0.117 (0.051)	5.92 (4.77) x 10 ⁻²	6.92 (2.83) x 10 ⁻²	0.488 (0.227)	nm	nm
Furfural (C ₅ H ₄ O ₂)	8.55 (6.05) x 10 ⁻²	4.28 (5.51) x 10 ⁻²	8.22 (5.09) x 10 ⁻²	0.316 (0.133)	nm	nm
Methanol (CH ₃ OH)	2.09 (1.14)	2.03 (2.01)	1.18 (0.40)	4.23 (3.40)	2.38 (0.90)	1.92 (0.61)
Ethanol (CH ₃ OH)	4.08 (5.93) x 10 ⁻²	2.18 (2.00) x 10 ⁻²	5.63 (6.69) x 10 ⁻²	7.62 (9.08) x 10 ⁻²	0.563 (0.589)	0.128 (0.017)

*From Jayarathne et al. (2017), but part of same NAMaSTE study

nm indicates the species was not measured

(-) from Stockwell et al. (2016) indicates that the measurement was not above background

Figure 2.2: Emission factors (g VOC/ kg fuel C) versus moisture content of the fuel. Red markers indicate dung fuel was used, while blue markers indicate brushwood fuel. Filled square markers indicate *chulha* stoves, while open circles indicate *angithi* stoves were used. If a significant correlation was observed ($r^2 > 0.70$) for a particular fuel-stove combination, the linear regression trendline is shown.

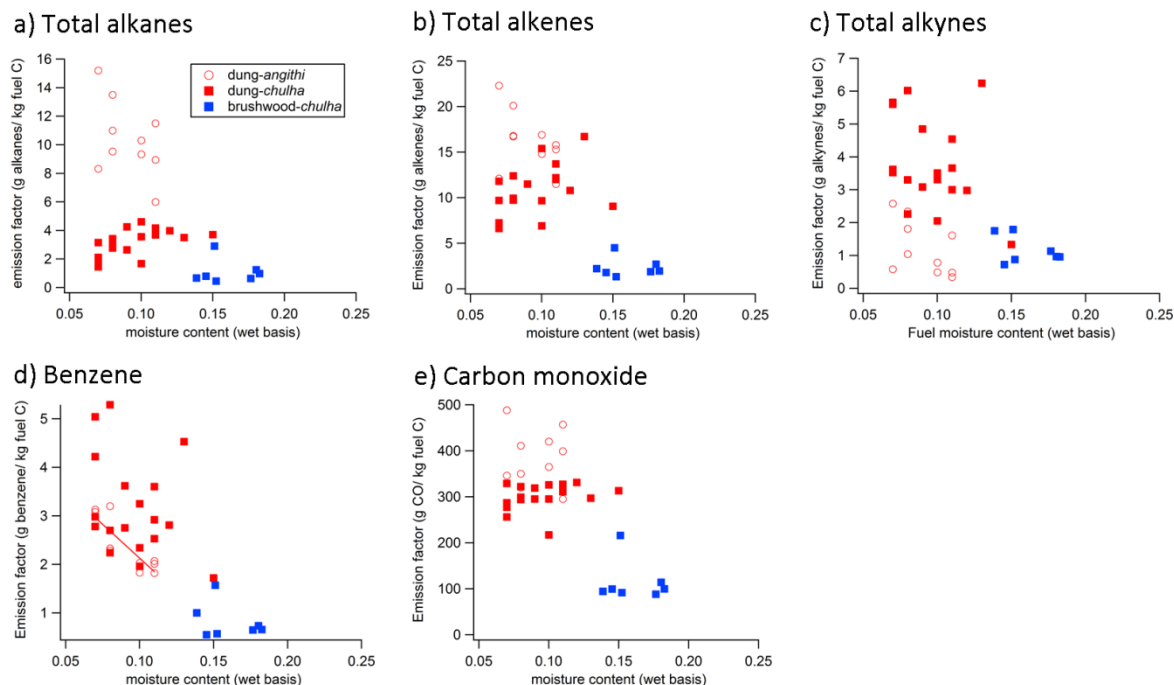
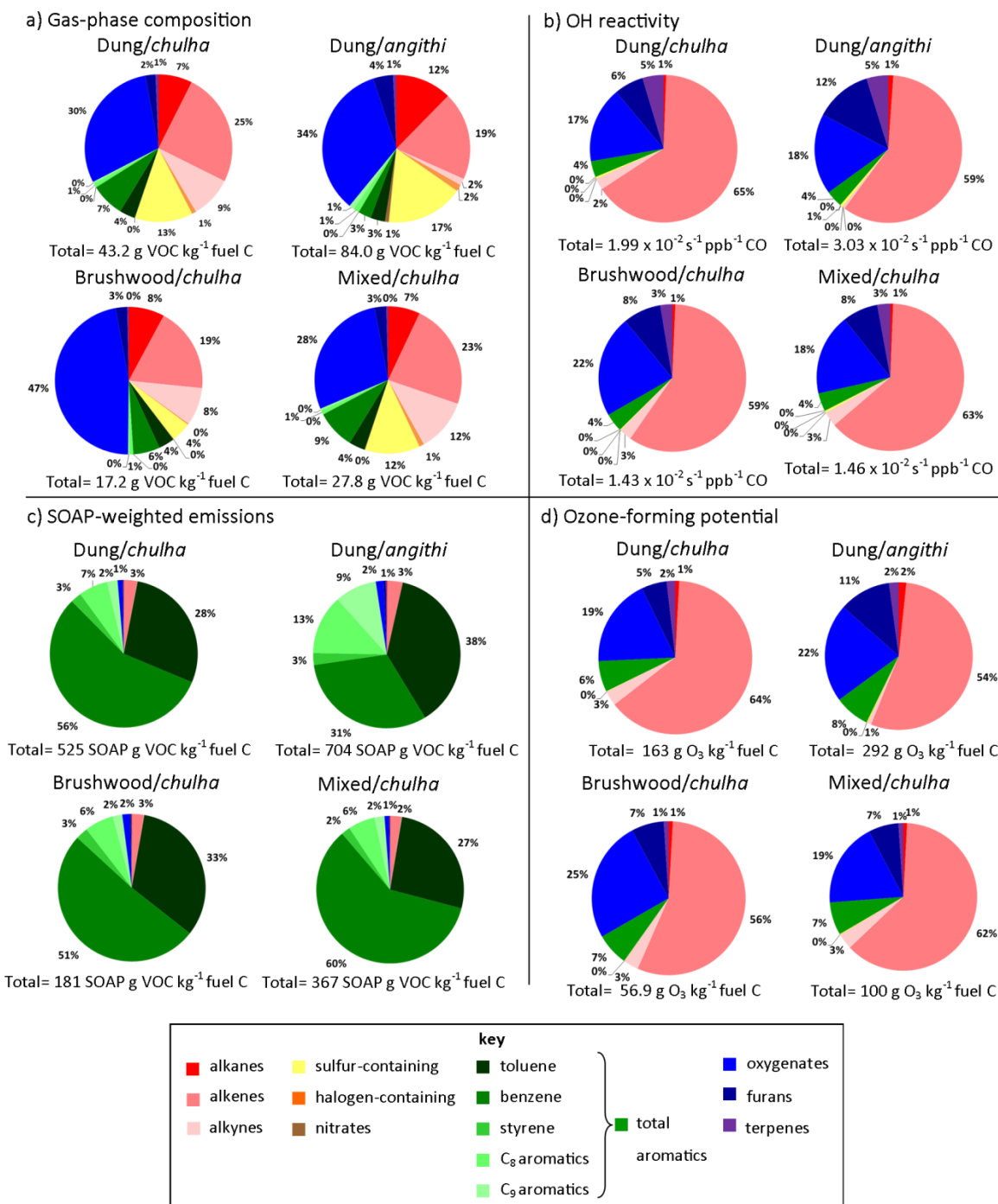


Figure 2.3a visually shows the mass fraction attributed to each compound class for the measured gas-phase emissions. The total EFs given below the pie charts are normalized by fuel carbon in Figure 2.3a in order to compare between cook fires generated with dung, wood, and wood-dung mixtures which have different carbon contents. The total measured VOC emissions from dung-*angithi* were roughly twice that of dung-*chulha* in terms of gram per kilogram fuel carbon. Further, dung-*chulha* emitted more than twice that of brushwood-*chulha*. The most prominent difference is non-furan oxygenates, making up almost half of all brushwood-*chulha* emissions and a smaller fraction for other fuel-stove combinations. While oxygenates make up a higher fraction of brushwood-*chulha* emissions, the absolute EFs for oxygenates from dung-burning and *angithi* cook fires are higher as discussed later in more detail.

Figure 2.3: Pie charts showing the contribution of each species class to gas-phase composition (a), OH reactivity (b), SOAP-weighted emissions (c), and ozone-forming potential (d). For (b) and (d), total aromatics are shown rather than the breakdown of aromatics shown in (a) and (c). Sums of all components are shown below the pie chart.



^a1-Buten-3-yne is grouped in with alkynes

Table 2.3 shows EFs (g/ kg fuel C) for select VOCs. The differences in mean EFs for each fuel-stove combination are also included in Table 2.3. Mean differences in EFs reported for *chulha* and *angithi* stoves were calculated for cook fires utilizing only dung fuels. Likewise, mean EFs for wood and dung cook fires only represent cooking events using the *chulha*. This was done to isolate a single variable—either fuel or stove type. For all alkanes and most alkenes, we measured higher emissions for dung-*angithi* cook fires (Table 2.3). Also, from the mean differences in EFs, we found that stove specific combustion conditions impacts emissions more than the selection of fuel type. The difference is so dramatic for alkanes and most alkenes that the mean difference in EFs for cookstoves burning dung is always larger than the mean EF of that compound. For comparison, the mean difference in EFs for *chulha* cookstoves is always lower than the overall mean EF. Ethene was an exception; there was no relationship between ethene emissions and stove type. On the other hand, the mean EF of ethene by dung cook fires was very large compared to mean EFs from brushwood cook fires with a mean difference in EFs of 4.05 g/ kg fuel C. Some alkenes with two double bonds were also exceptions. For 1,3-butadiene ($p= 0.06$) and 1,2-butadiene ($p= 0.089$), stove and EF may or may not have a significant relationship. 1,2-Propadiene emissions from *chulha* cookstoves are higher ($p< 0.01$). All three compounds still show a significant relationship to fuel type with EFs being higher for dung cook fires.

Similar to alkanes and alkenes, aromatics, oxygenates, halogen-, and sulfur-containing compounds all had higher emissions per kilogram of fuel carbon when dung fuels and *angithi* stoves were utilized compared to brushwood fuels and *chulha* stoves, respectively. We focus on the behavior of the most interesting groups of compounds in the discussion below.

Table 2.3: Emission factors (g VOC/ kg fuel C) for select compounds. The mean differences between dung/*angithi* and dung/*chulha* are shown and similarly for dung/*chulha* and brushwood/*chulha*. The significance between fuel or stove and EF is indicated with asterisks. Accompanying the mean differences is the average emission factor (g VOC/ kg fuel C) for dung cook fires and *chulha* cook fires, as well as the overall average for all performed cook fires.

Compound	Average EF for all cook fires (g/ kg fuel C)	<i>Angithi-chulha</i> average EF difference (g/ kg fuel C)	Average EF for dung fires (g/ kg fuel C)	Dung-brushwood average EF difference (g/ kg fuel C)	Average EF for <i>chulha</i> cook fires (g/ kg fuel C)
Ethane	2.47 (2.16)	4.18 ^{***}	3.70 (2.43)	1.19 ^{***}	1.60 (0.744)
Propane	0.827 (0.866)	1.88 ^{***}	1.32 (0.976)	0.397 ^{***}	0.448 (0.256)
n-Butane	0.200 (0.236)	0.52 ^{***}	0.331 (0.271)	0.0568 ^{***}	0.097 (0.063)
Ethene	4.17 (2.02)	N/A	5.64 (1.32)	4.05 ^{***}	3.88 (2.07)
Propene	2.24 (1.61)	2.50 ^{***}	3.38 (1.48)	1.72 ^{***}	1.63 (0.93)
1-Butene	0.473 (0.373)	0.644 ^{***}	0.718 (0.377)	0.213 ^{***}	0.327 (0.180)
Ethyne	2.32 (1.41)	-2.46 ^{***}	2.58 (1.63)	2.21 ^{***}	2.61 (1.37)
1-Propyne	0.196 (0.108)	-0.129 ^{**}	0.244 (0.116)	0.187 ^{***}	0.204 (0.112)
1-Butyne	1.74 x 10 ⁻² (7.74 x 10 ⁻³)	-0.101 ^{***}	0.219 (0.007)	0.105 ^{***}	0.017 (0.008)

* denotes p<0.05, ** p<0.01, *** p<0.001

The chlorine-containing organic compounds are generally expected to come from cook fires in large quantities. However, we observed an interesting practice in which the cook often used plastic bags to start the fire, which could be a source of chlorine-containing compounds if composed of polyvinyl chloride. Carbonyl sulfide (OCS) is largely responsible for the yellow sulfur-containing fraction in Figure 2.3a and biomass burning is a well-known source of OCS in the atmosphere (Crutzen et al., 1979). Similar to other VOCs, OCS was significantly emitted in higher quantities when *angithi* stoves and dung fuels were utilized.

Benzene had higher emissions from *chulha* stoves, which had higher MCEs when cooking with dung fuels compared to *angithi* stoves (dung-*chulha* 3.18 g/ kg fuel C and dung-

angithi 2.38 g/ kg fuel C). As the simplest aromatic compound, benzene also had the largest average difference in fuel type EFs compared to other aromatics (2.18 g/ kg fuel C, dung-wood). This information is relevant for exposure assessment, as benzene is a known human carcinogen. Higher benzene emissions from *chulha* cook fires could lead to higher benzene exposures which is a potential public health concern. However, it should be noted that the cook usually cannot control the stove used, as the *angithi* and *chulha* are used to prepare different types of meals, and exposure to benzene is not straightforward from its emission factors.

Higher emissions of alkynes were observed from dung fuels and *chulha* cookstoves. The latter observation is consistent with the literature showing flaming combustion generates more alkynes (Barrefors and Petersson, 1995; Lee et al., 2005). *Chulha* cook fires always had higher MCE than *angithi* cook fires (Table 2.2) which rely on smoldering combustion. Approximately the same difference in alkyne emissions results from comparing the *chulha* to the *angithi* using dung, in relation to using wood versus dung in combination with the *chulha*. There were two exceptions in stove type for 1-butane ($p= 0.055$) and 2-butane ($p \gg 0.05$). The former may or may not have a relationship with stove type, while the latter does not. Emissions of some compounds did not show a relationship with either fuel or stove type, and are listed in Table S2.

VOC emissions from Stockwell et al. (2016) are also provided in Table 2.2 for comparison of VOC EFs. Samples in Stockwell et al. (2016) were collected in April 2015 in and around Kathmandu and the Tarai plains, which border India. While both are EFs from cookstoves using similar fuels, there are differences in the studies that should be noted. Stockwell et al. (2016) collected measurements of simulated cooking in a laboratory and from cooking fires in households; it was not noted in the latter case what meals were cooked. EFs were calculated from similar WAS measurements, but as grab samples in an area of the kitchen

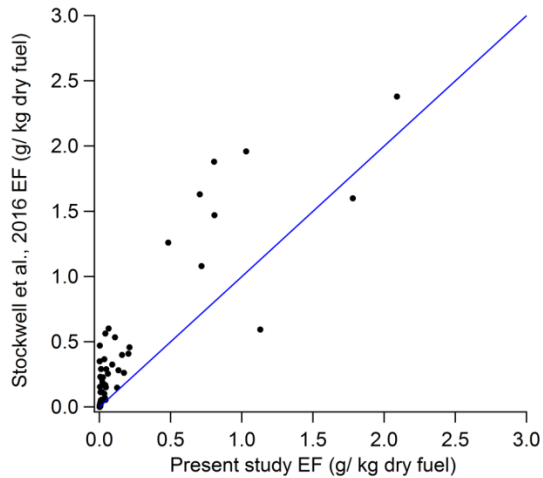
away from the fire (as opposed to the time-integrated approach used here). Emissions were assumed to be well-mixed in the kitchen prior to sampling. Stockwell et al. (2016) also used a range of stoves, including the traditional single-pot mud stove, open three-stone fire, *bhuse chulo*, rocket, chimney, and forced draft stoves. “Dung” cook fires sometimes used a combination of fuels, such as wood. Finally, our study also has a larger sample size than Stockwell et al. (2016) with $n=49$ versus $n\approx 10$.

The emission factors for most compounds determined in this study were lower compared to those reported in Table 4 of the Stockwell et al. (2016) paper. Figure 2.4 visually shows that the EFs were generally lower in the present study. In some cases, EFs in this study were an order of magnitude lower, most notably n-pentane and n-hexane. We also found that our emission factors were always higher for dung-*chulha* compared to brushwood-*chulha*, which was not always the case in Stockwell et al. (2016). The EFs in Stockwell et al. (2016) could be biased high due to calculations rather than real differences in emissions. For example, ignoring ash and char carbon and using the same carbon content inflates the EFs reported in our paper by 7% for dung and 24% for brushwood emissions. However, this is a small percentage compared to the observed differences between EFs between the two measurements. By examining the EFs reported in the supporting information section of the Stockwell et al. (2016), we found that the disagreement resulted from the way the final recommended EFs were obtained from the measurements. Because Stockwell et al. (2016) measured both laboratory and field cook fires, they elected to adjust the laboratory EFs to account for the lower MCEs observed in the field. It has been shown by Roden et al. (2009) and Johnson et al. (2008) that cooking activities can strongly influence emissions, for example due to the cook tending to the cook fire differently, thus affecting combustion conditions. However, such adjustments should be done with caution

because EF and MCE do not always follow a linear trend, as explained in the next section. Figure 2.5 plots the unadjusted laboratory and field emission factors as a function of MCE for all the measurements in Stockwell et al. (2016), as well as this study. Plotting the unadjusted EFs resolves most of the differences in observed EFs between the two studies. The data show an encouraging level agreement despite the differences in the experimental design between the two studies.

Figure 2.4: Comparison of EFs (g/ kg dry fuel) in the present study to those of Stockwell et al., 2016 (adjusted). The blue line indicates 1:1 agreement of the emission factors, with points above the blue line indicating higher EFs reported in Stockwell et al., 2016. Likewise, points below represent compounds that have a higher EF in the present study.

a) Dung



b) Brushwood

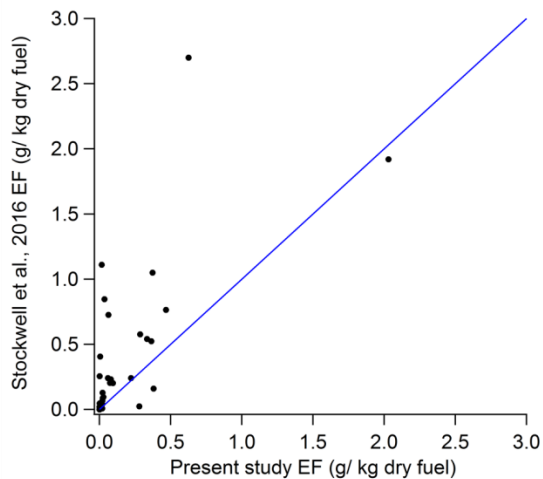
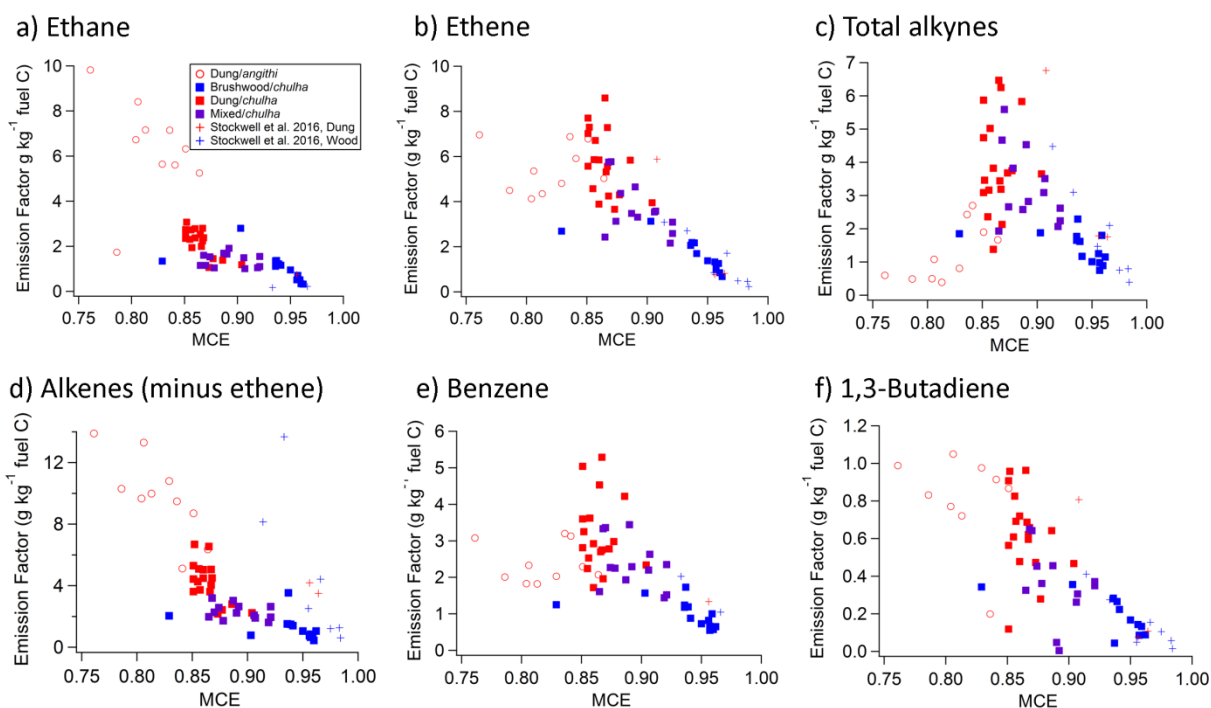


Figure 2.5: Emission factors ($\text{g}/\text{kg fuel C}$) plotted as a function of modified combustion efficiency for select species. Open circles indicate cooking events conducted with *angithi* stoves, whereas filled squares indicate *chulha* stoves. Color indicates fuel, either brushwood (blue), dung (red), or mixed (purple). Crosses indicate measurements from Stockwell et al. 2016.

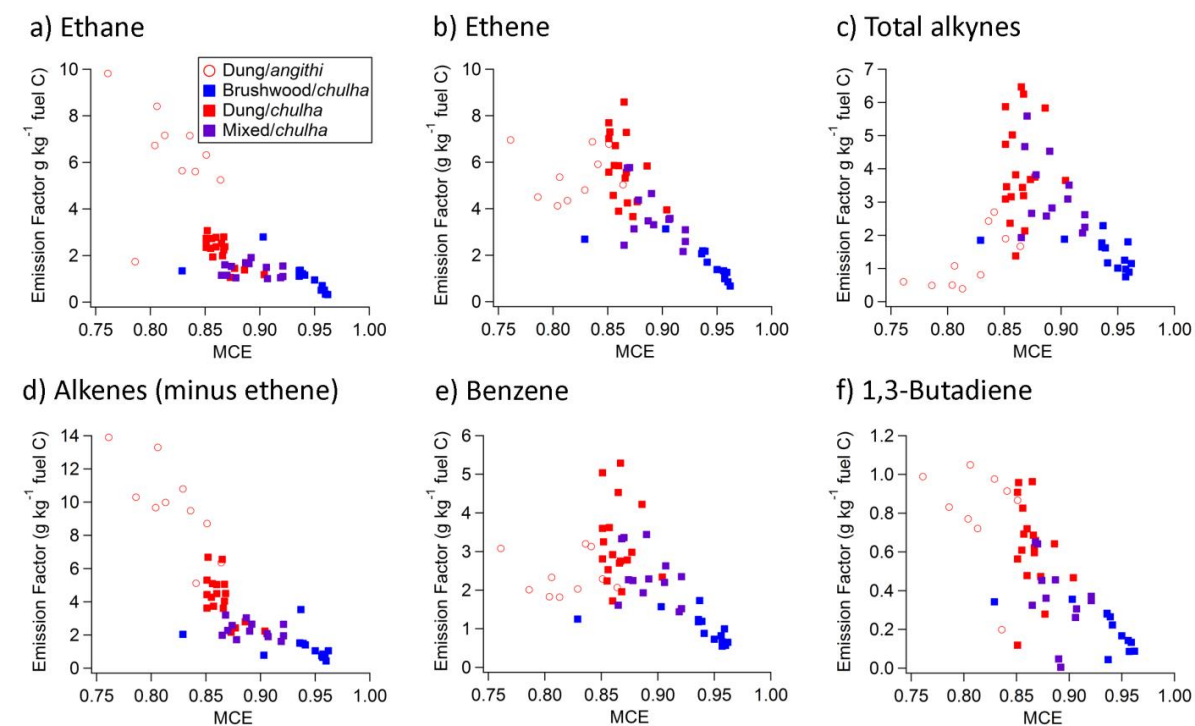


2.3.2 Modified combustion efficiency

The use of dung and *angithi*, rather than brushwood and *chulha*, respectively, results in lower modified combustion efficiencies as shown in Figure 2.6. In general, at lower MCEs we measured higher emissions of gas-phase compounds as discussed in Section 3.1. For example, emissions of ethane (Figure 2.6a) and other alkanes increase with decreasing MCE. However the dependence of ethane EF on MCE is not linear as observed in previous studies (Liu et al., 2017; Selimovic et al., 2018). For other VOCs, the dependence of the EF on MCE deviates from the linear trend even more, with the maximum EF observed at intermediate MCE values. For example, the ethene EF (Figure 2.6b) increases with decreasing MCE at MCEs > 0.85 , but it has the opposite trend at MCEs < 0.85 . Previously, we discussed that there is no relationship between ethene EF and stove type and we see this more clearly in Figure 2.6b. Alkynes have the

same relationship to MCE as ethene, but it is even more pronounced (Figure 2.6c). Benzene (Figure 2.6e) stands apart from other aromatics with a relationship with MCE similar to ethene, while other aromatics have an EF versus MCE curve similar to alkanes and most other VOCs. In Figure 2.6e, we see again that emissions from brushwood-*chulha* and dung-*angithi* cook fires result in lower emissions of benzene compared to dung-*chulha*. Alkenes with two double bonds generally have a negative correlation between emissions and MCE, such as 1,3-butadiene in Figure 2.6f. The 1,3-butadiene EF versus MCE plot is not necessarily representative of all analogous plots for alkenes with two double bonds, as they have different shapes. 1,3-butadiene was chosen as its emission is high compared to other compounds in its subcategory and it also has health implications. It also happens to have a more linear relationship with MCE, albeit noisy.

Figure 2.6: Emission factors as a function of modified combustion efficiency (MCE) for select species. Open circles indicate cooking events conducted with *angithi* stoves, whereas filled squares indicate *chulha* stoves. Color indicates fuel, either brushwood (blue), dung (red), or mixed (purple).



^a1-Buten-3-yne is grouped in with alkynes

It is of interest to compare EFs obtained from different fuel-stove combinations but with the same MCE. In the case of ethane, different cook fire types yield vastly different EFs at the same MCE. For example, at MCE ≈ 0.87, mixed-*chulha* has an EF of roughly 1.5 g/ kg fuel C, dung-*chulha* is 2.5 g/ kg fuel C, and dung-*angithi* is 5.5 g/ kg fuel C. Knowledge of the cook fire MCE alone is not sufficient to determine the EF of ethane. Combustion conditions specific to the fuel-stove combination is a significant factor in determining cook fire emissions. A similar conclusion can be reached for most of the measured gases, including non-ethene alkenes in Figure 2.6d.

2.3.3 Secondary pollutant formation and reactivity

2.3.3.1 OH reactivity and ozone forming potential

Total OH reactivity (s^{-1}) based on the measured VOCs in Figure 2.3b is given per ppbv of CO. Predicted OH reactivities in the village due to a single cooking event are 10.2, 6.73, 4.93, and $4.83 s^{-1}$ for emissions from *dung-angithi*, *dung-chulha*, *mixed-chulha*, and *brushwood-chulha* cook fires, respectively. This assumes a CO mixing ratio of 338 ppbv, which we measured as the average background mixing ratio over the whole campaign. The relative total OH reactivity is over twice as high for *dung-angithi* cook fires as it is for *brushwood-chulha* cook fires.

The classes of compounds that act as the most important OH radical sinks in descending order are alkenes, oxygenates, furans, terpenes, and aromatics. Alkenes make up more than 50% of OH reactivity for all cook fire types. Ethene (by fuel type) and propene (by fuel and stove combination) are mostly responsible for the differences in fuel-stove combination results for alkenes. For oxygenates, methanol ($p < 0.01$) and acrolein ($p < 0.05$) have significantly higher OH reactivity with wood fuel, while acetaldehyde has significantly higher OH reactivity with the *angithi* stove ($p < 0.001$). Differences in OH reactivity due to furans were observed for stove type but not fuel type. All three of the measured furans significantly contribute ($p < 0.001$) to a 6% increase in the fraction of OH reactivity due to furans for *dung-angithi* (12%) as opposed to *dung-chulha* (6%). The percentage of OH reactivity due to aromatics is constant at ~4% for the fuel-stove combinations. However, different aromatic compounds are responsible for this ~4% contribution depending on the cook fire type. Benzene dominates OH reactivity due to aromatics for *chulha* cook fires. For *angithi* cook fires aromatics other than benzene, in particular toluene,

dictate the OH reactivity for aromatics. Isoprene is solely responsible for the differences in OH reactivity due to terpenes.

Figure 2.3d shows the total ozone forming potential (g/ O₃ kg fuel) in the MIR scenario, as well as contributions to OFP by compound class. A critical step in photochemical ozone production is VOC reacting with OH. Therefore, the ozone forming potential contributions by compound class are similar to those for OH reactivity (Figure 2.3c). Total OFP is nearly a factor of 3 higher for dung-*chulha* compared to brushwood-*chulha*, while it's twice as high for dung-*angithi* as compared to dung-*chulha*.

2.3.3.2 SOA formation potential

SOAP-weighted emissions relate SOA production from the different cook fire types in a qualitative manner. The contribution of each compound class to the total SOA formation potential is shown in Figure 2.3c. We emphasize that the SOAP-weighted emissions are reflective of only the measured VOCs, and there are likely semi-volatile and intermediate volatility compounds that are not measured but also contribute to SOA formation. The sum of the contributions by each compound class, or the total SOA forming potential, is also shown below the pie charts. Dung fuels and *angithi* stoves yield larger amounts of SOA. However, fuel type is more important than stove type in terms of SOA formation. SOAP-weighted emissions are a factor of three higher for dung-*chulha* compared to brushwood-*chulha*. We discussed previously that benzene emissions are significantly higher from *chulha* cook fires compared to *angithi* cook fires. These higher benzene emissions directly impact public health and also dictate SOA formation for *chulha* emissions. Benzene emissions are responsible for at least half of the SOA formation from the *chulha* cook fire VOCs we measured. Beyond benzene, aromatics make up

on average roughly 95% of SOA precursors measured in this study for all cook fires. While benzene is prominent for *chulha* cook fires, C₈-C₉ aromatics, toluene, and benzene contribute in approximately equal proportions to SOA formation in dung-*angithi* smoke plumes.

2.4 Atmospheric implications and conclusions

The extent of ozone formation hinges on the villages' overall NO_x levels as well as VOC emissions. However, in a VOC-limited regime, with each household in this village cooking three meals a day using the *chulha* and mixed fuels (brushwood + dung), 3.3 x 10⁵ g ozone per day is expected to be produced due solely to cookstove use. This was estimated based off the Census of India 2011 data for the village of Khatela and assuming the same fuel consumption as that used in this study. Over the lunch hour, when solar radiation is most intense, 30 ppbv of excess ozone is predicted. For this calculation we assumed a calm wind speed of 0.5 m/s, and confined our analysis to the village of Khatela with a boundary layer height of 1 km and village length of 1 km. In a similar way we calculated the amount of ozone that could be generated from cooking animal fodder. We assumed that every household prepares animal fodder every three days in addition to the assumptions already discussed, resulting in an additional 7.9 x 10⁴ grams of O₃ produced per day from cooking. If we assume every household in the village prepares animal fodder in the same hour, excess ozone levels of 7 ppbv are predicted, using the same assumptions described earlier for the lunch hour. We should note that these estimations are approximate and a regional air quality model with detailed household level inputs should be used to more precisely predict the impact of cook fire emissions on ozone levels.

Using dung patties as opposed to brushwood has a large impact on local PM_{2.5} and ozone levels. Measured PM_{2.5} concentrations were more than a factor of two higher for dung-*chulha*

compared to brushwood-*chulha* in grams emitted per kilogram of fuel carbon burned. In addition to this, the total SOA forming potential is three times higher for dung-*chulha* than that of brushwood-*chulha*. We also estimated that dung-*chulha* cook fires produce roughly 3 times more ozone in the MIR regime than brushwood-*chulha* cook fires (163 g O₃ kg fuel C versus 56.9 g O₃ kg fuel C). However, compounds such as benzene are emitted in higher quantities from the *chulha* (1.03 g kg⁻¹ dry fuel) versus *angithi* (0.373 g kg⁻¹ dry fuel), and this public health concern should be investigated in more detail.

CHAPTER 3:

Molecular Composition of Particulate Matter Emissions from Dung and Brushwood Burning Household Cookstoves in Haryana, India

Abstract. Emissions of airborne particles from biomass burning are a significant source of black carbon (BC) and brown carbon (BrC) in rural areas of developing countries where biomass is the predominant energy source for cooking and heating. This study explores the molecular composition of organic aerosols from household cooking emissions with a focus on identifying fuel-specific compounds and BrC chromophores. Traditional meals were prepared by a local cook with dung and brushwood-fueled cookstoves in a village in Palwal district, Haryana, India. Cooking was done in a village kitchen while controlling for variables including stove type, fuel moisture, and meal. Fine particulate matter (PM_{2.5}) emissions were collected on filters, and then analyzed via nanospray desorption electrospray ionization/high resolution mass spectrometry (nano-DESI-HRMS) and high performance liquid chromatography/photodiode array/high resolution mass spectrometry (HPLC-PDA-HRMS) techniques. The nano-DESI-HRMS analysis provided an inventory of numerous compounds present in the particle phase. Although several compounds observed in this study have been previously characterized using gas chromatography methods, a majority of the species in the nano-DESI spectra were newly observed biomass-burning compounds. Both the stove (*chulha* or *angithi*) and the fuel (brushwood or dung) affected the composition of organic aerosols. The geometric mean of the PM_{2.5} emission factor and the observed molecular complexity increased in the following order: brushwood/*chulha* (7.3±1.8 g kg⁻¹ dry fuel, 93 compounds), dung/*chulha* (21.1±4.2 g kg⁻¹ dry fuel, 212 compounds), and dung/*angithi* (29.8±11.5 g kg⁻¹ dry fuel, 262 compounds). The mass-

normalized absorption coefficient (MAC_{bulk}) for the organic-solvent extractable material for brushwood $PM_{2.5}$ was $3.7 \pm 1.5 \text{ m}^2 \text{ g}^{-1}$ and $1.9 \pm 0.8 \text{ m}^2 \text{ g}^{-1}$ at 360 nm and 405 nm, respectively, which was approximately a factor of two higher than that for dung $PM_{2.5}$. The HPLC-PDA-HRMS analysis showed that, regardless of fuel type, the main chromophores were $C_xH_yO_z$ lignin fragments. The main chromophores accounting for the higher MAC_{bulk} values of brushwood $PM_{2.5}$ were $C_8H_{10}O_3$ (tentatively assigned to syringol), nitrophenols $C_8H_9NO_4$, and $C_{10}H_{10}O_3$ (tentatively assigned to methoxycinnamic acid).

3.1 Introduction

Approximately 3 billion people live in residences where solid fuels (coal, wood, charcoal, dung, and crop residues) are combusted for cooking (Smith et al., 2014). Approximately 57% of Indian households report use of wood (49%) or crop residues (9%) as their primary cookfuels, while 8% report dung as a primary cookfuel (Census of India, 2011). However, many households will routinely use two or more of these fuels in combination for their cooking needs in simple, home-made traditional stoves, or *chulhas*. These biomass-burning cookstoves have low combustion efficiencies and produce significant emissions of pollutants, including fine particulate matter ($PM_{2.5}$).

Epidemiological literature statistically links household air pollution from solid biomass combustion to acute lower respiratory infections in children, heart disease, stroke, cataracts, cancers in adults, and low birth weight for infants of women exposed during pregnancy (Smith et al., 2014). $PM_{2.5}$ are small enough to infiltrate deep into the lungs and penetrate the body's defenses, and therefore $PM_{2.5}$ exposure has been commonly used for estimating risks from both ambient air pollution and cigarette smoke (Finlayson-Pitts and Pitts, 2000). The degree of

adverse health effects of cookstove smoke likely depends on the chemical composition of the $PM_{2.5}$, however, the exact relationship between the chemical composition and health effects is largely unknown (Araujo et al., 2008).

Household cooking is estimated to be responsible for 26-50% of ambient $PM_{2.5}$ in India (Chafe et al., 2014; Guttikunda et al., 2016; Lelieveld et al., 2015). In this emissions mixture, carbonaceous particles affect climate directly by scattering and absorbing incoming solar radiation and indirectly by acting as cloud condensation nuclei (Crutzen and Andreae, 1990). In addition to black carbon (BC), which absorbs solar radiation across the entire visible spectrum, some molecules in biomass burning organic aerosols (BBOA) efficiently absorb blue and near-UV solar radiation resulting in classification of BBOA as brown carbon (BrC) (Laskin et al., 2015). Modeling studies have shown that in certain geographic areas climate warming by BrC has the potential to outweigh cooling by scattering organic aerosols (Feng et al., 2013). South Asia has been identified as one of these unique regions where emissions from cookstoves are a significant source of regional BrC (Feng et al., 2013).

Cookstove emissions have been studied in both the laboratory and field settings. Field studies typically involve observations and measurements during daily cooking activities in rural village homes. For example, Xiao et al., (2015) measured BC and $PM_{2.5}$ throughout the day for 6 different houses to monitor indoor concentrations in the household. In the laboratory, water boiling test (WBT) protocols are utilized to evaluate stove performance (Global Alliance for Clean Cookstoves, 2014). The WBT standard protocols are made up of three phases to represent the stove's combustion efficiency while cooking: (1) high power, cold start (2) high power, hot start (3) low power, simmer (Global Alliance for Clean Cookstoves, 2014). While the WBTs can be carried out under more controlled conditions, recent studies have found that the WBTs fail to

capture periods of low combustion efficiency in cooking events (Chen et al., 2012; Johnson et al., 2008, 2009). This is due to daily cooking activities involving more than just boiling water (Johnson et al., 2009). Some cooking techniques require a smoldering fire, for example, the cooking of *chapatti*, a traditional Indian flat bread (Johnson et al., 2009). Alternately, these low combustion efficiency periods may be a consequence of multitasking around the home (Johnson et al., 2009). The literature estimates that emissions of PM_{2.5} (Roden et al., 2009) and CO/CO₂ ratios (Johnson et al., 2008; Kituyi et al., 2001; Ludwig et al., 2003) are underrepresented by the WBTs relative to field measurements by a factor of 3. There are also concerns that WBTs cannot be scaled to real cooking events and that climate models may underrepresent global emissions from biomass-burning cookstoves (Chen et al., 2012; Johnson et al., 2008, 2009).

A number of studies have characterized optical properties of cookstove BBOA. Depending on the measurement approach different metrics of aerosol absorption have been reported. In general, methods that do direct measurements on aerosol particles without extraction report mass-normalized absorption cross section of aerosols (MAC_{aerosol}). Absorption measurements with the extracted material report mass-normalized absorption cross section of bulk material (MAC_{bulk}). In this paper, we use subscript “bulk” to help minimize confusion between MAC_{bulk} and MAC_{aerosol} . The two can be related if the particle size distribution is known (Laskin et al., 2015). An advantage of MAC_{bulk} is that it can be used to calculate the imaginary refractive index of the organic material (Laskin et al., 2015). For particles that are made of material with a real refractive index of 1.5 and that are small in diameter relative to the wavelength, $MAC_{\text{aerosol}} \sim 0.7 \times MAC_{\text{bulk}}$ (Laskin et al., 2015).

Stockwell et al., 2016 utilized photoacoustic extinctions (PAX) to conduct in situ absorption measurements at 405 and 870 nm, resulting in particle absorption coefficients from

cook fire emissions in Nepal. With a literature-recommended mass absorption coefficient for light-absorbing organic compounds (Lack and Langridge, 2013) and the measured aerosol absorption by PAX, they approximated particle absorption emission factors (EFs) due to the light-absorbing organic compounds in particles. OC absorption EFs were 1.5 times higher for the hardwood smoke (EF=8.40 g kg⁻¹ fuel) compared to the dung smoke (EF=5.43 g kg⁻¹ fuel). Pandey et al., 2016 collected PM_{2.5} on filters from cook fires in India, fueled by wood, agricultural residues, dung, and a mixture thereof and reported MAC_{aerosol} values. They found that the MAC_{aerosol} at 550 nm was a factor of 2.6 higher for fuel wood (1.3 m² g⁻¹) compared to dung (0.5 m² g⁻¹) (Pandey et al., 2016). This is consistent with Saleh et al., 2014, who found that for BBOA effective absorptivity of OA increases with BC to OA ratio. In Pandey et al., 2016, they measured EC/OC at 0.0649 for dung, and 0.0826 for fuel wood.

Many organic components of BBOA have been successfully characterized in previous studies by electrospray ionization high resolution mass spectrometry (ESI-HRMS) (Budisulistiorini et al., 2017; Laskin et al., 2009; Lin et al., 2012, 2016, 2017; Smith et al., 2009; Wang et al., 2017a; Willoughby et al., 2016). For example, ESI-HRMS was used to analyze the particle-phase organic constituents of smoke samples collected during the Fire Lab at Missoula Experiment (FLAME) campaign (Laskin et al., 2009; Smith et al., 2009). Fuels utilized in the FLAME studies were selected to represent North American wild fires and the publications focused on non-woody biomass fuels such as detritus and litter as well as *ceanothus* from the US Pacific Northwest. Smith et al., 2009 reported an inventory of species in particle-phase BBOA, with 70% of the compounds being reported for the first time. Laskin et al., 2009 examined the nitrogen-containing species and observed that a large fraction of the detected species were N-heterocyclic compounds. Lin et al., 2016 identifies fuel-specific BrC chromophores in particles

collected from the FLAME-4 experiments via high performance liquid chromatography/photodiode array/high resolution mass spectrometry (HPLC-PDA-HRMS). Two of the four fuels were woody biomass specific to North America. They found that nitroaromatics, PAHs, and polyphenols were responsible for the light absorption by BBOA (Lin et al., 2016). Recent papers investigated the chromophores in BBOA from Lag Ba'Omer, a nationwide bonfire festival in Israel (Bluvshstein et al., 2017; Lin et al., 2017). They found nitroaromatics to be the most prominent chromophores in these samples. Budisulistiorini et al. 2017 similarly identified 41 chromophores from Indonesian peat, charcoal, and fern/leaf burning with a method relying on chromatographic separation and simultaneous detection by spectrophotometry and ESI-MS. They identified three types of chromophores: oxygenated, nitroaromatics, or sulfur-containing (Budisulistiorini et al., 2017).

The goal of the current study is to understand the composition of cookstove BBOA in additional detail than afforded by previous measurements. We do this by 1) generating and collecting BBOA from prescribed cooking events carried out by a local cook and 2) using high-resolution mass spectrometry techniques to characterize their particle-phase composition. This is part of a larger study attempting to document the contribution of household solid fuel combustion to air pollution in India.

In this paper we provide an inventory of particle-phase compounds produced from actual cooking events detected by nano-DESI-HRMS and an assessment of BrC chromophores specific to the biomass type used based on HPLC-PDA-HRMS analysis. In addition, we compare particle-phase constituents in cook fire smoke produced from different traditional stoves and fuels.

3.2 Experimental Methods

3.2.1 Field site

This study was conducted at the SOMAARTH Demographic, Development, and Environmental Surveillance Site (Balakrishnan et al., 2015; Mukhopadhyay et al., 2012; Pillarisetti et al., 2014) run by the International Clinical Epidemiological Network (INCLEN) in Palwal District, located approximately 80 km south of New Delhi. SOMAARTH covers 51 villages across three administrative blocks, with an approximate population of 200,000. Palwal District has a population of approximately 1 million over ~1400 km²; 39% of households in the district utilize wood as their primary cookfuel, followed by dung (25%) and crop residues (7%) (Census of India, 2011).

3.2.2 Sample collection

Over 34 days in August-September 2015, PM_{2.5} samples were collected from a kitchen in the village of Khatela, Palwal, Haryana, India. Figure 3.1 shows (A) the kitchen setup and (B) the stoves (*angithi* and *chulha*) and fuels (dung and brushwood) used. The stoves and fuels were obtained locally and traditional meals were prepared by a local cook. The cook was instructed by the experimenters to prepare a particular, standard meal using the selected fuel and stove. All *angithi* cookstoves burned dung and were used to prepare buffalo fodder. *Chulha* cookstoves burned either brushwood or dung fuels and were used to prepare a traditional meal of *chapatti* and vegetables for 4 people. Vegetables were cooked in a pressure cooker that rests on top of the *chulha* (Figure 3.1B). *Chapatti* were cooked in the air space next to the fuel, as is typical for this

area. Brushwood/*angithi* cook fires were never tested because this combination is not frequently used in the local households.



Figure 3.1: The field site and set-up for cooking events. A) The kitchen set-up at the field site. B) The stoves and fuels used in this study: *angithi*, dung-burning *chulha*, and brushwood-burning *chulha*.

Figure 2.1 shows a diagram of sample collection. $PM_{2.5}$ emissions were sampled via three-pronged probes that hung above the cookstove. Air sampling pumps (PCXR-8, SKC Inc.) created a flow of BBOA emissions through aluminum tubing during cooking events. BBOA was captured through cyclone fractionators (2.5 μm cut point, URG Corporation) and the resultant flow was taken through a stainless steel filter holder containing a PTFE filter (Teflon B, SKC Inc., 47 mm). One filter was collected for chemical analysis (Teflon B), and another filter for gravimetric analysis (Teflon A). Flows were measured via a mass flowmeter (TSI 4140) before

and after each cooking event to ensure it had not varied more than 10%. The pumps were turned on before cooking began so that emissions from the entire cooking event were captured and turned off when the fire was out. Stove dimensions and their distance from the probe inlets are detailed in Figure 3.2. Prior to analysis, filters were stored in petri dish slides at -80°C other than during transportation and use. This includes time at the field site (1-6 hours) and transportation back to the United States (24 hours). During these times, samples were stored at ambient temperature.

Figure 3.2: Stoves used in the study, the *angithi* and *chulha*, are pictured. Stove measurements and distances from the stoves to the inlet probes are found in the tables below.



<i>Chulha</i> measurements	Distance (cm)	<i>Angithi</i> measurements	Distance (cm)
Inner height	25	Inner diameter	44
Inner width	21	Outer diameter	50
Inner depth	23	Outer height	20
Width of walls	4.6	Height from inside bottom of stove to probe inlets	83
Top of <i>chulha</i> to probe inlets	58	Top of <i>angithi</i> to probe inlets	64

3.2.3 PM_{2.5} emission factor calculation

PM_{2.5} emission factors are briefly mentioned when comparing absorbance by particles from different cookfire types (Section 3.3.6). Here we explain how they were calculated. Figure 2.1 shows the sampling lines used to collect emissions in this study. Emissions flowed through a PM_{2.5} cyclone and subsequent quartz filter to remove particles, so that gases were collected over the entire cooking event in an 80 L Kynar bag (Gases sampling line, Figure 2.1). After pumps were turned off, a whole air sample (WAS) of average gas-phase emissions over the cooking event was collected from the Kynar bag. Stainless steel canisters (2 L), evacuated and prepped prior to the trip, were used to collect WAS. The background WAS sample was collected as a grab sample in the kitchen before cooking began for the day. One background sample was collected per day and that measurement was used for all experiments that day. Ideally background samples should be an integrated sample collected at the same time as the sample. However, we were limited in the number of cans brought to India.

A separate filter reserved for gravimetric analysis was used for fine particle emissions measurements (Teflon A). These filters were pre-weighed on a Cahn-28 electrobalance after equilibrating for a minimum of 24 hours in a humidity and temperature-controlled environment (average temperature 18.9 degrees Celsius, standard deviation 0.4 degrees Celsius, average relative humidity 64%, standard deviation 7%). This PTFE filter collected cookstove emissions on a separate line than the filter analyzed by nano-DESI-HRMS and HPLC-PDA-HRMS techniques (Teflon B). Another gravimetric filter was collected in the background during the cooking event and was equilibrated and weighed in the same way. The masses for the background and sample filters were utilized after accounting for the difference in flow rates.

Then the background mass was subtracted from the sample mass to obtain the mass of PM (m_{PM}) in equation (3.1) below.

$$\frac{EF_{PM}}{EF_{CO}} = \frac{m_{PM}/V_{air}}{m_{CO}/V_{air}} \quad (3.1)$$

The concentration of CO was measured using WAS samples. The WAS samples were taken back to UCI where they were injected into a GC-FID with a Ni catalyst that converts CO into detectable CH₄. Other gases were also detected using a GC system comprised of 3 gas chromatographs equipped with 5 columns (DB-1, Restek 1701, DB-5ms) and detectors (FID, ECD, MS). A complete list of gaseous emission factors will be reported in a separate manuscript.

EF_{CO} was produced using the carbon-balance method. This method traces carbon in the form of emitted CO₂, CO, CH₄, other hydrocarbons, and PM and utilizes the relative concentrations of these compounds to evaluate emission factors. The total gas-phase carbon emissions were approximated with the concentrations of 86 gases measured using WAS. The ratio of the mass concentration of carbon in CO (C_{CO}) to the total mass concentration of detected gas-phase carbon was calculated using equation (3.2).

$$C_{CO} \text{ emitted (g)} = \frac{C_{CO}(\text{g m}^{-3})}{\sum_1^{86} C_1+C_2+C_3+\dots+C_{86}} \cdot C_T \text{ (kg)} \cdot \frac{1000 \text{ g}}{1 \text{ kg}} \quad (3.2)$$

In equation (3.2), C_i represents the mass of carbon in compound i per m³ of air. C_T specifically refers to the net mass of carbon in the fuel and is adjusted for ash and char carbon. The carbon content of the fuel was taken to be 33% for buffalo dung and 45% for brushwood fuels based on

standard values from Smith et al. (2000). Carbon in ash was estimated as 2.9% and 80.9% of the measured char mass for dry dung and dry brushwood, respectively (Smith et al., 2000b). Then, we calculated EF_{CO} using equation (3.3),

$$EF_{CO}(\text{g CO/kg fuel}) = \frac{C_{CO} \text{ emitted}(\text{g}) \cdot \frac{28.01 \text{ g}}{12.00 \text{ g}}}{\text{mass}_{\text{fuel}}(\text{kg})} \quad (3.3)$$

where $\text{mass}_{\text{fuel}}$ is the net dry fuel in kg burned for the cooking event.

3.2.4 Nano-DESI-HRMS analysis

$PM_{2.5}$ collected on PTFE filters were analyzed with an LTQ-OrbitrapTM high resolution mass spectrometer (ThermoFisher Scientific) equipped with a custom built nano-DESI source (Roach et al., 2010b, 2010a). Nano-DESI consists of two electrified capillaries with a small (< 1 mm) droplet, or solvent bridge, forming at the point of their contact. The nano-DESI solvent mixture (70% CH_3CN /30% H_2O , optimized for the stability of the nano-DESI source) flows through an electrified capillary at a flow rate of 0.3-1 $\mu\text{L}/\text{min}$. The droplet is lowered to the substrate's surface where the analyzed material is extracted by the solvent and immediately sprayed in the mass spectrometer inlet. It has been shown that the nano-DESI dissolves all extractable material on the filter surface (Roach et al., 2010a, 2010b). To ensure the material on the filter is not depleted the droplet is moved across the filter's surface at roughly 0.2 cm/min. The spray voltage was 3.5 kV and the instrument was operated in positive ion mode. The mass accuracy of the HRMS was calibrated over a wide m/z range with a ThermoFisher Scientific standard calibration mixture. Two separate mass spectra were obtained from different portions of the filter to ensure reproducibility. Only peaks that showed up in both spectra were retained for further analysis.

Peaks with signal-to-noise ratios of greater than 3 were extracted from the time-integrated nano-DESI chromatograms using Decon2LS software. Peaks containing ^{13}C isotopes were excluded from analysis. Sample and solvent-blank mass spectra peaks were clustered with a tolerance of 0.001 m/z using a second-order Kendrick analysis with CH_2 and H_2 base units (Roach et al., 2011). The spectra were internally mass-calibrated by assigning prominent peaks of common BBOA compounds first, and fitting the observed-exact m/z deviation to a linear regression curve. The m/z correction introduced by the internal calibration was <0.001 m/z units, but even at these small levels the correction helped reduce the ambiguity in the assignments of unknown peaks. We focused on analyzing peaks with $m/z < 350$, as peaks above this m/z value were small in abundance (on average 6% of total abundance), number of peaks (9% of the total number of peaks), and in many cases could not be assigned unambiguously. Exact masses were assigned using the freeware program Formula Calculator v1.1 (<http://magnet.fsu.edu/~midas/download.html>). The permitted elements and their maximal numbers of atoms were as follows: C (40), H (80), O (35), N (5), and Na (1). Peaks that could not be assigned within the described parameters had small abundances and were not pursued further. There were a few notable exceptions, namely, the potassium salt peaks discussed below. Conversely, potassium-organic adducts were not observed presumably due to the higher affinity of organic molecules to Na^+ compared to K^+ . Permitting sulfur, chloride, and phosphorus did not increase the fractions of assignable peaks, nor did it change the assignments for the peaks we report. The double-bond equivalent (DBE) values of the neutral formulas were calculated using the equation: $\text{DBE} = \text{C} - \text{H}/2 + \text{N}/2 + 1$, where C, H, and N correspond to the number of carbon, hydrogen, and nitrogen atoms, respectively.

3.2.5 HPLC-PDA-HRMS

The samples were further analyzed with an HPLC-PDA-HRMS platform (Lin et al., 2016). To prepare the samples for analysis half of the PTFE filter was extracted overnight in mixture of acetonitrile, dichloromethane, and hexane solvents (2:2:1 by volume, 5 mL total), which was empirically found to work well for extracting a broad range of BBOA compounds (Lin et al., 2017). The solutions were then filtered with PVDF filter syringes to remove insoluble particles (Millipore, Duropore, 13mm, 0.22 μm). The solutions were concentrated under N_2 flow, and then diluted with water and dimethyl sulfoxide (DMSO) to a final volume around 150 μL . The separation was performed on a reverse-phase column (Luna C18, 2 x 150 mm, 5 μm particles, 100 \AA pores, Phenomenex, Inc.). The mobile phase comprised of 0.05% formic acid in LC/MS grade acetonitrile (B) and 0.05% formic acid in LC/MS grade water (A). Gradient elution was performed by the A/B mixture at a flow rate of 200 $\mu\text{L}/\text{min}$: from 0-3 min hold at 90% A, 3-62 min linear gradient to 10% A, 63-75 min hold at 10% A, 76-89 min linear gradient to 0% A, 90-100 min hold at 0% A, then 101-120 min hold at 90% A. The ESI settings were as follows: 5 μL injection volume, 4.0 kV spray potential, 35 units of sheath gas flow, 10 units of auxiliary gas flow, and 8 units of sweep gas flow. The solutions were analyzed in both positive and negative ion ESI/HRMS modes.

The HPLC-PDA-HRMS data were acquired and first analyzed using Xcalibur 2.4 software (Thermo Scientific). Possible exact masses were identified by LC retention time using the open source software toolbox MZmine version 2.23 (<http://mzmine.github.io/>) (Pluskal et al., 2010). Formula assignments were obtained from their exact m/z values using the Formula Calculator v1.1.

3.2.6 MAC_{bulk} and AAE

Selected filter halves were extracted as described in section 3.2.4. Absorption spectra of the extracts were collected with a dual-beam UV-Vis spectrophotometer (Shimadzu UV-2450). MAC_{bulk} values were calculated from the following equation:

$$\text{MAC}_{\text{bulk}}(\lambda) = \frac{A_{10}(\lambda) \cdot \ln(10)}{b \cdot C_{\text{mass}}} \quad (3.4)$$

where A_{10} is the base-10 absorbance, b is the path length of the cuvette (m), and C_{mass} is the mass concentration of the extracted organic material in (g m^{-3}). The largest uncertainty in MAC_{bulk} came from uncertainty in C_{mass} of the extract. First, the overall mass of PM_{2.5} on the filter had to be estimated from another filter collected specifically for gravimetric analysis. The PM_{2.5} mass on the chemical analysis filter was calculated from the mass on the gravimetric analysis filter after accounting for different flows through the two filters (Figure 2.1). This calculation assumed the same PM_{2.5} collection efficiency for both filters. The particle mass distribution on the filter was assumed to be uniform, and the extraction efficiency of PM_{2.5} mass was estimated to be 50% by comparing the weights of filters before and after the extraction. Uncertainties incorporate flow rate measurements (10% relative error) and extraction efficiency of PM_{2.5} mass (40% relative error). Absorption angstrom exponents (AAE) were calculated for both samples by fitting the $\log(\text{MAC}_{\text{bulk}})$ vs. $\log(\lambda)$ to a linear function over the wavelength range of 300 to 700 nm. It should be noted that there are many methods for measuring optical properties of PM_{2.5} particles, and the method used here provides MAC_{bulk} and AAE of extractable organic bulk material. The advantages and limitations of other methods are explained in Laskin et al., 2015.

3.3 Results and Discussion

3.3.1 Nano-DESI-HRMS analysis of cookstove particles

Representative nano-DESI mass spectra from the three major types of cook fires sampled are shown in Figure 3.3. It is clear from the mass spectra in Figure 3.3 that the three combinations of fuel/stove types lead to distinct particle compositions. We compare the particle composition of the three major cook fire types by averaging the percentage of $C_xH_yN_w$, $C_xH_yO_z$, and $C_xH_yO_zN_w$ peaks in the nano-DESI spectra from multiple samples. Samples used and a summary of the following discussion is detailed in Table 3.1. The overwhelming majority of detected species by nano-DESI in dung cook fire smoke $PM_{2.5}$ was attributed to $C_xH_yN_w$ compounds that contain only carbon, hydrogen, and nitrogen atoms. The average count-based fractions from $C_xH_yN_w$ species were $79.9\% \pm 4.4\%$ and $82.1\% \pm 1.0\%$ for dung/*chulha* and dung/*angithi* experiments, respectively, but only $23.8\% \pm 7.8\%$ for brushwood/*chulha* experiments. All nitrogen-containing compounds in the smoke $PM_{2.5}$ come from the nitrogen content in the fuels (Coggon et al., 2016) which is likely higher for dung. Stockwell et al. 2016 reported the nitrogen content of yak dung as 1.9% by weight, while it is found to be lower for woods such as black spruce (0.66% by wt) and ponderosa pine (1.09% by wt) (Hatch et al., 2015). It should be noted that another study of fuels in India found the nitrogen content was roughly the same for brushwood ($1.4 \pm 0.3\%$ by wt) and dung ($1.4 \pm 0.1\%$ by wt) (Gautam et al., 2016), so additional characterization of fuel composition in the future is desirable. In contrast to dung fuel, $PM_{2.5}$ from brushwood cook fire smoke contained higher fractions of $C_xH_yO_z$ species. Specifically, the count-based fraction assigned as $C_xH_yO_z$ species was $43.1\% \pm 14.6\%$ in brushwood/*chulha* cook fires compared to only $4.1\% \pm 0.9\%$ and $3.2\% \pm 3.3\%$ for dung/*chulha* and

dung/*angithi* experiments, respectively. Many of the $C_xH_yO_z$ formulas were consistent with species reported previously as lignin-pyrolysis products (Collard and Blin, 2014; Simoneit et al., 1993). Fractions of $C_xH_yO_zN_w$ did not correlate well with fuel/stove variables and ranged from 4.1% to 34.4% in the analyzed samples.

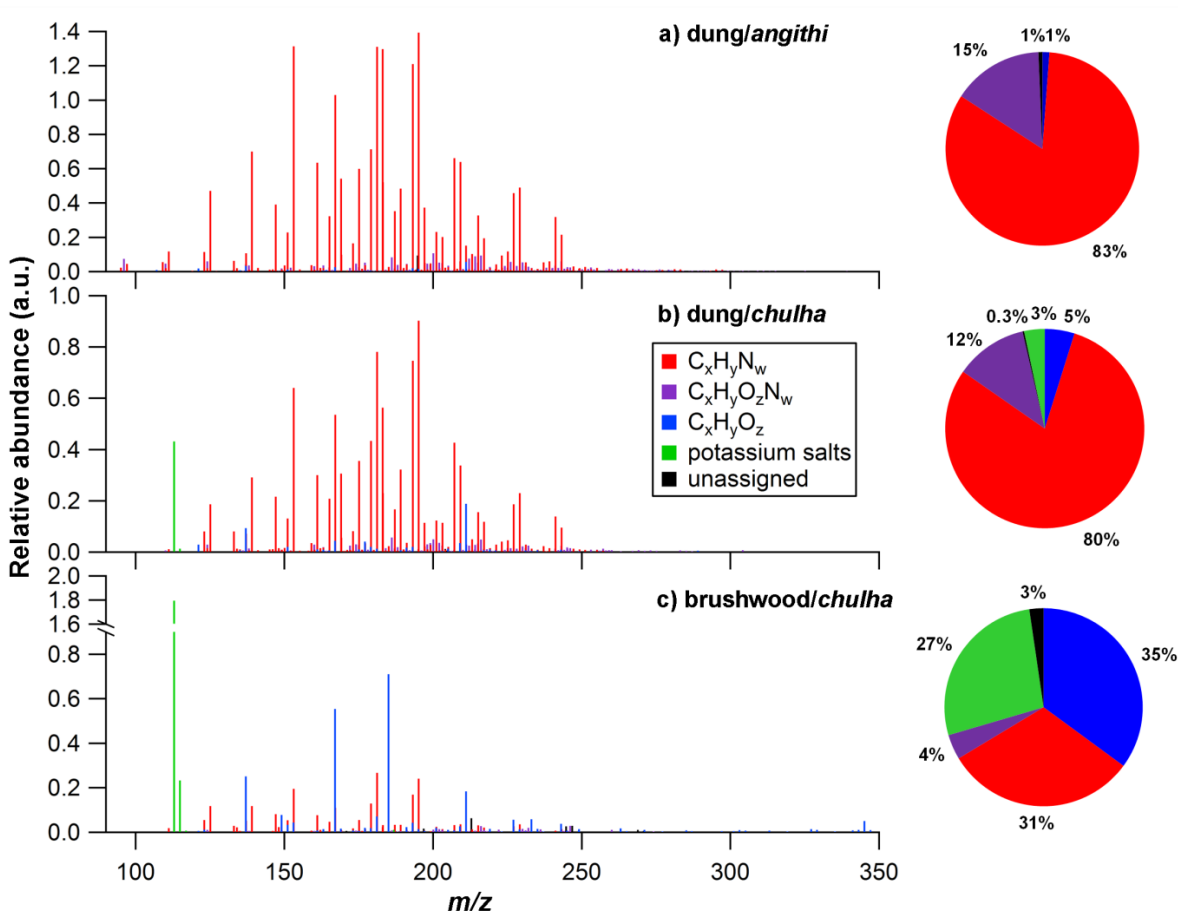


Figure 3.3: Representative nano-DESI mass spectra collected for a) dung/*angithi* b) dung/*chulha* and c) brushwood/*chulha* cookfires. Relative abundance is plotted against m/z . Peaks are colored by their elemental makeup, $C_xH_yN_w$ (red), $C_xH_yO_zN_w$ (purple), $C_xH_yO_z$ (blue), potassium salts (green), and unassigned (black). The pie charts illustrate the fraction of count-based, normalized peak abundance that is attributed to each elemental category.

Table 3.1: Samples utilized in sections 3.3.1-3.3.5. Representative mass spectra shown in Figure 3.3, section 3.3.1 correspond to samples M10, L7, and M1. The % abundance for $C_xH_yO_z$, $C_xH_yN_w$, and $C_xH_yO_zN_w$ peaks from the nano-DESI mass spectra are given as well as arithmetic means and standard deviations for each cookfire category: brushwood/*chulha*, dung/*chulha*, and dung/*angithi*.

Sample	Date	Fuel	Stove	Moisture (% wet basis)	Meal	$C_xH_yO_z$ (% abundance)	$C_xH_yN_w$ (% abundance)	$C_xH_yO_zN_w$ (% abundance)
M10	8/26/15	brushwood	Chulha	18.0	chapati	35.1	31.3	4.1
RE007	8/30/15	brushwood	chulha	29.5	chapati	34.3	15.8	34.4
RE032	8/28/15	brushwood	chulha	17.7	chapati	60.0	24.3	11.0
						43.1±14.6	23.8±7.8	16.5±15.9
H5	8/14/15	dung	chulha	6.9 ^a	chapati	4.4	75.6	14.1
L7	8/21/15	dung	chulha	10.5 ^a	chapati	4.8	79.8	11.7
P2	8/20/15	dung	chulha	10.8 ^a	chapati	3.2	84.4	11.9
						4.1±0.9	79.9±4.4	12.6±1.3
C7	8/11/15	dung	angithi	8.3 ^a	buffalo fodder	1.4	82.3	14.1
M1	8/17/15	dung	angithi	10.9 ^a	buffalo fodder	1.2	83.0	15.2
P1	8/19/15	dung	angithi	10.4 ^a	buffalo fodder	7.0	81.0	11.7
						3.2±3.3	82.1±1.0	13.6±1.8

^a Dung moisture content was measured using a commercial moisture probe, and converted to a real value, moisture on a % wet basis, using Gautam et al., 2016.

Potassium (Hosseini et al., 2013; Sullivan et al., 2014) and levoglucosan (Jayarathne et al., 2017; Simoneit et al., 1999) are well-established flaming and smoldering BB tracers, respectively. Gas-phase chlorine species have been observed in BBOA previously (Lobert et al., 1999; Stockwell et al., 2016). Therefore it is not surprising that inorganic salt peaks containing potassium and chlorine were observed in more than half of dung cook fires (8 out of 14) and all brushwood cook fires. These peaks were pursued apart from the original analysis because the peak abundance was very large in many mass spectra, and they served as convenient internal m/z calibration points. These mass spectra all contained K_2Cl^+ as the most prominent salt peak and $K_3Cl_2^+$ was also present in a few mass spectra. Isotopic variants of these salts, namely with either ^{37}Cl or ^{41}K (24% or 6.7% natural abundance) instead of ^{35}Cl or ^{39}K (76% or 93.3% natural abundance), were also found. The resolving power of the HRMS instrument is insufficient to distinguish the isotopic shifts from Cl and K ($\Delta \text{mass}_{^{37}Cl-^{35}Cl} = 1.997 \text{ Da}$, $\Delta \text{mass}_{^{41}K-^{39}K} = 1.998 \text{ Da}$) but one or both of the isotopes were consistently present in all mass spectra containing potassium ions. Adducts corresponding to a replacement of K by Na were also detected. The observed potassium signals may have depended not only on the potassium content of the fuel but also on the amount of flaming combustion (combustion efficiency), the specific food items cooked, or the stove material itself. Inorganic salts were observed in all *chulha* cook fire $PM_{2.5}$ samples regardless of fuel type and were absent in all *angithi* cook fire $PM_{2.5}$ samples. On average, *chulha* stoves have a higher combustion efficiency (dung/*chulha* $90.7\% \pm 0.6\%$, dung/*angithi* $87.5\% \pm 1.8\%$) consistent with more flaming combustion and therefore more potassium emissions. The *chulha* and *angithi* stoves produced meals for people or animal fodder, respectively. Also, the *chulha* was made mainly from brick with a local covering of local clay, whereas the *angithi* only from clay. With the presently available data it is impossible to

determine whether the potassium salts originated from flaming combustion, from the *chulha* material, or is the result of different food items cooked.

Levoglucosan was present in 3 out of 8 dung/*chulha* cook fires, 4 out of 6 dung/*angithi* cook fires, and 4 out of 11 brushwood/*chulha* cook fires. We expect levoglucosan to be found in BBOA from all fires based on other studies (Jayarathne et al., 2017), and we therefore conclude that levoglucosan peak must have been suppressed in the nano-DESI source by the more ionizable components of the mixture. By extension of the same logic, ions corresponding to other carbohydrates, and more broadly to lignin-derived CHO species, were likely suppressed by this technique, and therefore a significant fraction of BBOA constituents may be absent in this inventory. Due to the variability in observing levoglucosan we conclude that for ESI-MS studies levoglucosan serves as a marker rather than a tracer for digested biomass burning and woody biomass burning.

3.3.2 Particle-phase biomass burning markers

An inventory of compounds that were reproducibly observed in samples from three different cooking events using the same fuel/stove combination was compiled. Samples were chosen for the inventory considering the measured fuel moisture content and meal cooked, with the goal of comparing samples from similar cook fires (see Table 3.1 for sample details). Peaks that did not appear in mass spectra of all three samples were discarded to ensure reproducibility and help filter out noise peaks from the nano-DESI source. The remaining peak abundances were first normalized to the largest peak abundance then the three mass spectra were averaged. Since the absolute peak abundances varied in individual spectra, only approximate relative abundances are reported here grouped into three logarithmic bins, denoted as LOW (<1%), MEDIUM (1-

9.99%), HIGH (10-100%). This analysis was completed for the emissions from each of the three types of cookstove-fuel combinations studied in this work.

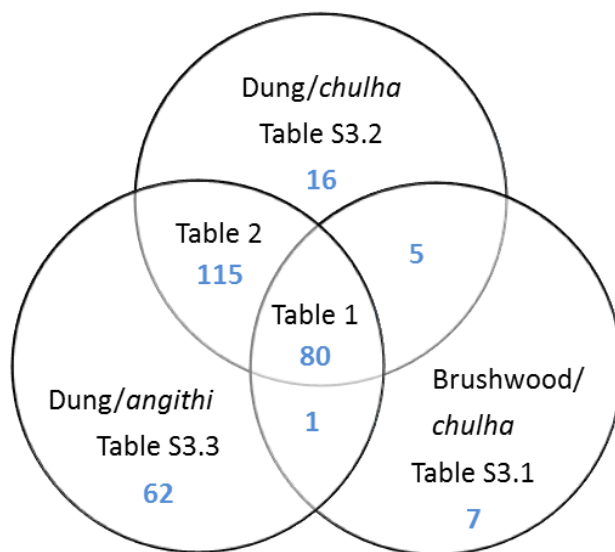


Figure 3.4: An overview of the particle-phase compounds inventory based on the results of molecular characterization using nano-DESI-HRMS. Each area of the Venn diagram contains the bolded number of reproducibly-detected formulas in blue as well as the Table that lists peaks for each category. Merging all the tables listed here provides a complete inventory of compounds detected in this study.

Figure 3.4 summarizes how reproducibly-detected PM_{2.5} compounds are organized in the inventory. First, we provide a list of compounds common to the emissions from all 3 types of cook fires including: dung/*chulha*, dung/*angithi*, and brushwood/*chulha* (Section 3.3.3, Table 3.2). Then, we discuss compounds exclusively found in the brushwood/*chulha* cook fire emissions (Section 3.3.4, Table 3.3). Within section 3.3.5 we discuss compounds unique to the dung/*chulha* (Table 3.5) and the dung/*angithi* (Table 3.6) cook fire experiments, as well as the compounds they had in common (Table 3.4).

The numbers of reproducibly-detected formulas are shown in Figure 3.4 in blue. PM_{2.5} from dung cook fires had a higher observed chemical complexity (i.e., had more observed peaks) than PM_{2.5} from brushwood cook fires. Further, there were more observed peaks in PM_{2.5} from dung/*angithi* cook fires compared to dung/*chulha* cook fires. There were 93 compounds reproducibly detected in the brushwood/*chulha* cook fire PM_{2.5} samples compared to 212 and 262 for dung/*chulha* and dung/*angithi* cook fires, respectively. There were five compounds the *chulha* cook fires had in common, with two of them being the potassium salt peaks described earlier. There was one compound (C₁₄H₁₆O₃) shared by only dung/*angithi* and brushwood/*chulha*. Because of the small number of these peaks, they will not be discussed in this paper. In the following sections, we discuss compounds that are common in all cook fires, as well as unique compounds.

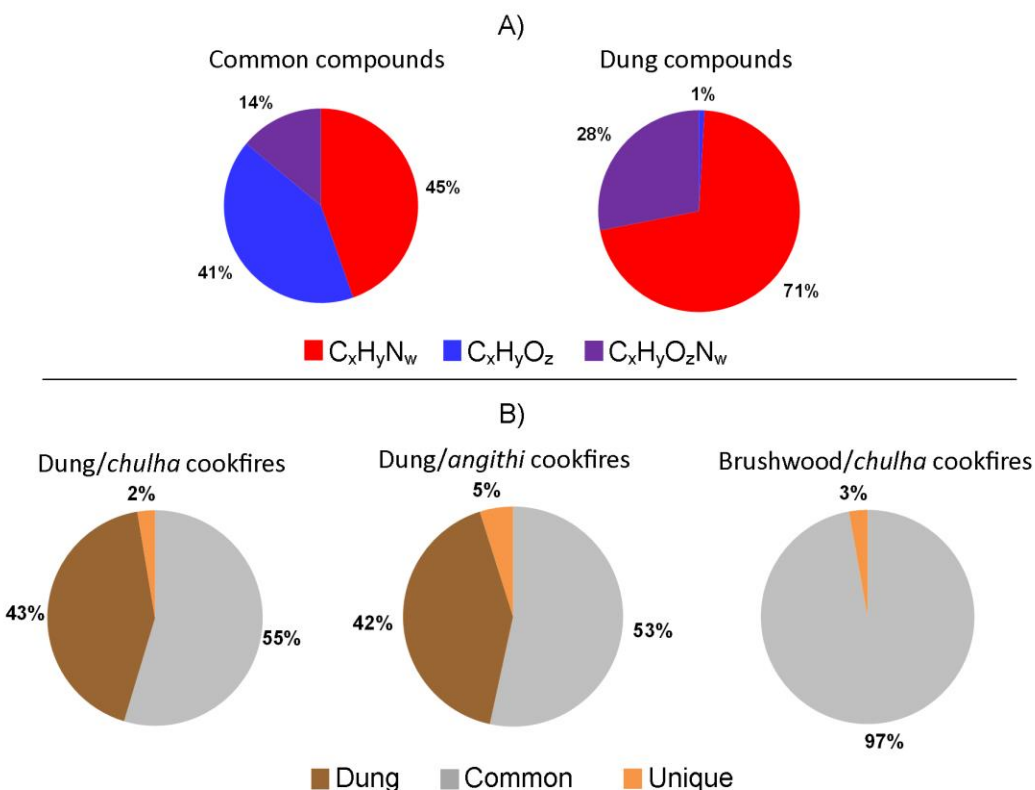


Figure 3.5: A summary of the inventory in terms of the count-based, normalized peak abundances. A) Contribution of $PM_{2.5}$ compounds to each elemental formula category for those found in all cookfires and those found in all dung-burning cookfires. B) The compounds by cookstove type classified as compounds common to all cookfires in grey, compounds common to all dung cookfires in brown, and unique compounds in orange.

Figure 3.5 summarizes the BBOA inventory described in more detail in sections 3.3.3-3.3.5, i.e., compounds common to dung/*chulha*, dung/*angithi*, brushwood/*chulha* cook fires; compounds found exclusively in the emissions from brushwood/*chulha* cook fires; and species that are unique to dung cook fires. Figure 3.5A compares the fraction of count-based, normalized abundance in each elemental category. $PM_{2.5}$ compounds shared among all samples of this study are diverse. In terms of count-based abundance, compounds emitted from all dung-burning cook fires are largely nitrogen-containing. From Figure 3.5B, the common compounds make up the vast majority (97%) of detected compounds from the brushwood/*chulha* cook fires. Similarly for the dung cook fires, the common cook fire compounds (grey) and dung cook fire compounds

(brown) make up 95% or more of the mass spectra abundance as shown in Figure 3.5B. Therefore, the common compounds (Table 3.2) and dung compounds inventories (Table 3.4) contain the bulk of the PM_{2.5} species in terms of count-based abundance.

3.3.3 Compounds common to dung/*chulha*, dung/*angithi*, brushwood/*chulha* cook fires

Table 3.2 provides a complete list of eighty reproducibly-detected compounds that were common to emissions from all cook fires. These common compounds make a large contribution to the mass spectra for every cook fire type (Figure 3.5), with MEDIUM being the most common relative abundance given in Table 3.2. More than half of the abundance (59%) was due to the nitrogen-containing compounds (C_xH_yN_w or C_xH_yO_zN_w), as shown in Figure 3.5A. ESI detection likely biases the elemental make up of smoke PM_{2.5}, as nitrogen-containing species are more easily ionized compared to sugars and lignin-derived compounds (Laskin et al., 2010; Wan and Yu, 2006). Nevertheless, a large overlap in the C_xH_yN_w and C_xH_yO_zN_w species was observed.

The common compounds make up a large fraction for all cook fire types. This is especially true for the sample from brushwood/*chulha* cook fires where their fraction is ~86% in number. Many of these C_xH_yO_z species have elemental formulas consistent with typical lignin and cellulose-derived products such as anisaldehyde, veratraldehyde, vinylguaiacol, syringylethanone, trimethoxyphenylethanone, etc. reported previously in the literature (Laskin et al., 2009; Simoneit et al., 1993; Smith et al., 2009). These tentative molecular assignments are listed in Table 3.2 alongside their elemental formulas.

Approximately 20% of the common compounds (17 out of 80 formulas) have been also identified in earlier studies reporting molecular characterization of PM_{2.5} samples collected from burning of one or more of the following fuels: Alaskan duff, ponderosa pine duff, southern

United States pine needles, or ceanothus fuels (Laskin et al., 2009; Smith et al., 2009). Many of these fuels are non-woody and all are undigested biomass, very different kinds of biomass from those used as cookstove fuels in this study and in this region of India. This suggests that perhaps 20% of the compounds listed in Table 3.2 might be reproducibly detected in BBOA samples using ESI-MS regardless of biomass type. The overlap is not surprising as all biomass is composed of three polymers: lignin, hemicellulose, and cellulose (Collard and Blin, 2014).

Table 3.2: List of common compounds found in all PM_{2.5} samples regardless of fuel or stove type. Tentative molecular structure assignments are listed when the compound has previously been identified in the chemical biomass-burning literature, supported by the references in the last column. Count-based, normalized peak abundances are designated LOW (<1%), MEDIUM (1-9.99%), HIGH (10-100%). All species were detected as protonated ions.

Observed <i>m/z</i>	Calculated <i>m/z</i>	Chemical formula of neutral species	DBE	Relative average abundance	Tentative assignment(s)	References
111.091	111.092	C ₆ H ₁₀ N ₂	3	MEDIUM		(Smith et al., 2009)
121.064	121.065	C ₈ H ₈ O	5	MEDIUM		
123.091	123.092	C ₇ H ₁₀ N ₂	4	MEDIUM		
124.075	124.076	C ₇ H ₉ ON	4	MEDIUM		
125.107	125.107	C ₇ H ₁₂ N ₂	3	MEDIUM		(Smith et al., 2009)
133.075	133.076	C ₈ H ₈ N ₂	6	MEDIUM		(Laskin et al., 2009)
134.071	134.071	C ₇ H ₇ N ₃	6	MEDIUM		(Laskin et al., 2009)
137.059	137.060	C ₈ H ₈ O ₂	5	HIGH	Anisaldehyde	(Simoneit et al., 1993)
						(Smith et al., 2009)
137.106	137.107	C ₈ H ₁₂ N ₂	4	MEDIUM		(Smith et al., 2009)
138.090	138.091	C ₈ H ₁₁ ON	4	LOW		
139.122	139.123	C ₈ H ₁₄ N ₂	3	MEDIUM		(Smith et al., 2009)
147.091	147.092	C ₉ H ₁₀ N ₂	6	MEDIUM		
151.074	151.075	C ₉ H ₁₀ O ₂	5	MEDIUM	Vinylguaiacol	
151.122	151.123	C ₉ H ₁₄ N ₂	4	MEDIUM		
153.138	153.139	C ₉ H ₁₆ N ₂	3	HIGH		
159.091	159.092	C ₁₀ H ₁₀ N ₂	7	MEDIUM		(Laskin et al., 2009)
160.075	160.076	C ₁₀ H ₉ ON	7	MEDIUM		(Laskin et al., 2009)
161.059	161.060	C ₁₀ H ₈ O ₂	7	MEDIUM		
161.106	161.107	C ₁₀ H ₁₂ N ₂	6	MEDIUM		
162.102	162.103	C ₉ H ₁₁ N ₃	6	LOW		
163.074	163.075	C ₁₀ H ₁₀ O ₂	6	MEDIUM		
165.138	165.139	C ₁₀ H ₁₆ N ₂	4	MEDIUM		
167.069	167.070	C ₉ H ₁₀ O ₃	5	HIGH	Veratraldehyde	(Simoneit et al., 1993)
167.153	167.154	C ₁₀ H ₁₈ N ₂	3	MEDIUM		
173.106	173.107	C ₁₁ H ₁₂ N ₂	7	MEDIUM		
174.090	174.091	C ₁₁ H ₁₁ ON	7	MEDIUM		
175.074	175.075	C ₁₁ H ₁₀ O ₂	7	MEDIUM		
175.122	175.123	C ₁₁ H ₁₄ N ₂	6	MEDIUM		

Observed <i>m/z</i>	Calculated <i>m/z</i>	Chemical formula of neutral species	DBE	Relative average abundance	Tentative assignment(s)	References	
177.053	177.055	C ₁₀ H ₈ O ₃	7	MEDIUM	Coniferaldehyde	(Laskin et al., 2009)	
177.090	177.091	C ₁₁ H ₁₂ O ₂	6	MEDIUM			
177.101	177.102	C ₁₀ H ₁₂ ON ₂	6	LOW			
177.137	177.139	C ₁₁ H ₁₆ N ₂	5	LOW			
179.069	179.070	C ₁₀ H ₁₀ O ₃	6	MEDIUM			
179.153	179.154	C ₁₁ H ₁₈ N ₂	4	MEDIUM			
181.169	181.170	C ₁₁ H ₂₀ N ₂	3	HIGH			
183.090	183.092	C ₁₂ H ₁₀ N ₂	9	HIGH			
183.184	183.186	C ₁₁ H ₂₂ N ₂	2	MEDIUM			
186.090	186.091	C ₁₂ H ₁₁ ON	8	MEDIUM			(Laskin et al., 2009)
187.122	187.123	C ₁₂ H ₁₄ N ₂	7	MEDIUM			
188.106	188.107	C ₁₂ H ₁₃ ON	7	MEDIUM			
189.101	189.102	C ₁₁ H ₁₂ ON ₂	7	MEDIUM			(Laskin et al., 2009)
189.137	189.139	C ₁₂ H ₁₆ N ₂	6	MEDIUM			
191.069	191.070	C ₁₁ H ₁₀ O ₃	7	MEDIUM			
191.117	191.118	C ₁₁ H ₁₄ ON ₂	6	LOW			
191.153	191.154	C ₁₂ H ₁₈ N ₂	5	LOW			
193.085	193.086	C ₁₁ H ₁₂ O ₃	6	MEDIUM			
193.169	193.170	C ₁₂ H ₂₀ N ₂	4	MEDIUM			
197.106	197.107	C ₁₃ H ₁₂ N ₂	9	MEDIUM			
199.122	199.123	C ₁₃ H ₁₄ N ₂	8	LOW			
200.106	200.107	C ₁₃ H ₁₃ ON	8	MEDIUM			
201.137	201.139	C ₁₃ H ₁₆ N ₂	7	MEDIUM			
202.085	202.086	C ₁₂ H ₁₁ O ₂ N	8	MEDIUM			(Laskin et al., 2009)
203.117	203.118	C ₁₂ H ₁₄ ON ₂	7	MEDIUM			
203.153	203.154	C ₁₃ H ₁₈ N ₂	6	MEDIUM			
205.085	205.086	C ₁₂ H ₁₂ O ₃	7	MEDIUM			
207.184	207.186	C ₁₃ H ₂₂ N ₂	4	MEDIUM			
209.079	209.081	C ₁₁ H ₁₂ O ₄	6	MEDIUM			
209.200	209.201	C ₁₃ H ₂₄ N ₂	3	MEDIUM			
211.095	211.096	C ₁₁ H ₁₄ O ₄	5	HIGH	Syringylethanone/ trimethoxyphenyl- ethanone	(Simoneit et al., 1993)	
211.121	211.123	C ₁₄ H ₁₄ N ₂	9	MEDIUM			

Observed <i>m/z</i>	Calculated <i>m/z</i>	Chemical formula of neutral species	DBE	Relative average abundance	Tentative assignment(s)	References
213.137	213.139	C ₁₄ H ₁₆ N ₂	8	MEDIUM		(Laskin et al., 2009)
214.121	214.123	C ₁₄ H ₁₅ ON	8	MEDIUM		
215.153	215.154	C ₁₄ H ₁₈ N ₂	7	MEDIUM		
216.100	216.102	C ₁₃ H ₁₃ O ₂ N	8	MEDIUM		
217.132	217.134	C ₁₃ H ₁₆ ON ₂	7	MEDIUM		
217.168	217.170	C ₁₄ H ₂₀ N ₂	6	MEDIUM		
219.100	219.102	C ₁₃ H ₁₄ O ₃	7	MEDIUM		
227.153	227.154	C ₁₅ H ₁₈ N ₂	8	MEDIUM		
229.132	229.134	C ₁₄ H ₁₆ ON ₂	8	MEDIUM		
229.168	229.170	C ₁₅ H ₂₀ N ₂	7	MEDIUM		
230.116	230.118	C ₁₄ H ₁₅ O ₂ N	8	MEDIUM		
231.147	231.149	C ₁₄ H ₁₈ ON ₂	7	LOW		
232.095	232.097	C ₁₃ H ₁₃ O ₃ N	8	MEDIUM		
235.095	235.096	C ₁₃ H ₁₄ O ₄	7	MEDIUM		
241.168	241.170	C ₁₆ H ₂₀ N ₂	8	MEDIUM		
243.147	243.149	C ₁₅ H ₁₈ ON ₂	8	MEDIUM		
243.184	243.186	C ₁₆ H ₂₂ N ₂	7	LOW		
244.131	244.133	C ₁₅ H ₁₇ O ₂ N	8	MEDIUM		
246.111	246.112	C ₁₄ H ₁₅ O ₃ N	8	MEDIUM		
249.110	249.112	C ₁₄ H ₁₆ O ₄	7	MEDIUM		

3.3.4 Compounds found exclusively in the emissions from brushwood/*chulha* cook fires

Table 3.3 lists the compounds observed exclusively in the samples from brushwood/*chulha* cook fires. Many of them correspond to lignin-derived products that have been previously identified in BBOA by gas chromatography methods, as indicated in Table 3.3 (Lee et al., 2005; Simoneit, 2002; Simoneit et al., 1993; Smith et al., 2009). Lignin is an essential component of wood comprising roughly a third of its dry mass (Collard and Blin, 2014; Simoneit, 2002). Lignin is generally composed of *p*-coumaryl, coniferyl, and syringyl alcohol units. During pyrolysis, the coumaryl, vanillyl, and syringyl moieties, respectively, are preserved and are found in smoke. More generally, the lignin pyrolysis products found in smoke contain a benzene ring often with hydroxy and/or methoxy substituents. Based on these previous observations, and the assumption that these are lignin pyrolysis products, tentative molecular structures were assigned to $C_xH_yO_z$ compounds. It is likely that some $C_xH_yO_z$ molecular species specific to the emissions from the brushwood burning were not detected in this study due to their low ionization efficiency.

Table 3.3. List of reproducible compounds found exclusively in the brushwood samples. Tentative molecular structure assignments are listed when the compound has previously been identified in the chemical biomass-burning literature. Normalized, relative peak abundances are designated LOW (<1%), MEDIUM (1-9%), High (10-100%). All species were detected as protonated ions.

Observed <i>m/z</i>	Calculated <i>m/z</i>	Chemical formula of neutral species	DBE	Relative average abundance	Tentative assignment(s)	References
123.043	123.044	C ₇ H ₆ O ₂	5	MEDIUM	Benzoic acid/hydroxybenzaldehyde	(Smith et al., 2009)
153.054	153.055	C ₈ H ₈ O ₃	5	MEDIUM	Vanillin/anisic acid	(Simoneit, 2002; Simoneit et al., 1993)
195.100	195.102	C ₁₁ H ₁₄ O ₃	5	MEDIUM	Dimethoxyphenylacetone	(Simoneit et al., 1993)
197.080	197.081	C ₁₀ H ₁₂ O ₄	5	LOW	Acetosyringone	(Simoneit et al., 1993)
207.100	207.102	C ₁₂ H ₁₄ O ₃	6	MEDIUM		
236.126	236.128	C ₁₃ H ₁₇ O ₃ N	6	MEDIUM		
335.147	335.149	C ₁₈ H ₂₂ O ₆	8	LOW	Disyringyl	(Simoneit, 2002)

3.3.5 Species unique to dung smoke PM_{2.5}

Overall, the chemical composition of PM_{2.5} samples of dung-burning emissions was observed to be far more complex than the samples from the brushwood-burning cook fires. Table 3.4 lists the 115 compounds found exclusively and reproducibly in the dung-fueled samples. These compounds are largely C_xH_yN_w, as shown in Figure 3.3B. Only a few of the elemental formulas, C₈H₁₆N₂, C₁₁H₈N₂, and C₁₃H₁₁ON, have been reported previously (Laskin et al., 2009; Smith et al., 2009).

Table 3.4: List of compounds found exclusively in the emissions from dung cookfires, regardless of stove type. The labels for the peak abundances are the same as in Table 3.2. All species were detected as protonated ions unless otherwise noted.

Observed <i>m/z</i>	Calculated <i>m/z</i>	Chemical formula of neutral species	DBE	Relative average abundance
124.099	124.099	C ₇ H ₁₂ N ₂ [*]	3	MEDIUM
135.08	135.08	C ₉ H ₁₀ O	5	LOW
135.092	135.092	C ₈ H ₁₀ N ₂	5	MEDIUM
136.076	136.076	C ₈ H ₉ ON	5	LOW
137.071	137.071	C ₇ H ₈ ON ₂	5	MEDIUM
138.115	138.115	C ₈ H ₁₄ N ₂ [*]	3	LOW
141.138	141.139	C ₈ H ₁₆ N ₂	2	LOW
145.076	145.076	C ₉ H ₈ N ₂	7	MEDIUM
146.06	146.06	C ₉ H ₇ ON	7	MEDIUM
146.084	146.084	C ₉ H ₁₀ N ₂ [*]	6	LOW
149.071	149.071	C ₈ H ₈ ON ₂	6	LOW
149.107	149.107	C ₉ H ₁₂ N ₂	5	LOW
151.086	151.087	C ₈ H ₁₀ ON ₂	5	LOW
152.107	152.107	C ₉ H ₁₃ ON	4	LOW
152.13	152.131	C ₉ H ₁₆ N ₂ [*]	3	LOW
155.154	155.154	C ₉ H ₁₈ N ₂	2	LOW
160.099	160.099	C ₁₀ H ₁₂ N ₂ [*]	6	LOW
162.091	162.091	C ₁₀ H ₁₁ ON	6	LOW
163.086	163.087	C ₉ H ₁₀ ON ₂	6	MEDIUM
163.123	163.123	C ₁₀ H ₁₄ N ₂	5	MEDIUM
164.107	164.107	C ₁₀ H ₁₃ ON	5	LOW
169.076	169.076	C ₁₁ H ₈ N ₂	9	HIGH
169.17	169.17	C ₁₀ H ₂₀ N ₂	2	MEDIUM
171.091	171.092	C ₁₁ H ₁₀ N ₂	8	MEDIUM
172.075	172.076	C ₁₁ H ₉ ON	8	MEDIUM
175.086	175.087	C ₁₀ H ₁₀ ON ₂	7	MEDIUM
176.07	176.071	C ₁₀ H ₉ O ₂ N	7	LOW
176.107	176.107	C ₁₁ H ₁₃ ON	6	LOW
176.118	176.118	C ₁₀ H ₁₃ N ₃	6	LOW
178.086	178.086	C ₁₀ H ₁₁ O ₂ N	6	LOW
184.075	184.076	C ₁₂ H ₉ ON	9	MEDIUM
185.107	185.107	C ₁₂ H ₁₂ N ₂	8	MEDIUM

Observed <i>m/z</i>	Calculated <i>m/z</i>	Chemical formula of neutral species	DBE	Relative average abundance
187.086	187.087	C ₁₁ H ₁₀ ON ₂	8	MEDIUM
188.118	188.118	C ₁₁ H ₁₃ N ₃	7	LOW
189.091	189.091	C ₁₂ H ₁₂ O ₂	7	LOW
190.086	190.086	C ₁₁ H ₁₁ O ₂ N	7	MEDIUM
190.133	190.134	C ₁₁ H ₁₅ N ₃	6	MEDIUM
191.081	191.082	C ₁₀ H ₁₀ O ₂ N ₂	7	LOW
192.102	192.102	C ₁₁ H ₁₃ O ₂ N	6	LOW
193.133	193.134	C ₁₁ H ₁₆ ON ₂	5	LOW
195.091	195.092	C ₁₃ H ₁₀ N ₂	10	MEDIUM
195.185	195.186	C ₁₂ H ₂₂ N ₂	3	HIGH
197.201	197.201	C ₁₂ H ₂₄ N ₂	2	MEDIUM
198.091	198.091	C ₁₃ H ₁₁ ON	9	MEDIUM
198.102	198.103	C ₁₂ H ₁₁ N ₃	9	LOW
199.086	199.087	C ₁₂ H ₁₀ ON ₂	9	MEDIUM
200.118	200.118	C ₁₂ H ₁₃ N ₃	8	LOW
201.102	201.102	C ₁₂ H ₁₂ ON ₂	8	MEDIUM
202.122	202.123	C ₁₃ H ₁₅ ON	7	LOW
202.133	202.134	C ₁₂ H ₁₅ N ₃	7	LOW
204.101	204.102	C ₁₂ H ₁₃ O ₂ N	7	LOW
204.149	204.15	C ₁₂ H ₁₇ N ₃	6	MEDIUM
205.097	205.097	C ₁₁ H ₁₂ O ₂ N ₂	7	LOW
205.133	205.134	C ₁₂ H ₁₆ ON ₂	6	MEDIUM
205.169	205.17	C ₁₃ H ₂₀ N ₂	5	MEDIUM
206.117	206.118	C ₁₂ H ₁₅ O ₂ N	6	LOW
207.112	207.113	C ₁₁ H ₁₄ O ₂ N ₂	6	LOW

Observed <i>m/z</i>	Calculated <i>m/z</i>	Chemical formula of neutral species	DBE	Relative average abundance
207.149	207.149	C ₁₂ H ₁₈ ON ₂	5	LOW
209.107	209.107	C ₁₄ H ₁₂ N ₂	10	MEDIUM
209.128	209.128	C ₁₁ H ₁₆ O ₂ N ₂	5	LOW
211.144	211.144	C ₁₁ H ₁₈ O ₂ N ₂	4	MEDIUM
212.106	212.107	C ₁₄ H ₁₃ ON	9	MEDIUM
212.118	212.118	C ₁₃ H ₁₃ N ₃	9	LOW
214.086	214.086	C ₁₃ H ₁₁ O ₂ N	9	MEDIUM
215.117	215.118	C ₁₃ H ₁₄ ON ₂	8	MEDIUM
216.149	216.15	C ₁₃ H ₁₇ N ₃	7	LOW
217.085	217.086	C ₁₃ H ₁₂ O ₃	8	LOW
217.097	217.097	C ₁₂ H ₁₂ O ₂ N ₂	8	MEDIUM
218.103	218.104	C ₁₀ H ₁₁ ON ₅	8	LOW
218.117	218.118	C ₁₃ H ₁₅ O ₂ N	7	LOW
218.165	218.165	C ₁₃ H ₁₉ N ₃	6	LOW
219.112	219.113	C ₁₂ H ₁₄ O ₂ N ₂	7	MEDIUM
219.149	219.149	C ₁₃ H ₁₈ ON ₂	6	LOW
219.185	219.186	C ₁₄ H ₂₂ N ₂	5	MEDIUM
221.08	221.081	C ₁₂ H ₁₂ O ₄	7	LOW
221.128	221.128	C ₁₂ H ₁₆ O ₂ N ₂	6	MEDIUM
221.201	221.201	C ₁₄ H ₂₄ N ₂	4	MEDIUM
223.122	223.123	C ₁₅ H ₁₄ N ₂	10	MEDIUM
223.216	223.217	C ₁₄ H ₂₆ N ₂	3	MEDIUM
224.107	224.107	C ₁₅ H ₁₃ ON	10	LOW
225.102	225.102	C ₁₄ H ₁₂ ON ₂	10	MEDIUM
225.138	225.139	C ₁₅ H ₁₆ N ₂	9	MEDIUM
226.122	226.123	C ₁₅ H ₁₅ ON	9	MEDIUM

Observed <i>m/z</i>	Calculated <i>m/z</i>	Chemical formula of neutral species	DBE	Relative average abundance
227.117	227.118	C ₁₄ H ₁₄ ON ₂	9	MEDIUM
228.101	228.102	C ₁₄ H ₁₃ O ₂ N	9	MEDIUM
228.138	228.138	C ₁₅ H ₁₇ ON	8	MEDIUM
230.164	230.165	C ₁₄ H ₁₉ N ₃	7	LOW
231.112	231.113	C ₁₃ H ₁₄ O ₂ N ₂	8	MEDIUM
232.133	232.133	C ₁₄ H ₁₇ O ₂ N	7	LOW
233.128	233.128	C ₁₃ H ₁₆ O ₂ N ₂	7	LOW
233.164	233.165	C ₁₄ H ₂₀ ON ₂	6	LOW
233.201	233.201	C ₁₅ H ₂₄ N ₂	5	MEDIUM
235.216	235.217	C ₁₅ H ₂₆ N ₂	4	MEDIUM
237.138	237.139	C ₁₆ H ₁₆ N ₂	10	MEDIUM
239.117	239.118	C ₁₅ H ₁₄ ON ₂	10	MEDIUM
239.153	239.154	C ₁₆ H ₁₈ N ₂	9	MEDIUM
241.133	241.134	C ₁₅ H ₁₆ ON ₂	9	MEDIUM
242.117	242.118	C ₁₅ H ₁₅ O ₂ N	9	LOW
243.112	243.113	C ₁₄ H ₁₄ O ₂ N ₂	9	LOW
244.096	244.097	C ₁₄ H ₁₃ O ₃ N	9	LOW
245.128	245.128	C ₁₄ H ₁₆ O ₂ N ₂	8	MEDIUM
245.164	245.165	C ₁₅ H ₂₀ ON ₂	7	MEDIUM
247.143	247.144	C ₁₄ H ₁₈ O ₂ N ₂	7	LOW
247.216	247.217	C ₁₆ H ₂₆ N ₂	5	MEDIUM
249.232	249.233	C ₁₆ H ₂₈ N ₂	4	MEDIUM
251.153	251.154	C ₁₇ H ₁₈ N ₂	10	LOW

Observed <i>m/z</i>	Calculated <i>m/z</i>	Chemical formula of neutral species	DBE	Relative average abundance
253.133	253.134	C ₁₆ H ₁₆ ON ₂	10	LOW
255.112	255.113	C ₁₅ H ₁₄ O ₂ N ₂	10	LOW
255.148	255.149	C ₁₆ H ₁₈ ON ₂	9	LOW
255.185	255.186	C ₁₇ H ₂₂ N ₂	8	LOW
258.112	258.112	C ₁₅ H ₁₅ O ₃ N	9	LOW
259.143	259.144	C ₁₅ H ₁₈ O ₂ N ₂	8	LOW
259.18	259.18	C ₁₆ H ₂₂ ON ₂	7	LOW
269.127	269.128	C ₁₆ H ₁₆ O ₂ N ₂	10	LOW
283.143	283.144	C ₁₇ H ₁₈ O ₂ N ₂	10	LOW

*species detected as an ion-radical

In addition to the common dung compounds listed in Table 3.4, there were compounds detected exclusively in the emissions from either dung/*chulha* cook fires (Table 3.5) or dung/*angithi* cook fires (Table 3.6). All of these compounds are nitrogen-containing, and none have been reported previously as BBOA compounds, to the best of our knowledge. However, in this section, we combine all compounds found in dung-burning cook fire PM_{2.5}, presented in Tables 2, S4.2, and S4.3, and discuss their possible molecular character.

Table 3.5: List of reproducible compounds detected exclusively in the emissions from dung/*chulha* cookfires. The labels for peak abundances are the same for Table 3.3. All species were detected as protonated ions.

Observed m/z	Calculated m/z	Chemical formula of the neutral species	DBE	Relative average abundance
260.127	260.128	$C_8H_9N_3$	8	MEDIUM
257.200	257.201	$C_6H_7N_5$	7	MEDIUM
257.164	257.165	$C_{11}H_{11}N$	8	LOW
257.128	257.128	$C_{12}H_{13}N$	9	LOW
238.133	238.134	$C_{13}H_9N$	10	MEDIUM
231.185	231.186	$C_{11}H_8ON_2$	6	MEDIUM
229.097	229.097	$C_{11}H_9O_2N$	9	LOW
211.086	211.087	$C_{14}H_{11}ON$	10	LOW
210.091	210.091	$C_{13}H_{10}ON_2$	10	LOW
188.070	188.071	$C_{13}H_{12}O_2N_2$	8	LOW
185.071	185.071	$C_{15}H_{22}N_2$	9	MEDIUM
180.081	180.081	$C_{15}H_{15}N_3$	10	LOW
172.112	172.112	$C_{15}H_{16}O_2N_2$	7	LOW
158.096	158.096	$C_{16}H_{20}ON_2$	7	MEDIUM
150.077	150.077	$C_{17}H_{24}N_2$	6	LOW
148.087	148.087	$C_{15}H_{17}O_3N$	6	LOW

Table 3.6: List of reproducible compounds detected exclusively in the emissions from dung/*angithi* cookfires. The labels for peak abundances are the same for Table 3.3. All species were detected as protonated ions, except for C₁₂H₁₃ON, which was detected as a [M+Na]⁺ ion.

Observed <i>m/z</i>	Calculated <i>m/z</i>	Chemical formula of the neutral species	DBE	Relative average abundance
110.060	110.060	C ₆ H ₇ ON	4	MEDIUM
139.086	139.087	C ₇ H ₁₀ ON ₂	4	LOW
148.075	148.076	C ₉ H ₉ ON	6	LOW
150.091	150.091	C ₉ H ₁₁ ON	5	LOW
153.102	153.102	C ₈ H ₁₂ ON ₂	4	LOW
164.082	164.082	C ₈ H ₉ ON ₃	6	LOW
165.077	165.077	C ₇ H ₈ ON ₄	6	LOW
165.102	165.102	C ₉ H ₁₂ ON ₂	5	LOW
167.118	167.118	C ₉ H ₁₄ ON ₂	4	LOW
168.065	168.066	C ₈ H ₉ O ₃ N	5	LOW
169.097	169.097	C ₈ H ₁₂ O ₂ N ₂	4	LOW
174.102	174.103	C ₁₀ H ₁₁ N ₃	7	LOW
178.097	178.097	C ₉ H ₁₁ ON ₃	6	LOW
178.122	178.123	C ₁₁ H ₁₅ ON	5	LOW
179.118	179.118	C ₁₀ H ₁₄ ON ₂	5	LOW
180.101	180.102	C ₁₀ H ₁₃ O ₂ N	5	LOW
181.097	181.097	C ₉ H ₁₂ O ₂ N ₂	5	LOW
182.081	182.081	C ₉ H ₁₁ O ₃ N	5	LOW
190.122	190.123	C ₁₂ H ₁₅ ON	6	LOW
192.113	192.113	C ₁₀ H ₁₃ ON ₃	6	LOW
195.112	195.113	C ₁₀ H ₁₄ O ₂ N ₂	5	LOW
197.128	197.128	C ₁₀ H ₁₆ O ₂ N ₂	4	LOW
198.127	198.128	C ₁₄ H ₁₅ N	8	LOW
204.113	204.113	C ₁₁ H ₁₃ ON ₃	7	LOW
206.128	206.129	C ₁₁ H ₁₅ ON ₃	6	LOW
208.144	208.144	C ₁₁ H ₁₇ ON ₃	5	LOW
209.164	209.165	C ₁₂ H ₂₀ ON ₂	4	LOW
210.088	210.089	C ₁₂ H ₁₃ ON ^a	7	LOW
213.102	213.102	C ₁₃ H ₁₂ ON ₂	9	MEDIUM
216.113	216.113	C ₁₂ H ₁₃ ON ₃	8	LOW
216.138	216.138	C ₁₄ H ₁₇ ON	7	LOW
220.144	220.144	C ₁₂ H ₁₇ ON ₃	6	LOW

Observed <i>m/z</i>	Calculated <i>m/z</i>	Chemical formula of the neutral species	DBE	Relative average abundance
221.164	221.165	C ₁₃ H ₂₀ ON ₂	5	LOW
222.160	222.160	C ₁₂ H ₁₉ ON ₃	5	LOW
223.180	223.180	C ₁₃ H ₂₂ ON ₂	4	LOW
230.128	230.129	C ₁₃ H ₁₅ ON ₃	8	LOW
231.185	231.186	C ₁₅ H ₂₂ N ₂	6	MEDIUM
232.144	232.144	C ₁₃ H ₁₇ ON ₃	7	LOW
232.180	232.181	C ₁₄ H ₂₁ N ₃	6	LOW
234.159	234.160	C ₁₃ H ₁₉ ON ₃	6	LOW
235.143	235.144	C ₁₃ H ₁₈ O ₂ N ₂	6	LOW
237.232	237.233	C ₁₅ H ₂₈ N ₂	3	LOW
238.122	238.123	C ₁₆ H ₁₅ ON	10	MEDIUM
240.138	240.138	C ₁₆ H ₁₇ ON	9	MEDIUM
242.153	242.154	C ₁₆ H ₁₉ ON	8	LOW
244.180	244.181	C ₁₅ H ₂₁ N ₃	7	LOW
245.200	245.201	C ₁₆ H ₂₄ N ₂	6	LOW
247.179	247.180	C ₁₅ H ₂₂ ON ₂	6	LOW
248.175	248.176	C ₁₄ H ₂₁ ON ₃	6	LOW
249.123	249.123	C ₁₃ H ₁₆ O ₃ N ₂	7	LOW
254.117	254.118	C ₁₆ H ₁₅ O ₂ N	10	LOW
263.247	263.248	C ₁₇ H ₃₀ N ₂	4	LOW
267.148	267.149	C ₁₇ H ₁₈ ON ₂	10	LOW
269.164	269.165	C ₁₇ H ₂₀ ON ₂	9	LOW
271.180	271.180	C ₁₇ H ₂₂ ON ₂	8	LOW
272.127	272.128	C ₁₆ H ₁₇ O ₃ N	9	LOW
273.159	273.160	C ₁₆ H ₂₀ O ₂ N ₂	8	LOW
274.106	274.107	C ₁₅ H ₁₅ O ₄ N	9	LOW
275.138	275.139	C ₁₅ H ₁₈ O ₃ N ₂	8	LOW
283.216	283.217	C ₁₉ H ₂₆ N ₂	8	LOW
287.138	287.139	C ₁₆ H ₁₈ O ₃ N ₂	9	LOW
299.138	299.139	C ₁₇ H ₁₈ O ₃ N ₂	10	LOW

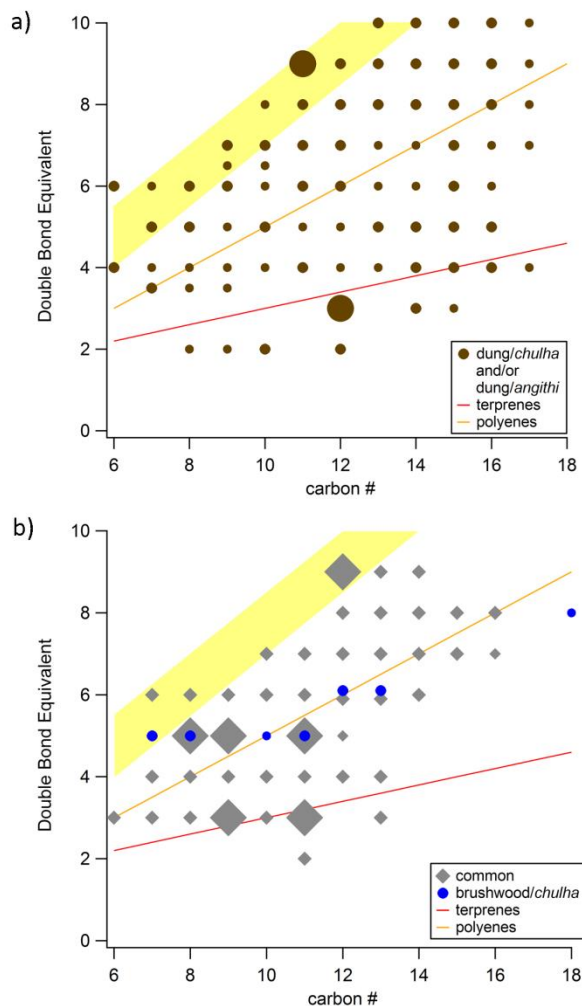


Figure 3.6: Double bond equivalent (DBE) as a function of the carbon number for a) a combined set of compounds detected from all dung cookfires (brown circle) and b) compounds all cookfires have in common (grey diamond) as well as compounds exclusively found in brushwood (blue circle). Markers representing one or multiple species are sized by their LOW, MEDIUM, and HIGH designations. The curves illustrate theoretically where terpenes (red) and polyenes (green) would fall. Similarly, the yellow-shaded region shows where PAHs would appear, including: cata-condensed PAHs with 0, 1, and 2 heterocyclic nitrogen atoms and circular PAHs.

Figure 3.6 shows the double bond equivalent (DBE) as a function of the carbon number of compounds detected in all investigated samples. The DBE versus C dependence for classes of compounds with different degrees of unsaturation, including: terpenes (red), polyenes (orange), polycyclic aromatic hydrocarbons (yellow shaded, PAHs) are also shown to aid the classification

of the compounds observed in the PM_{2.5} samples. Thirty of the 193 formulas fall in the PAH region of the plot suggesting that they have aromatic structures (Figure 3.6a). Figure 3.6b compares the DBE values of the molecular components detected in the emissions exclusive to brushwood/*chulha* cook fires (Table 3.3) and the common compounds from all studied samples (Table 3.2). In general, the DBE increases with carbon number for the compounds common to all cook fires. Only eight of the 87 compounds fall directly in the PAH region. There are more aromatic structures specific to the dung smoke compared to the compounds detected in all cook fires.

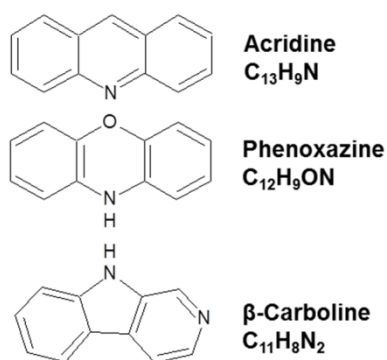


Figure 3.7: Possible structures of N-heterocyclic PAHs found in dung cookfire emissions. C₁₃H₉N was detected reproducibly in dung/*chulha* emissions only, while C₁₂H₉ON and C₁₁H₈N₂ were reproducibly detected in all dung cookfires.

Detected nitrogen compounds with high DBE values are likely N-heterocyclic PAH compounds. Figure 3.7 displays possible structures for the select detected nitrogen-containing compounds with a high DBE. Purcell et al. (2007) found that pyridinic PAH compounds were readily ionized from standard mixtures of N-heterocyclics in positive-ion ESI. This gives us more confidence in our observation of C₁₃H₉N, tentatively acridine, and C₁₁H₈N₂, tentatively β-carboline, which have pyridinic nitrogen atoms and likely have high ionization efficiencies. The peak abundances of these compounds are significant, with medium and high designations,

respectively. $C_{12}H_9ON$ cannot have a pyridinic nitrogen and is tentatively assigned as phenoxazine.

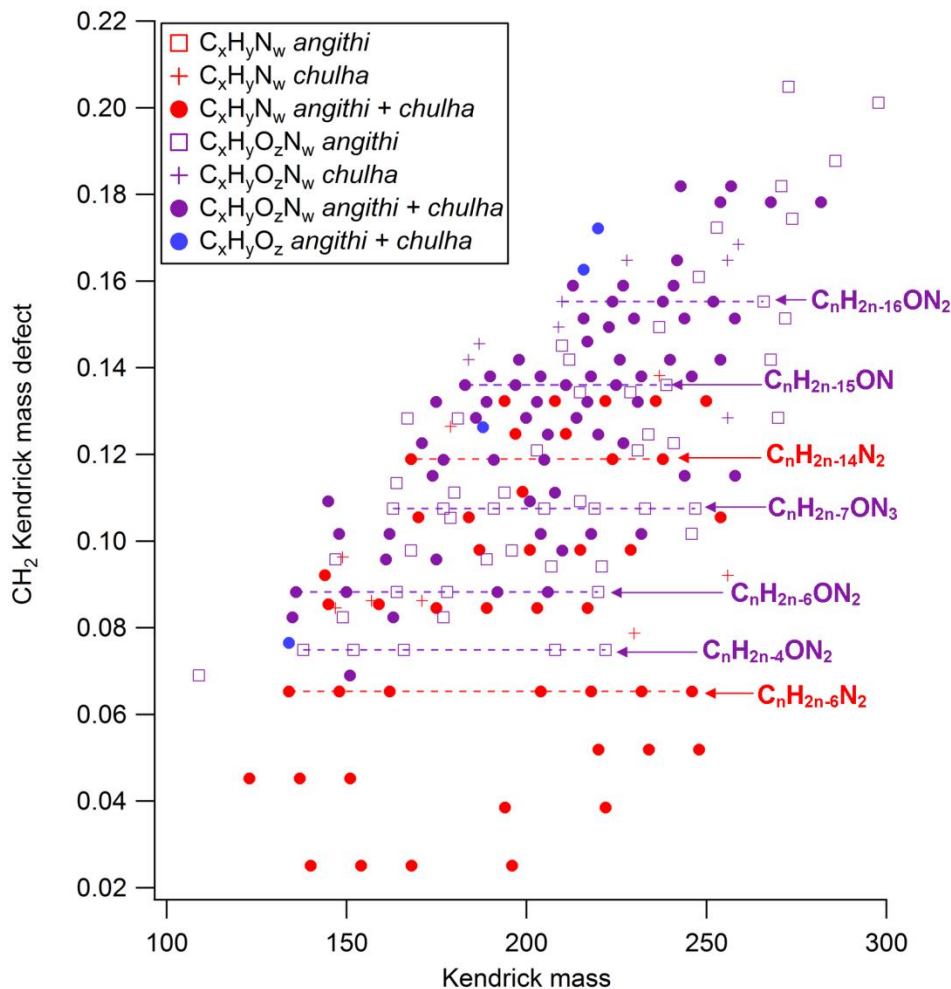


Figure 3.8: The CH_2 Kendrick mass defect plot for compounds emitted only from dung stoves. The marker color determines the compound category for $C_xH_yN_w$ compounds (red), $C_xH_yO_z$ (blue), or $C_xH_yO_zN_w$ (purple). Marker shape indicates the stove(s) that reproducibly produced the compound: *chulha* and *angithi* (\bullet), *angithi* (\square), or *chulha* ($+$). Homologous series are identified with dotted horizontal lines suggesting they have similar structures.

Kendrick analysis identifies homologous series of structurally-related compounds that share a core formula and differ in the number (n) of additional CH_2 units (Hughey et al., 2001). 172 of the 193 detected compounds from the dung-burning cook fire emissions can be grouped into 43 homologous series based on the Kendrick mass defect plot, as shown in Figure 3.8. There

are 15 homologous series and 5 independent formulas that make up the 61 total $C_xH_yN_w$ (red) compounds. This suggests that there are at least 20 distinct types of structures that made up the observed $C_xH_yN_w$ species. Similarly, there are 30 homologous series for $C_xH_yO_zN_w$ (purple) formulas and 12 $C_xH_yO_zN_w$ formulas yielding at least 42 distinct types of structures for this formula category. There are no homologous series from $C_xH_yO_z$ species, presumably because only a few members of this group can be detected by ESI-based methods in the $PM_{2.5}$ from the dung cook fires. From this analysis, there are at least 66 unique types of structures from the 193 compounds detected from dung-burning cook fire emissions. This Kendrick analysis suggests that some of the observed N-heterocyclic PAHs have alkyl substituents. For example, phenoxazine and β -carboline (Figure 3.7) serve as the core molecules in the homologous series $C_nH_{2n-15}ON$ and $C_nH_{2n-14}N_2$, respectively (Figure 3.8).

3.3.6 Light-absorbing properties and chromophores from cookstove emissions

Figure 3.9 show MAC_{bulk} values, which represent bulk absorption coefficient normalized by mass concentration of organic solvent extractable components. Sample information is given in Table 3.7. The MAC_{bulk} values were determined assuming that 50 percent of the particle mass could be extracted from the filter. Error bars account for the uncertainties in the extraction efficiency (relative error 40%), and flows during sample collection (relative error 10%). MAC_{bulk} values for the samples from the brushwood burning are roughly twice that of dung between 300-580 nm. Assuming higher EC/OC for wood compared to dung as reported in Jayarathne et al., 2017, the results are consistent with Saleh et al., 2014, who predict higher effective OA absorbance for higher BC to OA ratios.

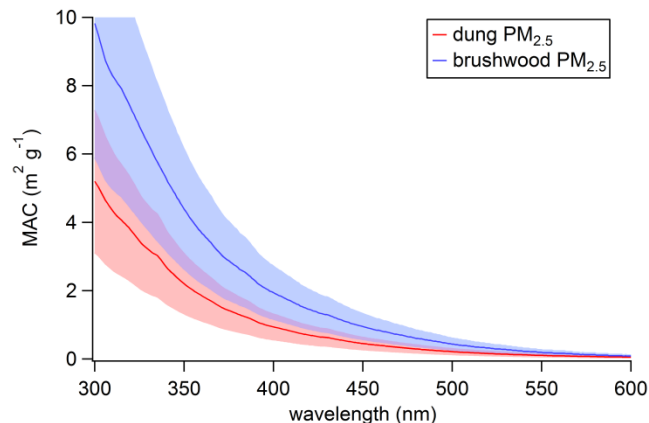


Figure 3.9: Comparing MAC_{bulk} ($\text{m}^2 \text{g}^{-1}$) for organic solvent extractable material from brushwood/*chulha* (blue) and dung/*chulha* (red) samples. Shaded regions represent errors due to extraction efficiency and sampling flow rates.

MAC_{bulk} values at 400 nm were $1.9 \pm 0.8 \text{ m}^2 \text{g}^{-1}$ and $0.9 \pm 0.4 \text{ m}^2 \text{g}^{-1}$ for the samples from brushwood/*chulha* and dung/*chulha* cook fires, respectively. For comparison, Kirchstetter and colleagues reported MAC_{bulk} of $2.9 \text{ m}^2 \text{g}^{-1}$ at 400 nm for the BrC in biomass smoke samples (Kirchstetter et al., 2004). Chen and Bond measured MAC_{bulk} values at 360 nm of nearly $2.0 \text{ m}^2 \text{g}^{-1}$ for methanol extracts of particles resulting from oak pyrolysis, and nearly $2.5 \text{ m}^2 \text{g}^{-1}$ for pine wood pyrolysis (Chen and Bond, 2010). Our MAC_{bulk} value at 360 nm for brushwood was larger at $3.7 \pm 1.5 \text{ m}^2 \text{g}^{-1}$, possibly due to a more efficient extraction of a broader range of chromophores by the solvents utilized. The pyrolysis temperature and wood composition could also contribute to the difference. Our MAC_{bulk} value at 360 nm for dung was lower compared to our brushwood sample at $1.8 \pm 0.8 \text{ m}^2 \text{g}^{-1}$. This could be a combined result of the likely lower pyrolysis temperature and difference in the biomass composition (Chen and Bond, 2010).

While the MAC_{bulk} values are smaller for the dung/*chulha* cook fires, the $PM_{2.5}$ emission factors (a detailed analysis of the emission factors will be reported in a follow up paper) are more than a factor of 2.5 higher for dung/*chulha* fires ($21.1 \pm 4.2 \text{ g kg}^{-1} \text{ fuel}$) compared to brushwood/*chulha* fires ($7.3 \pm 1.8 \text{ g kg}^{-1} \text{ fuel}$). The product $MAC_{\text{bulk}} \times \text{EF}$ can be used to estimate

the contribution of smoke to the absorption coefficient for the per unit mass of the fuel burned. At 400 nm, $MAC_{\text{bulk}} \times EF = 19.0 \pm 9.2 \text{ m}^2 \text{ kg}^{-1}$ fuel and $13.9 \pm 6.8 \text{ m}^2 \text{ kg}^{-1}$ fuel for dung/*chulha* fires and brushwood/*chulha* fires, respectively. For particles that are small in diameter relative to the wavelength, $MAC_{\text{aerosol}} \sim 0.7 \times MAC_{\text{bulk}}$ (Laskin et al., 2015). Based on this we can estimate $MAC_{\text{aerosol}} \times EF = 13.3 \pm 6.5 \text{ m}^2 \text{ kg}^{-1}$ fuel and $9.7 \pm 4.8 \text{ m}^2 \text{ kg}^{-1}$ fuel for dung/*chulha* fires and brushwood/*chulha* fires, respectively. The values are somewhat higher than the “EF B_{abs} 405 just BrC” values reported by Stockwell et al., 2016 at 405 nm, which were $8.40 \text{ m}^2 \text{ kg}^{-1}$ fuel and $5.43 \text{ m}^2 \text{ kg}^{-1}$ fuel for hardwood cooking smoke and dung cooking smoke, respectively. However, both the present results and the data from Stockwell et al., (2016) show that the dung-based and wood-based fuels make comparable contributions to the absorption coefficient of the smoke for same amount of fuel consumed.

Table 3.7: Samples utilized in section 3.3.6 for MAC and AAE analyses.

Sample	Date	Fuel	Stove	Moisture (% wet basis)	Meal
D2	8/8/2015	dung	chulha	8.3 ^a	chapati
N6	8/26/16	brushwood	chulha	13.9	rice

^a Dung moisture content was measured using a commercial moisture probe, and converted to a real value, moisture on a % wet basis, using Gautam et al., 2016.

The AAE values for the extractable organics in brushwood and dung samples are 7.5 and 6.8, respectively. Our brushwood AAE fits into the lower end of the AAE range for extracted organics presented in Chen and Bond, 6.9 to 11.4 (Chen and Bond, 2010). Typical AAE values cited in the literature for BrC in BBOA are in a range of 2-11 (Kirchstetter et al., 2004; Laskin et al., 2015). The AAE of the entire cooking aerosol (with the contribution of the insoluble BC included) should be lower. For example, Stockwell et al., 2016 reported in situ measurements of AAE of 3.01 and 4.63 for brushwood and dung cooking particles, respectively.

We now focus on identifying selected chromophores that contribute to the high MAC_{bulk} we observe for cookstove $PM_{2.5}$. Two cook fires using dung and brushwood fuels were selected for a more detailed analysis of the light-absorbing molecules (BrC chromophores). The dung cook fire utilized an *angithi* cookstove to prepare buffalo food. The brushwood cook fire was used to prepare a traditional meal of rice and lentils with a *chulha*. More detailed sample information is provided in Table 3.8. The samples were analyzed using HPLC-PDA-ESI/HRMS platform following the methods described elsewhere (Lin et al., 2015, 2016, 2017). The identified chromophores and their PDA chromatograms are illustrated in Figure 3.10, and the retention times and peaks in the absorption spectra are listed in Tables 3 and 4 for the emissions from brushwood and dung cook fires, respectively.

Table 3.8: Samples analyzed in section 3.3.6 via HPLC-PDA-HRMS.

Sample	Date	Fuel	Stove	Moisture (% wet basis)	Meal
RE015	8/28/15	brushwood	chulha	29.5	rice
T2	8/18/15	dung	angithi	10.8 ^a	buffalo fodder

^a Dung moisture content was measured using a commercial moisture probe, and converted to a real value, moisture on a % wet basis, using Gautam et al., 2016.

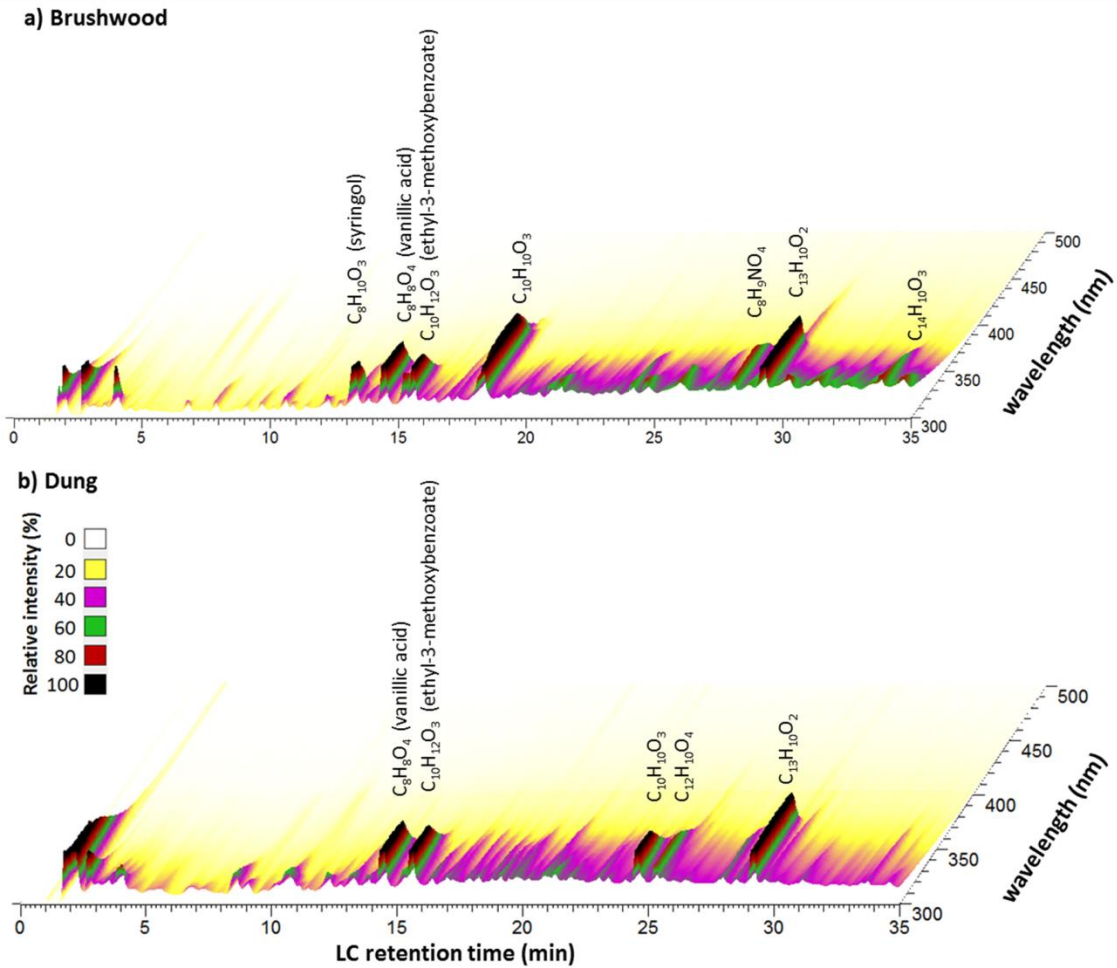


Figure 3.10: HPLC-PDA chromatogram showing BrC chromophores detected in the emission samples from a) brushwood and b) dung cookfires. Highly-absorbing molecules and their corresponding PDA retention times are given above the peak.

Table 3.9: The list of retention times, absorption peak maxima, and chemical formulas of the BrC chromophores detected in the brushwood smoke sample. Tentative assignments are given based on compounds previously identified in the lignin pyrolysis literature.

LC retention time (min)	λ_{\max} (nm)	Nominal molecular weight (amu)	Chemical formula(s)	Tentative assignment
6.26	383	192	C ₉ H ₈ N ₂ O ₃	
7.15	392	141	C ₇ H ₈ O ₃	
10.55	305	183	C ₉ H ₁₀ O ₄	Homovanillic acid/syringaldehyde
13.29	265	155	C ₈ H ₁₀ O ₃	Syringol
14.44	305	169 183	C ₈ H ₈ O ₄ C ₉ H ₁₀ O ₄	Vanillic acid Homovanillic acid/syringaldehyde
15.57	299	181 167	C ₁₀ H ₁₂ O ₃ C ₉ H ₁₀ O ₃	Ethyl-3-methoxybenzoate Veratraldehyde
16.95	313, 334	186	C ₁₁ H ₇ NO ₂	
17.25	331	165 162	C ₉ H ₈ O ₃ C ₉ H ₇ NO ₂	
18.13	341	209	C ₁₁ H ₁₂ O ₄	
18.32	229, 337	179	C ₁₀ H ₁₀ O ₃	
19.78	305, 330	194	C ₁₀ H ₁₀ O ₄	Ferulic acid
24.11	290, 330	259	C ₁₅ H ₁₄ O ₄	
28.07	334	184	C ₈ H ₉ NO ₄	
29.24	330	198 230	C ₁₃ H ₁₀ O ₂ C ₁₃ H ₁₀ O ₄	
33.81	340	227	C ₁₄ H ₁₀ O ₃	

Table 3.10: The list of retention times, absorption peak maxima, and chemical formulas of the BrC chromophores detected in the the dung smoke sample. Tentative assignments are given based on compounds previously identified in the lignin pyrolysis literature.

LC retention time (min)	λ_{\max} (nm)	Nominal molecular weight (amu)	Chemical formula(s)	Tentative assignment
8.50	295	167	C ₈ H ₉ NO ₃	
9.09	282,300	166 168	C ₉ H ₁₀ O ₃ C ₈ H ₈ O ₄	
10.59	252, 289, 393	182	C ₉ H ₁₀ O ₄	Homovanillic acid/syringaldehyde
12.22	282	122	C ₇ H ₆ O ₂	Benzoic acid
14.44	306	168 182 164	C ₈ H ₈ O ₄ C ₉ H ₁₀ O ₄ C ₉ H ₈ O ₃	Vanillic acid Homovanillic acid/syringaldehyde
15.57	300	174 166	C ₁₀ H ₁₂ O ₃ C ₉ H ₁₀ O ₃	Ethyl-3-methoxybenzoate Veratraldehyde
16.35	286	174	C ₁₁ H ₁₀ O ₂	
18.28	290, 330 ^a	162	C ₁₀ H ₁₀ O ₂	
19.5	323 ^a	220	C ₁₂ H ₁₂ O ₄	
19.72	331 ^a	194	C ₁₀ H ₁₀ O ₄	Ferulic acid
20.85	352 ^a	188	C ₁₂ H ₁₂ O ₂	
24.54	299, 308	178	C ₁₀ H ₁₀ O ₃	
25.28	290, 320	218	C ₁₂ H ₁₀ O ₄	
29.17	332	198 230	C ₁₃ H ₁₀ O ₂ C ₁₃ H ₁₀ O ₄	
29.60	358 ^a	213	C ₁₃ H ₉ O ₃	

^a signifies a shoulder, rather than a clear peak

The BrC chromophores for both brushwood and dung samples are largely C_xH_yO_z compounds (Tables 3 and 4). We conclude that lignin-derived BrC chromophores account for the majority of the extracted light-absorbing compounds in both samples. We also found a few nitrogen-containing BrC chromophores (e.g., C₉H₇NO₂ and C₈H₉NO₃) in both the brushwood and dung samples. The woody and digested biomasses shared 3 strongly-absorbing chromophores, C₈H₈O₄ (tentatively vanillic acid), C₁₀H₁₂O₃ (tentatively ethyl methoxybenzoate), and C₁₃H₁₀O₂, as well as comparably weaker-absorbing chromophores.

C₁₀H₁₀O₃ is another strong absorber of near-UV radiation that was found in both samples. In the brushwood-derived PM_{2.5}, C₁₀H₁₀O₃ elutes at 18.3 min (λ_{\max} = 337 nm), while in the dung smoke sample, it is not observed until 24.5 min (λ_{\max} = 299, 308 nm). These are clearly different

chromophores with the same chemical formula, possibly coniferaldehyde and methoxycinnamic acid. $C_9H_8O_3$ is a similar case, in which the same chemical formula appears at different retention times in the selected ion chromatograms (SICs) for brushwood- and dung-derived $PM_{2.5}$. In the brushwood-derived $PM_{2.5}$ sample, $C_9H_8O_3$ coelutes with $C_9H_7NO_2$ at 17.3 min (Table 3.9). In the dung $PM_{2.5}$ sample $C_9H_8O_3$ coelutes with $C_8H_8O_4$ and $C_9H_{10}O_4$ at 14.4 min (Table 3.10). The $C_9H_8O_3$ formula could correspond to coumaric acid for either retention time. Because the compound coelutes with other potential chromophores, we refrained from assigning a proposed structure to the chemical formula.

There were light-absorbing molecules specific to brushwood-derived $PM_{2.5}$ (Table 3.9) that could account for higher MAC_{bulk} values compared to the dung-derived $PM_{2.5}$. $C_8H_9NO_4$ is a possible nitroaromatic compound with its absorbance peaking around 335 nm. $C_8H_{10}O_3$, tentatively syringol, is closely related to syringic acid, a lignin monomer. The formula was also detected in the dung-derived $PM_{2.5}$ sample, but the absorption was lower by approximately a factor of 20 and therefore is not considered a main chromophore.

There were strongly-absorbing BrC chromophores in the $PM_{2.5}$ generated by burning dung fuel that eluted in the first couple of minutes of the sample run (See Figure 3.10b). These early-eluting chromophores were likely polar compounds that were not retained well by the column and thus could not be assigned. The challenges with assigning co-eluting chromophores in BBOA were previously noted by Lin et al., 2016. For both $PM_{2.5}$ samples, most of the chromophores eluted in the first 30 minutes of the run shown in Figure 3.10. Compounds eluting in the range of 30 to 60 min were also satisfactorily separated, but these were weakly absorbing. The non-polar PAH compounds absorbing in UV-Vis range are not ionized by the ESI source and subsequently not detected by HRMS (Lin et al., 2016). It is possible that additional light-

absorbing molecules essential to dung smoke were strongly retained by the column and eluted after 60 min.

Absorption spectra recorded in tandem with the mass spectra provide additional constraints on the assignments. For example, at 15.6 minutes $C_{10}H_{12}O_3$ and $C_9H_{10}O_3$ coeluted in both BBOA samples. These compounds were given the tentative assignments of ethyl-3-methoxybenzoate and veratraldehyde, respectively. The UV-Vis absorbance of ethyl-3-methoxybenzoate shown in Figure 3.11 provides a reasonable match for the recorded PDA spectra for both samples at a retention time of 15.6 min. Veratraldehyde, which is derived broadly from lignin, has an absorption spectrum that peaks at 308 nm in aqueous solution (Anastasio et al., 1997). Therefore, both ethyl-3-methoxybenzoate and veratraldehyde contribute to the spectrum observed by the PDA detector, although they cannot be completely separated with this HPLC protocol.

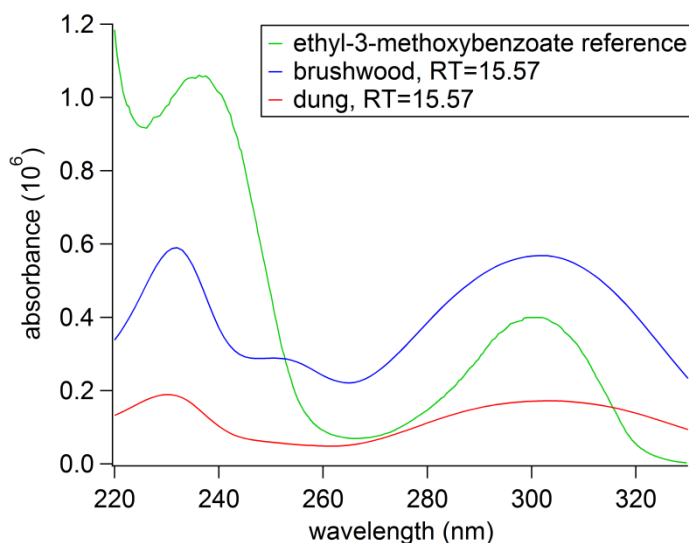


Figure 3.11: UV-Vis absorption spectra from the PDA analysis of cookstove BBOA samples. The blue and red curves represent the background-subtracted absorbance at retention time of 15.57 min for brushwood-derived $PM_{2.5}$ and dung-derived $PM_{2.5}$, respectively. The reference absorption spectrum of ethyl-3-methoxybenzoate (green) was reproduced from the NIST Chemistry WebBook database (Talrose et al., 2017). The structure of ethyl-3-methoxybenzoate is pictured.

For many formulas multiple structural isomers were observed in SICs with peaks appearing at more than one retention time. This behavior has been observed for other types of BBOA samples, described in Lin et al., 2016, and is inherent to lignin's nature such that a single $C_xH_yO_z$ chemical formula can correspond to multiple possible structural isomers. There are several cases in which chemical formulas show up multiple times in Tables 3-4. An example from the brushwood $PM_{2.5}$ (Table 3.9) is $C_9H_{10}O_4$ which elutes at 10.6 and 14.4 minutes. $C_9H_{10}O_4$ has been previously found in lignin pyrolysis BBOA in the forms of homovanillic acid and syringaldehyde (Simoneit et al., 1993). $C_8H_8O_4$ and $C_9H_{10}O_3$ are additional examples of the similar occurrence in the sample of dung-derived $PM_{2.5}$, as they both appear twice in the SICs as shown in Table 3.10. One peak corresponding to $C_8H_8O_4$ is very likely vanillic acid (Simoneit, 2002; Simoneit et al., 1993). $C_9H_{10}O_3$ could be either veratraldehyde or homoanisic acid, both have been observed from lignin pyrolysis (Simoneit et al., 1993). Collectively, these results indicate that many of the lignin-like chromophores have multiple structural isomers, some of which have likely been observed before (Simoneit, 2002; Simoneit et al., 1993).

3.4 Summary

Molecular analysis of $PM_{2.5}$ emissions from three types of cookstove-fuel combinations showed that the observed chemical complexity of particle composition increased in the following order: brushwood/*chulha*, dung/*chulha*, dung/*angithi*. The compounds accounting for the additional complexity in dung-derived emissions were mostly $C_xH_yO_zN_w$ and $C_xH_yN_w$ species, which have not been identified before in cookstove BBOA. A substantial portion of the compounds specific to dung cook fires appeared to be aromatic based on their degree of unsaturation. The CH_2 -Kendrick analysis of the nitrogen-containing species from dung cook fires

indicated that many may be structurally related by substitution with alkyl chains of variable length.

The estimated MAC_{bulk} values for the $PM_{2.5}$ emissions samples from brushwood/*chulha* and dung/*chulha* cook fires were comparable in magnitude and wavelength dependence to the values previously observed for BBOA samples. While the MAC_{bulk} values for the brushwood-derived BBOA were higher than those for the dung-derived BBOA, the particle emission factors had the opposite relationship. Therefore, per unit mass of burned fuel, the dung and brushwood fueled cookstoves may have comparable contribution to the overall light absorption. A set of $PM_{2.5}$ samples from brushwood/*chulha* and dung/*chulha* cook fires was analyzed using HPLC-PDA-HRMS to identify BrC chromophores. The vast majority of chromophores observed for both fuel types were lignin-like $C_xH_yO_z$ compounds. There were three retention times at which strongly-absorbing chromophores eluted for both samples: $C_8H_8O_4$ (vanillic acid), $C_{10}H_{12}O_3$ (methoxybenzoate), and $C_{13}H_{10}O_2$. There were also fuel-specific chromophores such as $C_{10}H_{10}O_3$ (distinct isomers for each fuel type), $C_8H_{10}O_3$ (syringol, brushwood), and $C_{12}H_{10}O_4$ (dung).

In this study, we characterized a wide range of particle-phase compounds produced by cookstoves, including the lignin-derived $C_xH_yO_z$ compounds that have commonly been identified in wood burning studies, and less common nitrogen-containing compounds. Specifically, from dung cook fires, we detected what we presume to be aromatic nitrogen-containing compounds with few or no oxygen atoms in them. Our inventory of chemical formulas is just the starting point for comprehensively characterizing particle-phase cookstove emissions. Future efforts should focus on the identification of compounds, precise emission factor quantification for specific compounds, evaluation of toxicity, and modeling the effect of these compounds on secondary air pollution formation in aging smoke plumes.

CHAPTER 4

Molecular composition and photochemical lifetimes of brown carbon chromophores in biomass burning organic aerosol particles generated during FIREX

Abstract. To better understand the effects of wildfires on air quality and climate, it is important to assess the occurrence of chromophoric compounds in smoke and characterize their optical properties. This study explores the molecular composition of light-absorbing organic aerosol, or brown carbon (BrC), for laboratory burns of twelve forest fire fuel types at the Missoula Fire Sciences laboratory as a part of the FIREX Fall 2016 lab intensive. Fuels span different plant types, including gymnosperm (coniferous) and angiosperm (flowering) plants, and different ecosystem components such as duff, litter, and canopy. Biomass Burning Organic Aerosol (BBOA) particles were collected onto Teflon filters and analyzed offline via high performance liquid chromatography/ photodiode array/ high resolution mass spectrometry (HPLC/PDA/HRMS). Separated BrC chromophores were classified by their retention times, absorption spectra, integrated PDA absorbance in the near-UV and visible spectral range (300-700 nm), and chemical formulas from the accurate m/z measurements. BrC chromophores were grouped into the following classes and subclasses: lignin-derived, which includes lignin pyrolysis products; distillation products, which include coumarins and flavonoids; nitroaromatics; and polycyclic aromatic hydrocarbons (PAHs). These classes/subclasses were observed across most fuel types, although specific BrC chromophores varied based on plant type (gymnosperm or angiosperm) and ecosystem component(s) burned. To study the stability of the

observed BrC compounds with respect to photodegradation, BBOA particles were irradiated directly on filters with near UV radiation, and analyzed by the HPLC/PDA/HRMS method. Lifetimes of individual BrC chromophores depended on the fuel type and the underlying combustion conditions but lignin-derived and flavonoid classes of BrC chromophores generally had the longest lifetimes with respect to UV photodegradation. Moreover, lifetimes for the same BrC chromophores varied depending on the BBOA type (created by different fuel and combustion conditions). While individual chromophores disappeared on a timescale of several days, the overall light absorption persisted longer, presumably because the photolysis processes converted one set of chromophores into another but did not lead to complete photobleaching. To model the effect of BrC on climate, it is important to understand the change in the absorption coefficient with time. We measured the equivalent atmospheric lifetimes of the overall BrC absorption coefficient which ranged from 10 to 41 days, with subalpine fir duff having the shortest lifetime, and conifer canopies having the longest lifetimes. BrC obtained from fuel loads encompassing multiple ecosystem components (duff, litter, shrub, canopy) had absorption lifetimes that fell in the middle of this range. These results indicate that photobleaching by photolysis is relatively slow. Other chemical aging mechanisms, such as heterogeneous oxidation by OH, may be more important than photolysis for predicting the decay of BBOA BrC absorption in models.

4.1 Introduction

Forests have predictable, naturally occurring wildfire cycles that have benefits for the forest ecosystem, but global climate change is accelerating the cycle (Shvidenko and Schepaschenko, 2013; Weber and Stocks, 1998). In addition to the impacts of wildfires on ecosystems, biomass burning plumes have pronounced effects on atmospheric chemistry and climate. Wildfires are expected to continue increasing in frequency and intensity worldwide with climate change (Boulanger et al., 2014; Moriondo et al., 2006; Shvidenko and Schepaschenko, 2013; Wotton et al., 2010; Wotton and Flannigan, 1993). Wildfire plumes are a complex mixture of greenhouse gases CO₂ and methane, multiple volatile organic compounds (VOCs), and carbonaceous particles. The warming effects of greenhouse gases and black carbon are relatively well-constrained in models. However, effects arising from biomass burning organic aerosol (BBOA) particles are not well understood because their composition and optical properties depend on many factors, such as the fuel burned and combustion conditions (Chen and Bond, 2010; Jen et al., 2019; Kirchstetter et al., 2004), wind direction and speed (Surawski et al., 2015), and fuel moisture content (Tihay-Felicelli et al., 2017). Global climate models are starting to include contributions from light-absorbing organic carbon, termed brown carbon (BrC), because treating BBOA particles as purely scattering leads to incorrect predictions of climate forcing (Laskin et al., 2015). One of the first studies incorporating BrC into models was by Feng et al. (2013), which found that in areas where primary BrC emissions are high, the absorbing component of BBOA particles can dominate over the scattering component, switching net radiative forcing by organic aerosols from negative (cooling) to positive (warming) at the top of the atmosphere. Other modeling studies have demonstrated that BrC can have large effects on the radiative forcing, as reviewed by Laskin et al. (2015). To better quantify their effect on

climate, the physical absorption properties and chemical composition of a broader range of BrC and BBOA particles should be studied.

Previous studies have identified important classes of molecules in BBOA particles that are responsible for light absorption. A major class includes lignin-pyrolysis products, which are typically substituted aromatics with a high degree of unsaturation, such as coniferaldehyde (Budisulistiorini et al., 2017; Fleming et al., 2018; Simoneit et al., 1993). Another class is nitroaromatics, such as nitrocatechols, which are readily produced under flaming conditions (in the presence of NO_x) and absorb strongly with a λ_{max} around 340 nm (Iinuma et al., 2010; Lin et al., 2017). Polycyclic aromatic compounds (PAHs) have long been known to be emitted from incomplete combustion processes, and large PAHs can be significantly light-absorbing at the near-UV and visible wavelengths (Simoneit, 2002). Budisulistiorini et al. (2017) observed sulfur-containing species from fern and peat pyrolysis, and suggested that they are formed via acid-catalyzed heterogeneous reactions. Tar balls are largely externally-mixed spheres or spherical aggregates produced from smoldering combustion or secondary chemistry (Sedlacek III et al., 2018; Tóth et al., 2014). In terms of chemical composition, tar balls are thought to be comprised of primarily oxygenated organic compounds, similar to that of BBOA particles (Chakrabarty et al., 2010; Giroto et al., 2018; Li et al., 2019; Pósfai et al., 2004; Sedlacek III et al., 2018).

BrC components may undergo photochemical transformations during atmospheric transport, resulting in either photobleaching or photoenhancement of their absorption coefficients. For example, Forrister et al. (2015) and Selimovic et al. (2019) observed substantial decay of aerosol UV light absorption in a biomass burning plume with half-life of 9 to 15 hours. Similarly, Lin et al. (2017) reported rapid evolution of both the BBOA composition and optical properties during a nationwide biomass burning event in Israel. These changes in BBOA

properties are supported by laboratory studies of photochemical aging of BBOA particles or their surrogates via heterogeneous photooxidation (exposure of particles to gaseous OH), aqueous photooxidation (exposure of BBOA compounds to OH within cloud/fog water droplets), direct photolysis (exposure of particles or their aqueous extracts to actinic UV radiation), and indirect photolysis (photosensitized reactions between BBOA molecules and electronically-excited triplet states of photosensitizers). Several studies have characterized changes in the UV-Vis spectra of nitrophenols, surrogates for BBOA particles, as they are exposed to UV radiation. For example, Hinks et al. (2016) irradiated 2,4-dinitrophenol incorporated in limonene secondary organic aerosol material and observed the absorbance decrease in the range of 250-320 nm, while the absorbance from 400-450 nm increased. Similarly, Zhao et al. (2015) observed a photoenhancement at 420 nm for a 4-nitrocatechol aqueous solution in response to direct photolysis. During photooxidation with OH (produced by an intentional addition of hydrogen peroxide to the photolyzed solution), photoenhancement at 420 nm was observed initially, but the solution photobleached within an hour. In Hems and Abbatt (2018), aqueous solutions of nitrophenols and hydrogen peroxide were irradiated, atomized, and then analyzed by an aerosol-CIMS with acetate ions. This study attributed the photoenhancement at 420 nm to the functionalization of nitrophenols. This is followed by photodegradation at 420 nm coupled to fragmentation of functionalized nitrophenols. Lignin pyrolysis products and other lignin-derived molecules have been shown to be oxidized into light-absorbing compounds under certain conditions. For example, Gelencsér et al. (2003) observed an increase in absorption at visible wavelengths during the photooxidation of single component aromatic hydroxyl acids in aqueous solutions. Chang and Thompson (2010) and Tang and Thompson (2012) observed production of light absorbing compounds during aqueous reactions of OH with multiple phenolic compounds.

Smith et al. (2016) found that triplet-excited molecules can react with phenolic compounds in cloud water mimics producing chromophoric products. There are many studies that have investigated the photodegradation of PAHs on ice surfaces, ocean water mimics, and soil (Smol and Włodarczyk-Makula, 2017). The degradation of the three-ring PAH phenanthrene had a half-life of 13.2 to 22.8 hours depending on the solvent it was dissolved in (Shankar et al., 2019). Using infrared spectroscopy they observed the emergence of carboxylic acid, aldehyde, and ketone functionalities during photolysis. Miller and Olejnik, 2001 irradiated aqueous solutions of PAH mixtures with UVC lamps. They found that the photodegradation of benzo[a]pyrene and chrysene photodegrades more rapidly at acidic pH values and proposed a mechanism based on their findings (Miller and Olejnik, 2001).

Studies have also examined the photochemical aging of actual mixtures of BBOA compounds, not just surrogates. For example, Tomaz et al. (2018) found that aqueous BBOA mixtures decayed rapidly, with most having lifetimes due to aqueous OH oxidation mimicking clouds of a half a day or less. The decay of compounds such as catechol, benzoic acid, and methylfurfural lead to the formation of oxalate, which made up 13-16% of total dissolved organic carbon after 150 hours. Saleh et al. (2013) burned pocosin pine and oak, and diluted smoke was irradiated with UV lights in a smog chamber. Aerosol optical properties were monitored with an aethalometer at 7 wavelengths. They found that aged emissions were more absorbing than fresh emissions at 370 and 470 nm after one hour. Zhong and Jang, (2014) tracked the absorption coefficients of BBOA during solar exposure in a smog chamber, and observed an increase of 11-54% in the integrated mass absorption cross section (280-600 nm) in the first half of the day followed by decrease in the afternoon. In Lin et al. (2016), BBOA particles collected from ponderosa pine and Indonesian peat burns were dissolved in a 50% by

volume water/acetonitrile solvent and irradiated with actinic wavelengths. They found that regardless of the fuel type the half-life of the absorbance at 300 nm was roughly 16 hours under sunlight for soluble BBOA particles. Wong et al. (2017) found that irradiated BBOA water extracts lost water soluble organic carbon (WSOC), while the absorption coefficients at 365 nm and 400 nm first increased and then decreased. In Sumlin et al. (2017), BBOA particles produced from Alaskan peat were aged by reactions with OH in an oxidation flow reactor (OFR), and light absorption coefficients of aged and unaged BBOA particles were measured by an integrated photoacoustic nephelometer. They found that mass absorption coefficients at 375 nm and 405 nm decreased after 3.5 equivalent aging days in the OFR, with no significant change before this time.

To summarize the brief literature survey above, progress has been made in terms of characterizing optical properties of photochemically aged BBOA particles, but a consensus on what drives the photobleaching and photoenhancement of chromophores in BBOA and the relative importance of these processes on atmospherically relevant time scales has not been reached. This study aims to better understand the molecular composition of BrC for different fuel types and combustion conditions as it may be key to understanding the optical properties of BBOA and predicting their evolution during photochemical aging.

This study explored the diversity in the molecular composition of BrC chromophores found in BBOA particles generated from burning forest fire fuels, and examined how the chemical composition and optical properties change during UV irradiation of particles in the absence of gas-phase oxidants. Forest fire fuels were burned at the Missoula Fire Sciences lab in Fall 2016 in conjunction with the Fire Influence on Regional and Global Environments Experiment (FIREX) led by NOAA. BBOA particles from twelve fuels collected from around

the United States, encompassing both gymnosperm and angiosperm plant types, and different parts of the ecosystem, including duff, litter, and canopy are examined. Filter samples were extracted by solvents with a wide range of polarities and analyzed by high performance liquid chromatography coupled to a photodiode array and high resolution mass spectrometer (HPLC/PDA/HRMS) to target BrC chromophores. To investigate whether the BrC chromophores are photolabile or photostable, BBOA particles were directly irradiated on filter substrates before analysis by HPLC/PDA/HRMS or UV-Vis spectrometry. By measuring the time resolved absorbance of individual chromophores, we estimated their photolysis lifetimes in BBOA particles. We found that the equivalent atmospheric lifetime due to photolysis of individual chromophores ranged from 0.4-1.6 days, which is a relevant timescale for the long-range aerosol transport through the atmosphere. Chromophores could survive the exposure to UV radiation on different timescales, depending on their molecular structure or their interactions with neighboring molecules dictated by BBOA type. However, the overall absorption by BrC (integrated 300-700 nm) persisted longer due to direct photolysis, with lifetimes ranging from 10-41 days, because the photolysis products of starting BrC are also absorbing. These equivalent atmospheric photolysis lifetimes of BrC absorption are long compared to typical lifetimes for heterogeneous oxidation of BBOA particles by OH. For climate modeling applications these results suggest that chemical aging mechanisms other than photolysis may play a more significant role in quantifying BrC absorption lifetimes.

4.2 Experimental methods

4.2.1 Sample collection and information

BBOA particles were generated at the Fire Influence on Regional and Global Environments Experiment (FIREX) Fall 2016 lab intensive at the Missoula Fire Lab. Selimovic et al. (2018) explains “room burns” and fuels in detail, but briefly, the combustion of forest fire fuels lasted 5-20 minutes followed by 60-90 minutes of the smoke mixing in the room, and lastly, the smoke was purged from the room by clean air. Sampling inlets were placed high and deep into the room while the pump and filter were located in an adjacent room. BBOA particles were collected on PTFE filter substrates (FGLP04700, Millipore, 47 mm diameter, 0.2 μm pore size) during the combustion and mixing stages of the room burns. The room burn protocols allowed for long collection times and therefore higher aerosol mass loading which is desirable for the analysis that is described below.

Fuels were collected from all over the US and brought to the Missoula Fire Lab for burning. This manuscript will focus on twelve fires covering gymnosperm or conifers, including ponderosa pine (*Pinus ponderosa*), lodgepole pine (*Pinus contorta*), Engelmann spruce (*Picea engelmannii*), Douglas fir (*Pseudotsuga menziesii*), juniper (*Juniperus*), longleaf pine (*Pinus palustris*), rotten log, and subalpine fir (*Abies lasiocarpa*). Angiosperm forest fire fuels included Montanan sagebrush and two types of chaparral, manzanita (*Arctostaphylos*) and chamise (*Adenostoma fasciculatum*). For some fires, a representative “ecosystem” was burned, including canopy, duff, litter, herbaceous, and shrub components. In other fires, single components of the ecosystem were burned. Information for each fire is provided in Table 4.1.

Table 4.1: Summary of the fires from which BBOA samples were collected.

Fuel name	Fire #	MCE	Max NO (ppmv)	Ecosystem components
Subalpine fir duff	90	0.92	0.27	Duff
Ceanothus	89	0.95	2.48	Shrub
Chamise	84	0.95	3.79	Canopy
Longleaf pine	97	0.93	0.67	Duff, litter, shrub, herbaceous, canopy
Juniper	88	0.95	1.72	Canopy
Ponderosa pine log	105	0.92	0.13	Log
Manzanita	91	0.95	2.33	Canopy
Lodgepole pine	87	0.93	0.99	Canopy
Engelmann spruce duff	83	0.82	0.08	Duff
Ponderosa pine	106	0.95	1.61	Litter, canopy needle and branch
Douglas fir	80	0.93	0.43	Duff, litter, shrub, herbaceous, canopy
Sagebrush	85	0.94	1.62	shrub

4.2.2 HPLC/PDA/HRMS

The molecular identity and relative abundance of BrC chromophores were determined using the High Performance Liquid Chromatography/Photodiode Array/High Resolution Mass Spectrometry (HPLC/PDA/HRMS) platform (Fleming et al., 2018; Lin et al., 2016). Segments of the filter were extracted in a mixture of organic solvents composed of 2 mL dichloromethane, 2 mL acetonitrile, and 1 mL of hexanes. The extraction occurred overnight on a shaker. The extracts were filtered with PVDF syringe filters (Millipore, Duro pore, 13 mm, 0.22 μ m) to remove undissolved suspended particles. Water (50 μ L) and DMSO (100 μ L) were added to the extracts, and then they were concentrated under a flow of N₂ until it appeared the volume was roughly 150 μ L, which signified that the extracting solvent evaporated and (mostly) water and DMSO remained in the solution. For photolyzed BBOA particles, exclusively DMSO (30 μ L) was added to the extract, and it was concentrated to 30 μ L.

The HPLC utilized a reverse-phase column (Luna C18, 2×150 mm, 2465 5 μm particles, 100 Å pores, Phenomenex, Inc.). The injection volume was 5 or 10 μL . The mobile phase consisted of 0.05 % formic acid in LC–MS grade water (A) and LC–MS grade acetonitrile (B). Gradient elution was performed with the A–B mixture at a flow rate of 200 $\mu\text{L min}^{-1}$: 0–3 min hold at 90 % A, 3– 62 min linear gradient to 10 % A, 63–75 min hold at 10 % A, 76–89 min linear gradient to 0 % A, 90–100 min hold at 0 % A, then 101–120 min hold at 90 % A. The electrospray ionization (ESI) settings were as follows: 4.0 kV spray potential, 35 units of sheath gas flow, 10 units of auxiliary gas flow, and 8 units of sweep gas flow. The solutions were analyzed in both positive and negative ion ESI–HRMS modes.

The HPLC/PDA/HRMS data were acquired and first analyzed using Xcalibur 2.4 software (Thermo Scientific). Possible exact masses were identified based on the corresponding LC retention time using the open source software toolbox MZmine version 2.23 (<http://mzmine.github.io/>) (Pluskal et al., 2010). Chemical formulas were assigned from exact m/z values using the Formula Calculator v1.1.

4.2.3 Condensed-phase photolysis

BBOA particles deposited on a quarter of the filter substrate were directly irradiated by one of the two different lamps, an ultraviolet light-emitting diode (LED, Thorlabs M300L4) and a filtered Xenon arc lamp. The LED was used in experiments aimed at estimating lifetimes of individual chromophores. The LED emission spectrum was centered around 300 nm with a FWHM of 20 nm. This wavelength was chosen because it corresponds to the most energetic UV photons available in the lower troposphere. The LED was fixed half a centimeter away from the filter resulting in an incident power density of 11.1 mW cm^{-2} . Irradiation was stopped when the

particles on the filter first appeared to bleach, based on visual inspection. After the irradiation step, the photolyzed BBOA particles were extracted and run on the HPLC/PDA/HRMS platform in the same way as described in the previous section.

Irradiation time by the LED was converted into equivalent time under sunlight by calculating the ratio of the 290-350 nm integrated spectral flux of the sun and the 300 nm LED, given in equation (4.1). This conversion assumes that photochemistry is limited to the < 350 nm range, but this assumption is consistent with photochemical behavior of many organic molecules, which exhibit sharp drop in the photochemical quantum yields at longer wavelengths (Turro et al., 2009). Because the radiation source does not replicate the solar spectrum, the lifetime calculated from the formula below should be regarded as order of magnitude estimates.

$$\tau_{atm} = \tau_{LED} \times \frac{\int_{290nm}^{350nm} F_{LED}(\lambda) d\lambda}{\int_{290nm}^{350nm} \langle F_{solar}(\lambda) \rangle_{24hr} d\lambda} \quad (4.1)$$

The spectral flux density for the LED and the sun as a function of wavelength is shown in Figure 4.1. The solar flux density was estimated every hour and averaged over a 24-hour period for Los Angeles, CA (34°N 118°W) on June 20, 2017 from the quick TUV calculator (Madronich et al., 2002) using the following parameters: 300 du overhead ozone column, 0.1 surface albedo (0-1), and ground elevation of 0 km with default outputs for aerosols and clouds. The procedure for calculating the spectral flux density is given in the next section. The maximum possible spectral flux density from the sun was also calculated at a solar zenith angle of 0°, also using the TUV calculator, to represent the instant when the sun is most intense. The equation for calculating the equivalent atmospheric lifetime at a solar zenith angle of 0° is the same as equation (4.1) except

that the 24-hour averaged flux density is replaced by the peak flux density at SZA = 0. The SZA=0° comparison represents the lower limit of BrC absorption lifetimes.

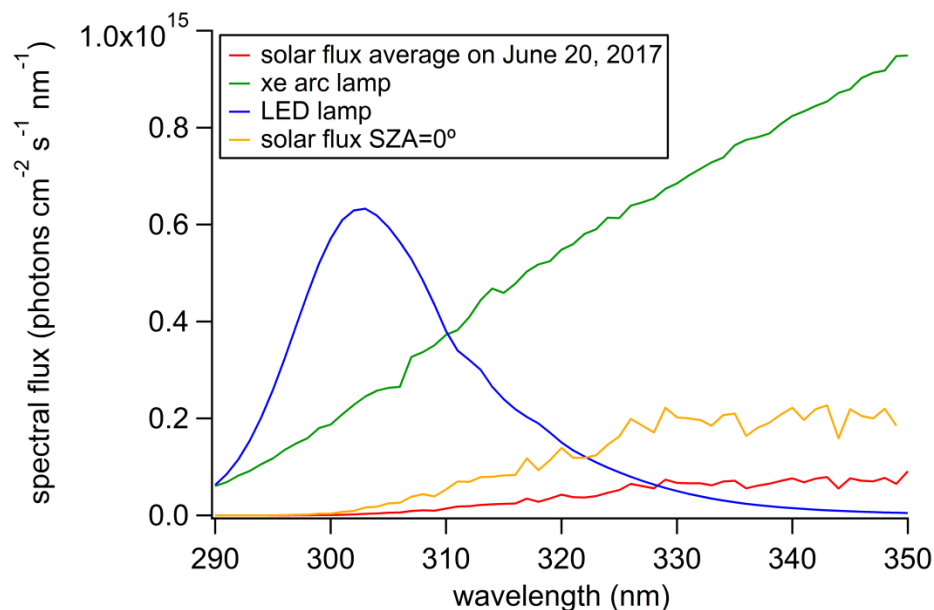


Figure 4.1: Spectral flux density ($\text{photons cm}^{-2} \text{s}^{-1} \text{nm}^{-1}$) approximated for a solar zenith angle of 0° (orange) as well as the 24-hour average for the latitude and longitude of Los Angeles (34° latitude, 118° longitude) on June 20, 2017 (red). The spectral flux density for the 300 nm LED (blue) and the filtered Xe arc lamp (green) are also shown.

In a separate set of experiments, filter samples were irradiated by the filtered radiation from a xenon arc lamp to determine the characteristic lifetime for photobleaching the overall absorption by BrC molecules. A quarter of a PTFE filter was exposed to filtered light emitted from a xenon-arc lamp (Newport 66902). Broadband light in the range of 280-400 nm was reflected at a ninety degree angle using a dichroic mirror, then filtered through a 295 nm long-pass filter (Schott WG295), and finally passed through a UV bandpass filter (Schott BG1) ultimately transmitting light in the range of 290-400 nm. The incident overall power density was 196 mW/cm^2 . Particles were irradiated for ~ 12 hours to 1.8 days; the exact time varied from sample to sample depending on the offline transmission spectra. Transmission spectra were acquired directly from the PTFE filter without any material extraction using a Jasco V-670 absorption spectrometer,

with a blank PTFE filter used as a reference. Four to six transmission spectra were collected at each time point as the filter was rotated, to minimize the effect of the filter orientation. The filter was then returned to the photolysis set up for further irradiation. When there was no longer any change in the transmission spectrum due to irradiation, the filter was extracted into an organic solvent mixture of mixture of 10 mL methanol, 5.0 mL acetonitrile, and 2.0 mL of hexanes in a scintillation vial using a vortex mixer. The solution was then evaporated in order to increase the concentration of analytes. For comparison, an un-irradiated quarter of the filter was prepared identically in another vial, and solution-phase transmission spectra of both solutions were recorded using a dual beam UV-Vis spectrometer (Shimadzu UV-2450). Sample filter-based and solution phase spectra are shown in Figure S2, with the Y-axis converted to effective base-10 absorbance, $A = -\log(T)$, where T is the wavelength-dependent transmittance through the filter or the cuvette. For filter-based transmission spectra, the baseline was manually corrected by assuming the absorbance at 850 nm was 0 for BrC.

4.2.4 Spectral flux/irradiance measurements for LED and Xe Arc lamps

The spectral flux density of the LED is calculated from actinometry measurements. The procedure is described in detail in Lignell et al. (2013) and described briefly here. We assume that the relative spectral density ($OO(\lambda)$) or the radiation from the LED lamp as detected by an Ocean Optics spectrometer (USB4000), is proportional to the spectral flux density ($D(\lambda)$) of the LED lamp as shown in equation (4.2).

$$D(\lambda) = \alpha \times OO(\lambda) \tag{4.2}$$

The proportionality constant, α , with units of photons $\text{cm}^{-2} \text{s}^{-1} \text{nm}^{-1}$ was calculated using equation (4.3). The parameters in this equation are: pathlength through the cuvette (b), the

average quantum yield of the actinometer ($\langle\varphi_{\text{act}}\rangle$), the fraction of the cuvette irradiated ($f_{\text{irradiated}}$), the base-e absorption cross section ($\sigma(\lambda)$), the number concentration in molecules cm^{-3} (n), and $\frac{-dn_{\text{act}}}{dt}$ (molecules $\text{cm}^{-3} \text{ s}^{-1}$), or the rate at which the actinometer is consumed as it is irradiated (see below for details).

$$\alpha = \frac{\frac{-dn_{\text{act}}}{dt} \times \frac{b}{\langle\varphi_{\text{act}}\rangle \times f_{\text{irradiated}}}}{\int_{290}^{320} \sigma(\lambda) [1 - e^{-\sigma(\lambda) \times n \times b}] d\lambda} \quad (4.3)$$

Azoxybenzene was selected as the actinometer because it has a known photoisomerization quantum yield of roughly 0.020 that is independent of temperature and concentration over the wavelength range of interest, 250-350 nm (Bunce et al., 1984). An ethanolic solution of 0.2 mM azoxybenzene and 6.0 mM KOH was prepared. A cuvette of the solution was irradiated by the LED or the Xe arc lamp in a similar configuration as the filter sample for 10 s intervals. UV-Vis spectra were collected at each interval using a UV-2450 Shimadzu UV-Vis spectrometer. The appearance of the photoisomerization product was probed from the absorbance at 458 nm. This absorbance is converted to concentration using the known molar absorptivity of the actinometer. Ultimately, after multiple unit conversions, we calculate $\frac{-dn_{\text{act}}}{dt}$ from this experiment. The calculated spectral flux density as a function of wavelength for the LED and Xe- Arc lamp are shown in Figure 4.1.

4.2.5 Calculation of the estimated BrC absorption lifetime

The natural log of the integrated absorbance (300-700 nm) divided by the initial integrated absorbance (300-700 nm) is plotted as a function of the irradiation time, as shown in Figure 4.2. This is done for both the condensed-phase and solution phase UV-Vis measurements (for solution only two points could be obtained at the start and end of the experiment because of

the limited number of filter samples). Example absorption spectra are shown in Figure 4.3. The data points are fitted to a linear trend line with the y-intercept forced through 0, from which the magnitude of the slope is the rate constant, k (min^{-1}). The reciprocal of k gives the lifetime of the absorption coefficient (300-700 nm) under the lamp. The lifetime is converted to an atmospheric lifetime with equation (4.1). This procedure is used for individual chromophores as well as overall BrC absorbance.

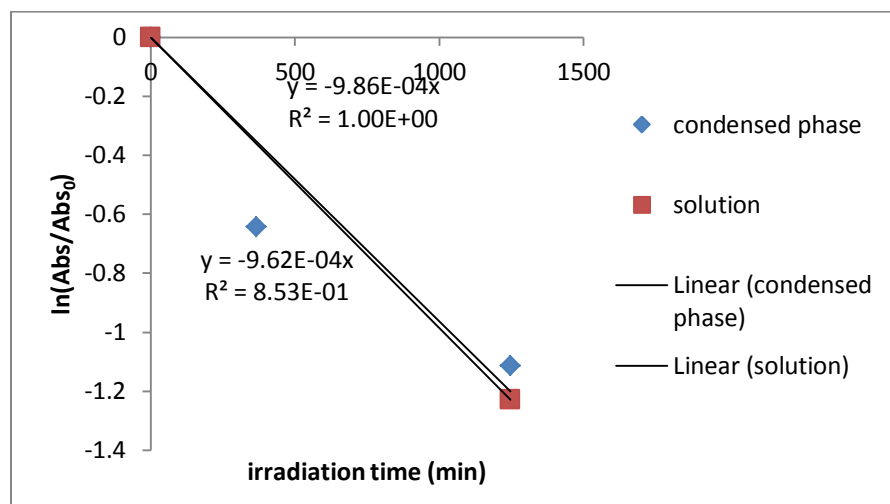


Figure 4.2: The natural logarithm of the integrated absorbance (300-700 nm), Abs/Abs_0 , plotted as a function of irradiation time. The magnitude of the slope of the trend line corresponds to the first-order decay constant (s^{-1}) according to the integrated first order rate law. The inverse of the first-order decay constant is the lifetime of the overall absorption (300-700 nm) of the BBOA material.

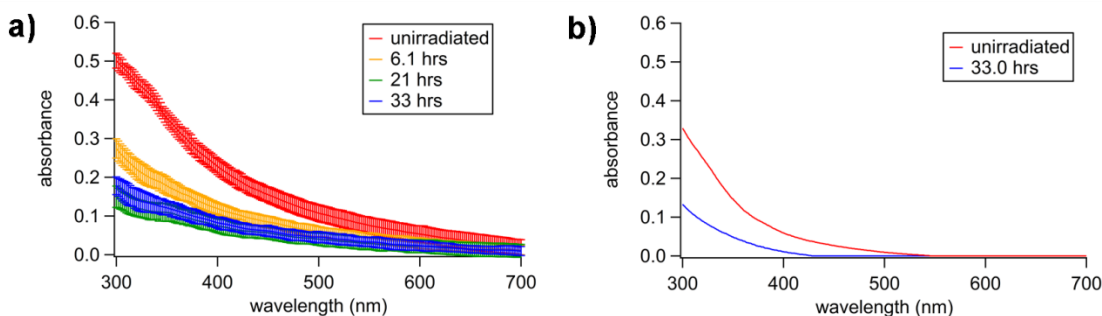


Figure 4.3: Absorption spectra of the same subalpine fir duff BBOA sample, recorded in a) the condensed phase (by measuring transmission through particle-loaded filter material) and b) the solution phase (by measuring transmission through a cuvette with a filter extract). The average of four absorption spectra is shown for each irradiation time point in a), and the standard deviation of these measurements are indicated with error bars.

4.3 Results and Discussion

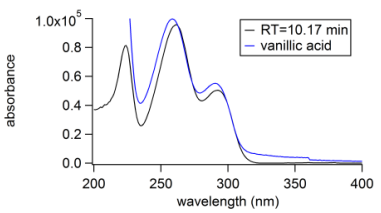
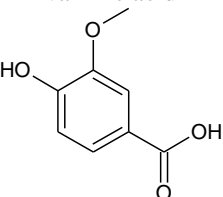
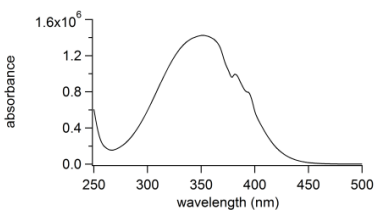
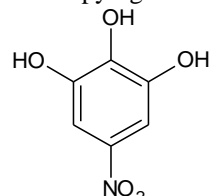
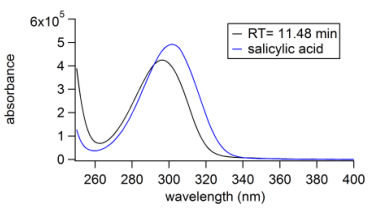
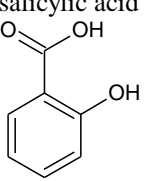
4.3.1 BrC Chromophores

Table 4.2 summarizes BrC chromophores observed in two or more fires or fuel types. The table numbers BrC chromophores by their ascending retention time on the HPLC column, i.e., with smaller, more polar compounds appearing first. Each entry includes the absorption spectrum recorded by the PDA detector, the chemical formula corresponding to the detected mass at that retention time, and the tentative structure based off a reference spectrum or observations in previous studies. All PDA chromatograms were integrated from 300-700 nm and normalized to the maximum integrated absorbance. Chromophores are binned with respect to their normalized PDA absorbance as M-Major (75%-100%), I-Intermediate (25%-75%), or W-Weak (5%-25%). Bins are calculated in relation to highest PDA signal for each fire.

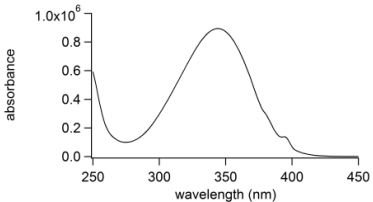
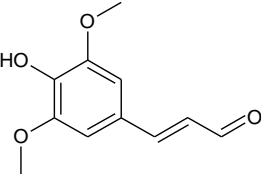
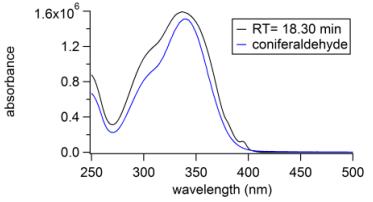
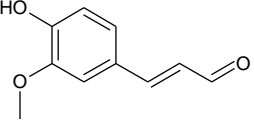
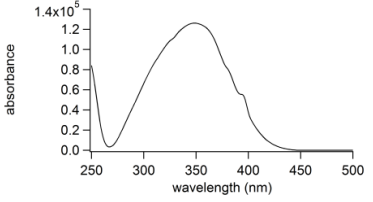
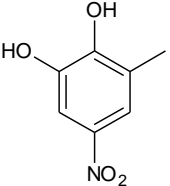
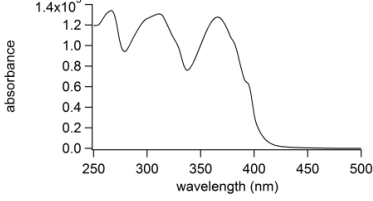
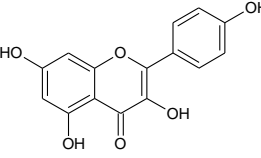
Lignin pyrolysis products make up one group of BrC chromophores observed. Lignin is a large, heterogeneous biopolymer that is a significant component of wood, along with cellulose and hemicellulose. Lignin monomer units vary depending on the class of the plant, but generally possess phenolic moieties that are largely preserved during pyrolysis (Simoneit et al., 1993). Sinapaldehyde (8) and coniferaldehyde (9) are known lignin pyrolysis products derived from the corresponding lignin monomer units, sinapyl and coniferyl alcohol, respectively. However, they are detected in varying abundance depending on the lignin monomer units of the plant class. Sinapaldehyde and coniferaldehyde are separated by the column, but elute only 0.3 minutes apart as shown in Figure 4.4. Sinapaldehyde is a major BrC chromophore for nearly all angiosperm or flowering fuel types, including ceanothus, chamise, and sagebrush, while coniferaldehyde is a major BrC chromophore largely among conifers or soft wood species such as subalpine fir duff,

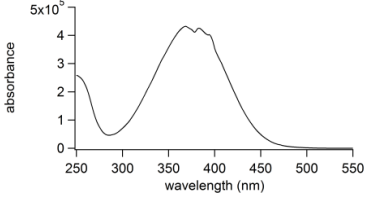
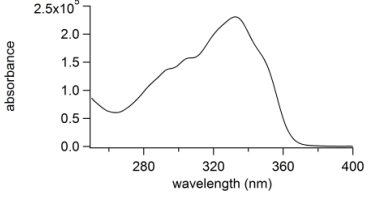
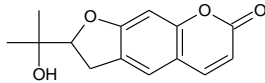
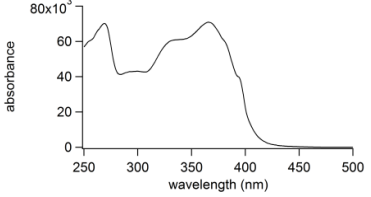
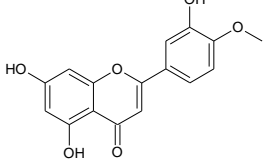
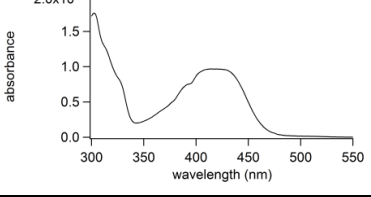
longleaf pine, juniper, and ponderosa pine litter. Coniferaldehyde has one less methoxy ring substituent compared to sinapaldehyde, and its PDA intensity is generally anti-correlated to that of sinapaldehyde. In other words, for fuel types with low sinapaldehyde absorbance, we observe coniferaldehyde as a major BrC chromophore and vice versa. This is consistent with the composition of lignin monomers for angiosperms and gymnosperms (Sarkanen and Ludwig, 1971; Simoneit et al., 1993).

Table 4.2: Chromophores common among multiple fuel types are listed by their range in HPLC retention times, absorption spectra, assigned elemental formulas, and examples of possible structures. The absorbance by each chromophore is binned by photodiode array absorbance normalized to the highest absorbance in each chromatogram: M-Major (75%-100%), I-Intermediate (25%-75%), or W-Weak (5%-25%). The absorption spectra of the standard may not fully match the absorption spectra of the eluents because the separation is not complete, and more than one compound is eluted at any given time. The shown absorption spectra are baseline corrected by subtracting the spectrum at a nearby retention time where the PDA absorbance is low.

Peak #	LC RT (min)	Absorption spectrum	Elemental formula	Tentative structures	subalpine fir duff	ceanothus	chamise	longleaf pine	juniper	ponderosa pine log	manzanita	lodgepole pine	engelmann spruce duff	ponderosa pine litter	douglas fir	sagebrush	
1	10.07-10.29		$C_8H_8O_4$	vanillic acid 	W					W			W				
2	10.52-10.71*		$C_6H_5NO_5$	nitropyrogallol 		W		I	W		M	W		I	W		
3	11.37-11.61		$C_7H_6O_3$	salicylic acid 				W			W	I		W	W		

Peak #	LC RT (min)	Absorption spectrum	Elemental formula	Tentative structures	subalpine fir duff	ceanothus	chamise	longleaf pine	juniper	ponderosa pine log	manzanita	lodgepole pine	engelmann spruce duff	ponderosa pine litter	douglas fir	sagebrush
4	14.37-14.56		$C_9H_8O_3$	veratraldehyde 	W	W	W	I	W		I	M	W	W	I	W
5	15.17-15.46		$C_9H_6O_3$	umbelliferone 	W	W		W	I	W	W	W	W		W	W
6	16.12-16.24		$C_6H_5NO_4$	nitrocatechol 		W	I	W						W		I
7	17.20-17.42		$C_7H_7NO_5$	hydroxynitroguaiacol 	W			W	W	I	W	W	W	W	W	W

Peak #	LC RT (min)	Absorption spectrum	Elemental formula	Tentative structures	subalpine fir duff	ceanothus	chamise	longleaf pine	juniper	ponderosa pine log	manzanita	lodgepole pine	engelmann spruce duff	ponderosa pine litter	douglas fir	sagebrush
8	18.13-18.18		$C_{11}H_{12}O_4$	sinapaldehyde 		M	M	W		M	W		M			M
9	18.33-18.47		$C_{10}H_{10}O_3$	coniferaldehyde 	M	I	W	M	M	M	W	M		M	M	M
10	23.32-23.49		$C_7H_7NO_4$	methyl nitrocatechol 		W	W	W		W	W	W		W		I
11	27.15-27.29		$C_{15}H_{10}O_6$	kaempferol 				I	W		W	M		W	I	

Peak #	LC RT (min)	Absorption spectrum	Elemental formula	Tentative structures	subalpine fir duff	ceanothus	chamise	longleaf pine	juniper	ponderosa pine log	manzanita	lodgepole pine	engelmann spruce duff	ponderosa pine litter	douglas fir	sagebrush	
12	28.80-28.85		$C_{11}H_{13}NO$ 5			W	M										M
13	29.08-29.34		$C_{14}H_{14}O_4$	nodakenetin 	M			M	M	I	W	M	I	M	M		I
14	31.85-31.90		$C_{16}H_{12}O_6$	diosmetin 				W				I		W			
15	41.63-41.98		$C_{18}H_{16}O_2$ $C_{17}H_{10}O$ $C_{16}H_{10}O$			W	W	W		W		W	W	W	W	W	W

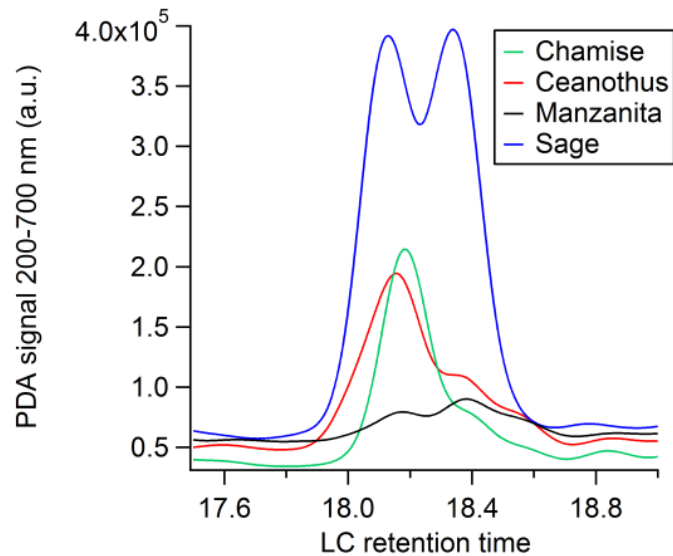


Figure 4.4: Lignin pyrolysis products sinapaldehyde ($C_{11}H_{12}O_4$) and coniferaldehyde ($C_{10}H_{10}O_3$) elute at slightly different retention times, at roughly 18.1 and 18.4 min, respectively.

Other BrC chromophores cannot be classified as lignin pyrolysis products but are clearly lignin-derived. Vanillic acid (1) elutes at 10.07-10.29 minutes as the first, shared chromophore that is notable in terms of absorption. It is observed in three fires as a weak chromophore, including subalpine fir duff, ponderosa pine rotten log, and Engelmann spruce duff. All three fires are dominated by smoldering combustion and have the lowest modified combustion efficiencies of all fires (Table 4.1). This evidence suggests vanillic acid is a low temperature product. Further, it also has the coniferyl moiety observed for softwoods. Salicylic acid (3) is an intermediate absorbing BrC chromophore produced during lodgepole pine burning, and weakly absorbing among other softwoods and duffs. Veratraldehyde (4) is another lignin-derived BrC chromophore, which appears in nearly every HPLC-PDA chromatogram.

There are other BrC chromophores composed only of carbon, hydrogen, and oxygen ($C_xH_yO_z$) that can be explained as distillation products, or the volatilization of molecules originating in plants as secondary metabolites (Agati et al., 2012; Iranshahi M et al., 2009). Found in plants, coumarins such as umbelliferone (5) and nodakenetin (13) have been researched

because of their positive pharmacological properties (Venugopala et al., 2013). The absorption spectrum for nodakenetin has not been reported, however, the molecule has previously been detected in plant tissues (Lee et al., 2003; Wang et al., 2014), and is a major/intermediate BrC chromophore in smoke from all fuel types except chamise and ceanothus. Another type of distillation product is flavonoids, which give leaves, flowers, and fruits their color protecting the plant from solar UV radiation, and are antioxidants-- guarding the plant from reactive oxygen species (Agati et al., 2012). Flavonoids such as flavones and flavonols have the backbone structure of 2-phenyl-1-benzopyran-4-one, and flavonols additionally require a hydroxy substituent on the only available carbon of the pyranone ring. BrC chromophores 11, 14, and 16 could have flavonoid structures based on their chemical formulas. Interestingly, 11 (tentatively kaempferol) and 14 (tentatively diosmetin) are observed in only conifer species, such as lodgepole pine and longleaf pine. On the other hand, chromophore 16 is only observed in angiosperm BBOA particles: ceanothus, chamise, and sagebrush. The former two plants appear to be related as they have the order *rosales* in common, which could explain the same flavone detected in both. Coumarins and flavonoids were distillation products observed across fuel types, although the observation of select BrC chromophores depends on the plant class, angiosperm or gymnosperm.

Nitroaromatics are a strongly-absorbing class of BrC chromophores that are formed from the reaction of aromatics with NO_x in plumes (Harrison et al., 2005). This class of compounds is represented in Table 4.2 with nitropyrogallol (2), nitrocatechol (6), hydroxynitroguaiacol (7), and methyl nitrocatechol (10). Xie et al. 2019 suggests that chromophore (12) with the chemical formula $\text{C}_{11}\text{H}_{13}\text{NO}_5$ is not a nitroaromatic compound, but rather, a compound containing a different nitrogen-containing functional group, such as a nitrile group. We did not observe this

group of chromophores for fires with low NO_x levels, such as duff, as evidenced by the peak NO level (Table 4.1). Nitrocatechol and methyl-nitrocatechol are tracers for aged BBOA emissions formed from the photooxidation of phenol or *m*-cresol or other aromatic compounds in the presence of NO_x (Iinuma et al., 2010, 2016). These chromophores are most prominent in chamise (3.79 ppmv peak NO) and sagebrush smoke (1.62 ppmv peak NO), with the former having the highest peak NO mixing ratio of all fires in this study. Nitropyrogallol (2) has an additional hydroxy group and is likely formed in the same way as nitrocatechol and methyl nitrocatechol, but is more oxidized. A compound with the same formula as nitropyrogallol (2) was observed during the photooxidation of nitrocatechol in the lab (Hems and Abbatt, 2018). This is an intermediate or major chromophore for longleaf pine, manzanita, and ponderosa pine litter fires. Hydroxynitroguaiacol (7) was observed in 10 of the 12 fires, and is most prominent in ponderosa pine log BBOA particles despite this fire having the lowest NO levels. However, it may still form through photooxidation of guaiacol in the presence of NO_x (Hems and Abbatt, 2018). Nitrocatechol and methyl nitrocatechol are often used as biomass burning tracers in aged plumes (Al-Naiema and Stone, 2017; Iinuma et al., 2010; Li et al., 2016), however in addition to these, we observed more oxidized versions of these nitroaromatic species. This suggests that the BBOA markers nitrocatechol and methyl nitrocatechol become more functionalized on relatively short time scales (less than two hours) due to photooxidative aging.

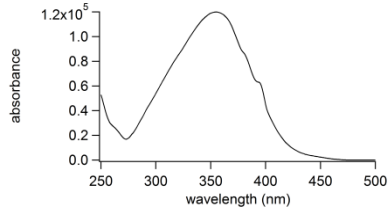
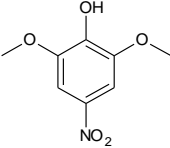
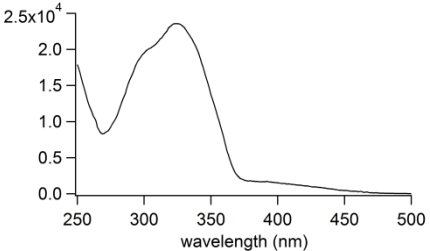
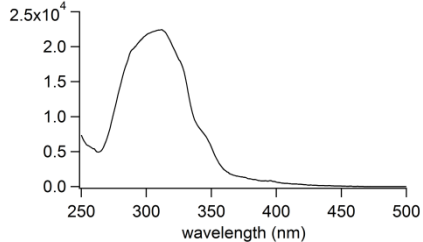
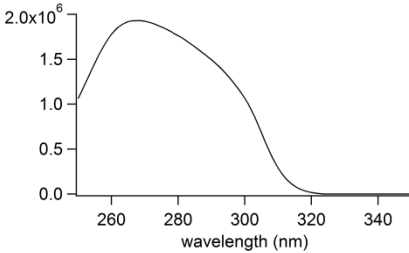
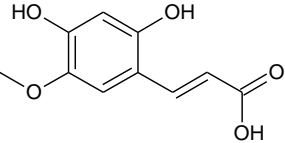
Polycyclic aromatic hydrocarbons (PAHs) are known to be products of incomplete combustion, and they have the potential to be long-lived BrC chromophores. PAHs have been observed in pristine environments, suggesting this class of BrC chromophores is stable during atmospheric transport (Fernández et al., 2002; Macdonald et al., 2000; Sofowote et al., 2011; Zhou et al., 2012). In addition to its climatic effects, PAHs are mutagenic and carcinogenic as

their metabolites, diol epoxides, bind to guanidine nucleobases in DNA effectively leading to mutations (Finlayson-Pitts and Pitts, 2000; Moorthy et al., 2015; Wood et al., 1984; Xue and Warshawsky, 2005; Zhou et al., 2017a). Various PAHs (17-25, Table 4.2) were observed in ceanothus, chamise, and sagebrush BBOA particles. PAHs in Table 4.2 are detected from positive ion mode ESI, and although positive mode ESI is not optimal for observing PAHs, larger PAHs are detectable by this method. The same PAHs were previously observed by Lin et al., 2018 for sagebrush using atmospheric pressure photoionization (APPI) coupled with HPLC/PDA/HRMS, which is better suited for detection of non-polar aromatic compounds. In general, individual PAH chromophores are binned as “weak” in Table 4.2 based on their contribution to optical absorption, but for sagebrush and chamise they make up a significant fraction of the observed absorption.

Table 4.3 presents abundant BrC chromophores observed only in a single HPLC-PDA chromatogram or fuel type. It should be noted that compounds making up less than 5% of the normalized PDA absorbance (integrated from 300-700 nm) are not included in the tables. Due to this, chromophores in Table 4.3 may also be present in other fires, but at very low PDA absorbance values. Despite BrC chromophores in Table 4.3 being observed significantly for only one fuel type, they belong to the same compound classes as the BrC chromophores in Table 4.2. For example, a coumarin known as scopoletin (compound 26) was observed in sagebrush. Previously we discussed these coumarins are possible distillation products, along with flavonoids, which we also observe in the ceanothus fire (compound 40). Distillation products (compounds 26 and 40) are among the most strongly absorbing of the BrC chromophores, characterized as intermediate or “I” in Table 4.3.

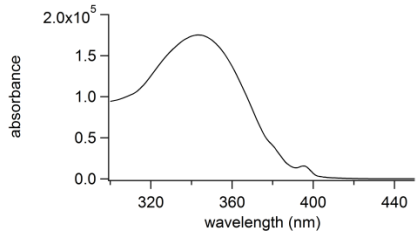
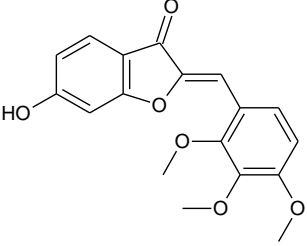
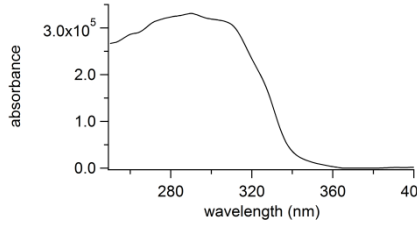
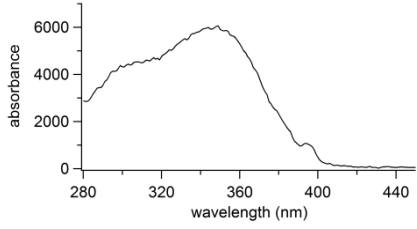
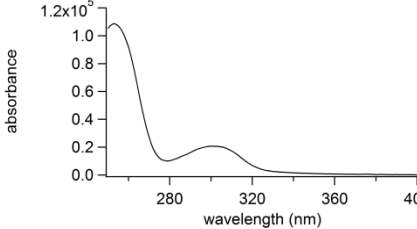
Table 4.3: Chromophores found appreciably in only one fuel type listed by their HPLC retention times, absorption spectra, assigned elemental formulas, and examples of possible structures. The absorbance by each chromophore is binned by photodiode array absorbance normalized to the highest absorbance in each chromatogram: M-Major (75%-100%), I-Intermediate (25%-75%), or W-Weak (5%-25%).

Peak #	LC RT (min)	Absorption spectrum	Elemental formula	Intensity bin	Tentative structures	Fuel type
26	14.22		$C_{10}H_8O_4$	I	<p>scopoletin</p>	sagebrush
27	17.08		$C_{13}H_{14}O_4$	W		chamise
28	18.87		$C_{10}H_{10}O_2$	W		subalpine fir duff
29	21.82		$C_7H_7NO_5$ (isomer of methyl nitrocatechol)	W		sagebrush

Peak #	LC RT (min)	Absorption spectrum	Elemental formula	Intensity bin	Tentative structures	Fuel type
30	22.21		$C_8H_9NO_5$	W	Dimethoxynitrophenol 	chamise
31	22.43		$C_{12}H_{12}O_4$	W		lodgepole pine
32	23.65		$C_{18}H_{18}O_5$	W		lodgepole pine
33	24.42		$C_{10}H_{10}O_5$	W		ceanothus

Peak #	LC RT (min)	Absorption spectrum	Elemental formula	Intensity bin	Tentative structures	Fuel type
34	26.17		$C_{20}H_{22}O_6$	W		ponderosa pine log
35	26.95		$C_{11}H_6O_3$ $C_{17}H_{14}O_8$	W		lodgepole pine
36	30.35		$C_{12}H_{13}NO_4$ $C_{16}H_{16}O_6$	W		ponderosa pine log
37	32.55		$C_{10}H_7NO_3$	W		sagebrush

Peak #	LC RT (min)	Absorption spectrum	Elemental formula	Intensity bin	Tentative structures	Fuel type
38	34.69	<p>The graph shows absorbance on the y-axis (0 to 5x10⁵) and wavelength in nm on the x-axis (250 to 450). The curve has a small peak at ~270 nm and a larger peak at ~340 nm, then decays towards zero.</p>	C ₁₆ H ₁₂ O ₅	W	<p>Chemical structure: A flavone core with hydroxyl groups at positions 5 and 7, and a 4-methoxyphenyl group at position 2.</p>	ceanothus
39	35.25	<p>The graph shows absorbance on the y-axis (0.0 to 1.0x10⁵) and wavelength in nm on the x-axis (250 to 550). The curve shows a sharp peak at ~280 nm and a broader peak at ~350 nm, then decays.</p>	C ₁₁ H ₉ NO ₃	W		chamise
40	35.37	<p>The graph shows absorbance on the y-axis (0 to 4x10⁵) and wavelength in nm on the x-axis (250 to 500). The curve has a small peak at ~270 nm and a larger peak at ~350 nm, then decays.</p>	C ₁₇ H ₁₄ O ₆	I	<p>Chemical structure: A flavone core with hydroxyl groups at positions 5 and 7, a methoxy group at position 3, and a 4-methoxyphenyl group at position 2.</p>	ceanothus
41	39.38	<p>The graph shows absorbance on the y-axis (0.0 to 1.2x10⁵) and wavelength in nm on the x-axis (300 to 600). The curve shows a peak at ~280 nm and a broader peak at ~380 nm, then decays.</p>	C ₁₆ H ₁₀ O ₃	W		chamise

Peak #	LC RT (min)	Absorption spectrum	Elemental formula	Intensity bin	Tentative structures	Fuel type
42	40.22	 <p>Absorbance vs wavelength (nm) plot for peak 42. The y-axis is labeled 'absorbance' and ranges from 0.0 to 2.0x10⁵. The x-axis is labeled 'wavelength (nm)' and ranges from 320 to 440. The curve shows a broad peak centered at approximately 340 nm with a maximum absorbance of about 1.8x10⁵.</p>	C ₁₈ H ₁₆ O ₆	I	 <p>Chemical structure of a tentative structure for peak 42. It features a benzofuran core with a hydroxyl group at the 6-position and a methoxy group at the 3-position. A side chain with a double bond and a methoxy group is attached to the 2-position of the furan ring.</p>	ceanothus
43	40.53	 <p>Absorbance vs wavelength (nm) plot for peak 43. The y-axis is labeled 'absorbance' and ranges from 0.0 to 3.0x10⁵. The x-axis is labeled 'wavelength (nm)' and ranges from 280 to 400. The curve shows a broad peak centered at approximately 300 nm with a maximum absorbance of about 3.2x10⁵.</p>	C ₁₇ H ₂₀ O ₄	W		ponderosa pine log
44	44.26	 <p>Absorbance vs wavelength (nm) plot for peak 44. The y-axis is labeled 'absorbance' and ranges from 0 to 6000. The x-axis is labeled 'wavelength (nm)' and ranges from 280 to 440. The curve shows a broad peak centered at approximately 340 nm with a maximum absorbance of about 6000.</p>	C ₃₂ H ₂₈ O ₄	W		subalpine fir duff
45	45.7	 <p>Absorbance vs wavelength (nm) plot for peak 45. The y-axis is labeled 'absorbance' and ranges from 0.0 to 1.2x10⁵. The x-axis is labeled 'wavelength (nm)' and ranges from 280 to 400. The curve shows a sharp peak at approximately 280 nm with a maximum absorbance of about 1.1x10⁵, and a smaller secondary peak at approximately 300 nm.</p>	C ₂₂ H ₂₆ N ₄ O	W		subalpine fir duff

Peak #	LC RT (min)	Absorption spectrum	Elemental formula	Intensity bin	Tentative structures	Fuel type
46	49.05	<p>The graph displays the absorption spectrum for peak 46. The x-axis represents wavelength in nanometers (nm), ranging from 260 to 340. The y-axis represents absorbance, scaled by 10⁵, ranging from 0 to 5. The curve shows a broad absorption band with a maximum absorbance of approximately 4.5 at a wavelength of about 300 nm.</p>	$C_{20}H_{24}O_4$	W		ponderosa pine log

*Lin et al., 2018

4.3.2 Condensed-phase photolysis

Gymnosperm (lodgepole pine) and angiosperm (ceanothus) BBOA particle samples were selected for the initial condensed-phase photolysis experiments. Filter samples with lodgepole pine particulate matter were photolyzed for 6 hours by an LED centered around 300 nm (which corresponds to approximately 33 hours of photochemical aging from 24-hour average spectral flux density or at an SZA=0°, see equation (4.1)). Ceanothus particulate matter was photolyzed by the same LED for 16 hours (equivalent to 88 hours of 24 hour averaged atmospheric sunlight). The burning of gymnosperm (lodgepole pine) and angiosperm (ceanothus) resulted in different distributions of BrC chromophore classes. However, the same compound classes were photo-resistant in both samples, lignin-derived and flavonoid species.

Most lodgepole pine chromophores experienced photobleaching during this exposure, but six (including coniferaldehyde (C₁₀H₁₀O₃, 80% decrease), salicylic acid (C₇H₆O₃, 70% decrease), veratraldehyde (C₉H₈O₃, 90% decrease), flavonoids (C₁₅H₁₀O₆ & C₁₆H₁₂O₆, both 70% decrease), and nodakenetin (C₁₄H₁₄O₄, 90% decrease) remained intact, as shown in Figure 4.5. Figure 4.6 shows five ceanothus chromophores that remain under those conditions including sinapaldehyde (C₁₁H₁₂O₄, 90% decrease), a lignin-derived chromophore (C₁₈H₁₆O₆, 80% decrease), and flavonoids (C₁₆H₁₂O₅, C₁₇H₁₄O₆, and C₁₇H₁₄O₅, all 80% decrease), some of which are observed exclusively in this fire. Such species are aromatic, which helps them be more resistant to photodegradation.

Figure 4.5: Chromophores present before (top panel) and after (bottom panel) photolysis for a conifer fuel, lodgepole pine.

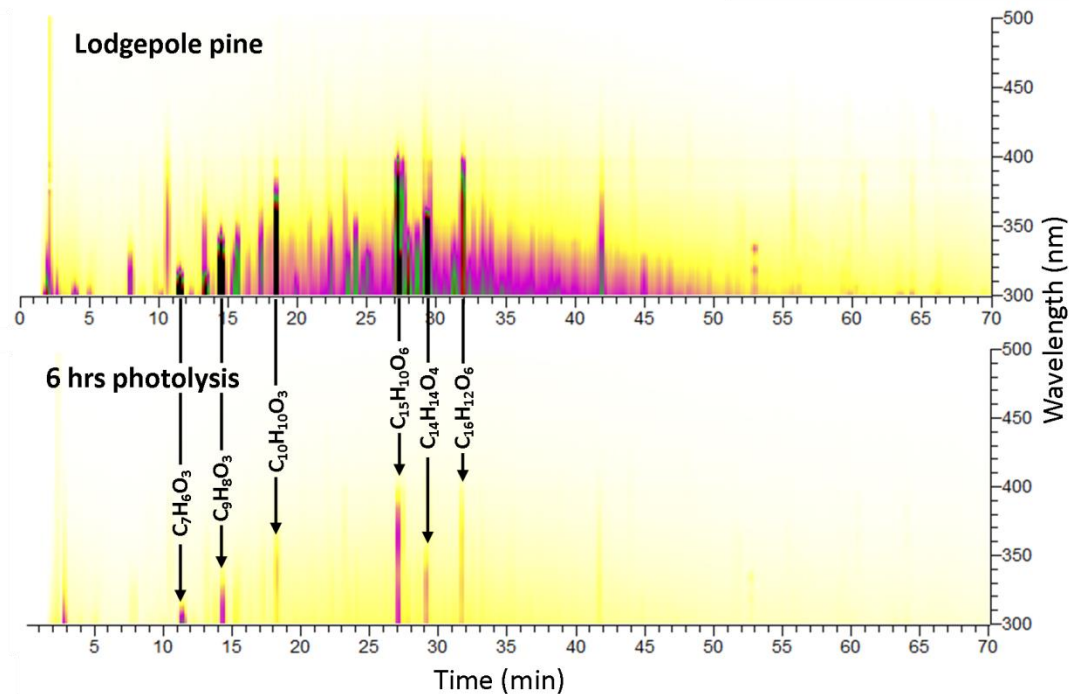
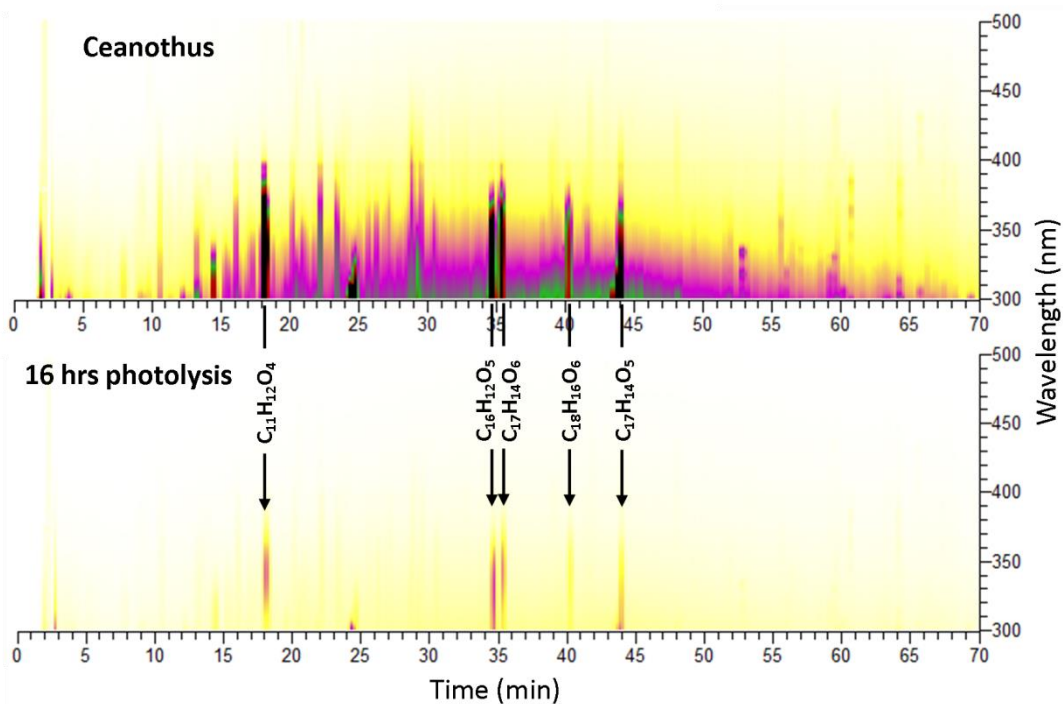


Figure 4.6: Chromophores present before (top panel) and after (bottom panel) photolysis for angiosperm fuel, ceanothus.

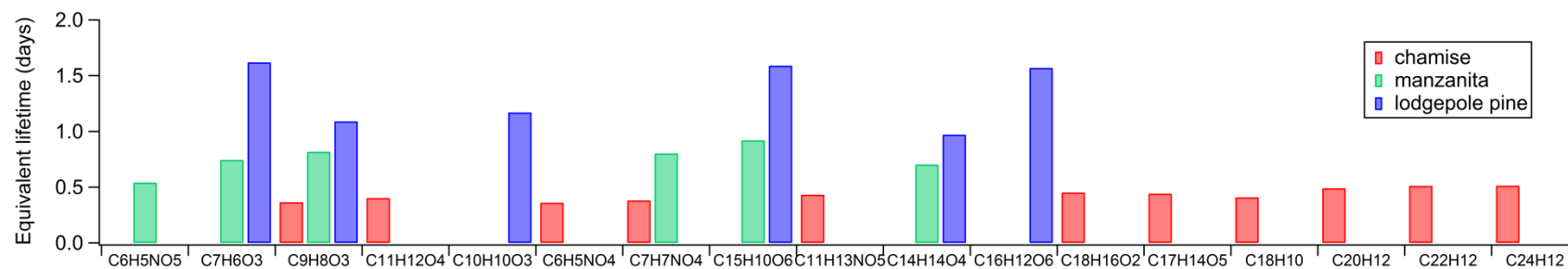


Next we estimate the lifetime of BrC chromophores in BBOA particles. For chamise, manzanita, and lodgepole pine fires we measured the integrated PDA intensity over 300-700 nm for resolved BrC chromophores for up to three photolysis time points (listed in Table 4.4) and before photolysis. The limited number of samples and destructive (as well as time-consuming) nature of the chemical analysis only made it possible to do measurements for very few time points. Integrated PDA intensities as a function of irradiation time were fit assuming that the decay was exponential in time. LED lifetimes were then converted to equivalent lifetimes in the atmosphere, calculated from the average spectral flux density over June 20, 2017 in Los Angeles. Regardless of the individual BrC chromophore, chamise BrC chromophores (0.4-0.5 days) have shorter predicted lifetimes than manzanita (0.5-0.9 days), which in turn has shorter predicted equivalent atmospheric lifetimes due to sunlight exposure than lodgepole pine (1.0-1.6 days), as shown in Figure 4.7. These lifetimes of BrC chromophores are consistent with atmospheric observations of a rapid evolution in a California wildfire (Forrister et al., 2015).

Table 4.4: Filter irradiation times for different samples used to estimate lifetimes of individual chromophores.

Fuel type	Irradiation time #1 (hrs)	Irradiation time #2 (hrs)	Irradiation time #3 (hrs)	Figure used
Lodgepole pine	6	16.8		3,5
Ceanothus	16			4
Chamise	1	3	12	5
Manzanita	6	16.8		5

Figure 4.7. Approximate atmospheric lifetime for select BrC chromophores due to direct photolysis that exist in BBOA particles from chamise, manzanita, and lodgepole pine fires (the photolysis times are listed in Table 4.4).



The same chromophore was found to decay at a different rate depending on the fuel/fire type (Figure 4.7). For example, very different equivalent atmospheric lifetimes due to photolysis were obtained across fuel types for veratraldehyde (#4 in Table 4.2, $C_9H_8O_3$), a BrC chromophore common to all three fires. One explanation is that there are multiple chromophores co-eluting at this retention time, and therefore the calculation is an average lifetime for multiple compounds. A more interesting explanation is that the surrounding matrix could affect the rate of photolysis for individual chromophores by several possible mechanisms. First, different matrices could quench the electronic excitation in the chromophores to a different extent. Another possibility is that photodegradation of BrC chromophores could be not direct but rather occurring through condensed-phase photosensitized reactions (Malecha and Nizkorodov, 2017; Monge et al., 2012), in which case the rate of decomposition would depend on concentration of photosensitizers in the samples as well as viscosity of the material (Hinks et al., 2016). Lastly, other absorbing species, such as black carbon could be shielding BrC chromophores from irradiation, altering the amount of radiation getting to BrC chromophores. Given the different mechanisms, the contributions from each are difficult to distinguish in this study. The particle matrix is different for all three BBOA particle samples and could contribute to the very different equivalent atmospheric lifetimes of individual BrC chromophores observed in Figure 4.7.

We also estimated the lifetime for the decay of the overall BrC absorption, integrated over 300-700 nm, from different fuel types. In these experiments, BBOA filters were irradiated with a filtered xenon arc lamp, which gave a spectral flux density more similar to the sun although more intense (Figure 4.1). The advantage of taking transmission spectra directly through the filters is that it makes it possible to monitor photodegradation of BrC absorption at several irradiation times, which is not possible with the solution-phase spectrophotometry, which

irreversibly destroys the filter sample by extraction. The filter transmission spectra indicated that the decay of absorbance was not actually exponential; after a certain irradiation time, the BrC absorbance no longer decreased, as observed for subalpine fir duff and longleaf pine samples. For example, in Figure 4.3, after 21 hours the “baseline BrC” level has already been reached, as revealed by the next measurement at 33 hours. The absorbance decreased 70% before it reached the baseline BrC level for subalpine fir duff, and 60% for longleaf pine. We only used the time before reaching the steady state to estimate the lifetimes. Table 4.5 summarizes the resulting lifetimes for four fuel types, longleaf pine, juniper, lodgepole pine, and subalpine fir duff.

Table 4.5. Lifetimes for the loss of the measured integrated absorbance from 300 to 700 nm (expressed in equivalent days of solar exposure). The lifetimes were calculated from the transmission spectra measured for particles on PTFE filters. The irradiation was done in the condensed phase, on the filter, for all samples.

Fuel type	BrC lifetime based on condensed phase measurements Average LA (equivalent days)	BrC lifetime based on condensed phase measurements SZA=0° (equivalent days)
Longleaf pine	25	8.5
Juniper	41	14
Ponderosa pine	17	6.0
Subalpine fir duff	10	3.4

Once there was no significant change in the transmission spectrum, the filter was extracted for the solution phase UV-Vis measurement, in order to compare the spectra obtained from the filter and in solution. The solution-phase spectra exhibited a reduction in the absorbance of the same order of magnitude as observed in the filter transmission spectra (Figure 4.3). However, there were differences in the shape of the spectra – there was no measurable absorbance above 550 nm in the extracted samples, but filter samples absorbed even at these

long wavelengths (Figure 4.3). It is likely that the extraction from the filter was not complete, and some of the absorbers remained on the filter after the extraction (this is another advantage of doing these experiments with filter samples as opposed to filter extracts).

BBOA from subalpine fir duff had the shortest equivalent absorption lifetime at 10 days, with ponderosa pine (litter + canopy) having the next shortest equivalent absorption lifetime at 17 days. Different ecosystem components were burned in the long leaf pine fire, such as duff, litter, and canopy. Longleaf pine was a mixed ecosystem burn, and had the next longest absorption lifetime of 25 days. The longest living absorbance was that of juniper (canopy only), at 41 days. Fuel components appear to affect BrC absorption lifetimes, as it does seem that non-canopy fuel components, such as litter and duff lower the BrC absorption lifetimes. However, it is difficult to correlate the BrC absorption lifetimes with quantitative measures such as NO levels or MCE (Table 4.1). Table 4.1 shows that the peak NO level was lower for long leaf pine (0.67 ppmv) compared to juniper (1.72 ppmv) and ponderosa pine (1.61 ppmv), suggesting less flaming combustion may have occurred for the long leaf pine fire (although this is not reflected in the MCE). Regardless, the data suggests that BrC absorption is relatively long-lived from direct photodegradation.

In general the lifetimes for the loss of the absorbance integrated over 300-700 nm (Table 4.5) are much longer than those of individual chromophores (Figure 4.7). There are two likely reasons for it. First, photodegradation of an individual chromophore creates product(s) that may also absorb in this wavelength range. The integrated BrC absorption (300-700 nm) will go down only after the compounds go through several stages of photodegradation finally resulting in products that no longer absorb above 300 nm. Second, equation (4.1) that we use to estimate lifetimes does not take into account photochemical quantum yields, which tend to increase

greatly at lower wavelengths. The LED, which was used in measurements of lifetimes of individual chromophores, has a higher density of higher energy photons compared to the Xe lamp (Figure 4.1), which could accelerate photodegradation.

The lifetimes for BrC photobleaching due to UV irradiation (10 to 41 days) are longer than what other studies have observed or approximated for other aging mechanisms. Lin et al. 2016 found that peat and ponderosa pine BBOA had similar half-lives of around 16 hours based on absorption coefficients at 300 nm. However, in Lin et al. 2016 BBOA was extracted and irradiated in solution where photodegradation could occur more rapidly (Lignell et al., 2014). Forrister et al., 2015 collected filter samples in the plumes of wildfires with different photochemical ages during the SEAC4RS campaign, and found that the BrC absorbance lifetime at 370 nm was 9-15 hours. Sumlin et al., 2017 aged smoldering peat BBOA in an OFR, and report a decrease of 40-50% in the aerosol absorption coefficients at 375 nm and 405 nm after 4.5 equivalent aging days. They attributed this decrease to fragmentation of BrC chromophores due to photooxidation. Based on the comparison of these observations, photooxidation (oxidation by gaseous OH) appears to be a more important aging mechanism affecting BrC absorption lifetimes compared to the UV-induced photochemical processes inside the particles.

4.4 Conclusions and Implications

BBOA particles from laboratory burns of twelve forest fire fuels collected around the United States were analyzed for BrC chromophores. Forest fire fuels spanned plant types (gymnosperm versus angiosperm) and ecosystem components (duff, litter, canopy, etc.). BrC chromophores were grouped among classes, including, lignin pyrolysis products, lignin-derived, distillation (coumarins and flavonoids), nitroaromatics, and PAHs. While most BrC chromophore classes were observed in all burns regardless of fuel type, there were specific BrC

chromophores that were divided across angiosperm (flowering) and gymnosperm (conifer) lines. For example, sinapaldehyde was mainly observed in BBOA particles when angiosperm fuels were burned and coniferaldehyde when gymnosperm fuels were burned. Additionally, there were flavonoids specific to conifers, tentatively kaempferol and diosmetin (Table 4.2, chromophores 11 & 14), and unique to angiosperms such as chromophore 16. PAHs are largely angiosperm BrC chromophores, showing up mainly for sagebrush, chamise, and ceanothus fuels. There are some BrC chromophores that are only appreciably observed in a single fuel type/burn; many of these are likely distillation or lignin-derived products. The most absorbing of these BrC chromophores are components of the angiosperm BBOA particles (Table 4.3).

UV irradiation of BBOA particles from different fuels directly on filters removes some BrC chromophores but some appear to be photo-stable, specifically, lignin-derived compounds (including lignin-pyrolysis products) and flavonoids. Interestingly, individual BrC chromophore lifetimes varied based on the fuel burned and perhaps the underlying combustion conditions, rather than just the structure of the chromophore. Part of the reason is that co-elution of chromophores with different stabilities complicates measurements of individual chromophore lifetimes. In addition, indirect photolysis mechanisms, such as photosensitized reactions, the release of absorbed energy by a neighboring molecule as heat depending on intermolecular forces, and shielding of light by other absorbing molecules could change depending on the specific BBOA material. The BrC chromophores of chaparral fuels had shorter equivalent photochemical lifetimes compared to BBOA generated from the canopies of conifer fuel types. On the whole, these results suggest that some of the primary BrC chromophores may be destroyed by UV irradiation after several hours.

Despite the rapid change in the distribution of individual chromophores, the overall integrated BrC absorbance from 300 nm to 700 nm decayed with a much longer lifetime of 10 days to 41 days. This contrasts with individual chromophores in particles that decayed on the time scale of 0.4 to 1.6 days. Taken together the two types of photolysis experiments suggest that the absorption by the pool of BrC compounds persists during irradiation longer than individual BrC chromophores. Our findings also show that ecosystem components, and the combustion conditions they create, could influence the apparent BrC absorption lifetimes. Smoldering subalpine fir duff BBOA had the shortest equivalent lifetime of 10 days, while BBOA from the canopy fuel had a longer BrC absorption lifetime of 41 days. The canopy fuels contributed to more flaming combustion. These fairly long BrC absorption lifetimes suggest that BrC is largely photostable upon direct photolysis, and other chemical aging mechanisms such as OH oxidation may be more important on atmospheric timescales. Based on these results, modelers should first focus on accounting for chemical aging mechanisms other than photolysis, such as heterogeneous oxidation by OH.

CHAPTER 5:

Formation of Light-Absorbing Organosulfates during Evaporation of Secondary Organic Material Extracts in the Presence of Sulfuric Acid

Abstract. Organic aerosols affect climate by scattering or absorbing incoming solar radiation. Secondary organic material (SOM), which represents the major chemical constituent of atmospheric aerosol particles, is produced by the oxidation of atmospheric volatile organic compounds (VOC). SOM in clouds, fogs, and aerosols undergoes concentration/dilution cycles due to the evaporation/condensation of water droplets. These physical processes could potentially result in the chemical processing of SOM, or the formation of new, light-absorbing compounds. In this study, model SOM was generated through smog chamber photo-oxidation and flow tube ozonolysis of various atmospherically-relevant anthropogenic and biogenic VOCs, including toluene (TOL), limonene, α -pinene, β -pinene (BPIN), and isoprene (ISO). Collected SOM was extracted in water, and the solutions were acidified with sulfuric acid to pH = 2 and dried to simulate the evaporation of the particle. Significant changes in mass absorption coefficients (MAC) were observed after evaporation and re-dissolution of SOM in the presence of sulfuric acid. At visible wavelengths, TOL/OH SOM had the highest MACs after evaporation, while BPIN/O₃ SOM had the lowest. Exceptions to evaporation increasing MACs in the presence of sulfuric acid were ISO/OH, and TOL/OH/NO_x. Additionally, light-absorbing species were separated and detected using an HPLC-PDA-HRMS platform. Overall, the abundance of organosulfates was correlated with MACs. Five brown carbon (BrC) chromophores were

separated and assigned chemical formulas, including $C_{10}H_{16}SO_6$, $C_{10}H_{14}SO_6$, $C_{10}H_{16}SO_5$, $C_{11}H_{16}SO_7$, and $C_{11}H_{18}SO_8$. This indicates that such processes may occur in the atmosphere, substantially modifying the molecular composition and optical properties of SOM. Evaporation of filter extracts from the field or laboratory could similarly produce organosulfates as artifacts if the extract is sufficiently acidic before the evaporation.

5.1 Introduction

Observations show that most atmospheric particles are dominated by secondary organic material (SOM) formed by the oxidation of VOCs by ozone (O_3), hydroxyl radicals (OH), and other oxidants. Atmospheric VOCs are highly variable, with over 3000 types thought to exist (Piccot et al., 1992). Trees are a major biogenic source of fragrant VOC molecules, such as limonene and α -pinene (Lamb et al., 1985). In urban areas, the major sources of volatile organic compounds are fossil fuel combustion and industrial emissions (World Health Organization, 1989). Aerosols produced from these VOCs directly affect the atmospheric energy balance by absorbing or scattering sunlight, depending on their optical properties. Additionally, aerosols serve as cloud condensation nuclei upon which liquid droplets can form (Boucher and Anderson, 1995). Aerosols that strongly absorb visible radiation are of particular interest, as they may contribute to the warming of the lower atmosphere by absorbing sunlight (IPCC, 2013).

SOM is known to undergo chemical changes resulting from interactions of particles with sunlight, water, and other atmospheric components. It is important to understand the nature of these changes in order to better predict the health and climate impacts of atmospheric aerosols. For example, condensed atmospheric water, associated with aerosols, clouds or fogs, is known to undergo various evaporation/condensation cycles that can induce specific chemical

transformations of SOM that need to be understood. These processes can be accompanied by the formation of new compounds, such as esters of sulfuric acid known as organosulfates, with the help of acid catalysis by sulfuric acid, which is commonly found in fog droplets and aerosol particles (Finlayson-Pitts and Pitts, 2000). The mechanisms by which organosulfates are formed could be through alcohol esterification (Darer et al., 2011; Minerath et al., 2008; Minerath and Elrod, 2009) and the ring opening of epoxides by sulfuric acid (Darer et al., 2011; Eddingsaas et al., 2010; Minerath and Elrod, 2009), both are acid-catalyzed. Under ambient conditions it is kinetically unlikely that the former mechanism is responsible for organosulfate formation, however, not many studies have examined organosulfate formation in evaporating droplets, which can have much lower pH and higher concentrations of SOM. The acid-catalyzed ring opening of epoxides by sulfate is kinetically favored under ambient conditions (Darer et al., 2011; Eddingsaas et al., 2010; Minerath and Elrod, 2009), and represents a more common mechanism of organosulfate formation.

Evaporation of cloud and fog droplets containing SOM and sulfuric acid not only produces new compounds, but can also make SOM light-absorbing. A previous study by Nguyen et al. 2012 found that light-absorbing chromophores were produced when aqueous extracts of SOM generated from d-limonene ozonolysis, acidified to pH=2 with sulfuric acid, were evaporated. The evaporation of acidified d-limonene SOM extracts was found to significantly accelerate otherwise slow aqueous phase acid-catalyzed aldol condensation reactions and lead to the formation of sulfur-containing organic compounds. Simultaneously, substantial changes in the optical properties of the SOM extract were observed.

The effects of evaporation in the presence of sulfuric acid on the optical properties of SOM other than d-limonene SOM have not been studied. This study focused on the evaporative

browning of model biogenic and anthropogenic SOM in the presence or absence of sulfuric acid. In addition, we explored the effect of the extraction solvent and the amount of solution on the mass absorption coefficient of the material produced during the evaporation. The goals of this work were twofold: first, to obtain a better understanding of the optical properties and second, to characterize chromophores and major products of SOM undergoing evaporative browning. Evaporation of SOM extracts in the presence of sulfuric acid enhanced the absorbance of visible wavelengths for most precursor/oxidant combinations.

5.2 Materials and Methods

5.2.1 SOM Generation

Model SOM was prepared from VOCs using O₃-initiated oxidation and OH-initiated photooxidation conditions, with and without added NO_x, as shown in Tables 1 and 2. VOCs, including isoprene (ISO), α -pinene (APIN), β -pinene (BPIN), limonene (LIM), and toluene (TOL) were used as purchased from Sigma-Aldrich (typically >99% pure) without further purification.

SOM generation by photooxidation occurred in a ~5 m³ Teflon chamber, equipped with UV-B lights (FS40T12/UVB, Solarc Systems Inc.) with emission centered at 310 nm. The reactions took place under dry conditions (relative humidity < 2%), in the absence of seed particles. Chamber experiments were carried out either under “high-NO_x” oxidation conditions, with approximately 500 ppb (parts per billion by volume) of NO added to the chamber to simulate an urban atmospheric environment, or “low-NO_x” oxidation conditions, without any NO added to the chamber in order to simulate a remote atmospheric environment. For the OH precursor, 90 μ L of H₂O₂ (Aldrich; 30% by volume) was injected in the chamber by evaporation

under a stream of zero air resulting in 5 ppm of H₂O₂ vapor in the chamber. Precursor VOC was added to the chamber using the same method, with the starting VOC mixing ratio in the chamber on the order of 1 ppm. The starting mixing ratio of isoprene, however, was larger at 15 ppm, and H₂O₂ was increased to 10 ppm, in order to generate adequate SOM mass loadings for the evaporation experiments. The chamber contents were mixed for several minutes using a Teflon™ fan, which was then turned off to minimize particle wall losses. The UV-B lamps were turned on for 2 to 5.5 hours to initiate photochemistry (Table 5.1). SOM particle concentration within the chamber was monitored by a TSI model 3936 scanning mobility particle sizer (SMPS). A Thermo Scientific model 49i ozone analyzer recorded O₃ data, while a Thermo Scientific model 42i-Y NO_y analyzer recorded NO/NO_y data. SOM passed through an activated carbon denuder at approximately 18 SLM (standard liters per minute) and particles were collected using PTFE filters (0.2 μm pore size, 47 mm diameter, Millipore Fluoropore). Collection times ranged from 2 to 3 hours, with approximately 0.3 to 2.9 mg of SOM collected on the filter, depending on the sample. The amount of SOM on the filter was estimated from SMPS data, assuming a particle density of 1.2 g/cm³ and 100% collection efficiency by the filters. This particle density reflects representative average densities of anthropogenic and biogenic SOM reported by Hallquist et al. 2009. In several cases, the amount was verified by explicit weighing of the filter. The SMPS and filter based measurements of the collected SOM mass were typically within 35% of each other.

The O₃-initiated reactions were carried out in a 17 L flow tube reactor described by Bones et al. (2010). Liquid VOC was injected by a syringe pump at a rate of 25 μL/h into a 5 SLM flow of zero air. A 0.5 SLM flow of oxygen (Airgas; 99.994% purity) was sent through an ozone generator and a custom-made ozone photometric detector. The O₃- and VOC-containing flows were mixed at the entrance of the flow cell. Typical mixing ratios in the flow cell ranged

from 60-100 ppm (parts per million by volume) of O₃ and 10 ppm of VOC. The residence time in the flow tube was less than 5 minutes, but this was sufficient to oxidize most of the VOC and to form SOM. A 1-m charcoal denuder scrubbed the residual O₃ and gas-phase organic compounds from the aerosol flow exiting the reactor. SOM was collected on pre-weighed polytetrafluoroethylene (PTFE) filters (Millipore Fluoropore, 0.2 μm pore size). Depending on the yield of SOM, collection time for the flow tube was approximately 30 min to 2 h. The samples were either analyzed immediately or sealed and frozen for future analysis. The amount of SOM on the filter was determined by weighing. The reaction conditions are summarized in Table 5.2.

Table 5.1: Names and abbreviations of VOCs used to generate SOM samples from OH photooxidation in the smog chamber. The samples are hereafter referred to as VOC/OH if prepared under low-NO_x conditions, and VOC/OH/NO_x if prepared under high-NO_x conditions. The reaction time in the chamber is equivalent to the irradiation time.

Precursor	Oxidant	Initial VOC (ppm)	Initial NO (ppb)	Reaction time (h)	Collection time (h)	Typical amount collected (mg)
d-Limonene (LIM)	OH	1	0	2	2.5	2.0
d-Limonene (LIM)	OH/NO _x	1	500	2	3	2.9
α-pinene (APIN)	OH	1	0	3	2.5	1.6
α-pinene (APIN)	OH/NO _x	1	500	2.5	2.5	2.2
Isoprene (ISO)	OH	15	0	5.5	3	0.3
Isoprene (ISO)	OH/NO _x	15	500	4	2.5	2.7
Toluene (TOL)	OH	1	0	3.5	3	0.9
Toluene (TOL)	OH/NO _x	1	500	3	2	1.6

Table 5.2: Names and abbreviations of VOCs used to generate SOM samples from flow tube ozonolysis. The initial VOC concentration in flow tube experiments is the steady-state mixing ratio the VOC would have in the absence of ozone. Ozone was added in small excess with respect to the VOC. The flow tube residence time is on the order of minutes. The samples are hereafter referred to as VOC/O₃.

Precursor	Initial VOC (ppm)	Typical amount collected (mg)
d-Limonene (LIM)	10	4.0
α-pinene (APIN)	10	2.4
β-pinene (BPIN)	10	2.0

5.2.2 SOM Extraction

In most experiments, the SOM was extracted into water by placing the filter on the bottom of a beaker, adding water, and shaking the beaker for about an hour. The amount of water was adjusted in each sample to obtain stock solutions with the same mass concentrations (~0.3 mg/mL) of the dissolved organics. The extraction was estimated to be at least 90% complete based on comparison of the absorption spectra of the primary and secondary extracts from the same filter (Romonosky et al., 2016). A fresh solution was prepared for each experiment and used immediately. In a few LIM/O₃ SOM experiments, methanol or acetonitrile were used as extracting solvents instead of water, since all three solvents are commonly used to extract SOM.

5.2.3 Evaporation Experiments and MAC Measurements

A 2 mL aliquot of the SOM extract was transferred in a 1 cm quartz cuvette, and an UV/Vis absorption spectrum was taken in a dual-beam spectrophotometer (Shimadzu UV-2450), with another cuvette filled with the pure solvent used as reference. For samples that were acidified, the pH of the solution was adjusted to pH = 2 using sulfuric acid, such that the volume of the sample solution did not increase by more than 300 µL, and the UV/Vis spectrum was recorded again. The pH of the solution was measured with a Mettler Toledo SevenEasy S20 pH meter.

The solution was then transferred to a 20 mL vial and evaporated to near-dryness using a rotary evaporator (Buchi R-210) at a water bath temperature of 50 °C. The evaporation rate was constant when using a particular solvent, as the water temperature was regulated to 50 °C. After evaporation, water was added to the vial to reach the initial pre-evaporation volume. Control experiments were performed in which the same procedure was followed, except for the

acidification step. In several cases, the evaporation and re-dissolution step was repeated to see if additional browning could be produced by one more evaporation step.

Wavelength-dependent mass absorption coefficients (MACs), in units of $\text{cm}^2 \text{g}^{-1}$, were calculated from the base-10 absorbance, A_{10} , of each SOM extract with the solution mass concentration, C_{mass} (g cm^{-3}), and path length, b (cm):

$$MAC(\lambda) = \frac{A_{10}^{\text{solution}}(\lambda) \times \ln(10)}{b \times C_{\text{mass}}} \quad (1)$$

5.2.4 Brown Carbon (BrC) Chromophore Analysis

High performance liquid chromatography coupled to a photodiode array detector and a high resolution mass spectrometer, referred to as HPLC-PDA-HRMS, was employed for the analysis of BrC chromophores. The evaporated SOM residue was re-constituted in a 60% water/40% acetonitrile by volume solution. The re-constituted extract was injected (5 μL) into a reverse-phase column (Acquity HSS T3 column 2.1 x 100 mm, 8 μm) at a flow rate of 0.3 mL/min with a mobile phase gradient utilizing 0.1% formic acid in water (A) or acetonitrile (B) solvents. A 17 min gradient was applied: eluent (B) was kept at 1% for 2 min and was increased to 100% in 11 min, this composition is maintained for 2 min before returning to the initial condition for 2 min (1% of eluent B). Separated compounds then passed through the PDA to record absorption spectra over a 200-700 nm range before entering the HRMS (Q-Exactive Hybrid Quadrupole-Orbitrap, Thermo Scientific, USA). Compounds were negatively charged by electrospray ionization using the following settings: a spray potential of 3 kV, Aux gas heater temperature of 250 $^{\circ}\text{C}$, sheath gas flow rate of 42 au, Aux gas flow rate 25 au, capillary temperature 350 $^{\circ}\text{C}$, S-lens RF level 50. Ions were subsequently detected within a range of 50-750 m/z , with a mass

accuracy of 0.5-2.0 ppm and a resolving power of 140,000 at m/z 200. Data were collected using Thermo Xcalibur software (2.2 SP1.48; Thermo Fisher Scientific Inc.). BrC chromophores were first analyzed in the same software, and ions corresponding to BrC chromophores were further analyzed using the open source software toolbox MZmine version 2.26 (Pluskal et al., 2010). Formula Calculator v1.1 was used to assign neutral chemical formulas to ions of interest.

5.3 Results and Discussion

5.3.1 Optical Properties

Wavelength-dependent MACs for various SOM during all stages of the experiment are summarized in Figure 5.1. The first step of the experiment was adjusting the pH of the solution to pH=2 by adding sulfuric acid. In some cases, the pH adjustment had a minimal effect on the absorbance spectrum of the solution (e.g., LIM samples) but for most other SOM the spectrum changed presumably due to shifting acid-base equilibria for carboxylic acids and possibly due to acid-catalyzed reactions between SOM compounds.

Next, the acidic SOM solution was evaporated in 1-5 minutes depending on the solvent, and the solution was re-constituted in the initial volume of solvent. Browning was observed to happen quickly when the solution was evaporated to near dryness. For most SOM, especially for LIM-derived SOM, evaporation enhanced the MACs for the visible wavelengths. TOL-derived SOM had the highest MACs after evaporation, while BPIN/O₃ had the lowest. Exceptions to evaporation increasing MACs in the presence of sulfuric acid were ISO/OH, and TOL/OH/NO_x. In the latter case, absorbing nitrophenols are present in SOM to begin with, resulting in the observed absorbance. Any additional chromophores produced by the evaporation made only a small contribution to the already high absorption coefficients.

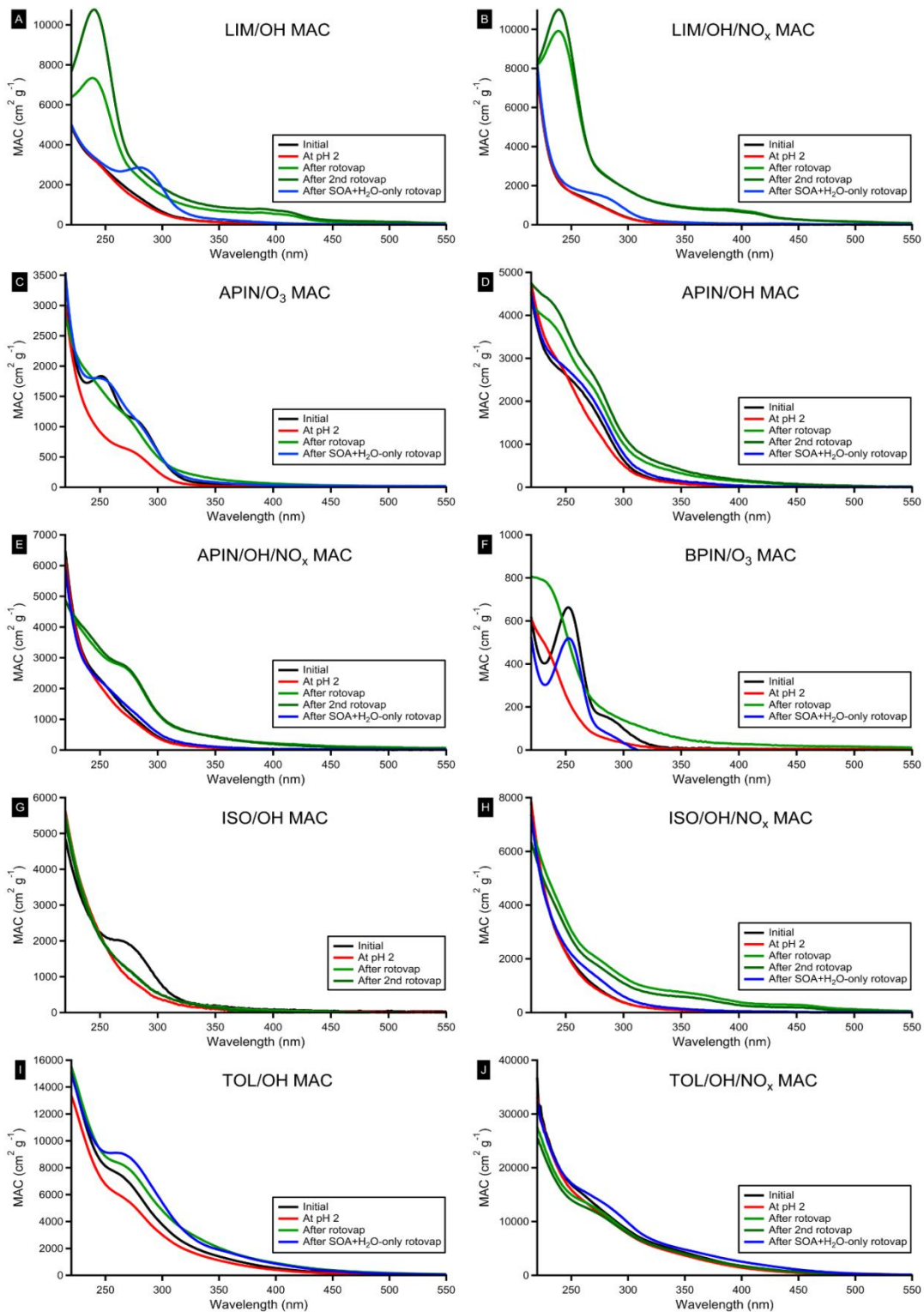


Figure 5.1: MAC values of SOM from (a) LIM/OH, (b) LIM/OH/NO_x, (c) APIN/O₃, (d) APIN/OH, (e) APIN/OH/NO_x, (f) BPIN/O₃, (g) ISO/OH, (h) ISO/OH/NO_x, (i) TOL/OH, and (j) TOL/OH/NO_x, in initial aqueous solution (black), after addition of H₂SO₄ to the solution until it reached pH 2 (red), after evaporation of acidified solution (green), after second evaporation of same solution (dark green), and after evaporation with SOM and water only (blue).

The effect of evaporating the reconstituted SOM a second time is also shown in Figure 5.1. The second evaporation produced only minor changes to MACs compared to the results of the first evaporation. This implies that the evaporative browning proceeded nearly to completion after the first evaporation step.

Control experiments were performed where non-acidified SOM solutions were evaporated. In most cases, this did not appreciably increase MACs in the visible wavelength range. However, in the case of TOL/OH, MACs increased after evaporation, even without the presence of sulfuric acid. This suggests that different types of BrC chromophores are formed during evaporation for this SOM, potentially by oligomerization of hydroxylated aromatic units.

The effect of the starting SOM solution volume was explored for the LIM/O₃ SOM solution in Figure 5.2. The initial 2 mL of 0.3 mg/mL solution at pH =2 was undiluted (a), diluted to 4 mL (b), or diluted to 20 mL, with pH increasing from 2 to 3 (c). Since the initial absolute amounts of sulfuric acid and SOM available for browning reactions were the same in all cases, we did not expect a strong effect. Indeed, the experiments showed that the effect was rather small. In doubling the volume of solvent (2 mL in Fig. 2a vs 4 mL in Fig 2b) MACs at 400 nm were approximately the same at 450 cm²/g. A tenfold increase in volume of solvent (Fig. 2c) resulted in a MAC at 400 nm of 610 cm²/g, representing an increase of 35%. The observed absorption of BrC chromophores was consistent with concentration; there was no evidence that the observed absorption for the evaporated extract was due to interactions between molecules i.e., charge transfer complexes (Phillips and Smith, 2014, 2015; Sharpless and Blough, 2014).

For the largest volume of LIM/O₃ SOM (20 mL), the SOM was reconstituted in either 2 mL or 20 mL after the first evaporation (Fig. 2c). The MACs calculated from these two dilutions was the same except in the vicinity of the 400 nm band. The change implies that the 400 nm

band is likely due to acidic compounds, and that the deprotonated forms of these compounds absorb weaker than the neutral forms.

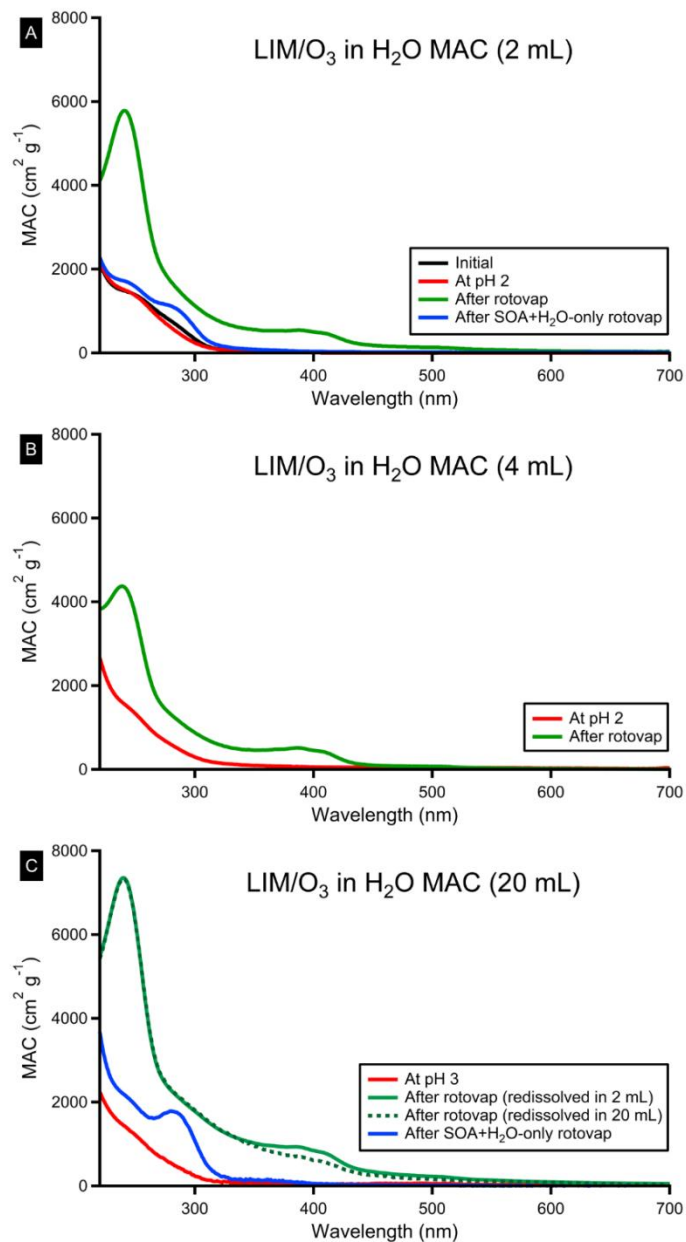


Figure 5.2: MAC values of LIM/O₃ SOM dissolved in 2 mL of water (black trace in panel a) (black). Also shown are MAC values after the addition of H₂SO₄ to pH 2 in 2 mL of water and further dilution to 4 mL and 20 mL (red); after evaporation of the solutions (green), and after evaporation with LIM/O₃ SOM and water only (blue). In (b), the evaporated solution was re-dissolved in 4 mL of H₂O, and MAC values were calculated (green). In (c), the evaporated solution was re-dissolved first in 2 mL of H₂O (green) and then to a total volume of 20 mL of H₂O (dark dashed green).

The choice of evaporated solvent strongly affected the MACs of the LIM/O₃ SOM, as shown in Figure 5.3. Three solvents commonly used to dissolve SOM were used here, namely, water (a), acetonitrile (b), and methanol (c). In water, we see a distinctive peak at 400 nm, likely due to acidic forms of compounds being more absorbing, resulting in an enhancement in this region. Acetonitrile and methanol extracts have much higher MACs, probably due to the fact that organic solvents are evaporated off more completely making it possible to achieve higher acidity due to higher concentrations at the end of the evaporation process.

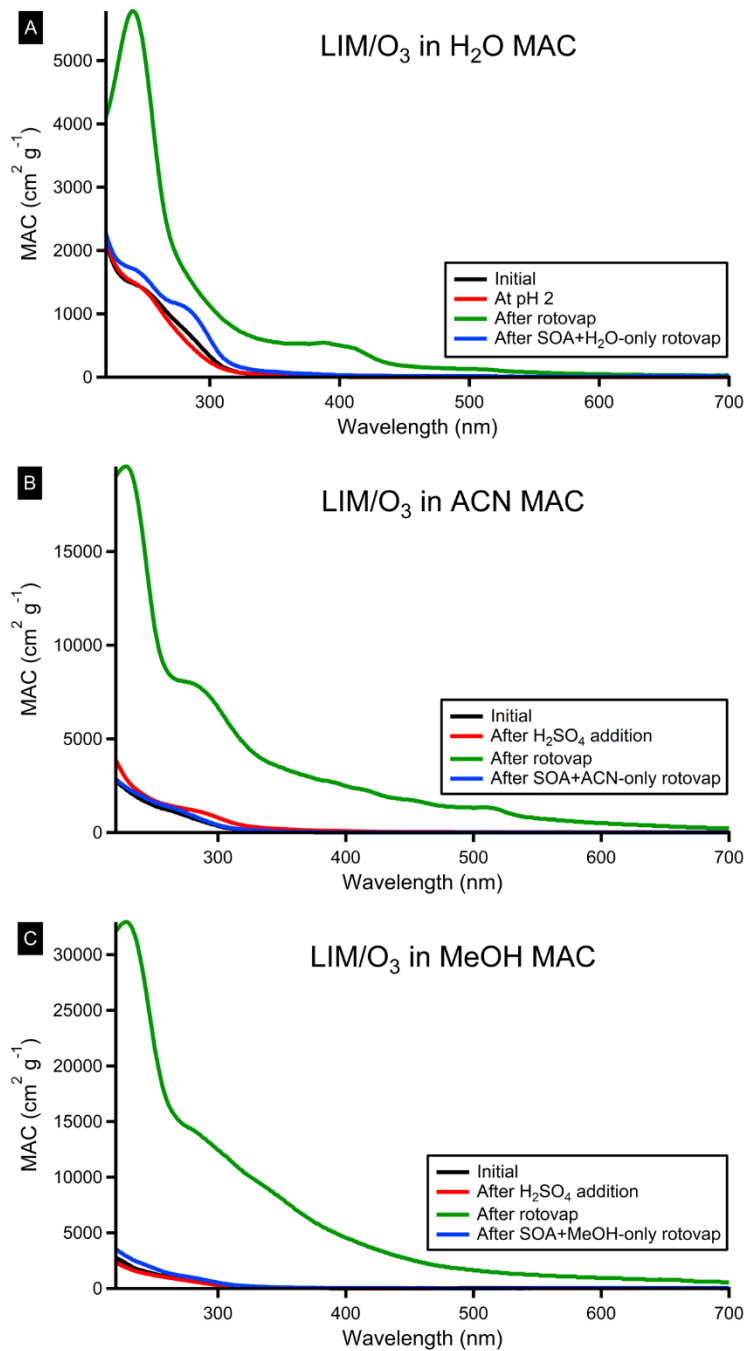


Figure 5.3: MAC values of LIM/O₃ SOM, with the solvent as (a) water, (b) acetonitrile, or (c) methanol, in initial solution (black), after addition of H₂SO₄ to pH 2 in water or addition of an equal amount of H₂SO₄ in acetonitrile and methanol (red), after evaporation of solution (green), and after evaporation with LIM/O₃ SOM and solvent only (blue).

5.3.2 BrC Chromophores

For the analysis of the possible products formed during the evaporative browning, we chose to focus on LIM/O₃ because its evaporation resulted in a large increase in MACs, and a distinct peak around 400 nm (Fig. 2). Figure 5.4 shows integrated ESI mass spectra for evaporated LIM/O₃ SOM extracted in acetonitrile (Figure 5.4a) or water (Figure 5.4b) in the presence or absence of sulfuric acid. Peaks corresponding to formulas with oxygen-to-sulfur ratios greater than or equal to 4 are highlighted because they are potential organosulfate species. The relative abundance of these organosulfate species positively correlates to the MACs in Figure 5.3. In other words, the acetonitrile extract has higher MACs (Figure 5.3) compared to the water extract while having a mass spectrum dominated by organosulfur compounds in the presence of sulfuric acid (Figure 5.4a). For the water extract evaporated in the presence of sulfuric acid, possible organosulfate species make up a lower fraction of total observed abundance. This implies that organosulfate compounds contribute to the pool of BrC species in the evaporated sample, and does not rule out the possibility that other BrC compounds are formed simultaneously.

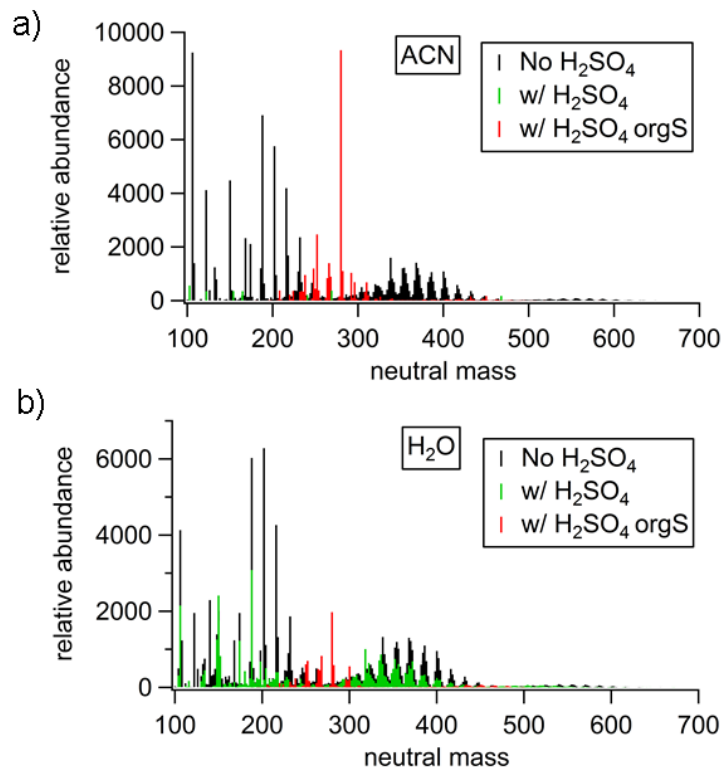


Figure 5.4: Combined positive and negative mass spectra when limonene ozonolysis SOM is extracted in a) acetonitrile and b) water, then evaporated and re-dissolved in the extraction solvent. Peaks in green and red appear when sulfuric acid (H_2SO_4) is added prior to evaporation. Peaks in red contain sulfur and four or more oxygens, and identified as potential organosulfates in this paper. Peaks in black occur when sulfuric acid is not added. The largest red peak corresponds to $\text{C}_{10}\text{H}_{16}\text{SO}_7$.

In both water and acetonitrile extracts, the most abundant organosulfate compound is $\text{C}_{10}\text{H}_{16}\text{SO}_7$ (Figure 5.4). The single ion chromatogram (SIC) for the corresponding ion with nominal m/z 279 in the negative mode is displayed in Figure 5.5. The SIC shows two major isomers of $\text{C}_{10}\text{H}_{16}\text{SO}_7$ in both extracts. Other prominent sulfur-containing compounds included $\text{C}_{10}\text{H}_{16}\text{SO}_5$, $\text{C}_{10}\text{H}_{18}\text{SO}_6$, $\text{C}_{10}\text{H}_{18}\text{SO}_7$, and other compounds containing the original 10 carbon atoms from the limonene skeleton. There were many prominent C_9 compounds as well, likely formed from the oxidation of the exocyclic carbon-carbon double bond, producing molecules related to ketolimonaldehyde (Nguyen et al., 2013). These compounds include $\text{C}_9\text{H}_{16}\text{SO}_6$, $\text{C}_9\text{H}_{14}\text{SO}_8$, $\text{C}_9\text{H}_{16}\text{SO}_7$, and $\text{C}_9\text{H}_{14}\text{SO}_6$.

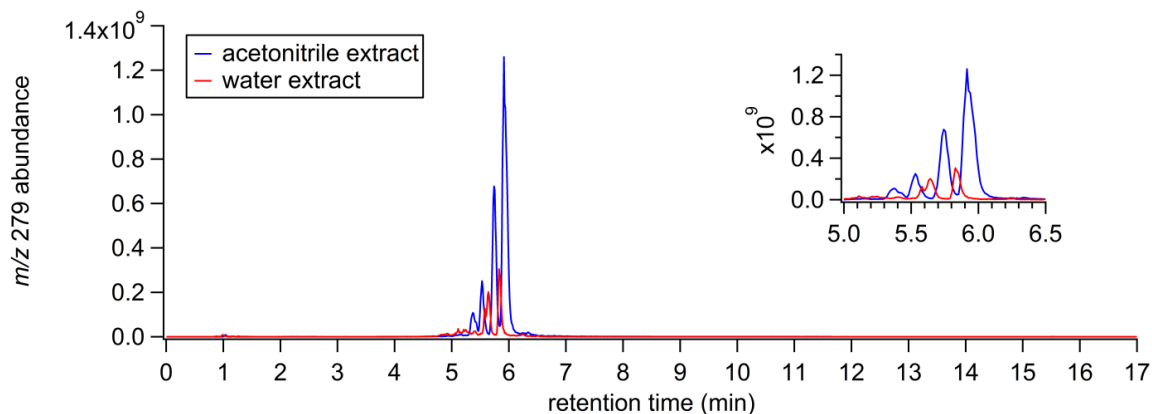


Figure 5.5: Single ion chromatogram for the m/z 279 ion in the negative mode, corresponding to $C_{10}H_{16}SO_7$. The acetonitrile extract is in blue and water extract in red.

The products observed during the evaporative browning may correlate to products of d-limonene ozonolysis formed in experiments with highly acidic seed particles. Iinuma et al. 2007 prepared LIM/ O_3 SOM in a chamber with sulfuric acid seed particles. The SOM were extracted, evaporated to dryness, and reconstituted before chemical analysis of organosulfates. The most prominent sulfur-containing ion they observed was $C_{10}H_{18}SO_7$. The structure that they proposed, based off tandem ion fragmentation analysis is shown in Figure 5.6a. The aldehyde and ketone functional groups result from ozone attacking the endocyclic double bond in d-limonene. An epoxide is then formed from ozone attacking the exocyclic double bond. Sulfuric acid attacks the epoxide, resulting in hydroxide and sulfate groups. We observed $C_{10}H_{18}SO_7$ in the water extract, but not the acetonitrile extract.

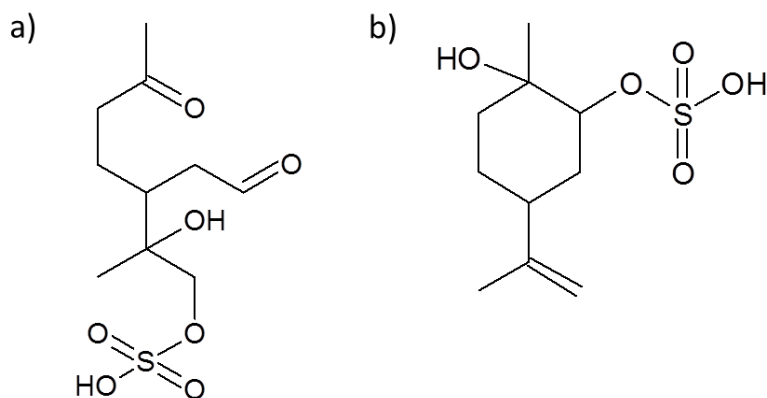


Figure 5.6: Structures of organosulfates a) C₁₀H₁₈SO₇ reported in Iinuma et al. (2007) based on MSⁿ analysis b) C₁₀H₁₈SO₅ reported in Wang et al. 2017 based on synthetic standards.

The structure for C₁₀H₁₈SO₇ identified by Iinuma et al. 2007 is providing hints for the structures and formation mechanisms of related organosulfates. For example, dehydration of C₁₀H₁₈SO₇ would give C₁₀H₁₆SO₆, which is observed in in the present study as the major product. Concentrated sulfuric acid is a classic desiccant, so it is conceivable that evaporating SOM in the presence of sulfuric acid dehydrates some of SOM compounds. Dehydration results in the formation of C=C bonds from alcohols, thus increasing the double bond equivalent (DBE) of the products. For example, in the absence of sulfuric acid, the abundance weighted average DBE for all observed compounds is 4.4, while in the presence of sulfuric acid it is 4.8. Additional evidence for the acid-catalyzed dehydration is shown in Figure 5.7. A number of the compounds formed in the presence of sulfuric acid are shifted to lower *m/z*, compared to the non-acidified extract, by the exact molecular weight of water. Some of the compounds with high enough DBE may become sufficiently conjugated to absorb near-UV and visible radiation, accounting for the brown color of the residue formed in the evaporation.

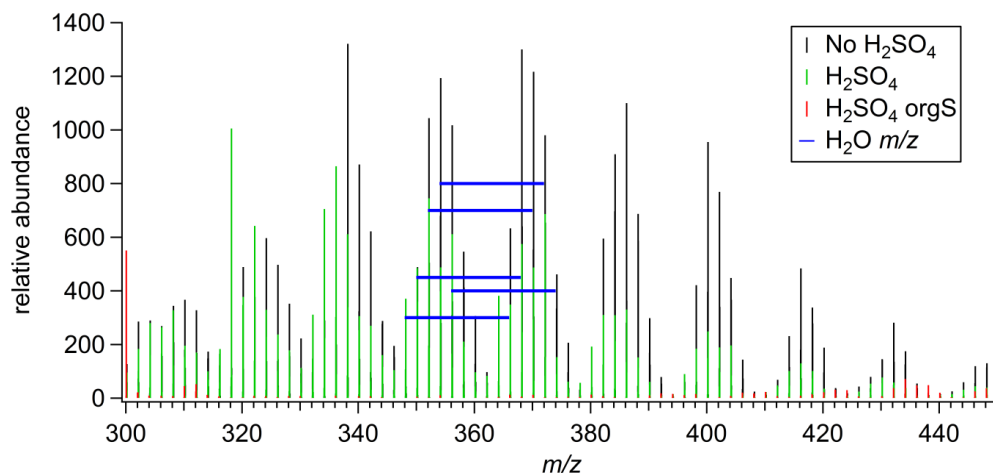


Figure 5.7: Dimer region of the mass spectrum corresponding to the LIM/O₃ SOM water extract evaporated in the presence of sulfuric acid. Horizontal blue lines indicate the loss of water.

We used HPLC-PDA-HRMS to determine specific elemental formulas for compounds that could contribute to absorbance in the near-UV and visible ranges. Table 5.3 lists assigned chemical formulas for separated compounds that absorb in these ranges. They are listed by their chromatographic retention times, the absorption spectrum detected by the PDA, and the assigned chemical formula(s). Chromophores are also ranked by abundance for each molecule in the mass spectrum in Figure 5.4 with 1 being the most abundant. All separated BrC chromophores are assigned as organosulfates, and are observed in both acetonitrile and water extracts. Due to limits in HPLC separation, we were not able to isolate and assign compounds responsible for the peak in absorption at 400 nm (Table 5.2). However, it is clear from the HPLC-PDA chromatogram in Figure 5.8 that there are compounds absorbing into the visible region that elute between about 8 and 12 minutes.

The first three chromophores in Table 5.3 are C₁₀, suggesting they are related to limonaldehyde in structure, and by extension, the structure in Figure 5.6a. However, they have higher DBEs, presumably resulting from the acid-catalyzed dehydration discussed above. In addition, compounds containing eleven carbon atoms, such as C₁₁H₁₆SO₇ and C₁₁H₁₈SO₈ were

also observed. Such C_{11} compounds have been previously observed in ozonolysis of monoterpenes (Bateman et al., 2009; Tu et al., 2016; Walser et al., 2008), but their formation mechanism is not very clear. Presumably they form by secondary reactions between the primary products, for examples reactions between C_{10} species and highly reactive formaldehyde (Nguyen et al., 2010), which is a direct product of d-limonene ozonolysis.

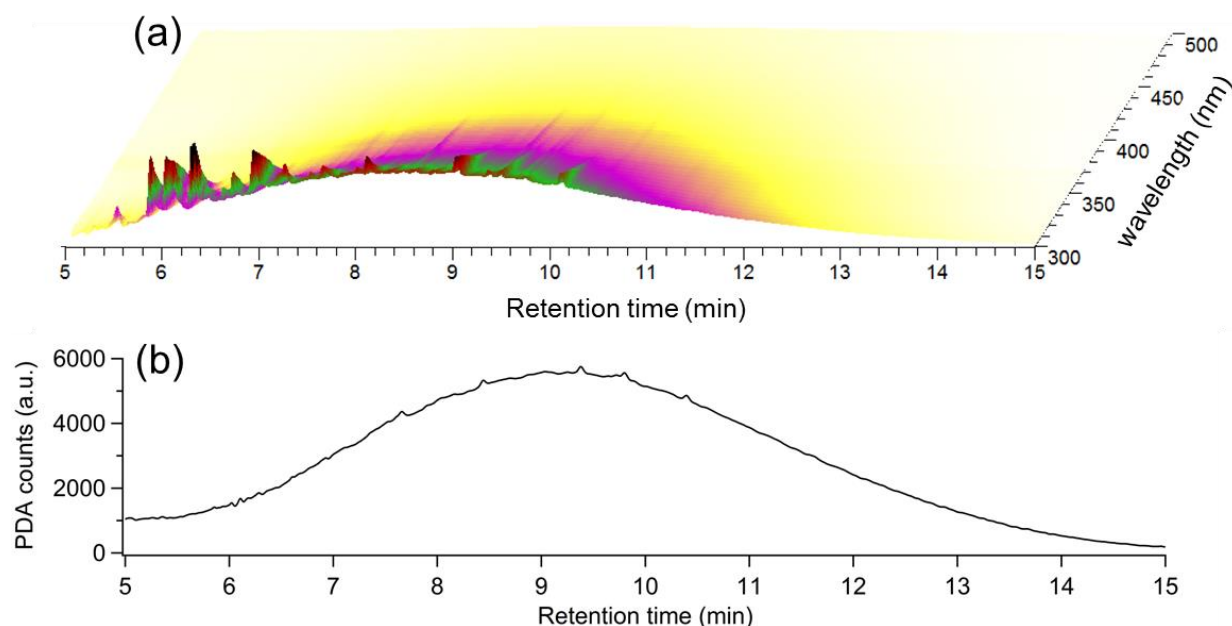
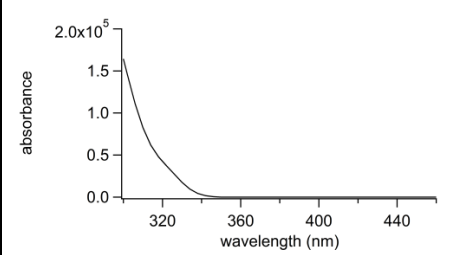
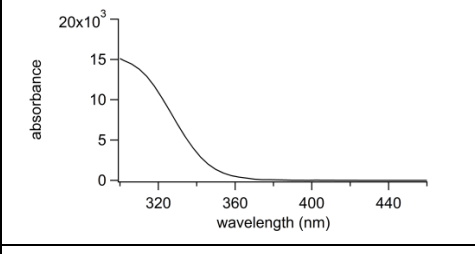
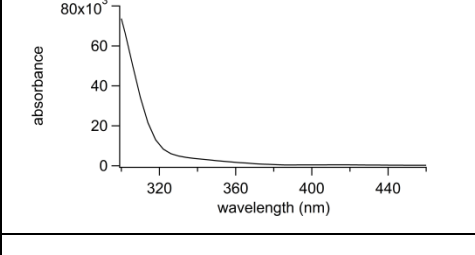
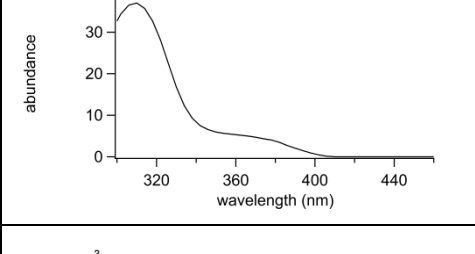
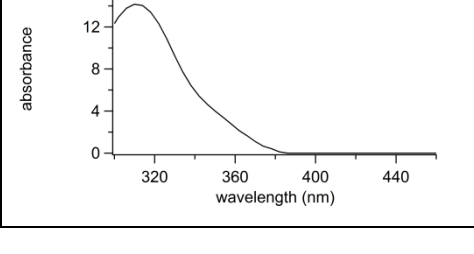


Figure 5.8: 3D (a) and 2D (b) HPLC-PDA chromatograms for the water LSOM extract. (b) shows the integrated PDA counts for 380 to 450 nm. Between 8 and 12 minutes, compounds absorbing visible light elute from the column, and are largely unresolved.

Table 5.3: Brown carbon chromophores in ACN and H₂O extracts with H₂SO₄ present that were separated with HPLC. For each separated absorbance, we give the observed PDA retention time, the PDA spectrum, assigned, neutral chemical formula, as well as the ranking of abundance in the mass spectrum with the most abundant compound being first, or 1.

PDA retention time (min) (extract observed)	PDA spectrum	Assigned, neutral chemical formula	Ranking of abundance in mass spectrum (Fig 4)	
5.90 (H ₂ O), 5.78 (ACN)		C ₁₀ H ₁₆ SO ₆ C ₁₀ H ₁₈ SO ₆	ACN w/ H ₂ SO ₄	10 3
			H ₂ O w/ H ₂ SO ₄	30 82
6.05 (H ₂ O)		C ₁₀ H ₁₄ SO ₆	ACN w/ H ₂ SO ₄	7
			H ₂ O w/ H ₂ SO ₄	139
6.41 (ACN)		C ₁₀ H ₁₆ SO ₅	ACN w/ H ₂ SO ₄	4
			H ₂ O w/ H ₂ SO ₄	482
6.50 (ACN)		C ₁₁ H ₁₆ SO ₇	ACN w/ H ₂ SO ₄	7
			H ₂ O w/ H ₂ SO ₄	693
6.65 (ACN)		C ₁₁ H ₁₈ SO ₈	ACN w/ H ₂ SO ₄	12
			H ₂ O w/ H ₂ SO ₄	276

5.4 Summary and Implications

Ten types of SOM were extracted, evaporated in the presence of sulfuric acid, and re-dissolved to monitor and characterize the chemical changes occurring from a common physical process in the atmosphere for cloud, fog, and aqueous aerosol droplets. MACs were measured during every step of the experiment, and in general, the evaporation produced highly-absorbing chromophores with absorption extending into the visible wavelength range. TOL/OH SOM had the highest MACs while BPIN/O₃ had the lowest. LIM/OH, LIM/OH/NO_x, APIN/OH, ISO/OH/NO_x all showed appreciable increases in MACs from the procedure. Evaporating and re-dissolving SOM a second time did not result in a large change in MACs. MACs are much higher when LIM/O₃ SOM was extracted in organic solvents and then evaporated, probably because more of the solvent is evaporated by the rotary evaporator in the cases of organic solvents. The structures of the proposed BrC chromophores are not known, but could be similar to those shown in Figure 5.6. The mechanism by which the structure shown in Figure 5.6a is obtained was discussed by Iinuma et al. (2007). The structure in Figure 5.6b is formed from the acid-catalyzed ring opening of an epoxide by sulfuric acid, and was observed in (Wang et al., 2017a).

The abundance of organosulfates in ESI mass spectra is correlated with MACs in the visible region. The acetonitrile extract in the presence of sulfuric acid was dominated by organosulfates, while the water extract had a significant fraction of C_xH_yO_z compounds. The organosulfates in this study had higher DBEs than those reported in Iinuma et al. (2007). We postulate that sulfuric acid plays a role in either acid-catalyzed dehydration or autooxidation reactions that result in more degrees of unsaturation. We separated five BrC chromophores, all of them organosulfates, including C₁₀H₁₆SO₆, C₁₀H₁₄SO₆, C₁₀H₁₆SO₅, C₁₁H₁₆SO₇, and C₁₁H₁₈SO₈. This physical process of evaporation in the presence of sulfuric acid could cause a significant

change in the optical properties of SOM under ambient conditions by making reactions producing organosulfates more kinetically favorable.

It is common when characterizing the organic fraction of particulate matter collected on filters to pre-concentrate the extracts by solvent evaporation. Such a protocol enables organic analytes to be in the dynamic range of the detection method. Evaporation occurs in a fume hood under a stream of inert gas, such as nitrogen, or by a rotary evaporator. Light-absorbing organosulfate compounds could be potentially produced in this process as artifacts of acid-catalyzed reactions, such as those characterized in this study. The resulting evaporation reaction products could be mistakenly identified as species occurring in field or laboratory particles. The experiments describe here approximate the conditions in the field and laboratory studies whereby producing these artifacts are feasible. For example, concentration of particulate $[H^+]$ measured in the southeastern United States have been shown to reach 10 nmol m^{-3} (Guo et al., 2015). Sampling such particles at 100 L/min for one day, and extracting the filter in 1 mL of solvent would result in a pH of 3, which is the same as the starting pH for the experiments describe here. In the laboratory experiments, ammonium bisulfate seeds are commonly used in smog chambers to study acid-catalyzed reactions in particles. Injecting $100 \text{ } \mu\text{g m}^{-3}$ of ammonium bisulfate seeds, collecting 1 m^3 of air from the chamber onto a filter, and then extracting the filter in 1 mL of solvent would also results in a pH of 3. We recommend checking for possible artifacts of the chemical analysis in all experiments in which extracts of acidified particles are evaporated in order to prevent spurious observation of organosulfates.

CHAPTER 6

The effect of water vapor and aerosol liquid water on the molecular composition of secondary organic aerosol

Abstract. Aerosol particle phase state affects radiative forcing by particles. This study investigates molecular composition of model aerosols in the presence of water vapor and aerosol liquid water and the effect that it has on phase state. The molecular composition was probed during formation and aging of particles in a humid atmosphere by nanospray desorption electrospray ionization high resolution mass spectrometry (nano-DESI-HRMS). The dimer-to-monomer ratio was the most discernable difference between experiments. An increase in monomers was attributed to hydrolysis reactions, and increase in dimers to condensation reactions (the reverse reaction). In general, in the presence of water (both ALW and water vapor), monomers increased relative to dimers. For the fresh SOA, it was predicted that particles were semi-solid based on their molecular composition. Except for SOA produced under dry conditions in the presence of ammonium sulfate seed particles, for which the phase state was predicted to be glassy. After exposing these particles to a humid atmosphere for 48 hours, the particles were predicted to be less viscous based on their molecular composition. The SOA composition also shifted to higher volatility bins, indicated by $\log(C^*)$.

6.1 Introduction

Aerosol particles impact global and regional climate directly by scattering incoming solar radiation. Indirectly, they may serve as cloud condensation nuclei (CCN), and affect the radiative properties of clouds. It is predicted that particles exist in a variety of phase states at the Earth's lower atmosphere, including liquid-like, semi-solid, and solid states, depending on environmental conditions at different locations (Shiraiwa et al., 2017). Depending on their phase state, particles can have different effects on climate. For example, particle phase state affects the rate and extent of chemical aging, which in turn affects particle composition and physical properties. In Slade et al. 2017, a surrogate for BBOA, Aerosolized Suwannee River fulvic acid, underwent photooxidative aging in a glassy (< 295 K) or liquid-like (>300 K) phase state, where the phase state was selected by changing the temperature. After photooxidation, the low temperature, glassy particles showed greater CCN activity likely due to developing a highly oxidized interface. However, for liquid-like particles, there was no difference in CCN activity after photooxidation likely due to the oxidized molecules mixing with the unoxidized molecules from the particle interior. Phase state and the presence of aerosol liquid water (ALW) may also determine SOA mass yield. In Faust et al. 2017 and Wong et al. 2015, SOA was formed and aged in an aerosol flow tube (70% RH) in the presence of effloresced or deliquesced ammonium sulfate seed particles. They observed increased SOA yields for deliquesced seeds, ranging from 13% to 60% depending on the SOA precursor. This could be due to the formation of SOA by aqueous chemistry, or enhanced partitioning of low volatility compounds to the particle phase due to greater surface area for deliquesced seeds.

Hydrolysis of larger organic molecules into smaller products and the reverse reaction of oligomerization of smaller molecules into dimers, trimers, etc. are competing reactions occurring

in ALW that affect SOA mass and composition. The hydrolysis reactions result in compounds with higher volatility, and may lead to the loss of material from organic particles by evaporation. By the reverse reaction, condensation reactions may result in oligomer formation, which do not readily evaporate from the particles. Water is also crucial for acid-base chemistry, which can result in acid-catalyzed oligomerization reactions in ALW. For example, the acid-catalyzed uptake of IEPOX, formed during gas-phase low-NO_x isoprene photooxidation reactions, further reacts in acidified aqueous particles to form low-volatility oligomers (Surratt et al., 2010). The presence of water also lowers the viscosity of SOA, and could affect the equilibrium partitioning of SVOCs or promote heterogeneous oxidation reactions (Perraud et al., 2012; Renbaum-Wolff et al., 2013; Shiraiwa and Seinfeld, 2012). Finally, ALW can be a medium for aqueous SOA formation, leading to dicarboxylic acids and humic-like substances (Ervens et al., 2011).

This study investigates the effect of water, both in the form of water vapor and ALW, on the molecular composition and phase state of α -pinene photooxidation SOA during formation and aging (in the absence of oxidants or light). The goal of this study is to relate specific mechanisms, such as hydrolysis of dimers or other types of ALW chemistry, to observed changes in mass spectra. The glass transition temperature (T_g), or the temperature below which the particle becomes a glass, was calculated as well as the viscosity and volatility of SOA particles based on their mass spectra. We found that relative humidity, presence of seed particles, and the interaction of these two conditions greatly impact the molecular composition, for example, the dimer-to-monomer ratio changed depending on conditions. The dry/seeds condition resulted in a glassy particle ($T_g=293$ K) with an abundance of dimer species. In contrast the humid/seeds condition is likely a liquid-liquid phase separated particle with the organic coating predicted to exist in a semi-solid state due to a lower dimer-to-monomer ratio. After prolonged exposure to

humid air, the dimer-to-monomer ratio generally decreased, increasing the volatility and lowering the viscosity of the SOA particles.

6.2 Experimental Methods

6.2.1 SOA generation

SOA was generated in a 5 m³ smog chamber at room temperature. For high relative humidity (RH) experiments, the chamber was first conditioned to 90% RH. Dry purge air (from a Parker FT-IR purge gas generator) was flowed into a Nafion exchanger (Perma Pure model FC125-240) with a water circulator (Julabo model HE-BASIS) heated to 30°C. Relative humidity was monitored using a Vaisala HMT333 humidity probe. An ammonium sulfate solution (1 g/ L) was atomized, creating ammonium sulfate seed particles for some experiments. For the 0% RH/seeded experiment, 50 µg m⁻³ was added, and for the 90%/seeded experiment 77 µg m⁻³ was added according to the SMPS (TSI model 3936), assuming a particle density of 1.2 g cm⁻³. After that, α-pinene (500 ppb) and hydrogen peroxide (2,000 ppb) were injected into the chamber through a heated inlet. A fan mixed the contents of the chamber until the 42 UV-B lamps (SolarcSystems, Inc. Model FS40T12/UBV) were turned on, beginning the photooxidation chemistry. Lamps were turned off, and collection began when the mass concentration on the SMPS reached a maximum. SOA particles were collected onto two PTFE filters (0.2 µm pore size, 47 mm diameter, Millipore Fluoropore) in parallel; each pump had a flow rate of approximately 15 LPM. The filters were frozen until HRMS analysis was performed.

6.2.2 Aging in humid air

A saturated solution of K_2SO_4 (6 g/50 mL) was prepared, and the 50 mL solution was added to a glass jar, serving as the RH aging chamber. Half of a filter was exposed to the humid atmosphere by placing it on a petri dish floating on top of the saturated solution. Parafilm secured the lid of the jar, and the jar was wrapped in foil. Based on the saturation vapor pressure of K_2SO_4 the headspace is expected to be controlled at 97.6% RH. The jars were left undisturbed for 48 hours, after which, the filters were removed, brought to ambient RH (about 50%), and frozen until they were analyzed by HRMS.

6.2.3 Nano-DESI HRMS

A custom-built nanospray desorption electrospray ionization source (Roach et al., 2010a, 2010b) coupled to a Q-Exactive HF-X Orbitrap (Thermo Electron, Inc) was used to analyze the SOA samples. The solvent mixture (30% CH_3CN /70% H_2O) passed through an electrified capillary (Spray voltage 3 kV) at 2 $\mu L/min$ by a syringe pump. The capillary temperature was set to 250 °C. The solvent enters the other, nanospray capillary, by capillary action. The point where the two capillary tips meet is joined by a solvent droplet, referred to as the solvent bridge. The solvent is then desorbed into the mass spectrometer inlet. The solvent droplet is lowered to the filter substrate to extract the SOA sample and collect mass spectra. The filter substrate is moved at a rate of 0.2 $cm\ min^{-1}$ by a programmed stage to constantly extract the sample. Mass spectra were collected for various locations on the filter to ensure reproducibility. Data was also acquired in both positive and negative modes. The instrument was calibrated at the beginning of each day with Pierce LTQ ESI calibration solutions. The data was acquired and first analyzed in Thermo Xcalibur 2.2.

Peaks from time-integrated mass spectra were extracted using Decon2LS software. Peaks with signal-to-noise of greater than 3 were retained. Peaks corresponding to ^{13}C -containing formulas were discarded. In addition, peaks appearing in the solvent, before the solvent bridge made contact with the sample, were discarded. Mass spectra were internally calibrated, determining chemical formulas corresponding to known α -pinene SOA compounds first. This did not change the exact mass by more than 0.001 m/z units. Peaks were assigned using Formula Calculator v1.1 (<http://magnet.fsu.edu/~midas/download.html>).

6.3 Results and Discussion

The mass spectra for α -pinene/photooxidation SOA formed under dry or humid conditions in the presence or absence of ammonium sulfate seed particles are shown in Figure 6.1. Most of the observed peaks in Figure 6.1 correspond to components of α -pinene SOA that have been identified previously. For example, terpenylic acid ($\text{C}_8\text{H}_{12}\text{O}_4$), pinic acid ($\text{C}_9\text{H}_{14}\text{O}_4$), and 2-hydroxypinonic acid ($\text{C}_{10}\text{H}_{16}\text{O}_5$) are significant peaks in all mass spectra. All four mass spectra have distinct monomer ($< m/z$ 250) and dimer (m/z 250-450) regions, in agreement with previous studies (Reinhardt et al., 2007; Romonosky et al., 2017). Figure 6.1 shows that the relative intensities of the dimer and monomer peaks vary based on these conditions. Despite these differences, the average O:C and H:C ratios, weighted by peak abundance, do not vary based on relative humidity or presence of seeds. Since many of the reactions involving water are condensation or hydrolysis to interconvert dimers and monomers, we will use the monomer-to-dimer ratio to discuss the role of water in SOA composition.

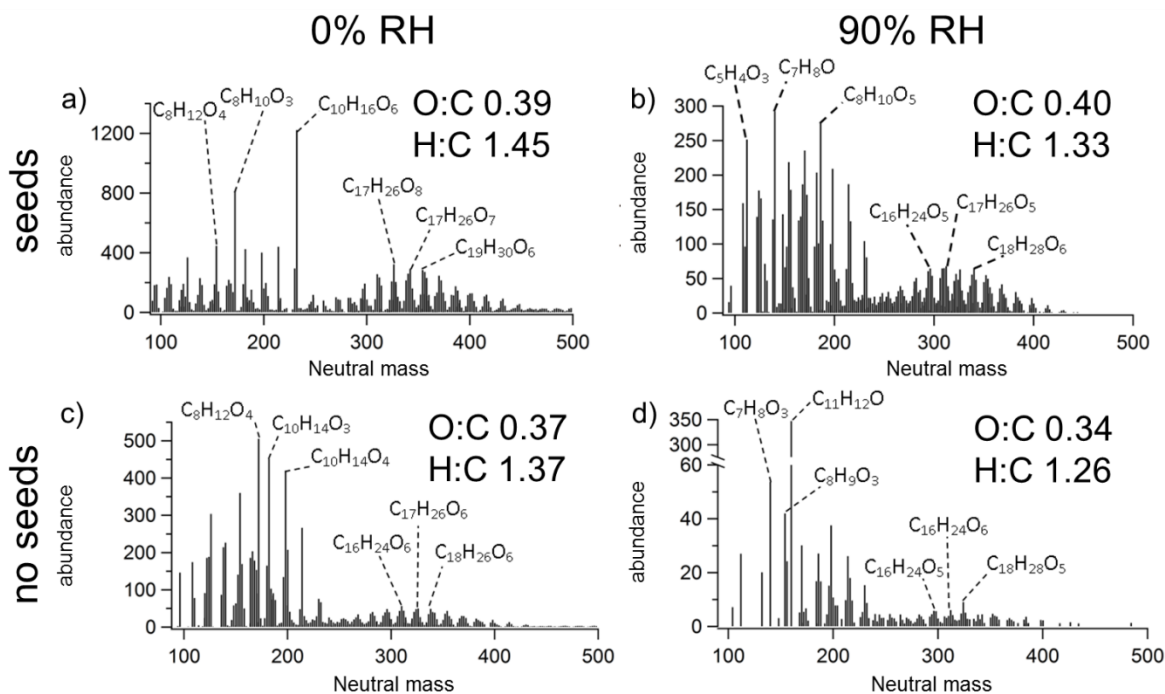


Figure 6.1: Combined positive and negative ion mode mass spectra of α -pinene/photooxidation SOA formed in the presence of ammonium sulfate seeds (a and b) or exclusively from gas to particle conversion (c and d). a) and c) were formed under dry conditions, while b) and d) were formed at approximately 90% RH. In each mass spectrum, chemical formulas corresponding to monomer and dimer peaks with the highest abundances are shown. The average O:C and H:C ratios weighted by peak abundances are given for each mass spectrum.

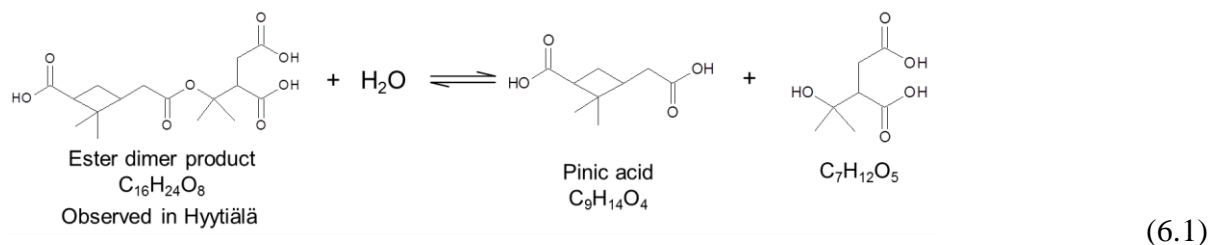
The ratios of integrated peak abundances for the dimer-to-monomer regions of the mass spectra are given in Table 6.1. Interestingly, when SOA is formed in the presence of seed particles, the dimer-to-monomer changes drastically depending on the relative humidity. At 0% RH with seeds, the dimer-to-monomer ratio is 1.5, suggesting there are more dimers relative to monomers. In contrast, at 90% RH in the presence of seeds the ratio is 0.6, suggesting there are more monomers present. This can be explained in the context of particle phase state. At 0% RH, the average particle is a solid core of ammonium sulfate covered by viscous α -pinene/photooxidation SOA material. In contrast, at 90% RH, we expect a deliquesced ammonium sulfate seed coated with mixture of organics and water, resulting in a liquid-liquid phase separated particle. The fluid aqueous/organic layer may explain the presence of primarily

monomers since hydrolysis reactions can occur more readily. On the other hand, dimer formation seems to be favorable at 0% RH in the absence of particle or gas-phase water. These interpretations are further reinforced by calculations of glass transition temperature (T_g) based on the mass spectra. T_g was calculated to be 293 K for SOA formed at 0% RH, and 271 K when formed at 90% RH. This suggests that SOA formed at 0% RH is more solid at room temperature, whereas SOA formed at 90% RH is less viscous when dried.

Table 6.1: Dimer-to-monomer ratio of integrated peak abundances in α -pinene photooxidation SOA mass spectra. “Chamber” refers to SOA generated in the chamber according to the “system” conditions, collected onto PTFE filters, and frozen until HRMS analysis. “Aged in humidity” refers to SOA that was suspended in a saturated K_2SO_4 solution for 48 hours (ensuring 97.6% RH) after collection from the chamber, and then frozen until HRMS analysis.

System	Dimers/monomers	
	Chamber	Aged in humidity
Seeds, 0% RH	1.5	0.5
Seeds, 90% RH	0.6	0.3
No seeds, 0% RH	0.5	0.3
No seeds, 90% RH	0.3	3.1

To look for evidence of the hydrolysis/condensation mechanism, we can focus on individual reactions and with well-known monomer/dimer products. For example, the ester dimer product $C_{16}H_{24}O_6$ which was observed in Hyytiälä (Kristensen et al., 2014, 2016; Venkatachari and Hopke, 2008; Yasmeen et al., 2010), and the well-known pinic acid monomer can be related by the hydrolysis mechanism in equation (6.1).



The dimer-to-monomer ratio for this particular reaction is visualized in Figure 6.2. Under all conditions, less ester dimer product was observed after the SOA was aged in a humid atmosphere. In the case of fresh SOA formed at 0% RH with seed particles, the ester dimer product had a very low abundance compared to the monomer species. For SOA formed at 90% RH in the absence of seed particles, and then aged in 98% RH, neither the dimer nor monomers were detected. This analysis suggests that hydrolysis reactions could be important in the chemical aging of SOA particles, just from exposure to high relative humidity. However, a limitation of this analysis is that abundance attributed to the monomers or the ester dimer product could actually be isomers of these molecules. In particular, the $\text{C}_7\text{H}_{12}\text{O}_5$ monomer has not been extensively characterized in the α -pinene SOA literature.

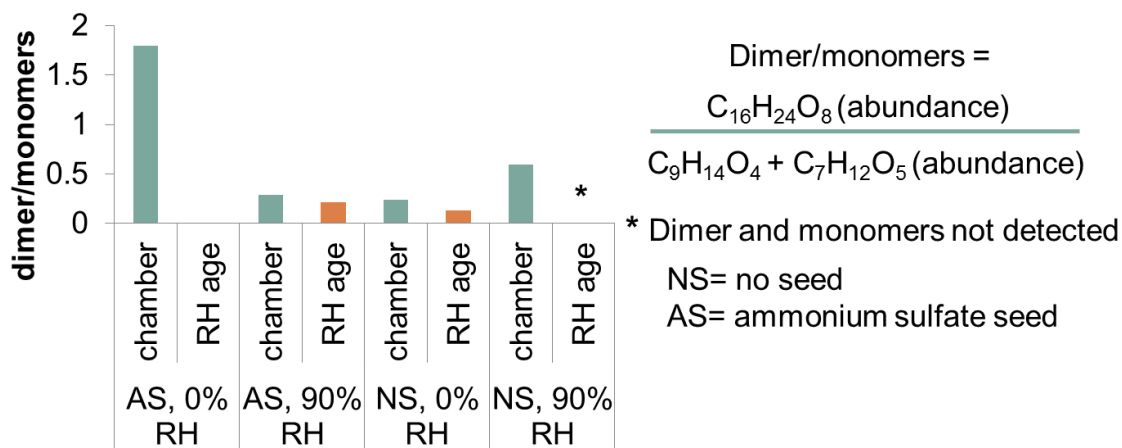


Figure 6.2: The dimer-to-monomer ratio for the reaction in equation (6.1) for fresh SOA and after it was aged in humid conditions.

Organic aerosol particle viscosity was modelled as a function of RH based on their mass spectra, as described in DeRieux et al. 2018, and the results are shown in Figure 6.3. To clarify, viscosity of each SOA component was first predicted based on a parameterization that depends on the number of O, C, and H atoms in the molecules. The viscosity of the SOA mixture at different RH levels was then predicted using mixing rules. The SOA particles are predicted to be semi-solid (10^2 - 10^{12} pa s) based on the mass spectra (Shiraiwa et al., 2011). Except for SOA formed at low RH in the presence of seed particles, at 0% RH the particles are predicted to be glassy (10^{12} pa s) with a T_g of 293 K. In general, aging particles in a humid atmosphere significantly lowers the viscosity of particles. This is reflected in a lowering of the dimer-to-monomer ratio, as shown in Table 6.1. The exception is SOA formed in the absence of seeds at high RH; the viscosity appears to increase after RH aging. This could be due to enhanced evaporation of monomer species during RH aging, artificially increasing the dimer-to-monomer ratio. This experiment needs to be repeated to confirm this observation.

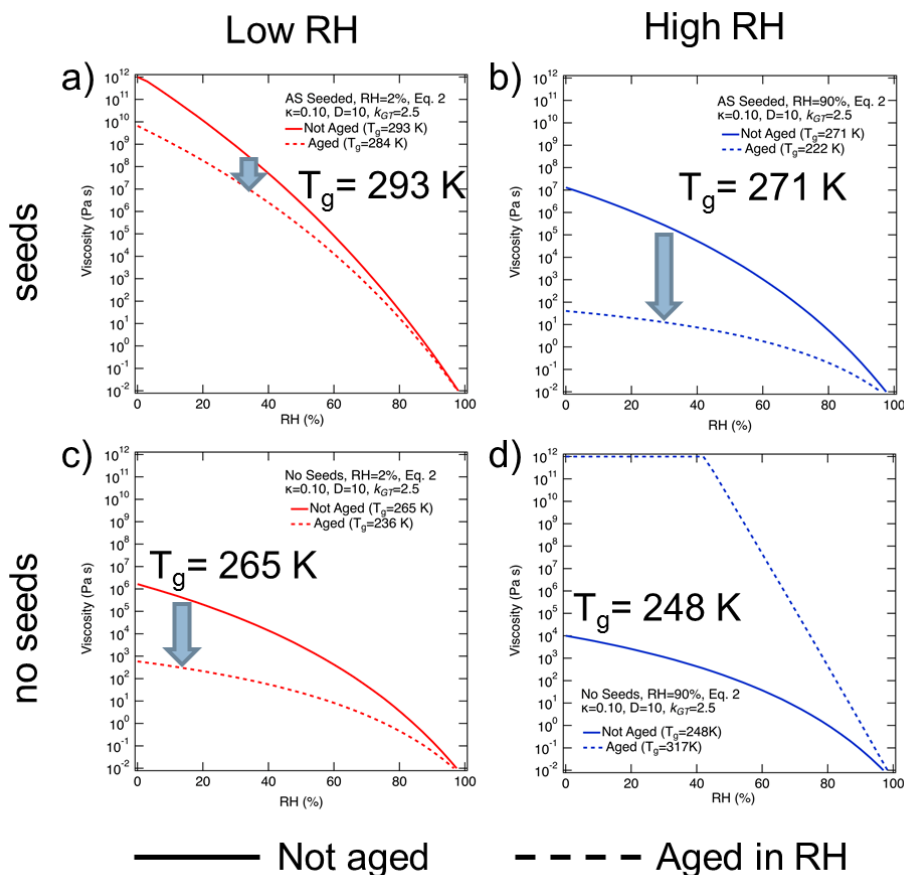


Figure 6.3: Modelled SOA particle viscosity as a function of RH for SOA formed in the presence of ammonium sulfate seeds (a and b) or exclusively from gas to particle conversion (c and d). a) and c) were formed under dry conditions, while b) and d) were formed at approximately 90% RH. The solid line indicates particles that were not aged, while the dashed line represents the particles that were aged in a humid atmosphere. The glass transition temperature (T_g) was calculated for the not aged particles, and is also indicated on the graph.

Displayed in Figure 6.4 are volatility distributions calculated from the mass spectra, where the X-axis corresponds to the logarithm of the saturation vapor pressure, C^* , spaced into bins separated by one $\log(C^*)$ unit, and Y-axis corresponds to the combined peak abundance of all detected compounds binned by their volatility. Organic compounds are often classified as extremely low volatility ($\log(C^*) < -4$), low volatility (-4 to -1), semi-volatile (-1 to 2), intermediate volatility (2 to 6), and VOC (> 6) (Ma et al., 2016). There is an observed difference in the volatility distribution for fresh and RH-aged SOA particles. Specifically, the composition

of RH aged SOA particles is shifted towards higher volatility bins. Again, this is consistent with the observed decrease in the dimer-to-monomer ratio after RH aging. The exception to this is SOA formed in the absence of seeds at high RH (Figure 6.4d). One explanation for observing the opposite trend in this case is enhanced evaporation of monomers during RH aging.

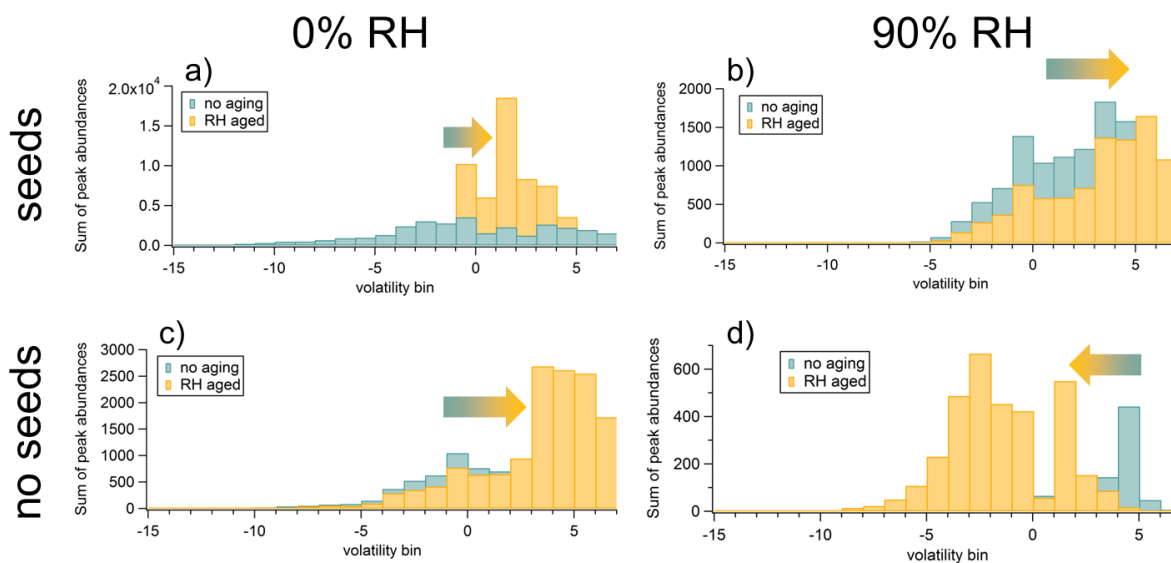


Figure 6.4: Peak abundances in the mass spectra are binned by their volatility. Blue bars are for the particles that were not aged, and the orange bars represent particles that were aged in a humid atmosphere.

6.4 Summary

Our data suggests that the presence of water vapor and ALW dictates the molecular composition of organics. Under the condition when ALW is present, i.e., under humid conditions (90% RH) and in the presence of ammonium sulfate seed, we observe more monomers than dimers in the mass spectrum, resulting in a less viscous particle. The calculated T_g of the dry SOA material is 271 K, indicating that the organic coating is in a semi-solid state when the particle is dried. On the other hand, under dry conditions and in the presence of a solid ammonium sulfate seed, more dimers than monomers are observed. This could be due to condensation reactions occurring more readily. As a result, these particles were calculated to be

glassy, with a T_g of 293 K. SOA particles formed in the absence of seeds, regardless of humidity, were predicted to have a semi-solid phase state when dried.

After collected SOA particles were aged in RH, monomers increased relative to dimers, and this could be due to dimer hydrolysis. It was predicted that the particles become less viscous and more volatile from aging the particles in relative humidity. Overall, relative humidity, related to viscosity and phase state, affects the chemical composition of SOA particles during both formation and aging stages of the aerosol life cycle by controlling the dimer-to-monomer ratio.

The experiments described above represent our initial test of the hypothesis that both gaseous water and ALW can affect the particle composition, and the preliminary results turned out to be very promising. These experiments could be improved upon to yield more conclusive results. First, the experiments should be done more than once for each condition. Multiple trials would give us more confidence in establishing if the no AS seed particles/90% RH experiment truly reversed the observed trend of increasing monomers relative to dimers under humid conditions. There was also some evidence of fragmentation in the nano-DESI mass spectra. Fragmentation is undesirable as we have no easy way of distinguishing fragments from actual SOA compounds, and inclusion of fragments has a strong effect on the predicted viscosity and volatility predictions– the particles appear to be less viscous and more volatile than they actually are. This was my first time using this particular instrument, but one should be more careful regarding the instrument settings to prevent fragmentation processes in the ion sources in the future. Lastly, the mass loadings of all of the samples were vastly different, since SOA yield is strongly humidity dependent in these experiments. Mass loading could potentially have an effect on the abundance of monomers and dimers observed (Kourtchev et al., 2016). For more faithful

comparison of mass spectra, the conditions should be adjusted to keep mass loadings in the chamber as well as on the filter comparable.

REFERENCES

- Adachi, K. and Buseck, P. R.: Atmospheric tar balls from biomass burning in Mexico, *J. Geophys. Res.*, 116(D5), D05204, doi:10.1029/2010JD015102, 2011.
- Agati, G., Azzarello, E., Pollastri, S. and Tattini, M.: Flavonoids as antioxidants in plants: location and functional significance, *Plant Sci.*, 196, 67–76, 2012.
- Aiken, A. C., Salcedo, D., Cubison, M. J., Huffman, J. A., DeCarlo, P. F., Ulbrich, I. M., Docherty, K. S., Sueper, D., Kimmel, J. R., Worsnop, D. R., Trimborn, A., Northway, M., Stone, E. A., Schauer, J. J., Volkamer, R. M., Fortner, E., de Foy, B., Wang, J., Laskin, A., Shutthanandan, V., Zheng, J., Zhang, R., Gaffney, J., Marley, N. A., Paredes-Miranda, G., Arnott, W. P., Molina, L. T., Sosa, G. and Jimenez, J. L.: Mexico City aerosol analysis during MILAGRO using high resolution aerosol mass spectrometry at the urban supersite (T0) – Part 1: Fine particle composition and organic source apportionment, *Atmos. Chem. Phys.*, 9(17), 6633–6653, doi:10.5194/acp-9-6633-2009, 2009.
- Aiona, P. K., Lee, H. J., Lin, P., Heller, F., Laskin, A., Laskin, J. and Nizkorodov, S. A.: A Role for 2-Methyl Pyrrole in the Browning of 4-Oxopentanal and Limonene Secondary Organic Aerosol, *Environ. Sci. Technol.*, 51(19), 11048–11056, doi:10.1021/acs.est.7b02293, 2017a.
- Aiona, P. K., Lee, H. J., Leslie, R., Lin, P., Laskin, A., Laskin, J. and Nizkorodov, S. A.: Photochemistry of Products of the Aqueous Reaction of Methylglyoxal with Ammonium Sulfate, , doi:10.1021/acsearthspacechem.7b00075, 2017b.
- Akagi, S. K., Craven, J. S., Taylor, J. W., McMeeking, G. R., Yokelson, R. J., Burling, I. R., Urbanski, S. P., Wold, C. E., Seinfeld, J. H., Coe, H., Alvarado, M. J. and Weise, D. R.: Evolution of trace gases and particles emitted by a chaparral fire in California, *Atmos. Chem. Phys.*, 12(3), 1397–1421, doi:10.5194/acp-12-1397-2012, 2012.
- Al-Naiema, I. M. and Stone, E. A.: Evaluation of anthropogenic secondary organic aerosol tracers from aromatic hydrocarbons, *Atmos. Chem. Phys.*, 17(3), 2053–2065, doi:10.5194/acp-17-2053-2017, 2017.
- Alvarado, M. J., Lonsdale, C. R., Yokelson, R. J., Akagi, S. K., Coe, H., Craven, J. S., Fischer, E. V., McMeeking, G. R., Seinfeld, J. H., Soni, T., Taylor, J. W., Weise, D. R. and Wold, C. E.: Investigating the links between ozone and organic aerosol chemistry in a biomass burning plume from a prescribed fire in California chaparral, *Atmos. Chem. Phys.*, 15(12), 6667–6688, doi:10.5194/acp-15-6667-2015, 2015.
- Anastasio, C., Faust, B. C. and Rao, C. J.: Aromatic Carbonyl Compounds as Aqueous-Phase Photochemical Sources of Hydrogen Peroxide in Acidic Sulfate Aerosols, Fogs, and Clouds. 1. Non-Phenolic Methoxybenzaldehydes and Methoxyacetophenones with Reductants (Phenols), *Environ. Sci. Technol.*, 31(1), 218–232, doi:10.1021/es960359g, 1997.
- Andreae, M. O. and Gelencsér, A.: Black carbon or brown carbon? The nature of light-absorbing

carbonaceous aerosols, *Atmos. Chem. Phys.*, 6(10), 3131–3148, doi:10.5194/acp-6-3131-2006, 2006.

Andreae, M. O. and Merlet, P.: Emission of trace gases and aerosols from biomass burning, *Global Biogeochem. Cycles*, 15(4), 955–966, doi:10.1029/2000gb001382, 2001.

Ångström, A.: On the Atmospheric Transmission of Sun Radiation and on Dust in the Air, *Geogr. Ann.*, 11(2), 156–166, doi:10.1080/20014422.1929.11880498, 1929.

Anttila, T., Kiendler-Scharr, A., Tillmann, R. and Mentel, T. F.: On the Reactive Uptake of Gaseous Compounds by Organic-Coated Aqueous Aerosols: Theoretical Analysis and Application to the Heterogeneous Hydrolysis of N₂O₅, *J. Phys. Chem. A*, 110(35), 10435–10443, doi:10.1021/jp062403c, 2006.

Araujo, J. A., Barajas, B., Kleinman, M., Wang, X., Bennett, B. J., Gong, K. W., Navab, M., Harkema, J., Sioutas, C., Lusic, A. J. and Nel, A. E.: Ambient Particulate Pollutants in the Ultrafine Range Promote Early Atherosclerosis and Systemic Oxidative Stress, *Circ. Res.*, 102(5), 589–596, doi:10.1161/CIRCRESAHA.107.164970, 2008.

Atkinson, R. W., Mills, I. C., Walton, H. A. and Anderson, H. R.: Fine particle components and health—a systematic review and meta-analysis of epidemiological time series studies of daily mortality and hospital admissions, *J. Expo. Sci. Environ. Epidemiol.*, 25(2), 208–214, doi:10.1038/jes.2014.63, 2015.

Baergen, A. M., Styler, S. A., van Pinxteren, D., Müller, K., Herrmann, H. and Donaldson, D. J.: Chemistry of Urban Grime: Inorganic Ion Composition of Grime vs Particles in Leipzig, Germany, *Environ. Sci. Technol.*, 49(21), 12688–12696, doi:10.1021/acs.est.5b03054, 2015.

Balakrishnan, K., Ghosh, S., Ganguli, B., Sambandam, S., Bruce, N., Barnes, D. F. and Smith, K. R.: State and national household concentrations of PM_{2.5} from solid cookfuel use: Results from measurements and modeling in India for estimation of the global burden of disease, *Environ. Heal.*, 12(1), 77, doi:10.1186/1476-069X-12-77, 2013.

Balakrishnan, K., Sambandam, S., Ghosh, S., Mukhopadhyay, K., Vaswani, M., Arora, N. K., Jack, D., Pillariseti, A., Bates, M. N. and Smith, K. R.: Household Air Pollution Exposures of Pregnant Women Receiving Advanced Combustion Cookstoves in India: Implications for Intervention, *Ann. Glob. Heal.*, 81(3), 375–385, doi:10.1016/j.aogh.2015.08.009, 2015.

Barrefors, G. and Petersson, G.: Volatile hydrocarbons from domestic wood burning, *Chemosphere*, 30(8), 1551–1556, doi:10.1016/0045-6535(95)00048-D, 1995.

Bateman, A. P., Nizkorodov, S. A., Laskin, J. and Laskin, A.: Time-resolved molecular characterization of limonene/ozone aerosol using high-resolution electrospray ionization mass spectrometry, *Phys. Chem. Chem. Phys.*, 11(36), 7931, doi:10.1039/b905288g, 2009.

Bergstrom, R. W., Russell, P. B., Hignett, P., Bergstrom, R. W., Russell, P. B. and Hignett, P.: Wavelength Dependence of the Absorption of Black Carbon Particles: Predictions and Results from the TARFOX Experiment and Implications for the Aerosol Single Scattering Albedo, *J.*

Atmos. Sci., 59(3), 567–577, doi:10.1175/1520-0469(2002)059<0567:WDOTAO>2.0.CO;2, 2002.

Bisht, D. S., Srivastava, A. K., Pipal, A. S., Srivastava, M. K., Pandey, A. K., Tiwari, S. and Pandithurai, G.: Aerosol characteristics at a rural station in southern peninsular India during CAIPEEX-IGOC: physical and chemical properties, *Environ. Sci. Pollut. Res.*, 22(7), 5293–5304, doi:10.1007/s11356-014-3836-1, 2015.

Bluvshstein, N., Lin, P., Flores, J. M., Segev, L., Mazar, Y., Tas, E., Snider, G., Weagle, C., Brown, S. S., Laskin, A. and Rudich, Y.: Broadband optical properties of biomass-burning aerosol and identification of brown carbon chromophores, *J. Geophys. Res. Atmos.*, 122(10), 5441–5456, doi:10.1002/2016JD026230, 2017.

Bohren, C. F. and Huffman, D. R.: *Absorption and scattering of light by small particles*, Wiley., 1998.

Bond, T. C. and Bergstrom, R. W.: *Light Absorption by Carbonaceous Particles: An Investigative Review*, *Aerosol Sci. Technol.*, 40(1), 27–67, doi:10.1080/02786820500421521, 2006.

Bones, D. L., Henricksen, D. K., Mang, S. A., Gonsior, M., Bateman, A. P., Nguyen, T. B., Cooper, W. J. and Nizkorodov, S. A.: Appearance of strong absorbers and fluorophores in limonene-O₃ secondary organic aerosol due to NH₄⁺-mediated chemical aging over long time scales, *J. Geophys. Res.*, 115(D5), D05203, doi:10.1029/2009JD012864, 2010.

Boucher, O. and Anderson, T. L.: General circulation model assessment of the sensitivity of direct climate forcing by anthropogenic sulfate aerosols to aerosol size and chemistry, *J. Geophys. Res.*, 100(D12), 26117, doi:10.1029/95JD02531, 1995.

Boulanger, Y., Gauthier, S. and Burton, P. J.: A refinement of models projecting future Canadian fire regimes using homogeneous fire regime zones, *Can. J. For. Res.*, 44(4), 365–376, doi:10.1139/cjfr-2013-0372, 2014.

Budisulistiorini, S. H., Riva, M., Williams, M., Chen, J., Itoh, M., Surratt, J. D. and Kuwata, M.: Light-Absorbing Brown Carbon Aerosol Constituents from Combustion of Indonesian Peat and Biomass, *Environ. Sci. Technol.*, 51(8), 4415–4423, doi:10.1021/acs.est.7b00397, 2017.

Bunce, N. J., Lamarre, J. and Vaish, S. P.: Photorearrangement of azoxybenzene to 2-hydroxyazobenzene: a convenient chemical actinometer, *Photochem. Photobiol.*, 39(4), 531–533, doi:10.1111/j.1751-1097.1984.tb03888.x, 1984.

Butt, E. W., Rap, A., Schmidt, A., Scott, C. E., Pringle, K. J., Reddington, C. L., Richards, N. A. D., Woodhouse, M. T., Ramirez-Villegas, J., Yang, H., Vakkari, V., Stone, E. A., Rupakheti, M., S. Praveen, P., G. van Zyl, P., P. Beukes, J., Josipovic, M., Mitchell, E. J. S., Sallu, S. M., Forster, P. M. and Spracklen, D. V.: The impact of residential combustion emissions on atmospheric aerosol, human health, and climate, *Atmos. Chem. Phys.*, 16(2), 873–905, doi:10.5194/acp-16-873-2016, 2016.

Carter, W. P. L.: Development of Ozone Reactivity Scales for Volatile Organic Compounds, *Air Waste*, 44(7), 881–899, doi:10.1080/1073161X.1994.10467290, 1994.

Carter, W. P. L.: Development of the SAPRC-07 chemical mechanism, *Atmos. Environ.*, 44(40), 5324–5335, doi:10.1016/J.ATMOSENV.2010.01.026, 2010.

Census of India: Households by Availability of Separate Kitchen and Type of Fuel Used for Cooking, [online] Available from: <http://www.censusindia.gov.in/2011census/Hlo-series/HH10.html> (Accessed 8 August 2017), 2011.

Chafe, Z. A., Brauer, M., Klimont, Z., Van Dingenen, R., Mehta, S., Rao, S., Riahi, K., Dentener, F. and Smith, K. R.: Household Cooking with Solid Fuels Contributes to Ambient PM_{2.5} Air Pollution and the Burden of Disease, *Environ. Health Perspect.*, 122(12), 1314–1320, doi:10.1289/ehp.1206340, 2014.

Chakrabarty, R. K., Moosmüller, H., Garro, M. A., Arnott, W. P., Walker, J., Susott, R. A., Babbitt, R. E., Wold, C. E., Lincoln, E. N. and Hao, W. M.: Emissions from the laboratory combustion of wildland fuels: Particle morphology and size, *J. Geophys. Res.*, 111(D7), D07204, doi:10.1029/2005JD006659, 2006.

Chakrabarty, R. K., Moosmüller, H., Chen, L.-W. A., Lewis, K., Arnott, W. P., Mazzoleni, C., Dubey, M. K., Wold, C. E., Hao, W. M. and Kreidenweis, S. M.: Brown carbon in tar balls from smoldering biomass combustion, *Atmos. Chem. Phys.*, 10(13), 6363–6370, doi:10.5194/acp-10-6363-2010, 2010.

Chang, E. I. and Pankow, J. F.: Prediction of activity coefficients in liquid aerosol particles containing organic compounds, dissolved inorganic salts, and water—Part 2: Consideration of phase separation effects by an X-UNIFAC model, *Atmos. Environ.*, 40(33), 6422–6436, doi:10.1016/J.ATMOSENV.2006.04.031, 2006.

Chang, J. L. and Thompson, J. E.: Characterization of colored products formed during irradiation of aqueous solutions containing H₂O₂ and phenolic compounds, *Atmos. Environ.*, 44(4), 541–551, doi:10.1016/J.ATMOSENV.2009.10.042, 2010.

Chen, Y. and Bond, T. C.: Light absorption by organic carbon from wood combustion, *Atmos. Chem. Phys.*, 10(4), 1773–1787, doi:10.5194/acp-10-1773-2010, 2010.

Chen, Y., Roden, C. A. and Bond, T. C.: Characterizing Biofuel Combustion with Patterns of Real-Time Emission Data (PaRTED), *Environ. Sci. Technol.*, 46(11), 6110–6117, doi:10.1021/es3003348, 2012.

China, S., Mazzoleni, C., Gorkowski, K., Aiken, A. C. and Dubey, M. K.: Morphology and mixing state of individual freshly emitted wildfire carbonaceous particles, *Nat. Commun.*, 4(1), 2122, doi:10.1038/ncomms3122, 2013.

Clafin, M. S., Krechmer, J. E., Hu, W., Jimenez, J. L. and Ziemann, P. J.: Functional Group Composition of Secondary Organic Aerosol Formed from Ozonolysis of α -Pinene Under High VOC and Autoxidation Conditions, *ACS Earth Sp. Chem.*, 2(11), 1196–1210,

doi:10.1021/acsearthspacechem.8b00117, 2018.

Coggon, M. M., Veres, P. R., Yuan, B., Koss, A., Warneke, C., Gilman, J. B., Lerner, B. M., Peischl, J., Aikin, K. C., Stockwell, C. E., Hatch, L. E., Ryerson, T. B., Roberts, J. M., Yokelson, R. J. and de Gouw, J. A.: Emissions of nitrogen-containing organic compounds from the burning of herbaceous and arboraceous biomass: Fuel composition dependence and the variability of commonly used nitrile tracers, *Geophys. Res. Lett.*, 43(18), 9903–9912, doi:10.1002/2016GL070562, 2016.

Collard, F.-X. and Blin, J.: A review on pyrolysis of biomass constituents: Mechanisms and composition of the products obtained from the conversion of cellulose, hemicelluloses and lignin, *Renew. Sustain. Energy Rev.*, 38, 594–608, doi:10.1016/j.rser.2014.06.013, 2014.

Colman, J. J., Swanson, A. L., Meinardi, S., Sive, B. C., Blake, D. R. and Rowland, F. S.: Description of the analysis of a wide range of volatile organic compounds in whole air samples collected during PEM-Tropics A and B, *Anal. Chem.*, 73(15), 3723–3731, doi:10.1021/ac010027g, 2001.

Cong, Z., Kang, S., Kawamura, K., Liu, B., Wan, X., Wang, Z., Gao, S. and Fu, P.: Carbonaceous aerosols on the south edge of the Tibetan Plateau: concentrations, seasonality and sources, *Atmos. Chem. Phys.*, 15(3), 1573–1584, doi:10.5194/acp-15-1573-2015, 2015.

Conibear, L., Butt, E. W., Knote, C., Arnold, S. R. and Spracklen, D. V.: Residential energy use emissions dominate health impacts from exposure to ambient particulate matter in India, *Nat. Commun.*, 9(1), 617, doi:10.1038/s41467-018-02986-7, 2018.

Cosman, L. M. and Bertram, A. K.: Reactive Uptake of N_2O_5 on Aqueous H_2SO_4 Solutions Coated with 1-Component and 2-Component Monolayers, *J. Phys. Chem. A*, 112(20), 4625–4635, doi:10.1021/jp8005469, 2008.

Cosman, L. M., Knopf, D. A. and Bertram, A. K.: N_2O_5 Reactive Uptake on Aqueous Sulfuric Acid Solutions Coated with Branched and Straight-Chain Insoluble Organic Surfactants, *J. Phys. Chem. A*, 112(11), 2386–2396, doi:10.1021/jp710685r, 2008.

Crutzen, P. J. and Andreae, M. O.: Biomass Burning in the Tropics - Impact on Atmospheric Chemistry and Biogeochemical Cycles, *Science*, 250(4988), 1669–1678, doi:10.1126/science.250.4988.1669, 1990.

Crutzen, P. J., Heidt, L. E., Krasnec, J. P., Pollock, W. H. and Seiler, W.: Biomass burning as a source of atmospheric gases CO , H_2 , N_2O , NO , CH_3Cl and COS , *Nature*, 282(5736), 253–256, doi:10.1038/282253a0, 1979.

Darer, A. I., Cole-Filipiak, N. C., O'Connor, A. E. and Elrod, M. J.: Formation and Stability of Atmospherically Relevant Isoprene-Derived Organosulfates and Organonitrates, *Environ. Sci. Technol.*, 45(5), 1895–1902, doi:10.1021/es103797z, 2011.

Dentener, F. J. and Crutzen, P. J.: Reaction of N_2O_5 on tropospheric aerosols: Impact on the global distributions of NO_x , O_3 , and OH, *J. Geophys. Res. Atmos.*, 98(D4), 7149–7163,

doi:10.1029/92JD02979, 1993.

DeRieux, W.-S. W., Li, Y., Lin, P., Laskin, J., Laskin, A., Bertram, A. K., Nizkorodov, S. A. and Shiraiwa, M.: Predicting the glass transition temperature and viscosity of secondary organic material using molecular composition, *Atmos. Chem. Phys.*, 18(9), 6331–6351, doi:10.5194/acp-18-6331-2018, 2018.

Derwent, R. G., Jenkin, M. E., Saunders, S. M. and Pilling, M. J.: Photochemical ozone creation potentials for organic compounds in northwest Europe calculated with a master chemical mechanism, *Atmos. Environ.*, 32(14–15), 2429–2441, doi:10.1016/S1352-2310(98)00053-3, 1998.

Derwent, R. G., Jenkin, M. E., Utembe, S. R., Shallcross, D. E., Murrells, T. P. and Passant, N. R.: Secondary organic aerosol formation from a large number of reactive man-made organic compounds, *Sci. Total Environ.*, 408(16), 3374–3381, doi:10.1016/j.scitotenv.2010.04.013, 2010.

Eddingsaas, N. C., VanderVelde, D. G. and Wennberg, P. O.: Kinetics and Products of the Acid-Catalyzed Ring-Opening of Atmospherically Relevant Butyl Epoxy Alcohols, *J. Phys. Chem. A*, 114(31), 8106–8113, doi:10.1021/jp103907c, 2010.

Ehn, M., Berndt, T., Wildt, J. and Mentel, T.: Highly Oxygenated Molecules from Atmospheric Autoxidation of Hydrocarbons: A Prominent Challenge for Chemical Kinetics Studies, *Int. J. Chem. Kinet.*, 49(11), 821–831, doi:10.1002/kin.21130, 2017.

Einfeld, W., Ward, D. E. and Hardy, C.: Effects of fire behavior on prescribed fire smoke characteristics: A case study, in *Global biomass burning: Atmospheric, climatic, and biospheric implications*, MIT Press, Cambridge, MA., 1991.

Elder, A. and Oberdörster, G.: Translocation and effects of ultrafine particles outside of the lung., *Clin. Occup. Environ. Med.*, 5(4), 785–96, doi:10.1016/j.coem.2006.07.003, 2006.

Environmental Protection Agency: 1,3-Butadiene, [online] Available from: <https://www.epa.gov/sites/production/files/2016-08/documents/13-butadiene.pdf> (Accessed 28 February 2019a), 2009.

Environmental Protection Agency: Acrolein, [online] Available from: <https://www.epa.gov/sites/production/files/2016-08/documents/acrolein.pdf> (Accessed 28 February 2019b), 2009.

Environmental Protection Agency: Benzene, [online] Available from: <https://www.epa.gov/sites/production/files/2016-09/documents/benzene.pdf> (Accessed 28 February 2019), 2012.

Epstein, S. A., Blair, S. L. and Nizkorodov, S. A.: Direct Photolysis of α -Pinene Ozonolysis Secondary Organic Aerosol: Effect on Particle Mass and Peroxide Content, *Environ. Sci. Technol.*, 48(19), 11251–11258, doi:10.1021/es502350u, 2014.

Ervens, B., Turpin, B. J. and Weber, R. J.: Secondary organic aerosol formation in cloud droplets and aqueous particles (aqSOA): a review of laboratory, field and model studies, *Atmos. Chem. Phys.*, 11(21), 11069–11102, doi:10.5194/acp-11-11069-2011, 2011.

Escorcia, E. N., Sjostedt, S. J. and Abbatt, J. P. D.: Kinetics of N₂O₅ Hydrolysis on Secondary Organic Aerosol and Mixed Ammonium Bisulfate–Secondary Organic Aerosol Particles, *J. Phys. Chem. A*, 114(50), 13113–13121, doi:10.1021/jp107721v, 2010.

Fang, T., Guo, H., Zeng, L., Verma, V., Nenes, A. and Weber, R. J.: Highly Acidic Ambient Particles, Soluble Metals, and Oxidative Potential: A Link between Sulfate and Aerosol Toxicity, *Environ. Sci. Technol.*, 51(5), 2611–2620, doi:10.1021/acs.est.6b06151, 2017.

Faust, J. A., Wong, J. P. S., Lee, A. K. Y. and Abbatt, J. P. D.: Role of Aerosol Liquid Water in Secondary Organic Aerosol Formation from Volatile Organic Compounds, *Environ. Sci. Technol.*, 51(3), 1405–1413, doi:10.1021/acs.est.6b04700, 2017.

Feng, Y., Ramanathan, V. and Kotamarthi, V. R.: Brown carbon: a significant atmospheric absorber of solar radiation?, *Atmos. Chem. Phys.*, 13(17), 8607–8621, doi:10.5194/acp-13-8607-2013, 2013.

Fernández, P., Grimalt, J. O. and Vilanova, R. M.: Atmospheric Gas-Particle Partitioning of Polycyclic Aromatic Hydrocarbons in High Mountain Regions of Europe, *Environ. Sci. Technol.*, 36(6), 1162–1168, doi:10.1021/es010190t, 2002.

Finlayson-Pitts, B. J. and Pitts, J. N.: *Chemistry of the Upper and Lower Atmosphere: Theory, Experiments, and Applications*, Academic Press, San Diego, CA., 2000.

Fleming, L. T., Lin, P., Laskin, A., Laskin, J., Weltman, R., Edwards, R. D., Arora, N. K., Yadav, A., Meinardi, S., Blake, D. R., Pillarisetti, A., Smith, K. R. and Nizkorodov, S. A.: Molecular composition of particulate matter emissions from dung and brushwood burning household cookstoves in Haryana, India, *Atmos. Chem. Phys.*, 18(4), 2461–2480, doi:10.5194/acp-18-2461-2018, 2018.

Folkers, M., Mentel, T. F. and Wahner, A.: Influence of an organic coating on the reactivity of aqueous aerosols probed by the heterogeneous hydrolysis of N₂O₅, *Geophys. Res. Lett.*, 30(12), doi:10.1029/2003GL017168, 2003.

Forrister, H., Liu, J., Scheuer, E., Dibb, J., Ziemba, L., Thornhill, K. L., Anderson, B., Diskin, G., Perring, A. E., Schwarz, J. P., Campuzano-Jost, P., Day, D. A., Palm, B. B., Jimenez, J. L., Nenes, A. and Weber, R. J.: Evolution of brown carbon in wildfire plumes, *Geophys. Res. Lett.*, 42(11), 4623–4630, doi:10.1002/2015GL063897, 2015.

Forster, P., Ramaswamy, V., Artaxo, P., Berntsen, T., Betts, R., Fahey, D. W., Haywood, J., Lean, J., Lowe, D. C., Myhre, J., Nganga, R., Prinn, R., Raga, G., Schulz, M. and Van Dorland, R.: Changes in Atmospheric Constituents and in Radiative Forcing, in *Climate Change 2007: The Physical Science Basis. Contribution of Working Group I to the Fourth Assessment Report of the Intergovernmental Panel on Climate Change*, edited by S. Solomon, D. Qin, M. Manning, Z. Chen, M. Marquis, M. T. Averyt, and H. L. Miller, Cambridge University Press, Cambridge,

United Kingdom and New York, NY, USA., 2007.

Gautam, S., Edwards, R., Yadav, A., Weltman, R., Pillarsetti, A., Arora, N. K. and Smith, K. R.: Probe-based measurements of moisture in dung fuel for emissions measurements, *Energy Sustain. Dev.*, 35, 1–6, doi:10.1016/j.esd.2016.09.003, 2016.

GBD MAPS Working Group: Summary for Policy Makers., in *Burden of Disease Attributable to Major Air Pollution Sources in India.*, Health Effects Institute, Boston, MA., 2018.

Gelencsér, A., Hoffer, A., Kiss, G., Tombácz, E., Kurdi, R. and Bencze, L.: In-situ Formation of Light-Absorbing Organic Matter in Cloud Water, *J. Atmos. Chem.*, 45(1), 25–33, doi:10.1023/A:1024060428172, 2003.

Gilardoni, S., Massoli, P., Paglione, M., Giulianelli, L., Carbone, C., Rinaldi, M., Decesari, S., Sandrini, S., Costabile, F., Gobbi, G. P., Pietrogrande, M. C., Visentin, M., Scotto, F., Fuzzi, S. and Facchini, M. C.: Direct observation of aqueous secondary organic aerosol from biomass-burning emissions, *Proc. Natl. Acad. Sci.*, 113(36), 10013–10018, doi:10.1073/pnas.1602212113, 2016.

Giroto, G., China, S., Bhandari, J., Gorkowski, K., Scarnato, B. V., Capek, T., Marinoni, A., Veghte, D. P., Kulkarni, G., Aiken, A. C., Dubey, M. and Mazzoleni, C.: Fractal-like Tar Ball Aggregates from Wildfire Smoke, *Environ. Sci. Technol. Lett.*, 5(6), 360–365, doi:10.1021/acs.estlett.8b00229, 2018.

Global Alliance for Clean Cookstoves: Protocols: Water Boiling Test, [online] Available from: <http://cleancookstoves.org/technology-and-fuels/testing/protocols.html>, 2014.

Grieshop, A. P., Logue, J. M., Donahue, N. M. and Robinson, A. L.: Laboratory investigation of photochemical oxidation of organic aerosol from wood fires 1: measurement and simulation of organic aerosol evolution, *Atmos. Chem. Phys.*, 9(4), 1263–1277, doi:10.5194/acp-9-1263-2009, 2009.

Guenther, A., Karl, T., Harley, P., Wiedinmyer, C., Palmer, P. I. and Geron, C.: Estimates of global terrestrial isoprene emissions using MEGAN (Model of Emissions of Gases and Aerosols from Nature), *Atmos. Chem. Phys.*, 6(11), 3181–3210, doi:10.5194/acp-6-3181-2006, 2006.

Guo, H., Xu, L., Bougiatioti, A., Cerully, K. M., Capps, S. L., Hite, J. R., Carlton, A. G., Lee, S.-H., Bergin, M. H., Ng, N. L., Nenes, A. and Weber, R. J.: Fine-particle water and pH in the southeastern United States, *Atmos. Chem. Phys.*, 15(9), 5211–5228, doi:10.5194/acp-15-5211-2015, 2015.

Guttikunda, S., Jawahar, P., Gota, S. and KA, N.: UrbanEmissions.info, [online] Available from: <http://www.urbanemissions.info/> (Accessed 10 August 2017), 2016.

De Haan, D. O., Corrigan, A. L., Tolbert, M. A., Jimenez, J. L., Wood, S. E. and Turley, J. J.: Secondary Organic Aerosol Formation by Self-Reactions of Methylglyoxal and Glyoxal in Evaporating Droplets, *Environ. Sci. Technol.*, 43(21), 8184–8190, doi:10.1021/es902152t, 2009.

De Haan, D. O., Hawkins, L. N., Kononenko, J. A., Turley, J. J., Corrigan, A. L., Tolbert, M. A. and Jimenez, J. L.: Formation of Nitrogen-Containing Oligomers by Methylglyoxal and Amines in Simulated Evaporating Cloud Droplets, *Environ. Sci. Technol.*, 45(3), 984–991, doi:10.1021/es102933x, 2011.

Hallquist, M., Wenger, J. C., Baltensperger, U., Rudich, Y., Simpson, D., Claeys, M., Dommen, J., Donahue, N. M., George, C., Goldstein, A. H., Hamilton, J. F., Herrmann, H., Hoffmann, T., Iinuma, Y., Jang, M., Jenkin, M. E., Jimenez, J. L., Kiendler-Scharr, A., Maenhaut, W., McFiggans, G., Mentel, T. F., Monod, A., Prévôt, A. S. H., Seinfeld, J. H., Surratt, J. D., Szmigielski, R. and Wildt, J.: The formation, properties and impact of secondary organic aerosol: current and emerging issues, *Atmos. Chem. Phys.*, 9(14), 5155–5236, doi:10.5194/acp-9-5155-2009, 2009.

Harrison, M. A. J., Barra, S., Borghesi, D., Vione, D., Arsene, C. and Iulian Olariu, R.: Nitrated phenols in the atmosphere: a review, *Atmos. Environ.*, 39(2), 231–248, doi:10.1016/J.ATMOSENV.2004.09.044, 2005.

Hatch, L. E., Luo, W., Pankow, J. F., Yokelson, R. J., Stockwell, C. E. and Barsanti, K. C.: Identification and quantification of gaseous organic compounds emitted from biomass burning using two-dimensional gas chromatography–time-of-flight mass spectrometry, *Atmos. Chem. Phys.*, 15(4), 1865–1899, doi:10.5194/acp-15-1865-2015, 2015.

Hatch, L. E., Rivas-Ubach, A., Jen, C. N., Lipton, M., Goldstein, A. H. and Barsanti, K. C.: Measurements of I/SVOCs in biomass-burning smoke using solid-phase extraction disks and two-dimensional gas chromatography, *Atmos. Chem. Phys.*, 18(24), 17801–17817, doi:10.5194/acp-18-17801-2018, 2018.

Hawkins, L. N., Lemire, A. N., Galloway, M. M., Corrigan, A. L., Turley, J. J., Espelien, B. M. and De Haan, D. O.: Maillard Chemistry in Clouds and Aqueous Aerosol As a Source of Atmospheric Humic-Like Substances, *Environ. Sci. Technol.*, 50(14), 7443–7452, doi:10.1021/acs.est.6b00909, 2016.

Hawkins, L. N., Welsh, H. G. and Alexander, M. V.: Evidence for pyrazine-based chromophores in cloud water mimics containing methylglyoxal and ammonium sulfate, *Atmos. Chem. Phys.*, 18(16), 12413–12431, doi:10.5194/acp-18-12413-2018, 2018.

Hems, R. F. and Abbatt, J. P. D.: Aqueous Phase Photo-oxidation of Brown Carbon Nitrophenols: Reaction Kinetics, Mechanism, and Evolution of Light Absorption, *ACS Earth Sp. Chem.*, 2(3), 225–234, doi:10.1021/acsearthspacechem.7b00123, 2018.

Hennigan, C. J., Miracolo, M. A., Engelhart, G. J., May, A. A., Presto, A. A., Lee, T., Sullivan, A. P., McMeeking, G. R., Coe, H., Wold, C. E., Hao, W. M., Gilman, J. B., Kuster, W. C., de Gouw, J., Schichtel, B. A., Collett Jr, J. L., Kreidenweis, S. M. and Robinson, A. L.: Chemical and physical transformations of organic aerosol from the photo-oxidation of open biomass burning emissions in an environmental chamber, *Atmos. Chem. Phys.*, 11(15), 7669–7686, doi:10.5194/acp-11-7669-2011, 2011.

Herrmann, H., Schaefer, T., Tilgner, A., Styler, S. A., Weller, C., Teich, M. and Otto, T.:

Tropospheric Aqueous-Phase Chemistry: Kinetics, Mechanisms, and Its Coupling to a Changing Gas Phase, *Chem. Rev.*, 115(10), 4259–4334, doi:10.1021/cr500447k, 2015.

Hinks, M. L., Brady, M. V., Lignell, H., Song, M., Grayson, J. W., Bertram, A. K., Lin, P., Laskin, A., Laskin, J. and Nizkorodov, S. A.: Effect of viscosity on photodegradation rates in complex secondary organic aerosol materials, *Phys. Chem. Chem. Phys.*, 18(13), 8785–8793, doi:10.1039/C5CP05226B, 2016.

Hinks, M. L., Montoya-Aguilera, J., Ellison, L., Lin, P., Laskin, A., Laskin, J., Shiraiwa, M., Dabdub, D. and Nizkorodov, S. A.: Effect of relative humidity on the composition of secondary organic aerosol from the oxidation of toluene, *Atmos. Chem. Phys.*, 18(3), 1643–1652, doi:10.5194/acp-18-1643-2018, 2018.

Hodzic, A., Madronich, S., Kasibhatla, P. S., Tyndall, G., Aumont, B., Jimenez, J. L., Lee-Taylor, J. and Orlando, J.: Organic photolysis reactions in tropospheric aerosols: effect on secondary organic aerosol formation and lifetime, *Atmos. Chem. Phys. Discuss.*, 15(6), 8113–8149, doi:10.5194/acpd-15-8113-2015, 2015.

Hosseini, S., Urbanski, S. P., Dixit, P., Qi, L., Burling, I. R., Yokelson, R. J., Johnson, T. J., Shrivastava, M., Jung, H. S., Weise, D. R., Miller, J. W. and Cocker, D. R.: Laboratory characterization of PM emissions from combustion of wildland biomass fuels, *J. Geophys. Res.*, 118(17), 9914–9929, doi:10.1002/jgrd.50481, 2013.

Huang, R.-J., Zhang, Y., Bozzetti, C., Ho, K.-F., Cao, J.-J., Han, Y., Daellenbach, K. R., Slowik, J. G., Platt, S. M., Canonaco, F., Zotter, P., Wolf, R., Pieber, S. M., Bruns, E. A., Crippa, M., Ciarelli, G., Piazzalunga, A., Schwikowski, M., Abbaszade, G., Schnelle-Kreis, J., Zimmermann, R., An, Z., Szidat, S., Baltensperger, U., Haddad, I. El and Prévôt, A. S. H.: High secondary aerosol contribution to particulate pollution during haze events in China, *Nature*, 514(7521), 218–222, doi:10.1038/nature13774, 2014.

Hughey, C. A., Hendrickson, C. L., Rodgers, R. P., Marshall, A. G. and Qian, K.: Kendrick Mass Defect Spectrum: A Compact Visual Analysis for Ultrahigh-Resolution Broadband Mass Spectra, *Anal. Chem.*, 73(19), 4676–4681, doi:10.1021/AC010560W, 2001.

Iinuma, Y., Müller, C., Böge, O., Gnauk, T. and Herrmann, H.: The formation of organic sulfate esters in the limonene ozonolysis secondary organic aerosol (SOA) under acidic conditions, *Atmos. Environ.*, 41(27), 5571–5583, doi:10.1016/J.ATMOSENV.2007.03.007, 2007.

Iinuma, Y., Böge, O., Gräfe, R. and Herrmann, H.: Methyl-Nitrocatechols: Atmospheric Tracer Compounds for Biomass Burning Secondary Organic Aerosols, *Environ. Sci. Technol.*, 44(22), 8453–8459, doi:10.1021/es102938a, 2010.

Iinuma, Y., Keywood, M. and Herrmann, H.: Characterization of primary and secondary organic aerosols in Melbourne airshed: The influence of biogenic emissions, wood smoke and bushfires, *Atmos. Environ.*, 130, 54–63, doi:10.1016/J.ATMOSENV.2015.12.014, 2016.

IPCC: Climate Change 2013: The Physical Science Basis. Contribution of Working Group I to the Fifth Assessment Report of the Intergovernmental Panel on Climate Change., edited by T. F.

Stocker, D. Qin, G.-K. Plattner, M. Tignor, S. K. Allen, J. Boschung, A. Nauels, Y. Xia, V. Bex, and P. M. Midgley, Cambridge University Press, Cambridge, United Kingdom and New York, NY, USA., 2013.

Iranshahi M, Askari M, Sahebkar A and Hadjipavlou-Litina D: Evaluation of antioxidant, anti-inflammatory and lipoxygenase inhibitory activities of the prenylated coumarin umbelliprenin., 2009.

Isaacman-VanWertz, G., Massoli, P., O'Brien, R., Lim, C., Franklin, J. P., Moss, J. A., Hunter, J. F., Nowak, J. B., Canagaratna, M. R., Misztal, P. K., Arata, C., Roscioli, J. R., Herndon, S. T., Onasch, T. B., Lambe, A. T., Jayne, J. T., Su, L., Knopf, D. A., Goldstein, A. H., Worsnop, D. R. and Kroll, J. H.: Chemical evolution of atmospheric organic carbon over multiple generations of oxidation, *Nat. Chem.*, 10(4), 462–468, doi:10.1038/s41557-018-0002-2, 2018.

Jayarathne, T., Stockwell, C. E., Bhave, P. V., Praveen, P. S., Rathnayake, C. M., Islam, M. R., Panday, A. K., Adhikari, S., Maharjan, R., Goetz, J. D., DeCarlo, P. F., Saikawa, E., Yokelson, R. J. and Stone, E. A.: Nepal Ambient Monitoring and Source Testing Experiment (NAMaSTE): Emissions of particulate matter from wood and dung cooking fires, garbage and crop residue burning, brick kilns, and other sources, *Atmos. Chem. Phys. Discuss.*, 1–51, doi:10.5194/acp-2017-510, 2017.

Jen, C. N., Hatch, L. E., Selimovic, V., Yokelson, R. J., Weber, R., Fernandez, A. E., Kreisberg, N. M., Barsanti, K. C. and Goldstein, A. H.: Speciated and total emission factors of particulate organics from burning western US wildland fuels and their dependence on combustion efficiency, *Atmos. Chem. Phys.*, 19(2), 1013–1026, doi:10.5194/acp-19-1013-2019, 2019.

Johnson, M., Edwards, R., Alatorre Frenk, C. and Masera, O.: In-field greenhouse gas emissions from cookstoves in rural Mexican households, *Atmos. Environ.*, 42(6), 1206–1222, doi:10.1016/j.atmosenv.2007.10.034, 2008.

Johnson, M., Edwards, R., Ghilardi, A., Berrueta, V., Gillen, D., Frenk, C. A. and Masera, O.: Quantification of Carbon Savings from Improved Biomass Cookstove Projects, *Environ. Sci. Technol.*, 43(7), 2456–2462, doi:10.1021/es801564u, 2009.

Jokinen, T., Sipilä, M., Richters, S., Kerminen, V.-M., Paasonen, P., Stratmann, F., Worsnop, D., Kulmala, M., Ehn, M., Herrmann, H. and Berndt, T.: Rapid Autoxidation Forms Highly Oxidized RO₂ Radicals in the Atmosphere, *Angew. Chemie Int. Ed.*, 53(52), 14596–14600, doi:10.1002/anie.201408566, 2014.

Kampf, C. J., Jakob, R. and Hoffmann, T.: Identification and characterization of aging products in the glyoxal/ammonium sulfate system – implications for light-absorbing material in atmospheric aerosols, *Atmos. Chem. Phys.*, 12(14), 6323–6333, doi:10.5194/acp-12-6323-2012, 2012.

Kirchstetter, T. W., Novakov, T. and Hobbs, P. V.: Evidence that the spectral dependence of light absorption by aerosols is affected by organic carbon, *J. Geophys. Res. Atmos.*, 109(D21), doi:10.1029/2004JD004999, 2004.

- Kituyi, E., Marufu, L., Wandiga, S. O., Jumba, I. O., Andreae, M. O. and Helas, G.: Carbon monoxide and nitric oxide from biofuel fires in Kenya, *Energy Convers. Manag.*, 42(13), 1517–1542, doi:10.1016/S0196-8904(00)00158-8, 2001.
- Klimont, Z., Kupiainen, K., Heyes, C., Purohit, P., Cofala, J., Rafaj, P., Borken-Kleefeld, J. and Schöpp, W.: Global anthropogenic emissions of particulate matter including black carbon, *Atmos. Chem. Phys.*, 17(14), 8681–8723, doi:10.5194/acp-17-8681-2017, 2017.
- Koss, A. R., Sekimoto, K., Gilman, J. B., Selimovic, V., Coggon, M. M., Zarzana, K. J., Yuan, B., Lerner, B. M., Brown, S. S., Jimenez, J. L., Krechmer, J., Roberts, J. M., Warneke, C., Yokelson, R. J. and de Gouw, J.: Non-methane organic gas emissions from biomass burning: identification, quantification, and emission factors from PTR-ToF during the FIREX 2016 laboratory experiment, *Atmos. Chem. Phys.*, 18(5), 3299–3319, doi:10.5194/acp-18-3299-2018, 2018.
- Kourtchev, I., Giorio, C., Manninen, A., Wilson, E., Mahon, B., Aalto, J., Kajos, M., Venables, D., Ruuskanen, T., Levula, J., Loponen, M., Connors, S., Harris, N., Zhao, D., Kiendler-Scharr, A., Mentel, T., Rudich, Y., Hallquist, M., Doussin, J.-F., Maenhaut, W., Bäck, J., Petäjä, T., Wenger, J., Kulmala, M. and Kalberer, M.: Enhanced Volatile Organic Compounds emissions and organic aerosol mass increase the oligomer content of atmospheric aerosols, *Sci. Rep.*, 6(1), 35038, doi:10.1038/srep35038, 2016.
- Kristensen, K., Cui, T., Zhang, H., Gold, A., Glasius, M. and Surratt, J. D.: Dimers in α -pinene secondary organic aerosol: effect of hydroxyl radical, ozone, relative humidity and aerosol acidity, *Atmos. Chem. Phys.*, 14(8), 4201–4218, doi:10.5194/acp-14-4201-2014, 2014.
- Kristensen, K., Watne, Å. K., Hammes, J., Lutz, A., Petäjä, T., Hallquist, M., Bilde, M. and Glasius, M.: High-Molecular Weight Dimer Esters Are Major Products in Aerosols from α -Pinene Ozonolysis and the Boreal Forest, *Environ. Sci. Technol. Lett.*, 3(8), 280–285, doi:10.1021/acs.estlett.6b00152, 2016.
- Kumar, V., Chandra, B. P. and Sinha, V.: Large unexplained suite of chemically reactive compounds present in ambient air due to biomass fires, *Sci. Rep.*, 8(1), 626, doi:10.1038/s41598-017-19139-3, 2018.
- Lack, D. A. and Langridge, J. M.: On the attribution of black and brown carbon light absorption using the Ångström exponent, *Atmos. Chem. Phys.*, 13(20), 10535–10543, doi:10.5194/acp-13-10535-2013, 2013.
- Laden, F., Schwartz, J., Speizer, F. E. and Dockery, D. W.: Reduction in Fine Particulate Air Pollution and Mortality, *Am. J. Respir. Crit. Care Med.*, 173(6), 667–672, doi:10.1164/rccm.200503-443OC, 2006.
- Lamb, B., Westberg, H., Allwine, G. and Quarles, T.: Biogenic hydrocarbon emissions from deciduous and coniferous trees in the United States, *J. Geophys. Res.*, 90(D1), 2380, doi:10.1029/JD090iD01p02380, 1985.
- Laskin, A., Smith, J. S. and Laskin, J.: Molecular Characterization of Nitrogen-Containing

Organic Compounds in Biomass Burning Aerosols Using High-Resolution Mass Spectrometry, *Environ. Sci. Technol.*, 43(10), 3764–3771, doi:10.1021/es803456n, 2009.

Laskin, A., Laskin, J. and Nizkorodov, S. A.: Chemistry of Atmospheric Brown Carbon, *Chem. Rev.*, 115(10), 4335–4382, doi:10.1021/cr5006167, 2015.

Laskin, A., Lin, P., Laskin, J., Fleming, L. T. and Nizkorodov, S. A.: Molecular Characterization of Atmospheric Brown Carbon, in *Multiphase Environmental Chemistry in the Atmosphere*, American Chemical Society., 2018.

Laskin, J., Laskin, A., Roach, P. J., Slysz, G. W., Anderson, G. A., Nizkorodov, S. A., Bones, D. L. and Nguyen, L. Q.: High-Resolution Desorption Electrospray Ionization Mass Spectrometry for Chemical Characterization of Organic Aerosols, *Anal. Chem.*, 82(5), 2048–2058, doi:10.1021/ac902801f, 2010.

Laskin, J., Laskin, A., Nizkorodov, S. A., Roach, P., Eckert, P., Gilles, M. K., Wang, B., Lee, H. J. (Julie) and Hu, Q.: Molecular Selectivity of Brown Carbon Chromophores, *Environ. Sci. Technol.*, 48(20), 12047–12055, doi:10.1021/es503432r, 2014.

Lee, A. K. Y., Zhao, R., Li, R., Liggio, J., Li, S.-M. and Abbatt, J. P. D.: Formation of Light Absorbing Organo-Nitrogen Species from Evaporation of Droplets Containing Glyoxal and Ammonium Sulfate, *Environ. Sci. Technol.*, 47(22), 12819–12826, doi:10.1021/es402687w, 2013.

Lee, S., Shin, D.-S., Kim, J. S., Oh, K.-B. and Kang, S. S.: Antibacterial coumarins from *Angelica gigas* roots, *Arch. Pharm. Res.*, 26(6), 449–452, doi:10.1007/BF02976860, 2003.

Lee, S., Baumann, K., Schauer, J. J., Sheesley, R. J., Naeher, L. P., Meinardi, S., Blake, D. R., Edgerton, E. S., Russell, A. G. and Clements, M.: Gaseous and particulate emissions from prescribed burning in Georgia, *Environ. Sci. Technol.*, 39(23), 9049–9056, doi:10.1021/es051583l, 2005.

Lelieveld, J., Evans, J. S., Fnais, M., Giannadaki, D. and Pozzer, A.: The contribution of outdoor air pollution sources to premature mortality on a global scale, *Nature*, 525(7569), 367–371, doi:10.1038/nature15371, 2015.

Li, C., He, Q., Schade, J., Passig, J., Zimmermann, R., Meidan, D., Laskin, A. and Rudich, Y.: Dynamic changes in optical and chemical properties of tar ball aerosols by atmospheric photochemical aging, *Atmos. Chem. Phys.*, 19(1), 139–163, doi:10.5194/acp-19-139-2019, 2019.

Li, X., Jiang, L., Hoa, L. P., Lyu, Y., Xu, T., Yang, X., Iinuma, Y., Chen, J. and Herrmann, H.: Size distribution of particle-phase sugar and nitrophenol tracers during severe urban haze episodes in Shanghai, *Atmos. Environ.*, 145, 115–127, doi:10.1016/j.atmosenv.2016.09.030, 2016.

Li, Z., Smith, K. A. and Cappa, C. D.: Influence of relative humidity on the heterogeneous oxidation of secondary organic aerosol, *Atmos. Chem. Phys.*, 18(19), 14585–14608, doi:10.5194/acp-18-14585-2018, 2018.

Lignell, H., Epstein, S. A., Marvin, M. R., Shemesh, D., Gerber, B. and Nizkorodov, S.: Experimental and Theoretical Study of Aqueous *cis*-Pinonic Acid Photolysis, *J. Phys. Chem. A*, 117(48), 12930–12945, doi:10.1021/jp4093018, 2013.

Lignell, H., Hinks, M. L. and Nizkorodov, S. A.: Exploring matrix effects on photochemistry of organic aerosols., *Proc. Natl. Acad. Sci. U. S. A.*, 111(38), 13780–5, doi:10.1073/pnas.1322106111, 2014.

Lim, Y. B., Tan, Y., Perri, M. J., Seitzinger, S. P. and Turpin, B. J.: Aqueous chemistry and its role in secondary organic aerosol (SOA) formation, *Atmos. Chem. Phys.*, 10(21), 10521–10539, doi:10.5194/acp-10-10521-2010, 2010.

Lin, P., Rincon, A. G., Kalberer, M. and Yu, J. Z.: Elemental Composition of HULIS in the Pearl River Delta Region, China: Results Inferred from Positive and Negative Electrospray High Resolution Mass Spectrometric Data, *Environ. Sci. Technol.*, 46(14), 7454–7462, doi:10.1021/es300285d, 2012.

Lin, P., Laskin, J., Nizkorodov, S. A. and Laskin, A.: Revealing Brown Carbon Chromophores Produced in Reactions of Methylglyoxal with Ammonium Sulfate, *Environ. Sci. Technol.*, 49(24), 14257–14266, doi:10.1021/acs.est.5b03608, 2015.

Lin, P., Aiona, P. K., Li, Y., Shiraiwa, M., Laskin, J., Nizkorodov, S. A. and Laskin, A.: Molecular Characterization of Brown Carbon in Biomass Burning Aerosol Particles, *Environ. Sci. Technol.*, 50(21), 11815–11824, doi:10.1021/acs.est.6b03024, 2016.

Lin, P., Bluvshstein, N., Rudich, Y., Nizkorodov, S., Laskin, J. and Laskin, A.: Molecular Chemistry of Atmospheric Brown Carbon Inferred from a Nationwide Biomass-Burning Event, *Environ. Sci. Technol.*, 51(20), 11561–11570, doi:10.1021/acs.est.7b02276, 2017.

Lin, P., Fleming, L. T., Nizkorodov, S. A., Laskin, J. and Laskin, A.: Comprehensive Molecular Characterization of Atmospheric Brown Carbon by High Resolution Mass Spectrometry with Electrospray and Atmospheric Pressure Photoionization, *Anal. Chem.*, 90(21), 12493–12502, doi:10.1021/acs.analchem.8b02177, 2018.

Liu, X., Huey, L. G., Yokelson, R. J., Selimovic, V., Simpson, I. J., Müller, M., Jimenez, J. L., Campuzano-Jost, P., Beyersdorf, A. J., Blake, D. R., Butterfield, Z., Choi, Y., Crounse, J. D., Day, D. A., Diskin, G. S., Dubey, M. K., Fortner, E., Hanisco, T. F., Hu, W., King, L. E., Kleinman, L., Meinardi, S., Mikoviny, T., Onasch, T. B., Palm, B. B., Peischl, J., Pollack, I. B., Ryerson, T. B., Sachse, G. W., Sedlacek, A. J., Shilling, J. E., Springston, S., St. Clair, J. M., Tanner, D. J., Teng, A. P., Wennberg, P. O., Wisthaler, A. and Wolfe, G. M.: Airborne measurements of western U.S. wildfire emissions: Comparison with prescribed burning and air quality implications, *J. Geophys. Res. Atmos.*, 122(11), 6108–6129, doi:10.1002/2016JD026315, 2017.

Lobert, J. M., Keene, W. C., Logan, J. A. and Yevich, R.: Global chlorine emissions from biomass burning: Reactive Chlorine Emissions Inventory, *J. Geophys. Res. Atmos.*, 104(D7), 8373–8389, doi:10.1029/1998JD100077, 1999.

Ludwig, J., Marufu, L. T., Huber, B., Andreae, M. O. and Helas, G.: Domestic Combustion of Biomass Fuels in Developing Countries: A Major Source of Atmospheric Pollutants, *J. Atmos. Chem.*, 44(1), 23–37, doi:10.1023/A:1022159910667, 2003.

Ma, J., Li, X., Gu, P., Dallmann, T. R., Presto, A. A. and Donahue, N. M.: Estimating ambient particulate organic carbon concentrations and partitioning using thermal optical measurements and the volatility basis set, *Aerosol Sci. Technol.*, 50(6), 638–651, doi:10.1080/02786826.2016.1158778, 2016.

Macdonald, R. W., Barrie, L. A., Bidleman, T. F., Diamond, M. L., Gregor, D. J., Semkin, R. G., Strachan, W. M. J., Li, Y. F., Wania, F., Alae, M., Alexeeva, L. B., Backus, S. M., Bailey, R., Bewers, J. M., Gobeil, C., Halsall, C. J., Harner, T., Hoff, J. T., Jantunen, L. M. M., Lockhart, W. L., Mackay, D., Muir, D. C. G., Pudykiewicz, J., Reimer, K. J., Smith, J. N., Stern, G. ., Schroeder, W. H., Wagemann, R. and Yunker, M. B.: Contaminants in the Canadian Arctic: 5 years of progress in understanding sources, occurrence and pathways, *Sci. Total Environ.*, 254(2–3), 93–234, doi:10.1016/S0048-9697(00)00434-4, 2000.

Madronich, S., Flocke, S., Zeng, J., Petropavlovskikh, I. and Lee-Taylor, J.: Tropospheric Ultraviolet and Visible (TUV) Radiation Model, [online] Available from: http://cprm.acom.ucar.edu/Models/TUV/Interactive_TUV/, 2002.

Malecha, K. T. and Nizkorodov, S. A.: Feasibility of Photosensitized Reactions with Secondary Organic Aerosol Particles in the Presence of Volatile Organic Compounds, *J. Phys. Chem. A*, 121(26), 4961–4967, doi:10.1021/acs.jpca.7b04066, 2017.

Malecha, K. T., Cai, Z. and Nizkorodov, S. A.: Photodegradation of Secondary Organic Aerosol Material Quantified with a Quartz Crystal Microbalance, *Environ. Sci. Technol. Lett.*, 5(6), 366–371, doi:10.1021/acs.estlett.8b00231, 2018.

Manion, J. A., Huie, R. E., Levin, R. D., Burgess Jr., D. R., Orkin, V. L., Tsang, W., McGivern, W. S., Hudgens, J. W., Knyazev, V. D., Atkinson, D. B., Chai, E., Tereza, A. M., Lin, C. Y., Allison, T. C., Mallard, W. G., Westley, F., Herron, J. T., Hampson, R. F. and Frizzell, D. H.: NIST Chemical Kinetics Database, in NIST Standard Reference Database 17, National Institute of Standards and Technology, Gaithersburg, Maryland, 20899-8320., 2015.

Martin, S. T., Hung, H.-M., Park, R. J., Jacob, D. J., Spurr, R. J. D., Chance, K. V. and Chin, M.: Effects of the physical state of tropospheric ammonium-sulfate-nitrate particles on global aerosol direct radiative forcing, *Atmos. Chem. Phys.*, 4(1), 183–214, doi:10.5194/acp-4-183-2004, 2004.

McNeill, V. F.: Aqueous Organic Chemistry in the Atmosphere: Sources and Chemical Processing of Organic Aerosols, *Environ. Sci. Technol.*, 49(3), 1237–1244, doi:10.1021/es5043707, 2015.

McNeill, V. F., Patterson, J., Wolfe, G. M. and Thornton, J. A.: The effect of varying levels of surfactant on the reactive uptake of N_2O_5 to aqueous aerosol, *Atmos. Chem. Phys.*, 6(6), 1635–1644, doi:10.5194/acp-6-1635-2006, 2006.

Miller, J. S. and Olejnik, D.: Photolysis of polycyclic aromatic hydrocarbons in water, *Water*

Res., 35(1), 233–243, doi:10.1016/S0043-1354(00)00230-X, 2001.

Minerath, E. C. and Elrod, M. J.: Assessing the Potential for Diol and Hydroxy Sulfate Ester Formation from the Reaction of Epoxides in Tropospheric Aerosols, *Environ. Sci. Technol.*, 43(5), 1386–1392, doi:10.1021/es8029076, 2009.

Minerath, E. C., Casale, M. T. and Elrod, M. J.: Kinetics Feasibility Study of Alcohol Sulfate Esterification Reactions in Tropospheric Aerosols, *Environ. Sci. Technol.*, 42(12), 4410–4415, doi:10.1021/es8004333, 2008.

Monge, M. E., Rosenørn, T., Favez, O., Müller, M., Adler, G., Abo Riziq, A., Rudich, Y., Herrmann, H., George, C. and D'Anna, B.: Alternative pathway for atmospheric particles growth., *Proc. Natl. Acad. Sci. U. S. A.*, 109(18), 6840–4, doi:10.1073/pnas.1120593109, 2012.

Moorthy, B., Chu, C. and Carlin, D. J.: Polycyclic Aromatic Hydrocarbons: From Metabolism to Lung Cancer, *Toxicol. Sci.*, 145(1), 5–15, doi:10.1093/toxsci/kfv040, 2015.

Moosmüller, H., Chakrabarty, R. K. and Arnott, W. P.: Aerosol light absorption and its measurement: A review, *J. Quant. Spectrosc. Radiat. Transf.*, 110(11), 844–878, doi:10.1016/J.JQSRT.2009.02.035, 2009.

Moriondo, M., Good, P., Durao, R., Bindi, M., Giannakopoulos, C. and Corte-Real, J.: Potential impact of climate change on fire risk in the Mediterranean area, *Clim. Res.*, 31(1), 85–95, doi:10.3354/cr031085, 2006.

Mukhopadhyay, R., Sambandam, S., Pillarisetti, A., Jack, D., Mukhopadhyay, K., Balakrishnan, K., Vaswani, M., Bates, M. N., Kinney, P. L., Arora, N. and Smith, K. R.: Cooking practices, air quality, and the acceptability of advanced cookstoves in Haryana, India: an exploratory study to inform large-scale interventions., *Glob. Health Action*, 5, 1–13, doi:10.3402/gha.v5i0.19016, 2012.

Nguyen, T. B., Bateman, A. P., Bones, D. L., Nizkorodov, S. A., Laskin, J. and Laskin, A.: High-resolution mass spectrometry analysis of secondary organic aerosol generated by ozonolysis of isoprene, *Atmos. Environ.*, 44(8), 1032–1042, doi:10.1016/J.ATMOENV.2009.12.019, 2010.

Nguyen, T. B., Roach, P. J., Laskin, J., Laskin, A. and Nizkorodov, S. A.: Effect of humidity on the composition of isoprene photooxidation secondary organic aerosol, *Atmos. Chem. Phys.*, 11(14), 6931–6944, doi:10.5194/acp-11-6931-2011, 2011.

Nguyen, T. B., Laskin, A., Laskin, J. and Nizkorodov, S. A.: Direct aqueous photochemistry of isoprene high-NO_x secondary organic aerosol, *Phys. Chem. Chem. Phys.*, 14(27), 9702, doi:10.1039/c2cp40944e, 2012a.

Nguyen, T. B., Lee, P. B., Updyke, K. M., Bones, D. L., Laskin, J., Laskin, A. and Nizkorodov, S. A.: Formation of nitrogen- and sulfur-containing light-absorbing compounds accelerated by evaporation of water from secondary organic aerosols, *J. Geophys. Res. Atmos.*, 117(D1), D01207, doi:10.1029/2011JD016944, 2012b.

- Nguyen, T. B., Laskin, A., Laskin, J. and Nizkorodov, S. A.: Brown carbon formation from ketoaldehydes of biogenic monoterpenes, *Faraday Discuss.*, 165(0), 473, doi:10.1039/c3fd00036b, 2013.
- Nozière, B. and Esteve, W.: Light-absorbing aldol condensation products in acidic aerosols: Spectra, kinetics, and contribution to the absorption index, *Atmos. Environ.*, 41(6), 1150–1163, doi:10.1016/J.ATMOSENV.2006.10.001, 2007.
- Oberdörster, G., Sharp, Z., Atudorei, V., Elder, A., Gelein, R., Kreyling, W. and Cox, C.: Translocation of Inhaled Ultrafine Particles to the Brain, *Inhal. Toxicol.*, 16(6–7), 437–445, doi:10.1080/08958370490439597, 2004.
- Ojha, N., Naja, M., Singh, K. P., Sarangi, T., Kumar, R., Lal, S., Lawrence, M. G., Butler, T. M. and Chandola, H. C.: Variabilities in ozone at a semi-urban site in the Indo-Gangetic Plain region: Association with the meteorology and regional processes, *J. Geophys. Res. Atmos.*, 117(D20), doi:10.1029/2012JD017716, 2012.
- Ortega, A. M., Day, D. A., Cubison, M. J., Brune, W. H., Bon, D., de Gouw, J. A. and Jimenez, J. L.: Secondary organic aerosol formation and primary organic aerosol oxidation from biomass-burning smoke in a flow reactor during FLAME-3, *Atmos. Chem. Phys.*, 13(22), 11551–11571, doi:10.5194/acp-13-11551-2013, 2013.
- Ortega, A. M., Hayes, P. L., Peng, Z., Palm, B. B., Hu, W., Day, D. A., Li, R., Cubison, M. J., Brune, W. H., Graus, M., Warneke, C., Gilman, J. B., Kuster, W. C., de Gouw, J., Gutiérrez-Montes, C. and Jimenez, J. L.: Real-time measurements of secondary organic aerosol formation and aging from ambient air in an oxidation flow reactor in the Los Angeles area, *Atmos. Chem. Phys.*, 16(11), 7411–7433, doi:10.5194/acp-16-7411-2016, 2016.
- Pandey, A., Sadavarte, P., Rao, A. and Venkataraman, C.: Trends in multi-pollutant emissions from a technology-linked inventory for India: II. Residential, agricultural and informal industry sectors, *Atmos. Environ.*, 99, 341–352, doi:10.1016/J.ATMOSENV.2014.09.080, 2014.
- Pandey, A., Pervez, S. and Chakrabarty, R. K.: Filter-based measurements of UV–vis mass absorption cross sections of organic carbon aerosol from residential biomass combustion: Preliminary findings and sources of uncertainty, *J. Quant. Spectrosc. Radiat. Transf.*, 182, 296–304, doi:10.1016/j.jqsrt.2016.06.023, 2016.
- Pankow, J. F.: An absorption model of the gas/aerosol partitioning involved in the formation of secondary organic aerosol, *Atmos. Environ.*, 28(2), 189–193, doi:10.1016/1352-2310(94)90094-9, 1994.
- Park, S.-C., Burden, D. K. and Nathanson, G. M.: The Inhibition of N₂O₅ Hydrolysis in Sulfuric Acid by 1-Butanol and 1-Hexanol Surfactant Coatings, *J. Phys. Chem. A*, 111(15), 2921–2929, doi:10.1021/jp068228h, 2007.
- Perraud, V., Bruns, E. A., Ezell, M. J., Johnson, S. N., Yu, Y., Alexander, M. L., Zelenyuk, A., Imre, D., Chang, W. L., Dabdub, D., Pankow, J. F. and Finlayson-Pitts, B. J.: Nonequilibrium atmospheric secondary organic aerosol formation and growth., *Proc. Natl. Acad. Sci. U. S. A.*,

109(8), 2836–41, doi:10.1073/pnas.1119909109, 2012.

Phillips, S. M. and Smith, G. D.: Light Absorption by Charge Transfer Complexes in Brown Carbon Aerosols, *Environ. Sci. Technol. Lett.*, 1(10), 382–386, doi:10.1021/ez500263j, 2014.

Phillips, S. M. and Smith, G. D.: Further Evidence for Charge Transfer Complexes in Brown Carbon Aerosols from Excitation–Emission Matrix Fluorescence Spectroscopy, *J. Phys. Chem. A*, 119(19), 4545–4551, doi:10.1021/jp510709e, 2015.

Piccot, S. D., Watson, J. J. and Jones, J. W.: A global inventory of volatile organic compound emissions from anthropogenic sources, *J. Geophys. Res. Atmos.*, 97(D9), 9897–9912, doi:10.1029/92JD00682, 1992.

Pillarisetti, A., Vaswani, M., Jack, D., Balakrishnan, K., Bates, M. N., Arora, N. K. and Smith, K. R.: Patterns of Stove Usage after Introduction of an Advanced Cookstove: The Long-Term Application of Household Sensors, *Environ. Sci. Technol.*, 48(24), 14525–14533, doi:10.1021/es504624c, 2014.

Pluskal, T., Castillo, S., Villar-Briones, A. and Orešič, M.: MZmine 2: Modular framework for processing, visualizing, and analyzing mass spectrometry-based molecular profile data, *BMC Bioinformatics*, 11(1), 395, doi:10.1186/1471-2105-11-395, 2010.

Pöschl, U.: Atmospheric Aerosols: Composition, Transformation, Climate and Health Effects, *Angew. Chemie Int. Ed.*, 44(46), 7520–7540, doi:10.1002/anie.200501122, 2005.

Pósfai, M., Gelencsér, A., Simonics, R., Arató, K., Li, J., Hobbs, P. V. and Buseck, P. R.: Atmospheric tar balls: Particles from biomass and biofuel burning, *J. Geophys. Res. Atmos.*, 109(D6), n/a-n/a, doi:10.1029/2003JD004169, 2004.

Praske, E., Otkjaer, R. V., Crouse, J. D., Hethcox, J. C., Stoltz, B. M., Kjaergaard, H. G., Wennberg, P. O. and Lester, M. I.: Atmospheric autoxidation is increasingly important in urban and suburban North America, *Proc. Natl. Acad. Sci.*, 115(1), 64–69, doi:10.1073/pnas.1715540115, 2018.

Purcell, J. M., Rodgers, R. P., Hendrickson, C. L. and Marshall, A. G.: Speciation of nitrogen containing aromatics by atmospheric pressure photoionization or electrospray ionization fourier transform ion cyclotron resonance mass spectrometry, *J. Am. Soc. Mass Spectrom.*, 18(7), 1265–1273, doi:10.1016/j.jasms.2007.03.030, 2007.

Raes, F., Dingenen, R. Van, Vignati, E., Wilson, J., Putaud, J.-P., Seinfeld, J. H. and Adams, P.: Formation and cycling of aerosols in the global troposphere, *Atmos. Environ.*, 34(25), 4215–4240, doi:10.1016/S1352-2310(00)00239-9, 2000.

Reddy, B. S. K.: Analysis of Diurnal and Seasonal Behavior of Surface Ozone and Its Precursors (NO_x) at a Semi-Arid Rural Site in Southern India, *Aerosol Air Qual. Res.*, 12(6), 1081–1094, doi:10.4209/aaqr.2012.03.0055, 2012.

Reinhardt, A., Emmenegger, C., Gerrits, B., Panse, C., Dommen, J., Baltensperger, U., Zenobi,

R. and Kalberer, M.: Ultrahigh Mass Resolution and Accurate Mass Measurements as a Tool To Characterize Oligomers in Secondary Organic Aerosols, *Anal. Chem.*, 79(11), 4074–4082, doi:10.1021/ac062425v, 2007.

Renbaum-Wolff, L., Grayson, J. W., Bateman, A. P., Kuwata, M., Sellier, M., Murray, B. J., Shilling, J. E., Martin, S. T. and Bertram, A. K.: Viscosity of α -pinene secondary organic material and implications for particle growth and reactivity, *Proc. Natl. Acad. Sci.*, 110(20), 8014–8019, doi:10.1073/PNAS.1219548110, 2013.

Roach, P. J., Laskin, J. and Laskin, A.: Molecular Characterization of Organic Aerosols Using Nanospray-Desorption/Electrospray Ionization-Mass Spectrometry, *Anal. Chem.*, 82(19), 7979–7986, doi:10.1021/ac101449p, 2010a.

Roach, P. J., Laskin, J. and Laskin, A.: Nanospray desorption electrospray ionization: an ambient method for liquid-extraction surface sampling in mass spectrometry, *Analyst*, 135(9), 2233–2236, doi:10.1039/c0an00312c, 2010b.

Roach, P. J., Laskin, J. and Laskin, A.: Higher-Order Mass Defect Analysis for Mass Spectra of Complex Organic Mixtures, *Anal. Chem.*, 83(12), 4924–4929, doi:10.1021/ac200654j, 2011.

Roden, C. A. and Bond, T. C.: Emission Factors and Real-Time Optical Properties of Particles Emitted from Traditional Wood Burning Cookstoves, *Environ. Sci. Technol.*, 40(21), 6750–6757, doi:10.1021/ES052080I, 2006.

Roden, C. A., Bond, T. C., Conway, S., Osorto Pinel, A. B., MacCarty, N. and Still, D.: Laboratory and field investigations of particulate and carbon monoxide emissions from traditional and improved cookstoves, *Atmos. Environ.*, 43(6), 1170–1181, doi:10.1016/j.atmosenv.2008.05.041, 2009.

Romonosky, D. E., Ali, N. N., Saiduddin, M. N., Wu, M., Lee, H. J. (Julie), Aiona, P. K. and Nizkorodov, S. A.: Effective absorption cross sections and photolysis rates of anthropogenic and biogenic secondary organic aerosols, *Atmos. Environ.*, 130, 172–179, doi:10.1016/j.atmosenv.2015.10.019, 2016.

Romonosky, D. E., Li, Y., Shiraiwa, M., Laskin, A., Laskin, J. and Nizkorodov, S. A.: Aqueous Photochemistry of Secondary Organic Aerosol of α -Pinene and α -Humulene Oxidized with Ozone, Hydroxyl Radical, and Nitrate Radical, *J. Phys. Chem. A*, 121(6), 1298–1309, doi:10.1021/acs.jpca.6b10900, 2017.

RStudio Inc: RStudio: Integrated Development Environment for R, 2016.

Saleh, R., Hennigan, C. J., McMeeking, G. R., Chuang, W. K., Robinson, E. S., Coe, H., Donahue, N. M. and Robinson, A. L.: Absorptivity of brown carbon in fresh and photochemically aged biomass-burning emissions, *Atmos. Chem. Phys.*, 13(15), 7683–7693, doi:10.5194/acp-13-7683-2013, 2013.

Saleh, R., Robinson, E. S., Tkacik, D. S., Ahern, A. T., Liu, S., Aiken, A. C., Sullivan, R. C., Presto, A. A., Dubey, M. K., Yokelson, R. J., Donahue, N. M. and Robinson, A. L.: Brownness

of organics in aerosols from biomass burning linked to their black carbon content, *Nat. Geosci.*, 7, 647–650, 2014.

Sareen, N., Schwier, A. N., Shapiro, E. L., Mitroo, D. and McNeill, V. F.: Secondary organic material formed by methylglyoxal in aqueous aerosol mimics, *Atmos. Chem. Phys.*, 10(3), 997–1016, doi:10.5194/acp-10-997-2010, 2010.

Sarkanen, K. V. and Ludwig, C. H.: *Lignins*, J. Wiley & Sons, New York City., 1971.

Schill, G. P. and Tolbert, M. A.: Heterogeneous ice nucleation on phase-separated organic-sulfate particles: effect of liquid vs. glassy coatings, *Atmos. Chem. Phys.*, 13(9), 4681–4695, doi:10.5194/acp-13-4681-2013, 2013.

Sedlacek III, A. J., Buseck, P. R., Adachi, K., Onasch, T. B., Springston, S. R. and Kleinman, L.: Formation and evolution of tar balls from northwestern US wildfires, *Atmos. Chem. Phys.*, 18(15), 11289–11301, doi:10.5194/acp-18-11289-2018, 2018.

Selimovic, V., Yokelson, R. J., Warneke, C., Roberts, J. M., de Gouw, J., Reardon, J. and Griffith, D. W. T.: Aerosol optical properties and trace gas emissions by PAX and OP-FTIR for laboratory-simulated western US wildfires during FIREX, *Atmos. Chem. Phys.*, 18(4), 2929–2948, doi:10.5194/acp-18-2929-2018, 2018.

Selimovic, V., Yokelson, R. J., McMeeking, G. R. and Coefield, S.: In situ measurements of trace gases, PM, and aerosol optical properties during the 2017 NW US wildfire smoke event, *Atmos. Chem. Phys.*, 19(6), 3905–3926, doi:10.5194/acp-19-3905-2019, 2019.

Shankar, R., An, J. G., Loh, A. and Yim, U. H.: A systematic study of the effects of solvents on phenanthrene photooxidation, *Chemosphere*, 220, 900–909, doi:10.1016/J.CHEMOSPHERE.2018.12.206, 2019.

Shapiro, E. L., Szprengiel, J., Sareen, N., Jen, C. N., Giordano, M. R. and McNeill, V. F.: Light-absorbing secondary organic material formed by glyoxal in aqueous aerosol mimics, *Atmos. Chem. Phys.*, 9(7), 2289–2300, doi:10.5194/acp-9-2289-2009, 2009.

Sharpless, C. M. and Blough, N. V.: The importance of charge-transfer interactions in determining chromophoric dissolved organic matter (CDOM) optical and photochemical properties, *Environ. Sci. Process. Impacts*, 16(4), 654–671, doi:10.1039/C3EM00573A, 2014.

Shiraiwa, M. and Seinfeld, J. H.: Equilibration timescale of atmospheric secondary organic aerosol partitioning, *Geophys. Res. Lett.*, 39(24), n/a-n/a, doi:10.1029/2012GL054008, 2012.

Shiraiwa, M., Ammann, M., Koop, T. and Poschl, U.: Gas uptake and chemical aging of semisolid organic aerosol particles, *Proc. Natl. Acad. Sci.*, 108(27), 11003–11008, doi:10.1073/pnas.1103045108, 2011.

Shiraiwa, M., Li, Y., Tsimpidi, A. P., Karydis, V. A., Berkemeier, T., Pandis, S. N., Lelieveld, J., Koop, T. and Pöschl, U.: Global distribution of particle phase state in atmospheric secondary organic aerosols, *Nat. Commun.*, 8, 15002, doi:10.1038/ncomms15002, 2017.

- Shvidenko, A. Z. and Schepaschenko, D. G.: Climate change and wildfires in Russia, *Contemp. Probl. Ecol.*, 6(7), 683–692, doi:10.1134/S199542551307010X, 2013.
- Silva, R. A., Adelman, Z., Fry, M. M. and West, J. J.: The Impact of Individual Anthropogenic Emissions Sectors on the Global Burden of Human Mortality due to Ambient Air Pollution, *Environ. Health Perspect.*, 124(11), 1776–1784, doi:10.1289/EHP177, 2016.
- Simoneit, B. R. T.: Biomass burning — a review of organic tracers for smoke from incomplete combustion, *Appl. Geochemistry*, 17(3), 129–162, doi:10.1016/S0883-2927(01)00061-0, 2002.
- Simoneit, B. R. T., Rogge, W. F., Mazurek, M. A., Standley, L. J., Hildemann, L. M. and Cass, G. R.: Lignin pyrolysis products, lignans, and resin acids as specific tracers of plant classes in emissions from biomass combustion, *Environ. Sci. Technol.*, 27(12), 2533–2541, doi:10.1021/es00048a034, 1993.
- Simoneit, B. R. T., Schauer, J. J., Nolte, C. G., Oros, D. R., Elias, V. O., Fraser, M. P., Rogge, W. F. and Cass, G. R.: Levoglucosan, a tracer for cellulose in biomass burning and atmospheric particles, *Atmos. Environ.*, 33(2), 173–182, doi:10.1016/S1352-2310(98)00145-9, 1999.
- Simpson, I. J., Aburizaiza, O. S., Siddique, A., Barletta, B., Blake, N. J., Gartner, A., Khwaja, H., Meinardi, S., Zeb, J. and Blake, D. R.: Air Quality in Mecca and Surrounding Holy Places in Saudi Arabia During Hajj: Initial Survey, *Environ. Sci. Technol.*, 48(15), 8529–8537, doi:10.1021/es5017476, 2014.
- Slade, J. H., Shiraiwa, M., Arangio, A., Su, H., Pöschl, U., Wang, J. and Knopf, D. A.: Cloud droplet activation through oxidation of organic aerosol influenced by temperature and particle phase state, *Geophys. Res. Lett.*, 44(3), 1583–1591, doi:10.1002/2016GL072424, 2017.
- Smith, J. D., Kinney, H. and Anastasio, C.: Phenolic carbonyls undergo rapid aqueous photodegradation to form low-volatility, light-absorbing products, *Atmos. Environ.*, 126, 36–44, doi:10.1016/J.ATMOSENV.2015.11.035, 2016.
- Smith, J. S., Laskin, A. and Laskin, J.: Molecular Characterization of Biomass Burning Aerosols Using High-Resolution Mass Spectrometry, *Anal. Chem.*, 81(4), 1512–1521, doi:10.1021/ac8020664, 2009.
- Smith, K. R., Khalil, M. A. K., Rasmussen, R. A., Thorneloe, S. A., Manegdeg, F. and Apte, M.: Greenhouse gases from biomass and fossil fuel stoves in developing countries: A Manila pilot study, *Chemosphere*, 26(1–4), 479–505, doi:10.1016/0045-6535(93)90440-G, 1993.
- Smith, K. R., Uma, R., Kishore, V., Lata, K., Joshi, V., Zhang, J., Rasmussen, R. and Khalil, M.: Greenhouse gases from small-scale combustion devices in developing countries, phase IIA. Household stoves in India (EPA/600/R-00/052), U.S. Environmental Protection Agency, Washington D.C., 2000a.
- Smith, K. R., Uma, R., Kishore, V. V. N., Zhang, J., Joshi, V. and Khalil, M. A. K.: Greenhouse Implications of Household Stoves: An Analysis for India, *Annu. Rev. Energy Env.*, 25, 741–63, 2000b.

Smith, K. R., Bruce, N., Balakrishnan, K., Adair-Rohani, H., Balmes, J., Chafe, Z., Dherani, M., Hosgood, H. D., Mehta, S., Pope, D., Rehfuess, E. and HAP CRA Risk Expert Group: Millions dead: how do we know and what does it mean? Methods used in the comparative risk assessment of household air pollution., *Annu. Rev. Public Health*, 35, 185–206, doi:10.1146/annurev-publhealth-032013-182356, 2014.

Smol, M. and Włodarczyk-Makula, M.: The Effectiveness in the Removal of PAHs from Aqueous Solutions in Physical and Chemical Processes: A Review, *Polycycl. Aromat. Compd.*, 37(4), 292–313, doi:10.1080/10406638.2015.1105828, 2017.

Sofowote, U. M., Hung, H., Rastogi, A. K., Westgate, J. N., Deluca, P. F., Su, Y. and McCarry, B. E.: Assessing the long-range transport of PAH to a sub-Arctic site using positive matrix factorization and potential source contribution function, *Atmos. Environ.*, 45(4), 967–976, doi:10.1016/J.ATMOSENV.2010.11.005, 2011.

Song, J., Li, M., Jiang, B., Wei, S., Fan, X. and Peng, P.: Molecular Characterization of Water-Soluble Humic like Substances in Smoke Particles Emitted from Combustion of Biomass Materials and Coal Using Ultrahigh-Resolution Electrospray Ionization Fourier Transform Ion Cyclotron Resonance Mass Spectrometry, *Environ. Sci. Technol.*, 52(5), 2575–2585, doi:10.1021/acs.est.7b06126, 2018.

Stockwell, C. E., Veres, P. R., Williams, J. and Yokelson, R. J.: Characterization of biomass burning emissions from cooking fires, peat, crop residue, and other fuels with high-resolution proton-transfer-reaction time-of-flight mass spectrometry, *Atmos. Chem. Phys.*, 15(2), 845–865, doi:10.5194/acp-15-845-2015, 2015.

Stockwell, C. E., Christian, T. J., Goetz, J. D., Jayarathne, T., Bhave, P. V., Praveen, P. S., Adhikari, S., Maharjan, R., DeCarlo, P. F., Stone, E. A., Saikawa, E., Blake, D. R., Simpson, I. J., Yokelson, R. J. and Panday, A. K.: Nepal Ambient Monitoring and Source Testing Experiment (NAMaSTE): emissions of trace gases and light-absorbing carbon from wood and dung cooking fires, garbage and crop residue burning, brick kilns, and other sources, *Atmos. Chem. Phys.*, 16(17), 11043–11081, doi:10.5194/acp-16-11043-2016, 2016.

Styler, S. A., Baergen, A. M., Donaldson, D. J. and Herrmann, H.: Organic Composition, Chemistry, and Photochemistry of Urban Film in Leipzig, Germany, *ACS Earth Sp. Chem.*, 2(9), 935–945, doi:10.1021/acsearthspacechem.8b00087, 2018.

Sullivan, A. P., May, A. A., Lee, T., McMeeking, G. R., Kreidenweis, S. M., Akagi, S. K., Yokelson, R. J., Urbanski, S. P. and Collett Jr., J. L.: Airborne characterization of smoke marker ratios from prescribed burning, *Atmos. Chem. Phys.*, 14(19), 10535–10545, doi:10.5194/acp-14-10535-2014, 2014.

Sumlin, B. J., Pandey, A., Walker, M. J., Pattison, R. S., Williams, B. J. and Chakrabarty, R. K.: Atmospheric Photooxidation Diminishes Light Absorption by Primary Brown Carbon Aerosol from Biomass Burning, *Environ. Sci. Technol. Lett.*, 4(12), 540–545, doi:10.1021/acs.estlett.7b00393, 2017.

Surawski, N. C., Sullivan, A. L., Meyer, C. P., Roxburgh, S. H. and Polglase, P. J.: Greenhouse

gas emissions from laboratory-scale fires in wildland fuels depend on fire spread mode and phase of combustion, *Atmos. Chem. Phys.*, 15(9), 5259–5273, doi:10.5194/acp-15-5259-2015, 2015.

Surratt, J. D., Chan, A. W. H., Eddingsaas, N. C., Chan, M., Loza, C. L., Kwan, A. J., Hersey, S. P., Flagan, R. C., Wennberg, P. O. and Seinfeld, J. H.: Reactive intermediates revealed in secondary organic aerosol formation from isoprene., *Proc. Natl. Acad. Sci. U. S. A.*, 107(15), 6640–5, doi:10.1073/pnas.0911114107, 2010.

Talrose, V., Yermakov, A. N., Usov, A. A., Goncharova, A. A., Leskin, A. N., Messineva, N. A., Trusova, N. V. and Efimkina, M. V.: UV/Visible Spectra, in NIST Chemistry WebBook, NIST Standard Reference Database Number 69, edited by P. J. Linstrom and W. G. Mallard, National Institute of Standards and Technology, Gaithersburg MD, 20899., 2017.

Tang, H. and Thompson, J. E.: Light-Absorbing Products Form during the Aqueous Phase Reaction of Phenolic Compounds in the Presence of Nitrate and Nitrite with UV Illumination, *Open J. Air Pollut.*, 01(02), 13–21, doi:10.4236/ojap.2012.12002, 2012.

Tasoglou, A. and Pandis, S. N.: Formation and chemical aging of secondary organic aerosol during the β -caryophyllene oxidation, *Atmos. Chem. Phys.*, 15(11), 6035–6046, doi:10.5194/acp-15-6035-2015, 2015.

Thornton, J. A. and Abbatt, J. P. D.: N_2O_5 Reaction on Submicron Sea Salt Aerosol: Kinetics, Products, and the Effect of Surface Active Organics, *J. Phys. Chem. A*, 109(44), 10004–10012, doi:10.1021/jp054183t, 2005.

Thornton, J. A., Braban, C. F. and Abbatt, J. P. D.: N_2O_5 hydrolysis on sub-micron organic aerosols: the effect of relative humidity, particle phase, and particle size, *Phys. Chem. Chem. Phys.*, 5(20), 4593, doi:10.1039/b307498f, 2003.

Tihay-Felicelli, V., Santoni, P. A., Gerandi, G. and Barboni, T.: Smoke emissions due to burning of green waste in the Mediterranean area: Influence of fuel moisture content and fuel mass, *Atmos. Environ.*, 159, 92–106, doi:10.1016/J.ATMOSENV.2017.04.002, 2017.

Tivanski, A. V., Hopkins, R. J., Tyliczszak, T. and Gilles, M. K.: Oxygenated Interface on Biomass Burn Tar Balls Determined by Single Particle Scanning Transmission X-ray Microscopy, *J. Phys. Chem. A*, 111(25), 5448–5458, doi:10.1021/jp070155u, 2007.

Tkacik, D. S., Robinson, E. S., Ahern, A., Saleh, R., Stockwell, C., Veres, P., Simpson, I. J., Meinardi, S., Blake, D. R., Yokelson, R. J., Presto, A. A., Sullivan, R. C., Donahue, N. M. and Robinson, A. L.: A dual-chamber method for quantifying the effects of atmospheric perturbations on secondary organic aerosol formation from biomass burning emissions, *J. Geophys. Res. Atmos.*, 122(11), 6043–6058, doi:10.1002/2016JD025784, 2017.

Tomaz, S., Cui, T., Chen, Y., Sexton, K. G., Roberts, J. M., Warneke, C., Yokelson, R. J., Surratt, J. D. and Turpin, B. J.: Photochemical Cloud Processing of Primary Wildfire Emissions as a Potential Source of Secondary Organic Aerosol, *Environ. Sci. Technol.*, 52(19), 11027–11037, doi:10.1021/acs.est.8b03293, 2018.

- Tóth, A., Hoffer, A., Nyiró-Kósa, I., Pósfai, M. and Gelencsér, A.: Atmospheric tar balls: aged primary droplets from biomass burning?, *Atmos. Chem. Phys.*, 14(13), 6669–6675, doi:10.5194/acp-14-6669-2014, 2014.
- Tsai, S. M., Zhang, J. (Jim), Smith, K. R., Ma, Y., Rasmussen, R. A. and Khalil, M. A. K.: Characterization of Non-methane Hydrocarbons Emitted from Various Cookstoves Used in China, *Environ. Sci. Technol.*, 37(13), 2869–2877, doi:10.1021/es026232a, 2003.
- Tu, P., Hall, W. A. and Johnston, M. V.: Characterization of Highly Oxidized Molecules in Fresh and Aged Biogenic Secondary Organic Aerosol, *Anal. Chem.*, 88(8), 4495–4501, doi:10.1021/acs.analchem.6b00378, 2016.
- Turro, N. J., Ramamurthy, V. and Scaiano, J. C.: *Modern molecular photochemistry of organic molecules*, University Science Books, Sausalito, CA., 2009.
- Venkatachari, P. and Hopke, P. K.: Characterization of products formed in the reaction of ozone with α -pinene: case for organic peroxides, *J. Environ. Monit.*, 10(8), 966, doi:10.1039/b804357d, 2008.
- Venugopala, K. N., Rashmi, V. and Odhav, B.: Review on natural coumarin lead compounds for their pharmacological activity., *Biomed Res. Int.*, 2013, 963248, doi:10.1155/2013/963248, 2013.
- Walser, M. L., Desyaterik, Y., Laskin, J., Laskin, A. and Nizkorodov, S. A.: High-resolution mass spectrometric analysis of secondary organic aerosol produced by ozonation of limonene, *Phys. Chem. Chem. Phys.*, 10(7), 1009–1022, doi:10.1039/B712620D, 2008.
- Wan, E. C. H. and Yu, J. Z.: Determination of sugar compounds in atmospheric aerosols by liquid chromatography combined with positive electrospray ionization mass spectrometry, *J. Chromatogr. A*, 1107(1–2), 175–181, doi:10.1016/j.chroma.2005.12.062, 2006.
- Wang, J., Jacob, D. J. and Martin, S. T.: Sensitivity of sulfate direct climate forcing to the hysteresis of particle phase transitions, *J. Geophys. Res.*, 113(D11), D11207, doi:10.1029/2007JD009368, 2008.
- Wang, M. and Penner, J. E.: Aerosol indirect forcing in a global model with particle nucleation, *Atmos. Chem. Phys.*, 9(1), 239–260, doi:10.5194/acp-9-239-2009, 2009.
- Wang, Y., Liang, H., Zhang, Q., Cheng, W. and Yi, S.: Phytochemical and chemotaxonomic study on *Ficus tsiangii* Merr. ex Corner, *Biochem. Syst. Ecol.*, 57, 210–215, doi:10.1016/j.bse.2014.08.003, 2014.
- Wang, Y., Hu, M., Lin, P., Guo, Q., Wu, Z., Li, M., Zeng, L., Song, Y., Zeng, L., Wu, Y., Guo, S., Huang, X. and He, L.: Molecular Characterization of Nitrogen-Containing Organic Compounds in Humic-like Substances Emitted from Straw Residue Burning, *Environ. Sci. Technol.*, 51(11), 5951–5961, doi:10.1021/acs.est.7b00248, 2017a.
- Wang, Y., Ren, J., Huang, X. H. H., Tong, R. and Yu, J. Z.: Synthesis of Four Monoterpene-

Derived Organosulfates and Their Quantification in Atmospheric Aerosol Samples, *Environ. Sci. Technol.*, 51(12), 6791–6801, doi:10.1021/acs.est.7b01179, 2017b.

Wathore, R., Mortimer, K. and Grieshop, A. P.: In-Use Emissions and Estimated Impacts of Traditional, Natural- and Forced-Draft Cookstoves in Rural Malawi, *Environ. Sci. Technol.*, 51(3), 1929–1938, doi:10.1021/acs.est.6b05557, 2017.

Weber, M. G. and Stocks, B. J.: Forest Fires and Sustainability in the Boreal Forests of Canada, *Ambio*, 27(7), 545–550, 1998.

Williams, J., de Reus, M., Krejci, R., Fischer, H. and Ström, J.: Application of the variability-size relationship to atmospheric aerosol studies: estimating aerosol lifetimes and ages, *Atmos. Chem. Phys.*, 2(2), 133–145, doi:10.5194/acp-2-133-2002, 2002.

Willoughby, A., Wozniak, A. and Hatcher, P.: Detailed Source-Specific Molecular Composition of Ambient Aerosol Organic Matter Using Ultrahigh Resolution Mass Spectrometry and ¹H NMR, *Atmosphere*, 7(6), 79, doi:10.3390/atmos7060079, 2016.

Wilson, J., Imre, D., Beránek, J., Shrivastava, M. and Zelenyuk, A.: Evaporation Kinetics of Laboratory-Generated Secondary Organic Aerosols at Elevated Relative Humidity, *Environ. Sci. Technol.*, 49(1), 243–249, doi:10.1021/es505331d, 2015.

Wong, J. P. S., Zhou, S. and Abbatt, J. P. D.: Changes in Secondary Organic Aerosol Composition and Mass due to Photolysis: Relative Humidity Dependence., *J. Phys. Chem. A*, 119(19), 4309–16, doi:10.1021/jp506898c, 2015a.

Wong, J. P. S., Lee, A. K. Y. and Abbatt, J. P. D.: Impacts of Sulfate Seed Acidity and Water Content on Isoprene Secondary Organic Aerosol Formation, *Environ. Sci. Technol.*, 49(22), 13215–13221, doi:10.1021/acs.est.5b02686, 2015b.

Wong, J. P. S., Nenes, A. and Weber, R. J.: Changes in Light Absorptivity of Molecular Weight Separated Brown Carbon Due to Photolytic Aging, *Environ. Sci. Technol.*, 51(15), 8414–8421, doi:10.1021/acs.est.7b01739, 2017.

Wood, A. W., Chang, R. L., Levin, W., Thakker, D. R., Yagi, H., Sayer, J. M., Jerina, D. M. and Conney, A. H.: Mutagenicity of the Enantiomers of the Diastereomeric Bay-Region Benzo(c)phenanthrene 3,4-Diol-1,2-epoxides in Bacterial and Mammalian Cells., 1984.

World Health Organization, W. H.: Indoor air quality: Organic pollutants, *Environ. Technol. Lett.*, 10(9), 855–858, doi:10.1080/09593338909384805, 1989.

Wotton, B. M. and Flannigan, M. D.: Length of the fire season in a changing climate, *For. Chron.*, 69(2), 187–192, doi:10.5558/tfc69187-2, 1993.

Wotton, B. M., Nock, C. A. and Flannigan, M. D.: Forest fire occurrence and climate change in Canada, *Int. J. Wildl. Fire*, 19(3), 253, doi:10.1071/WF09002, 2010.

Xiao, Q. Y., Saikawa, E., Yokelson, R. J., Chen, P. F., Li, C. L. and Kang, S. C.: Indoor air

pollution from burning yak dung as a household fuel in Tibet, *Atmos. Environ.*, 102, 406–412, doi:10.1016/j.atmosenv.2014.11.060, 2015.

Xie, M., Chen, X., Hays, M. D. and Holder, A. L.: Composition and light absorption of N-containing aromatic compounds in organic aerosols from laboratory biomass burning, *Atmos. Chem. Phys.*, 19(5), 2899–2915, doi:10.5194/acp-19-2899-2019, 2019.

Xu, J., Zhou, W., Hou, J., Pu, S., Yan, L. and Wang, J.: Electrosyntheses of high-quality poly(5-nitroindole) films in boron trifluoride diethyl etherate containing additional diethyl ether, *J. Polym. Sci. Part A Polym. Chem.*, 43(17), 3986–3997, doi:10.1002/pola.20893, 2005.

Xue, W. and Warshawsky, D.: Metabolic activation of polycyclic and heterocyclic aromatic hydrocarbons and DNA damage: A review, *Toxicol. Appl. Pharmacol.*, 206(1), 73–93, doi:10.1016/J.TAAP.2004.11.006, 2005.

Yasmeen, F., Vermeylen, R., Szmigielski, R., Inuma, Y., Böge, O., Herrmann, H., Maenhaut, W. and Claeys, M.: Terpenylic acid and related compounds: precursors for dimers in secondary organic aerosol from the ozonolysis of α - and β -pinene, *Atmos. Chem. Phys.*, 10(19), 9383–9392, doi:10.5194/acp-10-9383-2010, 2010.

Yevich, R. and Logan, J. A.: An assessment of biofuel use and burning of agricultural waste in the developing world, *Global Biogeochem. Cycles*, 17(4), n/a-n/a, doi:10.1029/2002GB001952, 2003.

Yokelson, R. J., Griffith, D. W. T. and Ward, D. E.: Open-path Fourier transform infrared studies of large-scale laboratory biomass fires, *J. Geophys. Res. Atmos.*, 101(D15), 21067–21080, doi:10.1029/96JD01800, 1996.

Yokelson, R. J., Christian, T. J., Karl, T. G. and Guenther, A.: The tropical forest and fire emissions experiment: laboratory fire measurements and synthesis of campaign data, *Atmos. Chem. Phys.*, 8(13), 3509–3527, doi:10.5194/acp-8-3509-2008, 2008.

You, Y., Renbaum-Wolff, L., Carreras-Sospedra, M., Hanna, S. J., Hiranuma, N., Kamal, S., Smith, M. L., Zhang, X., Weber, R. J., Shilling, J. E., Dabdub, D., Martin, S. T. and Bertram, A. K.: Images reveal that atmospheric particles can undergo liquid-liquid phase separations, *Proc. Natl. Acad. Sci.*, 109(33), 13188–13193, doi:10.1073/pnas.1206414109, 2012.

You, Y., Smith, M. L., Song, M., Martin, S. T. and Bertram, A. K.: Liquid–liquid phase separation in atmospherically relevant particles consisting of organic species and inorganic salts, *Int. Rev. Phys. Chem.*, 33(1), 43–77, doi:10.1080/0144235X.2014.890786, 2014.

Zhang, J., Smith, K. ., Ma, Y., Ye, S., Jiang, F., Qi, W., Liu, P., Khalil, M. A. ., Rasmussen, R. . and Thorneloe, S. .: Greenhouse gases and other airborne pollutants from household stoves in China: a database for emission factors, *Atmos. Environ.*, 34(26), 4537–4549, doi:10.1016/S1352-2310(99)00450-1, 2000.

Zhao, R., Lee, A. K. Y., Huang, L., Li, X., Yang, F. and Abbatt, J. P. D.: Photochemical processing of aqueous atmospheric brown carbon, *Atmos. Chem. Phys.*, 15(11), 6087–6100,

doi:10.5194/acp-15-6087-2015, 2015.

Zhong, M. and Jang, M.: Dynamic light absorption of biomass-burning organic carbon photochemically aged under natural sunlight, *Atmos. Chem. Phys.*, 14(3), 1517–1525, doi:10.5194/acp-14-1517-2014, 2014.

Zhou, S., Lee, A. K. Y., McWhinney, R. D. and Abbatt, J. P. D.: Burial Effects of Organic Coatings on the Heterogeneous Reactivity of Particle-Borne Benzo[a]pyrene (BaP) toward Ozone, *J. Phys. Chem. A*, 116(26), 7050–7056, doi:10.1021/jp3030705, 2012.

Zhou, S., Yeung, L. W. Y., Forbes, M. W., Mabury, S. and Abbatt, J. P. D.: Epoxide formation from heterogeneous oxidation of benzo[a]pyrene with gas-phase ozone and indoor air †, *Environ. Sci. Process. Impacts*, 19(10), 1292–1299, doi:10.1039/c7em00181a, 2017a.

Zhou, S., Collier, S., Jaffe, D. A., Briggs, N. L., Hee, J., Sedlacek III, A. J., Kleinman, L., Onasch, T. B. and Zhang, Q.: Regional influence of wildfires on aerosol chemistry in the western US and insights into atmospheric aging of biomass burning organic aerosol, *Atmos. Chem. Phys.*, 17(3), 2477–2493, doi:10.5194/acp-17-2477-2017, 2017b.

Zuend, A., Marcolli, C., Peter, T. and Seinfeld, J. H.: Computation of liquid-liquid equilibria and phase stabilities: implications for RH-dependent gas/particle partitioning of organic-inorganic aerosols, *Atmos. Chem. Phys.*, 10(16), 7795–7820, doi:10.5194/acp-10-7795-2010, 2010.